Measurement of the cross-section for W boson production in association with b-jets in proton-proton collisions at $\sqrt{s} = 7$ TeV at the LHC using the ATLAS detector

A dissertation presented

by

Giovanni Zevi Della Porta

to

The Department of Physics

in partial fulfillment of the requirements

for the degree of

Doctor of Philosophy

in the subject of

Physics

Harvard University

Cambridge, Massachusetts

May 2013

Thesis advisor

Melissa Franklin

Author

Giovanni Zevi Della Porta

Measurement of the cross-section for W boson production in association with b-jets in proton-proton collisions at $\sqrt{s} = 7$ TeV at the LHC using the ATLAS detector

Abstract

This dissertation presents a measurement of the W+b-jets ($pp \rightarrow W + b(\bar{b}) + X$) production cross-section in proton–proton collisions at a center-of-mass energy of 7 TeV at the LHC. The results are based on data corresponding to an integrated luminosity of 4.6 fb^{-1}, collected with the ATLAS detector. The measurement probes the QCD sector of the Standard Model at high energy, in a region where b-quark mass and double parton scattering play an important role. In addition, the measurement is relevant for searches for physics beyond the Standard Model in final states with a W boson and b-jets.

The measurement relies on the leptonic decay modes of the W, and on the identification of b-jets. The backgrounds to the W+b-jets process are estimated using Monte Carlo simulation and data-driven techniques. Cross-sections, corrected for all known detector effects and quoted in a limited kinematic range, are presented as a function of jet multiplicity and of the transverse momentum of the leading b-jet for both the muon and electron decay modes of the W boson.

Contents

List of Figures

List of Tables

Acknowledgments

I am grateful to my mother Elisabetta and my father Francesco, as well as to my aunt Susanna, for their love and support, and for being extraordinary people who never fail to inspire me.

In the Harvard ATLAS group, I am particularly grateful to Melissa Franklin for being a great advisor, for her guidance, support, and for her infinite thought-provoking questions.

I am also grateful to the other professors, Joao Guimaraes da Costa, John Huth, Masahiro Morii, as well as George Brandenburg, for their encouragement and teachings. In my four years at CERN, one of you was always there to help me in times of need.

Among the post-docs and students, I thank in particular Alberto Belloni, for teaching me how to work on detectors; Ben Smith, for teaching me how to write code; and most importantly Pierluigi Catastini, for teaching me how to make a measurement, from the beginning to the end.

I thank Laura Jeanty and Michael Kagan, my teammates in many muon-related adventures, for the time we spent understanding physics together, always having each other's backs and speaking our mind openly.

It has been a pleasure to work with everyone else in the group: Kevin Black, Shulamit Moed, Corrinne Mills, Geraldine Conti, David Lopez Mateos, Bart Butler, Lashkar Kashif, Verena Martinez Outschoorn, Srivas Prasad, Kevin Mercurio, William Spearman, Jake Connors, Tomo Lazovich, Siyuan Sun, Emma Tolley. As well as the undergraduates: Jeremy Cushman, John Montroy, Max Swiatlowski and many others who made the summers brighter. Thank you all for making my graduate

years at CERN such a memorable experience.

I would like to thank Doug Finkbeiner for his enthusiasm and curiosity, and for being on my thesis committee, and Ludovico Pontecorvo for being so supportive of my future plans.

I would also like to thank my collaborators in ATLAS and at CERN, who have enabled this work to go forward. In particular Tiesheng Dai, Roberto Ferrari, Mauro Iodice, Andrea Messina, Enrico Pasqualucci, Frank Taylor, Sotiris Vlachos, Stephanie Zimmermann, and many others who I've enjoyed working with, as well as Fabiola Gianotti and Gigi Rolandi for their precious advice.

I take this occasion to thank Charles Baltay and Andrew Szymkowiak at Yale and Stephan Simion at CERN for letting me take my first look at experimental physics while I was still an undergraduate student.

I am grateful to my graduate class at Harvard, Eddie, Jack, Michael and everyone else for being such a fun group. In fact, I could not have done this without my friends in the US, in Geneva, and at home: thank you for being there for me, even when I was far away. And a special thank you to Sofia and Jon, for being wonderful people with beautiful minds.

Anna, thank you for bringing out the best in me and for making me happy.

Chapter 1

Overview

This thesis describes a measurement of the W+b-jets production cross-section in proton-proton collisions, $pp \to W + b(\bar{b}) + X$, at the $\sqrt{s} = 7$ TeV LHC using the ATLAS detector. This brief overview includes the most important characteristics of the measurement, as well as a summary of its motivations in terms of theoretical aspects and previous experimental results.

From the theoretical point of view, W+b-jets events can be produced in single-parton scattering and double-parton scattering (DPS) events. In double-parton scattering events, a W boson and b-jets can be produced from different parton–parton interactions within the same proton-proton collision. Perturbative Quantum Chromodynamics (pQCD) can be used to calculate the single-parton cross-section, while the double-parton-scattering cross-section can only be calculated through effective formalism. The W+b-jets process is thus a probe into pQCD calculations, as well as into the assumptions behind the effective description of DPS.

From the experimental point of view, the W+b-jets process plays an important

role in many physics analyses that use final states with a W and one or more b-jets. It is a background to the Higgs boson associated-production process WH, with $H \to b\bar{b}$ decays [87]. Additionally, the W+b-jets process is also an irreducible background in some searches for physics beyond the Standard Model [89], and in measurements of single top-quark properties [90], due to the large branching fraction of the $t \to Wb$ decay. In such analyses, the poorly known W+b-jets yield and kinematics can result in large uncertainties.

Previous measurements of the W+b-jets process have a relatively short history, starting in 2009, due to the small cross-section and the experimental challenges involved. Measurements of the W+b-jets cross-section in proton–antiproton collisions at $\sqrt{s} = 1.96$ TeV have been reported by the CDF Collaboration [91] and by the D0 Collaboration [92]. The ATLAS Collaboration reported a previous measurement based on 36 pb^{-1} of data collected in pp collisions at $\sqrt{s} = 7$ TeV [93]. These measurements cannot be compared directly to each other, since they are based on different collision energies and on different final states. However, each measurement can be compared to a corresponding theoretical prediction, made using a common pQCD calculation [84, 85, 81], as shown in Table 1.1. The CDF measurement of $\sigma(p\bar{p} \to W + b + X) \times \mathcal{B}(W \to \ell\nu) + 2 * \sigma(p\bar{p} \to W + b\bar{b}) \times \mathcal{B}(W \to \ell\nu)$, and the ATLAS measurement of $\sigma(pp \to W + b(\bar{b}) + X) \times \mathcal{B}(W \to \ell\nu)$ are both found to be larger than the corresponding theoretical cross-sections calculated at NLO. The statistical significance of the discrepancy is 2.8 (1.5) standard deviations for CDF (ATLAS). The D0 measurement of $\sigma(p\bar{p} \to W + b(\bar{b}) + X) \times \mathcal{B}(W \to \ell\nu)$ is found to be lower than the theoretical prediction , but in agreement within one standard

deviation.

Table 1.1: Previous measurements of the W+b-jets process. The CDF result is based on measuring the number of b-jets, while the ATLAS and D0 results measure the number events with $N_{b-\text{jets}} > 1$.

Experiment	N_{jets}	$N_{b-\text{jets}}$	σ_{measured} [pb]	$\sigma_{\text{predicted}}$ [pb]
CDF [91]	1, 2	measured	2.74 ± 0.27 (stat) ± 0.42 (syst)	1.22 ± 0.14
ATLAS [93]	1, 2	> 1	10.2 ± 1.9 (stat) ± 2.6 (syst)	4.8 ± 1.3
D0 [92]	> 1	> 1	1.05 ± 0.12	$1.34^{+0.41}_{-0.34}$

The events used to perform the measurement described in this thesis have been collected during the 2011 LHC run, and they correspond to an integrated luminosity of 4.6 fb^{-1}. The W+b-jets measurement is performed within a limited phase space due to the large backgrounds and the detector capabilities. To obtain the greatest amount of information, this phase space is subdivided whenever possible, resulting in separate measurements for the 1-jet and 2-jet final states, and differential measurements as a function of the b-jet transverse momentum (p_{T}). To be selected, events are required to be consistent with the decay of a W boson to the $\ell\nu$ ($\ell = \mu, e$) final state, and to contain either one or two jets. Additionally, a single jet is required to pass the b-tagging requirements.

The selected sample is dominated by backgrounds, since various processes can produce a final state with a W boson or a b-tagged jet. The main backgrounds are W+c-jets and W+light-jets events, with a real W and fake b-jets, and multijet events, with a fake W and real b-jets. The resonant production of W and b through a top decay ($t \to Wb$) is not included in the measurement, so the $t\bar{t}$ ($pp \to t\bar{t} \to Wb W\bar{b}$) and single-top ($pp \to t \to Wb$ and $pp \to t\bar{b} \to Wb\bar{b}$) processes are also treated as backgrounds. These backgrounds are reduced using selection criteria, such as lepton

and b-tagging requirements (for the multijet and W backgrounds) and by rejecting events with three or more jets, or two or more b-tagged jets (for the top background). The background contributions which enter the selected sample are estimated using several techniques, based on the properties of each background process. In order to cross-check the W+b-jets measurement, and to produce a more precise result, an additional set of measurements is performed including the contribution from single top-quark production as part of the signal.

The chapters of this thesis are organized as follows. Chapter 2 introduces the W boson, jets, and b-jets, while Chapter 3 presents a historical account of the development of W+b-jets theoretical calculations, and of the existing experimental results. Chapter 4 introduces the Large Hadron Collider, used to generate proton-proton collisions. Chapter 5 provides an overview of the ATLAS detector, focusing on the components most relevant for the W+b-jets final state. Chapter 6 covers the reconstruction of physics objects such as electrons, muons, jets, based on the detector signals originating in the ATLAS detector. Finally, Chapter 7 describes the measurement of the W+b-jets cross-section and its comparison to theoretical predictions.

Chapter 2

Background: the W boson, jets and b-jets

The W+b-jets process is relatively new to particle physicists. Its production cross-section was first calculated in 1993, in the context of top-quark searches, but its first inclusive measurement dates only from 2009, and this thesis presents its first differential measurement. On the other hand, the W boson and the b-quark have had long and independent histories. This short chapter introduces the W boson, the W+jets process, and the b-quark.

The W boson is a charged massive ($m_W = 80.38$ GeV) gauge boson that is responsible, together with the Z boson, for mediating weak interactions. It was predicted in the 1960s by Glashow, Weinberg and Salam in the context of the unification of the electromagnetic and weak forces [70]. The W boson mass is understood in the Standard Model as originating from the Higgs mechanism, which has recently been validated by the discovery of a Higgs particle with mass $m_H \sim 125$ GeV [88]. The W

boson itself was first observed by the UA1 and UA2 experiments in 1983, at the Super Proton-Antiproton Synchrotron (S$p\bar{p}$S) accelerator at CERN [71, 72]. W bosons at hadron colliders are produced primarily through quark-antiquark annihilation, in which the quark and antiquark need not be of the same family, but they need to be an up-type quark (charge $\frac{2}{3}e$) and a down-type antiquark ($\frac{1}{3}e$), or an up-type antiquark ($-\frac{2}{3}e$) and a down-type quark ($-\frac{1}{3}e$). After being produced, W bosons decay to quark-antiquark roughly 67% of the time and lepton-neutrino roughly 33% of the time. The leptonic decays of the W boson have played an essential role in modern particle physics, enabling physicists at hadron colliders to study weak processes despite the large backgrounds due to strong interactions.

The production of W bosons in association with jets has been studied in detail starting from the 1980s. The W+jets process has played an important role as a background in the discovery of the top quark, and continues to play a major role in searches for physics beyond the Standard Model, and in measurements of Higgs boson couplings. The W+jets process is understood in terms of the radiation of additional gluons and quarks in association with W production, and it can be modeled using perturbative Quantum Chromodynamics (pQCD). The transition from colored particles (quarks and gluons) to color-neutral hadrons is the result of a complicated process that cannot be modeled perturbatively. This non-pertubative process is commonly modeled using an effective approach implemented by Monte Carlo simulators, taking place in two steps. At first, high-energy colored particles radiate low-energy colored particles, forming a *parton shower*. Then, during the *hadronization* phase, low-energy colored particles are combined to form color-neutral hadrons. The over-

all process result in a large number of individual hadrons which can be clustered as *jets* using the algorithms described in Section 6.5. As a result of showering and hadronization, the number of jets with transverse momenta above a given threshold can often be different from the number of outgoing partons considered in the pQCD calculation for a specific event. This is relevant when exclusive pQCD calculations (such as $W + 0$, $W + 1$, $W + 2$ partons) are combined to form an inclusive sample (such as the W+jets sample). In these cases, a procedure known as *matching* can be used to avoid double-counting. An overview of the theoretical issues in the study of W+jets production can be found in reference [68]. A recent comparison between data collected by the ATLAS detector in proton-proton collisions at 7 TeV and different W+jets calculations is presented in Figure 2.1 [35]. The left plot represents the W+jets differential cross-section as a function of jet multiplicity for jets with $p_{\mathrm{T}} > 20$ GeV, and the right plot for jets with $p_{\mathrm{T}} > 30$ GeV. The $\mathcal{O}(\alpha_s)$ scaling characteristic of additional parton emissions is visible in both plots as a cross-section reduction of $\mathcal{O}(\alpha_s)$ for each additional jet. The scaling is steeper for higher p_{T} jets (right), where α_s is smaller, and less steep for lower p_{T} jets (left), where α_s is larger. The ALPGEN [95] Monte Carlo, which uses HERWIG [96] for the parton shower and hardonization, agrees well with the data in the description of W+jets production, and it is used as the primary MC simulation in the W+b-jets analysis.

The b or *bottom* quark was predicted by Kobayashi and Maskawa in the 1970s while extending Cabibbo's weak mixing angle [73] to account for the CP (Charge conjugation – Parity) violation observed in the neutral K mesons [74]. The first indication of the existence b-quarks was at Fermilab, through the observation of the

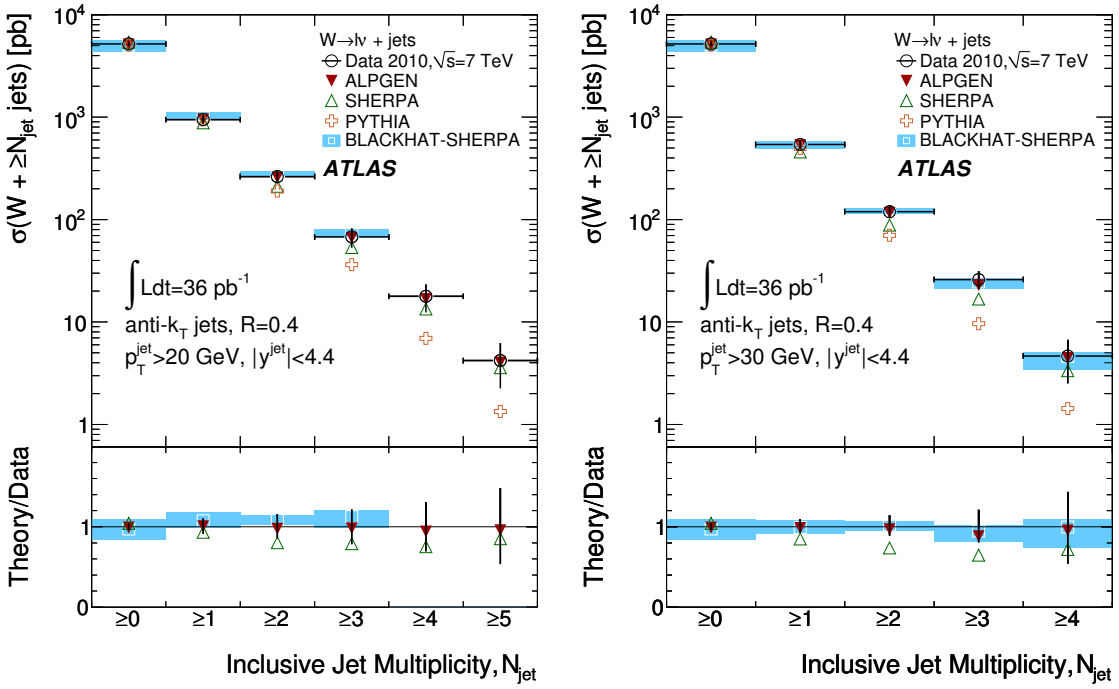

Figure 2.1: Number of jets distribution in the W+jets process at the LHC. The left plot refers to jets with $p_{\mathrm{T}} > 20$ GeV, while the right plot refers to jets with $p_{\mathrm{T}} > 30$ GeV [35].

Υ resonance ($m_\Upsilon = 9.46$ GeV) [48]. At the LHC, b-quarks ($m_b = 4.7$ GeV) are primarily produced through strong interaction ($gg \to b\bar{b}$, $q\bar{q} \to g \to b\bar{b}$, or any other diagram with a $g \to b\bar{b}$), as well as the decay of the top quark ($t \to Wb$). Individual b-quarks undergo hadronization by producing color-neutral B hadrons, which can be in the ground state or in excited states. Most excited B hadrons decay to one the ground state B hadrons either strongly or electromagnetically, but these ground state B hadrons decay weakly, resulting in a long lifetime of ~ 1.5 ps and a typical decay length of hundreds of μm. The b-quark can decay into a c or a u quark, according to the Cabibbo-Kobayashi-Maskawa (CKM) matrix elements $|V_{ub}| = (3.89 \pm 0.44) \times 10^{-3}$ and $|V_{cb}| = (40.6 \pm 1.3) \times 10^{-3}$. The small size of the CKM elements explains the

long lifetime of the b-quark, while their relative size indicates that more than 95% of the b-quarks decays to c-quarks through the process ($b \rightarrow W^* + c$). At the LHC, a high momentum b-quark undergoes parton showering and hadronization, giving rise to a jet of particles containing a B hadron. Such a b-jet can be distinguished from a light-flavour jet by associating its tracks to the presence of a long-lived B-hadron through a reconstruction technique called b-tagging, discussed in Section 6.6.

Chapter 3

$W+b$-jets: Theory and Previous Measurements

The theory describing the production of $W+b$-jets events in high-energy hadron colliders has been studied with improving accuracy for almost 20 years, first as a background to the top quark searches ($t \to Wb$), and later as a background to Higgs searches ($WH \to Wb\bar{b}$). However, it is only in the last four years that hadron collider experiments have acquired the necessary integrated luminosity and tools to measure this process.

The first diagram to be calculated at leading order (LO) was the $q\bar{q}' \to Wb\bar{b}$ one, discussed in Section 3.2. While this process is related to the $q\bar{q}' \to Wq\bar{q}$ one, the large mass of the b-quark (4.7 GeV) differentiates the two calculations. In particular, calculations such as $q\bar{q}' \to Wq\bar{q}$ need to implement explicit criteria on the final state to avoid collinear and soft divergences. Collinear divergences originate from configurations with a small opening angle between the quarks. Soft divergences are

due to a quark or a gluon being emitted with a low momentum. For the $q\bar{q}' \to Wb\bar{b}$ process, the non-zero b-quark mass avoids these divergences by preventing the energy scale from going below $m_b = 4.7$ GeV. As a result, the collinear and soft final states lead to finite and calculable results. However, the scale dependence of these results is large, leading to uncertainties of a factor of two on the cross-section.

The scale dependence is reduced when leading order diagrams with additional parton emissions are included, as discussed in Section 3.3. These additional diagrams can be seen as approximating an NLO calculation, without including the 1-loop effects. Leading order calculations of $W + b\bar{b}$ with up to three additional parton emissions are often used in ATLAS to describe the W+b-jets process[1]. They are heavily used in this thesis, as implemented by the ALPGEN Monte Carlo (MC) generator, for comparisons at the detector level and for unfolding the results to the particle level. As will be shown in Section 7.10, they are in very good agreement with the NLO calculations.

Next-to-leading-order (NLO) perturbative QCD calculations of the W+b-jets process, discussed in Section 3.4, have recently become available in MC simulations, both at the parton level and enhanced with parton shower models. Several processes contribute to W+b-jets production at NLO. In the four-flavour number scheme (4FNS), where only u, d, c, s are considered as initial-state quarks, these are $q\bar{q}' \to Wb\bar{b}(g)$ and $gq \to Wb\bar{b}q$. In the five-flavor number scheme (5FNS), b-quarks can be extracted from the proton giving rise to the processes $bq \to Wbq(g)$ and $bg \to Wbq\bar{q}$, which play a significant role at LHC energies.

[1]Similarly, LO calculations of W production with up to 5 additional parton emissions, such as ALPGEN and SHERPA, are used to describe the W+jets process, as in Figure 2.1.

An additional source of W+b-jets events is double parton scattering (DPS), discussed in Section 3.5. In double parton scattering events, a W boson and b-jets can be produced from different parton–parton interactions within the same pp collision. For example, a single pp collision can give rise to $q\bar{q}' \to W$ and $gg \to b\bar{b}$. The probability of such a double interaction occurring within the same collision cannot be calculated using perturbative QCD. An effective formalism is used to describe such probability, and tuned MC generators are used to make predictions on the expected rates.

This chapter describes the development of the theoretical calculations used to predict the W+b-jets cross-section. The first section, 3.1, introduces the basic structure of cross-section calculations at hadron colliders, and it motivates the factorization between hard scattering and parton distribution functions (PDFs). Section 3.2 describes the LO prediction for the W+b-jets production process, focusing on the effects of the b-quark mass. The inclusion of final states with additional parton emissions at LO is discussed in Section 3.3. Finally, Section 3.4 describes the full next-to-leading-order (NLO) calculation. It also discusses the use of the b-quark PDF to evaluate the contribution of initial state b-quarks (3.4.1). Section 3.5 discusses the production of W+b-jets events through double parton scattering.

At the end of this chapter, in Section 3.6, previous measurements of the W+b-jets cross-section are discussed. The CDF, D0 and ATLAS measurements are briefly described. The three measurements are made at different energies, and with slightly different final states. They cannot be directly compared to each other, but their agreement with theoretical predictions is presented.

3.1 Cross-sections at a hadron collider

The proton is a hadron composed of *partons*, quarks and gluons, which interact through the strong force. Quantum Chromo Dynamics (QCD) describes these strong interactions, and is the basis of the description of hadron-hadron collisions. Two principles of QCD make it possible to calculate proton-proton cross-sections: *asymptotic freedom* and the *factorization theorem*. Asymptotic freedom refers to the fact that the QCD coupling strength (α_s) is small for interactions with a large momentum transfer, $Q \gg \Lambda_{\mathrm{QCD}}$, where $\Lambda_{\mathrm{QCD}} \sim 200$ MeV. Collisions between highly energetic *partons* can therefore be calculated as a perturbative expansion in $\alpha_s \ll 1$. These expansions characterize perturbative QCD (pQCD).

Perturbative QCD cannot, however, be used to calculate the internal structure of the colliding protons. In each proton's rest frame, the relevant momentum transfer between partons is much smaller ($Q \sim \Lambda_{\mathrm{QCD}}$), and therefore $\alpha_s \sim 1$, giving rise to the *confinement* of partons inside the proton. To get around this issue, the factorization theorem [40] is used to treat the hard scattering between partons as independent from the internal structure of the incoming protons. Factorization can be seen as a consequence of the energy dependence of the QCD coupling strength. The value of α_s is very different for large and small energy scales, resulting in very different timescales for these two types of interactions. A sketch of factorization can be seen in Figure 3.1.

As a result of asymptotic freedom and the factorization theorem, cross-section predictions at a hadron collider, $\sigma_{pp\to X}(s)$, can be expressed as a convolution of three processes: a perturbative cross-section describing the hard scattering between two

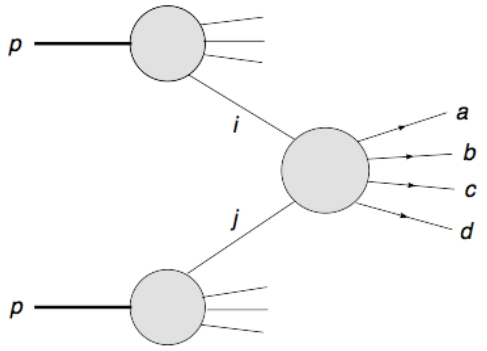

Figure 3.1: Sketch of the factorization between the non-perturbative dynamics within the proton and the perturbative hard scattering. Partons i and j are extracted from the incoming protons, and the hard scattering process is $ij \to abcd$

partons, and two non-perturbative parton distribution functions (PDFs) describing the dynamics of the incoming protons. This convolution can be written as:

$$\sum_{n=1}^{\infty} \alpha_s^n(\mu_R^2) \sum_{i,j} \int dx_1 dx_2 f_{i/p}\left(x_1, \mu_F^2\right) f_{j/p}\left(x_2, \mu_F^2\right) \sigma_{ij\to X}^{(n)}\left(x_1 x_2 s, \mu_R^2, \mu_F^2\right) \qquad (3.1)$$

Equation 3.1 is a perturbation series in α_s, and the coefficients $\sigma_{ij\to X}^{(n)}$ represent the parton-level cross-sections calculated at order n ($n = 1$ being the LO, $n = 2$ the NLO, and so on). The i and j represent the initial state partons, and they are summed over by the $\sum_{i,j}$ term.

The functions of type $f_{i/p}(x)$ are parton distribution functions (PDFs), describing the density within the proton p of partons of type i carrying a fraction x of the proton momentum. The PDFs cannot be calculated in perturbative QCD, but they can be extracted from other measurements or experiments[2]. The integral over dx_1 and dx_2

[2]One important class of events used for the study of PDFs is deep inelastic scattering (DIS), in which an electron and a proton interact ($ep \to e + X$), and the virtual photon mediating the interaction accesses directly the structure of the proton.

covers the phase space of possible momenta for the initial state partons i and j, and it is usually carried out by Monte Carlo calculations.

The remaining arguments of equation 3.1, μ_R, μ_F and s, are defined below. The variable s is the squared center-of-mass energy of the pp collision, and $x_1 x_2 s$ is the squared energy of the colliding partons.

The variables μ_R and μ_F are arbitrary scales used to cut off non-perturbative effects and allow for perturbative cross-section calculations. Physical observables cannot depend on them, and the μ_R and μ_F dependencies are expected to cancel out in a Taylor expansion for which all terms are known. When using only the first few terms of an expansion, a residual μ_R and μ_F dependency is expected. This dependency can be used to estimate the uncertainty associated with the missing higher order terms.

The factorization scale, μ_F, is necessary to control soft and collinear emissions in the initial state. These emissions could spoil the perturbative behavior of the hard-scattering $\sigma_{ij\to X}$. Therefore they are absorbed into the PDFs for all transverse momenta smaller than $\sim \mu_F$. The $\sigma_{ij\to X}$ is then calculated only for emissions with transverse momenta larger than μ_F. This approach is successful because the evolution of the PDFs as a function of μ_F, $f_{i/p}(x, \mu_F)$, can be calculated [70]. The PDFs can therefore be measured at one scale and evolved to another scale.

An example of the PDFs evolution between two different scales is shown in Figure 3.2. The left figure ($Q^2 = 10$ GeV) shows the PDFs at relatively small scales, while the right figure ($Q^2 = 10^4$ GeV) shows the PDFs at scales similar to the ones involved in the production of W bosons ($Q \sim m_W \sim 100$ GeV). The proton structure

undergoes large changes between the two scales. At the smaller scale its momentum is mostly carried by the *valence* quarks (u and d), while at the large scale the *sea* quarks and the gluons play a much larger role. At the large scales, the b and $\bar{b}$ distributions also become relevant.

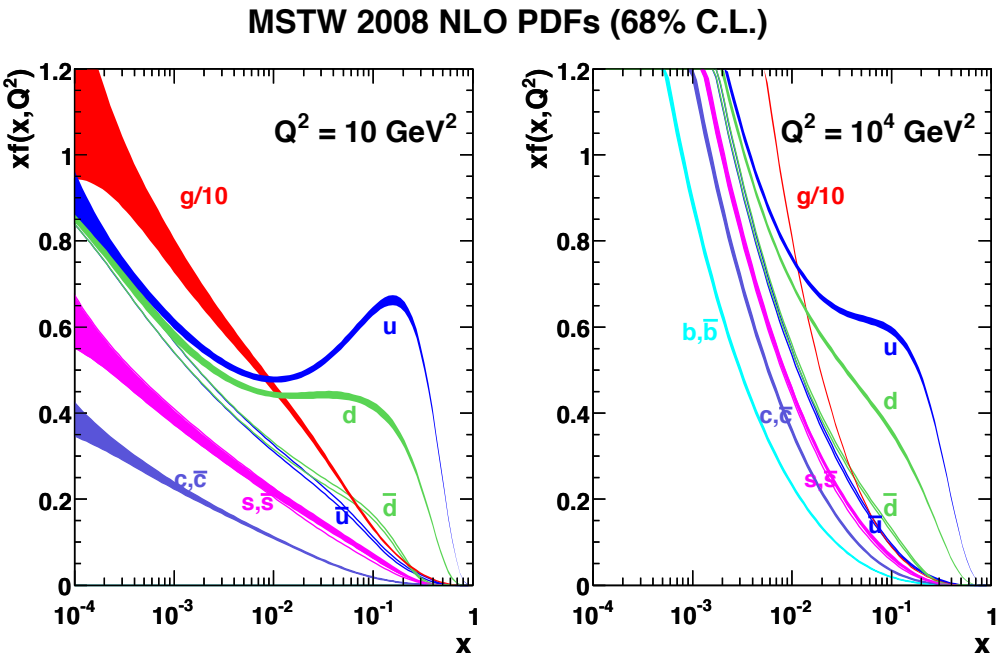

Figure 3.2: Parton distribution functions at two different scales, $Q^2 = 10$ GeV and $Q^2 = 10^4$ GeV, as calculated by the MSTW group [57].

The renormalization scale, μ_R, is also used as a cut-off. The renormalization scale is necessary to control the divergences coming from high-momentum loops in the parton-level cross-section $\sigma_{ij\to X}$. Instead of integrating over these loops up to infinitely high momentum, the loops are absorbed in a redefined (or renormalized) coupling strength, α_s, as long as they have momenta larger than μ_R. The $\sigma_{ij\to X}$ is then calculated only for loops with momenta larger than μ_R. The resulting dependency

of the coupling on the renormalization scale, $\alpha_s(\mu_R^2)$, can be calculated through the Renormalization Group Equation (RGE) [70]. This approach, imposing a cut-off scale and redefining the coupling constant, is common to renormalizable quantum field theories. However, the peculiarity of QCD over Quantum Electrodynamics is that the coupling constant α_s varies substantially over the accessible energy range, allowing for the *factorization* of different processes, and that it becomes weaker at large energy scales (giving rise to *asymptotic freedom*) and stronger at small energy scales (giving rise to *confinement*).

The renormalization and factorization scales, μ_R and μ_F, are usually chosen to be identical and close to the scale of the process of interest $\mu_F = \mu_R = \mu_0 \sim Q$. The choice of $\mu_0 \sim Q$ is often referred to as *natural*. For W boson production, a possible scale choice would be $\mu_0^2 = m_W^2$. Alternatively, a dynamic scale can be chosen, such as $\mu_0^2 = m_W^2 + p_{\mathrm{T},W}^2$, based on the specific kinematic properties of each event. For W+b-jets production, choices range from $\mu_0^2 = m_W^2 + m_b^2$ to $\mu_0^2 = m_W^2 + m_b^2 + p_{\mathrm{T},W}^2 + p_{\mathrm{T},b}^2$.

3.2 Leading Order with b-quark mass effects

The first leading-order calculation of $W + b\bar{b}$ production in $p\bar{p}$ collisions that used a non-zero b-quark mass was performed in 1993 [63]. The Feynmann diagram for this process, shown in Figure 3.3, includes an incoming quark-antiquark pair with the necessary flavors to form a W, and a gluon which splits into a $b\bar{b}$ pair.

The inclusion of non-zero b-quark mass is useful when considering final states in which the b and $\bar{b}$ are separated by a very small angle (*collinear*), or in which one of the quarks has low momentum (*soft*). In $W + q\bar{q}$ events with two light quarks, both

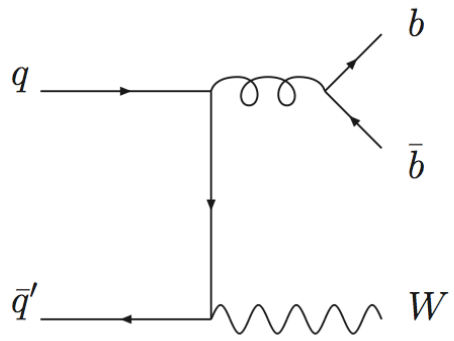

Figure 3.3: Leading order production of $W + bb$.

collinear and soft final states lead to a divergent cross-section. They can be taken into account using non-perturbative techniques (parton showering), or they can be avoided completely by imposing angular and momentum cuts. But they cannot be included in the perturbative calculation. On the other hand, in $W+b\bar{b}$ events these configurations don't lead to diverging amplitudes, because the scale of the process does not reach below $2m_b$. These configuration can therefore be calculated perturbatively, leading to logarithms of the form $(\alpha_s \ln(\mu/m_b))$. These logarithms result in a large scale (μ) dependence of the result.

The result of the LO calculation for a center of mass energy of 1.8 TeV is summarized in Figure 3.4, which shows the differential cross section as a function of the b-jet p_{T}. Due to the inclusion of the non-zero b-quark mass, the p_{T} reaches all the way down to 0 GeV. The dashed line will not be discussed, since they correspond to $t\bar{t}$ cross-section predictions for different hypotheses for the top quark mass. The plain and dotted lines represent the p_{T} distribution of b-jets from $p\bar{p} \to Wb\bar{b}$ events. The plain line is calculated using the scale $\mu_0^2 = m_{b\bar{b}}^2$, where $m_{b\bar{b}}$ is the invariant mass of

the $b\bar{b}$ pair. The dotted line is calculated using the scale $\mu_0^2 = m_W^2 + p_{\mathrm{T},W}^2$. Looking at their normalization, it is clear that the total production cross-section has a large scale dependence. However, at least at LO, the scale dependence appears to only affect the total cross section, and not the shape of the b-jet p_{T} distribution. The total cross-sections are in the range 22–48 pb, depending on the scale choice.

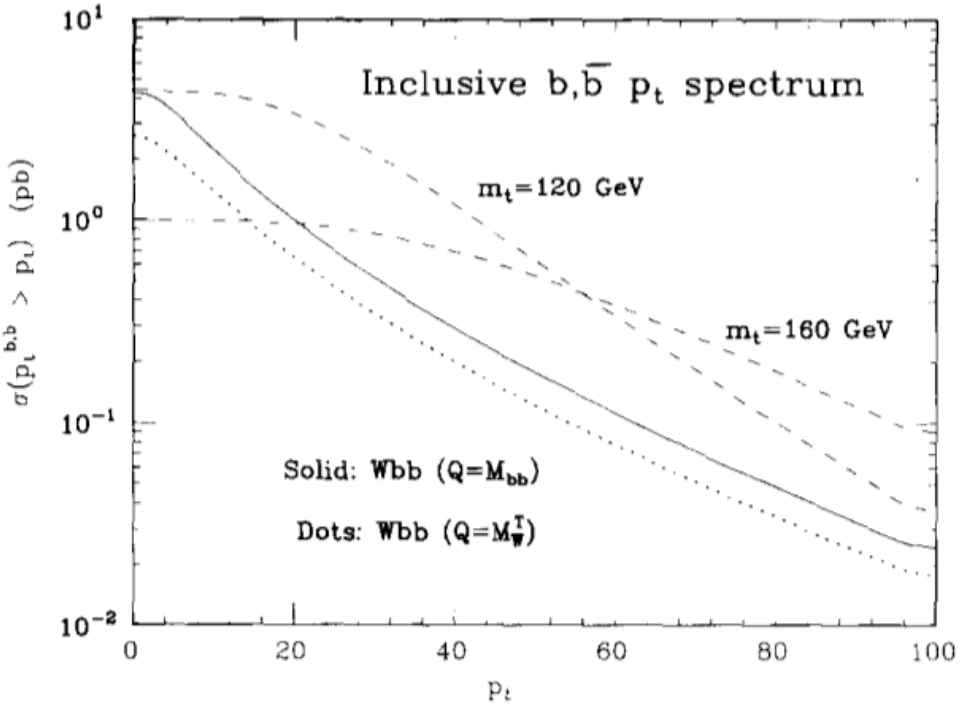

Figure 3.4: Leading-order $p\bar{p} \to Wb\bar{b}$ production at the Tevatron. Inclusive p_{T} distribution of central b and $\bar{b}$ quark, with two choices of scale [63]. The dashed lines represent spectra obtained from $t\bar{t}$ production with different top-quark masses.

3.3 Additional partons at LO and the parton shower

The next step in $W + b\bar{b}$ predictions was to add additional parton emissions at leading order. This was first done, including the non-zero b-quark mass, in 2001 [64]. The calculation used the algorithm ALPHA, first proposed in 1995 [65] which eventually developed into the currently used ALPGEN Monte Carlo [95]. The calculation also included the shower evolution and hadronization of final state partons, using the HERWIG Monte Carlo [96].

Leading order calculations with additional partons have often been a very good compromise to obtain reliable predictions, before the development of full NLO calculations. Given a process involving n particles at tree-level, the NLO calculation requires supplementing the LO result with: (a) tree-level processes involving $n + 1$ particles, and (b) 1-loop effects in the n-particle process. Therefore, the inclusion of additional partons at LO covers the effects of (a), while ignoring (b). As a result, calculations with additional partons at LO are more susceptible to scale uncertainties than full NLO calculations, but they can provide access to otherwise inaccessible kinematics.

In this particular case, the processes considered at LO in the ALPHA/ALPGEN calculation[3] are:

1. $q\bar{q}' \to Wb\bar{b}$
2. $qg \to Wb\bar{b}\bar{q}'$
3. $gg \to Wb\bar{b}q\bar{q}'$

[3]Processes with additional final state gluons are not listed for convenience

4. $q\bar{q}' \to Wb\bar{b}q''\bar{q}''$

5. $qg \to Wb\bar{b}\bar{q}'q''\bar{q}''$

6. $gg \to Wb\bar{b}q\bar{q}'q''\bar{q}''$

In terms of final states, this list is straightforward, in that it simply includes additional partons: process 2 describes events with at least one additional light parton, processes 3 and 4 with at least two, processes 5 and 6 with at least three and four, respectively. In terms of initial states, new production channels are opened up, including qg and gg. These channels are particularly important for the proton-proton collisions of the LHC, where the gluon PDF is much larger than the anti-quark PDF. Process 2, shown in Figure 3.5, plays a particularly important role due to the presence of a b-quark in the initial state, and it will be further discussed in Section 3.4.1.

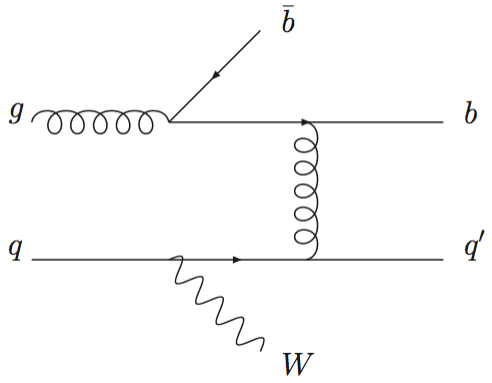

Figure 3.5: Diagram for $W + b\bar{b}$ production with one additional parton emission: $qg \to Wb\bar{b}\bar{q}'$. The initial configuration qg is very important at the LHC, due to the large gluon PDF, making this diagram predominant over the one in Figure 3.3 despite the additional α_s vertex. The $g \to b\bar{b}$ process in which one of the b-quarks is soft can be described using a b-quark PDF, as in Figure 3.6.

The results of this calculation allow us to draw the first quantitative conclusions

with respect to the different diagrams contributing to $W + b\bar{b}$, and to the different parton multiplicities expected. In this calculation, the final state quarks and gluons are required to have $|\eta| < 2.5$ and $p_{\mathrm{T}} > 20$ GeV, and to be separated from each other by $\Delta R > 0.4$. This is necessary to avoid collinear and soft divergences, and it is convenient for matching the detector acceptance. When it comes to b-quarks, however, no such requirements are imposed. Therefore, events in which one of the b-quarks is either at low p_{T} or within $\Delta R = 0.4$ of the other one, are acceptable. These events give rise to a second set of predictions for the $W + b$ process.

Table 3.1: Contribution to the $W + b\bar{b}$ cross-section, at the Tevatron and LHC, as a function of additional final state partons with $|\eta| < 2.5$ and $p_{\mathrm{T}} > 20$ GeV [64]. The rates do not follow an α_s scaling, and the difference in scaling between the Tevatron and the LHC is due to the predominance of the qg initial state at the LHC.

$W + b\bar{b} + N$(partons) [pb]				
	$N = 0$	$N = 1$	$N = 2$	$N = 3$
Tevatron	0.36	0.106	0.027	0.006
LHC	2.60	3.60	2.54	1.38

Table 3.2: Contribution to the $W + b$ cross-section, at the Tevatron and LHC, as a function of additional final state partons with $|\eta| < 2.5$ and $p_{\mathrm{T}} > 20$ GeV [64].

$W + b + N$(partons) [pb]					
	$N = 0$	$N = 1$	$N = 2$	$N = 3$	$N = 4$
Tevatron	1.316	0.37	0.09	0.02	0.003
LHC	9.38	12.3	7.4	3.7	1.7

The predictions for the $W + b\bar{b}$ process with two high momentum and well-separated b-quarks, as a function of the number of additional partons, are reported in Table 3.1 for the Tevatron ($p\bar{p}$ collisions at $\sqrt{s} = 2$ TeV) and for the LHC (pp collisions at $\sqrt{s} = 14$ TeV). The corresponding prediction for the case with only one high momentum b-quark ($W + b$) are reported in Table 3.2. The first striking result is

that the rates do not follow an α_s scaling with parton multiplicity. This is particular evident at the LHC at 14 TeV, where the cross-section increases with a higher number of parton emissions[4]. This behavior is due to the new initial state contributions, and in particular to the appearance of the qg initial configuration which results in an additional final state parton. Another interesting result is the relative size of the $W + b$ and $W + b\bar{b}$ processes. When considering all parton multiplicities, events with two b's are found to be produced at approximately one third of the rate of single-b events, both at the Tevatron and at the LHC. But when considering events with exactly two final state partons ($N = 0$ for $W + b\bar{b}$, $N = 1$ in the se), the split between $W + b\bar{b}$ and $W + b$ events is 50/50 at the Tevatron, and 20/80 at the LHC.

These conclusions continue to be valid after events have been processed with the HERWIG parton shower simulation. However, they are still the result of leading-order calculations, and they carry a large scale uncertainty enhanced by the numerous powers of α_s (one for each additional parton). The authors use a dynamic scale given by the W mass and the average parton $p_{\mathrm{T}}(\mu_0^2 = m_W^2 + < p_{\mathrm{T},part}^2 >)$, and they suggest applying uncertainties of the order of a factor of 2 to 4 to all the cross-sections, depending on parton multiplicity. Despite these large uncertainties, the leading order plus parton shower predictions of ALPGEN/HERWIG based on the results presented in this section are in very good agreement with the NLO results, as will be shown in Section 7.10, and they are heavily used in current experiments.

[4]This effect is also visible at the 7 TeV LHC, although the $W + b + j$ cross-section never becomes larger than the $W + b$ one as in Table 3.2.

3.4 Next to Leading Order with b-quark PDF

The next step in W+b-jets calculations, necessary to reduce the large scale dependence, was to evaluate the production rate at next-to-leading order. With respect to leading order, an NLO calculation adds the effect of tree-level processes involving an additional particle, as well as the 1-loop effects. Therefore, the NLO calculation of the $W + b\bar{b}$ process considers:

1. $q\bar{q}' \to Wb\bar{b}$ at tree level and one loop
2. $q\bar{q}' \to Wb\bar{b}g$ at tree level
3. $qg \to Wb\bar{b}\bar{q}'$ at tree level

This calculation was first performed in 2006 [66], with a final state characterized by two well-separated b-quarks with $p_{\mathrm{T}} > 15$ GeV. The b-quark mass, which was included in the calculation, was observed to have only a small effect (8%) on the total cross section. This was expected since the collinear and soft configurations regulated by the b-quark mass are not an issue when considering well-separated hard b-quarks. The main result, however, was the reduction of the scale uncertainty by about a factor of two with respect to the LO calculation of the same process.

The picture changed in 2007, when a new calculation [67] shifted the focus to final states with only one hard b-quark, or with two aligned b-quarks, explicitly reaching into the soft and collinear regions. In this final state, logarithms of the form $(\alpha_s \ln(\mu/m_b))^n$ appear, leading to large uncertainties related to the choice of scale μ. To mitigate this effect, a new technique was introduced which resulted in a more precise estimate of the $qg \to Wb\bar{b}\bar{q}'$ process.

3.4.1 Adding the b-quark PDF

The $qg \to Wb\bar{b}\bar{q}'$ process (Figure 3.5) is particularly important in pp collisions at the LHC, and it involves a gluon splitting ($g \to b\bar{b}$) either in the initial or in the final state. The configuration in which the gluon splitting takes place in the initial state, and with one of the b-quark either collinear or very soft, can be written as $bq \to Wb\bar{q}'$ (Figure 3.6).

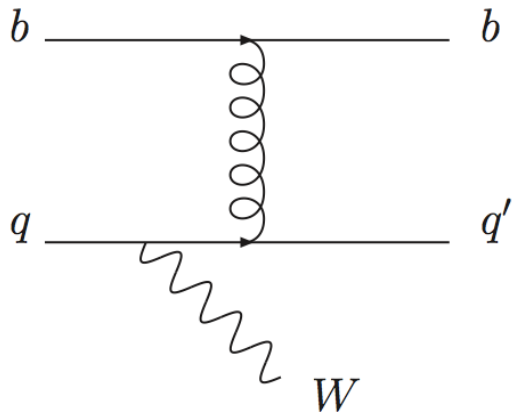

Figure 3.6: Diagram for $bq \to Wb\bar{q}'$, where the b-quark is extracted directly from the proton through a b-quark PDF. This diagram corresponds to the one in Figure 3.5 for the case in which one of the b-quarks is soft. This compact representation makes it possible for the $bq \to Wb\bar{q}'$ process to be calculated at NLO.

In this configuration, the initial-state b-quark is not generated through an explicit gluon splitting, but it is extracted directly from the proton through a PDF. To describe this configuration, a technique called "5-flavor-number-scheme" (5FNS) is used, in which 5 quark flavors are considered in the proton (u, d, c, s, b), as opposed to the standard "4-flavor-number-scheme" in which only u, d, c, s are considered. The advantages to this approach are two: first, the large logarithms coming from the initial state gluon splitting are avoided, and the DGLAP evolution equations are in-

stead used to account for the scale dependence of the b-quark PDF. Second: what was initially an NLO process can be treated as a leading order one, allowing one to calculate tree level and loop corrections which further reduce the overall scale uncertainty. Effectively, the following diagrams are added to the calculation:

4. $bq \to Wb\bar{q}'$ at tree level and one loop

5. $bq \to Wb\bar{q}'g$ at tree level

6. $bg \to Wbq\bar{q}'$ at tree level

There are some complications connected to this approach: the first one is the overlap between processes 3 ($qg \to Wb\bar{b}\bar{q}'$ with gluon splitting in the initial state, as in Figure 3.5) and process 4 ($bq \to Wb\bar{q}'$ in Figure 3.6)

The second complication is the treatment of the b-quark PDF $b(x, \mu_F)$. To give an idea of this PDF, the following is its first order approximation for scales close to m_b:

$$\tilde{b}(x, \mu_F) = \frac{\alpha_s(\mu_R)}{\pi} \ln\left(\frac{\mu_F}{m_b}\right) \int_x^1 \frac{dy}{y} P_{qg}\left(\frac{x}{y}\right) f_{g/p}(y, \mu_F) \tag{3.2}$$

Here $f_{g/p}(y, \mu_F)$ represents the probability of extracting a gluon with momentum y from the proton, and $P_{qg}(x/y)$ represents the gluon splitting function, that is the probability that the gluon will emit a quark with fraction x/y of its momentum. The equation can be understood as indicating that, for scales close to m_b, the probability of extracting a b-quark with momentum fraction x from a proton is simply proportional to the convolution of the gluon density times the probability of the gluon to emit

a quark, multiplied by the coupling α_s. The DGLAP equations have to be used to evaluate the b-quark PDF for scales different from m_b.

Once these additional effects are included, processes 1–6 can be combined to yield an inclusive NLO cross-section of the W+b-jets process. The results, calculated in 2011 for the 7 TeV LHC [85], are presented in Table 3.3 as a function of the scale, and in Table 3.4 split by final state[5]. With respect to the scale (Table 3.3), the improved treatment of initial state b-quarks translates directly into a much smaller scale dependence of the final result. When changing the scale from $4 * \mu$ to $\mu/4$, the W+b-jets cross-section varies by $^{+60\%}_{-30\%}$ in the 4 flavor scheme calculation and only by $^{+26\%}_{-15\%}$ in the 5 flavor scheme. In Table 3.4, the W+b-jets process is split into three bins, $W+b$, $W+b+j$ and $W+b+b$. The last bin, $W+b+b$, can only be produced in the 4 flavor scheme, while the first two bins are enhanced by 20–40% when adding the NLO description of diagrams with initial state b-quarks.

Table 3.3: Scale dependence for inclusive W+b-jets results in the 4 flavor and 5 flavor schemes [85]. In the 5 flavor scheme, the full NLO calculation of the $bq \to Wb\bar{q}'$ process results in a reduced scale dependence of the overall W+b-jets cross-section.

	Processes 1–3 (4FNS) [pb]	Processes 1–6 (5FNS) [pb]
$\mu = \mu_0/4$	138.5	137.1
$\mu = \mu_0/2$	107.1	120
$\mu = \mu_0$	86.6	109.2
$\mu = 2\mu_0$	71.6	100.1
$\mu = 4\mu_0$	60.7	92.6

ADD CONCLUSIONS TO THIS SECTION

[5]Tables 2, 3 and 9 of reference [85] are combined to extract these results.

Table 3.4: Different components of the W+b-jets final state in the 4 flavor and 5 flavor schemes [85]. The $bq \to Wb\bar{q}'$ NLO calculation contributes to both the $W + b$ and $W + b + j$ final states.

	Processes 1–3 (4FNS) [pb]	Processes 1–6 (5FNS) [pb]
$W + b$	53.4	65.6 (+23%)
$W + b + j$	25.3	35.7 (+41%)
$W + b + b$	7.9	7.9 (+0%)

3.5 Another source of W+b-jets events: Double Parton Scattering

Up to this section, only collisions in which the hard scattering takes place between two partons, each originating from one of the incoming protons, have been considered (see Figure 3.1). However, due to the composite nature of protons, it is also possible to extract additional partons from each of the incoming protons, and these additional partons can collide giving rise to Multiple Parton Interactions (MPI).

In general, given a hard scattering between two partons with a large momentum fraction x, the remaining partons available for secondary scatterings only have a smaller fraction of momentum available, resulting in softer scatterings. But in some cases, two pairs of partons with comparable x can be extracted from the incoming protons, giving rise to two simultaneous hard scatterings, as shown in Figure 3.7: this phenomenon is called Double Parton Scattering (DPS) or Double Parton Interaction (DPI). While the general case of MPI takes place in the non-perturbative regime, the two hard scatterings of DPS can be modeled using pQCD.

The DPS phenomenology is based on the factorization among the two hard scattering processes, and between the hard scatterings and the proton dynamics. The

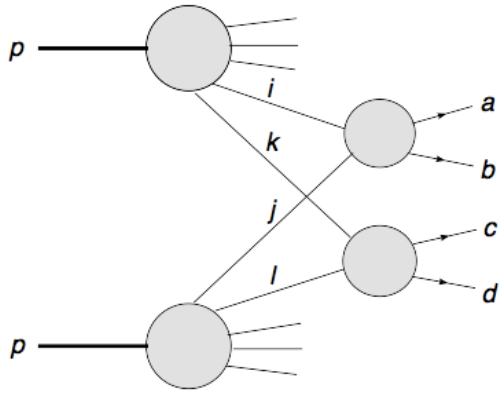

Figure 3.7: Sketch of a double-parton process in which the active partons are i and k from one proton and j and l from the second proton. The two hard scattering subprocesses are $(ij \to ab)$ and $(kl \to cd)$

general expression, adapted to the W+b-jets case, is:

$$\sigma^{\mathrm{DPS}}(pp \to W + b + X) = \sum_{i,j,k,l} \int dx_1 dx_2 dx_1' dx_2' db^2 \; \Gamma_{ik}(x_1, x_2, b, \mu_F)\Gamma_{jl}(x_1', x_2', b, \mu_F) \times \sigma_{ij\to W}(x_1 x_2' s, \mu_F^2)\sigma_{kl\to b+X}(x_2 x_2' s, \mu_F^2) \tag{3.3}$$

In this equation, the two parton-level cross-sections represent the independent processes $ij \to W$ and $kl \to b + X$. They are each calculated using pQCD, as perturbation series in α_s, in the same way as they would be calculated for a single hard scattering. The $\Gamma_{ik}(x_1, x_2, b, \mu_F)$ functions represent the *double parton distribution functions* (DPDFs), describing the probability to extract partons i and k, with respective momentum fractions x_1 and x_2, from the same proton. The parameter b, new with respect to the standard PDFs, represents the separation between i and j, as well as between k and l, in the transverse plane perpendicular to the proton momentum.

The analytic study of double parton distribution functions lies beyond the scope of this thesis, and a review of the recent development can be found in reference [79]. There is no generally accepted form for DPDFs, but two assumptions are usually applied to allow for DPS cross-sections to be estimated. First, it is assumed that the dependence of the DPDFs on the transverse parton-parton distance (b) can be factorized:

$$\Gamma_{ik}(x_1, x_2, b, \mu_F) = F(b) D_{ik}(x_1, x_2, \mu_F) \tag{3.4}$$

$F(b)$ represents the probability distribution of separations between two partons in the same proton. Since only $F(b)$ depends on the parameter b, it can be integrated separately, giving rise to a new constant:

$$\sigma_{\text{eff}} = \left[\int db^2 \left(F(b)\right)^2 \right]^{-1} \tag{3.5}$$

The constant σ_{eff}, called *effective cross section*, is a scale factor with dimensions of a cross-section, resulting from integrating on the transverse distance b. It can be seen as the transverse size of the interaction region between the two protons, and therefore related to the size of the proton.

To further simplify the picture of DPDFs, and to allow for their treatment using the available tools and PDFs, it is assumed that each DPDF can be written as a product of two independent PDFs:

$$D_{ik}(x_1, x_2, \mu_F) = f_{i/p}(x_1, \mu_F) f_{k/p}(x_2, \mu_F) \tag{3.6}$$

It is clear that this assumption must be violated at some level: $x_1 + x_2 < 1$ should be enforced to conserve momentum, and the second PDF should be modified to avoid

extracting the same quark twice from a single proton. Nevertheless, this assumption results in a simplified expression for equation 3.3, as a combination of single-parton scattering cross-sections:

$$\sigma^{\mathrm{DPS}}(pp \to W + b) = \frac{\sigma(pp \to W)\sigma(pp \to b + X)}{\sigma_{\mathrm{eff}}} \tag{3.7}$$

In this picture, the DPS cross-section is simply the product of the single-parton cross-sections, divided by σ_{eff}, a quantity which is independent from the hard processes and has dimensions of a cross-section. While this simplification can be used to estimate total cross-sections, the acceptance effects brought about by kinematic selection will spoil the equation in the case of fiducial cross-sections. For example, event-level variables such as the missing transverse energy can be affected by the presence of additional jets, resulting in acceptances for W events which depend on the presence of a second hard scattering. For this reason, a full simulation of the kinematics is necessary to estimate the acceptance of the DPS process, and its resulting contribution to the observed cross-section.

The effective cross section σ_{eff} has been measured by different experiments in different final states, as summarized in Figure 3.8. The measurements indicate that σ_{eff} is smaller than the geometrical size of the proton ($\pi R^2 \sim 35$ mb), and that it depends only weakly on the center-of-mass energy of the collisions. The effective cross section ranges from 5 mb at 63 GeV, measured by the AFS Collaboration at the ISR [80], to $15 \pm 3(\mathrm{stat.})^{+5}_{-3}(\mathrm{syst.})$ mb at 7 TeV, measured by ATLAS [141]. The ATLAS measurement is performed by studying the kinematics of the dijet system in events with a W boson and 2 jets. In this measurement, variables based on the

transverse momenta of the jets are used to separate statistically single-parton and double-parton scattering events.

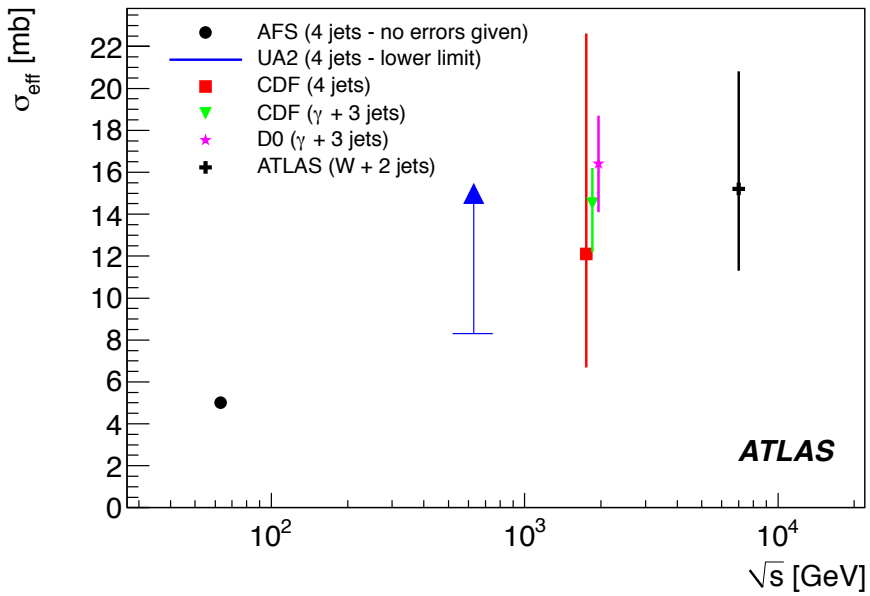

Figure 3.8: The centre-of-mass energy, $\sqrt{(s)}$, dependence of σ_{eff} extracted in different processes in different experiments. The error bars on the data points represent the statistical and systematic uncertainties added in quadrature. [141]

The DPS estimate used in this thesis for the W+b-jets process is based on a Monte Carlo simulation. This simulation is performed using the JIMMY program [97] in association with the HERWIG parton shower, based on the assumptions discussed above. JIMMY effectively overlays additional scatterings on top of the primary one, accounting for momentum conservation in the proton ($x_1 + x_2 < 1$). Due to the simplicity of the code, only QCD $2 \to 2$ processes are considered as additional hard scatterings. This is sufficient for the purposes of the W+b-jets analysis, but would not be able to account for other types of DPS, for example in the WW process. The JIMMY code includes parameters describing the effective radius of the proton (which

can be related to σ_{eff}) and the range of transverse momenta of secondary partons. These parameters are tuned to ATLAS collision events, as described in reference [140]. Most importantly, the JIMMY DPS prediction has been found to be consistent with the measured DPS contribution in W+2-jets events [141], justifying the choice to use it in the context of W+b-jets events.

Table 3.5: Single and double parton scattering predictions for the W+b-jets process in the fiducial region defined by Table 7.12. The "1 jet" region includes events with exactly one b-jet passing the fiducial selection. The "2 jet" region includes events with exactly two jets, of which at least one must be a b-jet.

W+b-jets cross-section [pb]	1 jet	2 jet
Single parton scattering (NLO)	2.0	1.4
Double parton scattering (JIMMY)	1.0	0.3

The fiducial cross-section for the DPS W+b-jets process estimated by JIMMY are presented in Table 3.5, together with the NLO single-parton scattering estimates described in Section 3.4. Both cross-sections are estimated in the fiducial region described in Table 7.12. In the "1 jet" region, the DPS contribution represents a third of the total expected cross-section, while in the "2 jet" region it accounts for less than 20% of the total. These large contributions make the W+b-jets final state one of the most promising channels for future studies double parton scattering.

3.6 Previous Measurements of W+b-jets

Measurements of the production of a W boson in association with b-jets have been performed by the CDF [91] and D0 [92] experiments at the Tevatron using $p\bar{p}$ collisions at $\sqrt{s} = 1.96$ TeV. The ATLAS collaboration reported a measurement based on 36 pb^{-1} of data collected in pp collisions at $\sqrt{s} = 7$ TeV [93].

The CDF measurement is the first one, dating from 2009, and it is based on 1.9 fb^{-1} of integrated luminosity. The cross-section measured is that of "jets from b-quarks produced with a W boson", meaning that it is a jet-level measurement. The alternative approach, at event-level, would count "events where jets from b-quarks are produced with a W boson". The advantage of a jet-level measurement is that it is independent from the modeling of the number of b-jets per event, without explicitly splitting the samples in events with 1 or 2 b-jets. The fiducial region for the measurement requires an electron or muon with $p_{\mathrm{T}} > 20$ GeV and $|\eta| < 1.1$, a neutrino with $p_{\mathrm{T}} > 25$ GeV, and one or two jets with $E_{\mathrm{T}} > 20$ GeV and $|\eta| < 2.0$. Given the lepton requirements, the measured cross-section already includes the leptonic branching ratio of the W boson.

The CDF event selection is based on reconstructing a leptonically decaying W boson, and one or two jets, at least one of which must be b-tagged. Backgrounds with c-jets and light-jets are separated statistically using the secondary-vertex mass of b-tagged jets. Backgrounds with b-jets ($t\bar{t}$, single-top) are subtracted based on Monte Carlo simulation scaled to theoretical predictions. The measured b-jets cross-section is 2.74 ± 0.27 (stat) ± 0.42 (syst) pb. The result is found to be larger than the NLO calculation described in Section 3.4, which predicts 1.22 ± 0.14 (syst.) pb, and the Alpgen multi-parton LO described in Section 3.3, which predicts 0.78 pb.

The D0 measurement is performed more recently, in 2012, and uses a slightly different fiducial region definition. The cross-section is measured at the event level, requiring an electron or muon with $p_{\mathrm{T}} > 20$ GeV and $|\eta| < 1.7$[6], a neutrino with

[6]The pseudo-rapidity requirement is changed to $|\eta| < 1.1$ or $1.5 < |\eta| < 2.5$ for electrons.

$p_{\mathrm{T}} > 25$ GeV, and at least one b-jet with $p_{\mathrm{T}} > 20$ GeV and $|\eta| < 1.1$. With respect to CDF, noticeable differences are the inclusion of 3-jet events, the halving of the jet pseudorapidity range, and the single-counting of events with two b-jets. The measurement technique is similar to the CDF one, although different variables are used for b-tagging and for separating jet flavors in the tagged region. The measured cross-section is $1.05 \pm 0.03(\mathrm{stat.}) \pm 0.12(\mathrm{syst.})$ pb. The results are found to be smaller than, but consistent with, the NLO prediction of $1.34 \pm^{+0.40}_{-0.33}(\mathrm{scale}) \pm 0.06(\mathrm{PDF})^{+0.09}_{-0.05}(m_b)$ pb.

The ATLAS measurement prior to the one presented in this thesis is based on the 2010 dataset. It uses a strategy similar to the CDF one, but a different fiducial region. The cross-section is measured at the event level, requiring an electron or muon with $p_{\mathrm{T}} > 20$ GeV and $|\eta| < 2.5$, a neutrino with $p_{\mathrm{T}} > 25$ GeV, a W transverse mass[7] $m_{\mathrm{T}}^{W} > 40$ GeV, and one or two jets with $p_{\mathrm{T}} > 25$ GeV and $|y| < 2.1$. With respect to CDF, the jet p_{T} is raised, and events with two b-jets are counted only once. The cross-section is for the first time measured separately for 1-jet events and for 2-jet events, where the 2-jet events include both $W + bq$ and $W + b\bar{b}$ final states. The measurement is compared to LO and NLO predictions in Figure 3.9, and it is found to be larger than the predictions, but consistent with them.

The Tevatron and LHC measurements cannot be directly compared. They use different fiducial regions, and, most importantly, they probe very different production processes for W+b-jets events. As discussed in Sections 3.3 and 3.4, W+b-jets production at the the Tevatron is essentially dominated by the quark-antiquark initial state, while at the LHC it is dominated by the quark-gluon and the quark-b-quark ones.

[7]The W transverse mass is defined as $m_{\mathrm{T}}^{W} = \sqrt{2p_{\mathrm{T}}^{\ell} p_{\mathrm{T}}^{\nu}(1 - \cos(\phi^{\ell} - \phi^{\nu}))}$.

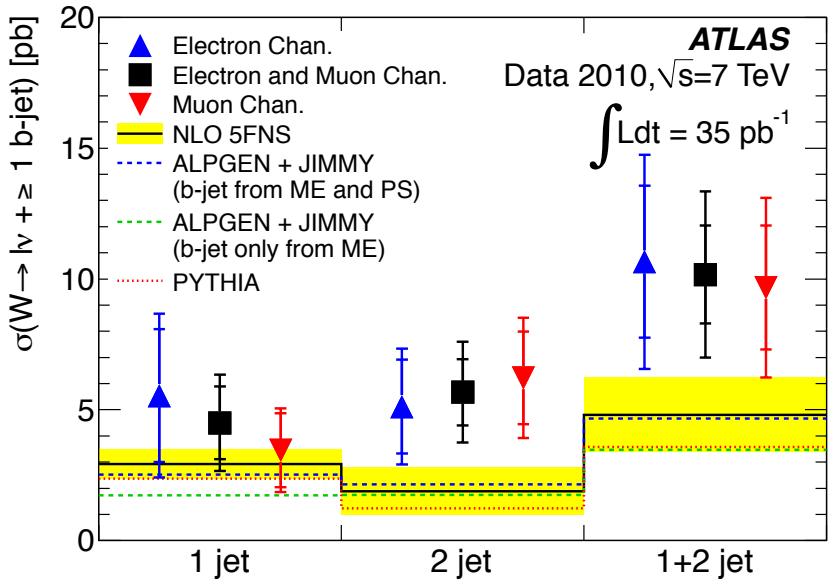

Figure 3.9: Measured fiducial cross-section with the statistical (inner error bar) and statistical plus systematic (outer error bar) uncertainty in the electron, muon, and combined electron plus muon channel. The cross-section is given in the 1, 2, and 1+2 jet exclusive bins. The measurements are compared with NLO predictions. The leading order predictions from ALPGEN/HERWIG/JIMMYare given for b-jets generated only by the matrix element and by the matrix element and parton shower. The prediction from PYTHIA is also shown.

Additionally, the double-parton scattering contribution is negligible at the Tevatron, while it has a large contribution at the LHC.

To summarize, W+b-jets events can be produced in single-parton scattering and double-parton scattering processes. These processes are calculated using different tools, which include perturbative QCD, b-quark PDFs and effective formalisms. Previous measurements at the Tevatron and at the LHC do not provide a complete picture of the W+b-jets process, and such an understanding can only be achieved by studying this process in multiple final states, and measuring its differential properties.

Chapter 4

The Large Hadron Collider

The Large Hadron Collider (LHC) is a circular machine dedicated to accelerating and colliding protons, as well as ions. Designed to provide proton-proton collisions with a center-of-mass energy of 14 TeV, and an instantaneous luminosity of 10^{34} cm^{-2} s^{-1}, the LHC is the highest energy collider ever built. In addition to the proton-proton collisions used in this thesis, the LHC is also designed to provide lead ion collisions at a center-of-mass energy of 2.76 TeV per nucleon, and an instantaneous luminosity of 10^{27} cm^{-2} s^{-1}.

The counter-rotating proton beams of the LHC collide in four interaction points, as can be seen in Figure 4.1. Particle detectors have been built at each interaction point in order to analyze the products of the high-energy collisions. The data used in this thesis was recorded with the ATLAS ("**A** **T**oroidal **L**HC **A**pparatu**S**") detector [20]. The other three detectors, CMS ("**C**ompact **M**uon **S**olenoid"), ALICE ("**A** **L**arge **I**on **C**ollider **E**xperiment") and LHCb ("**LHC** **B**eauty"), are described in references [33], [5] and [53], respectively. In addition, smaller experiments, such as

TOTEM [61] and LHCf [54] have been installed at some distance from the interaction points to study the production of particles along the beam direction.

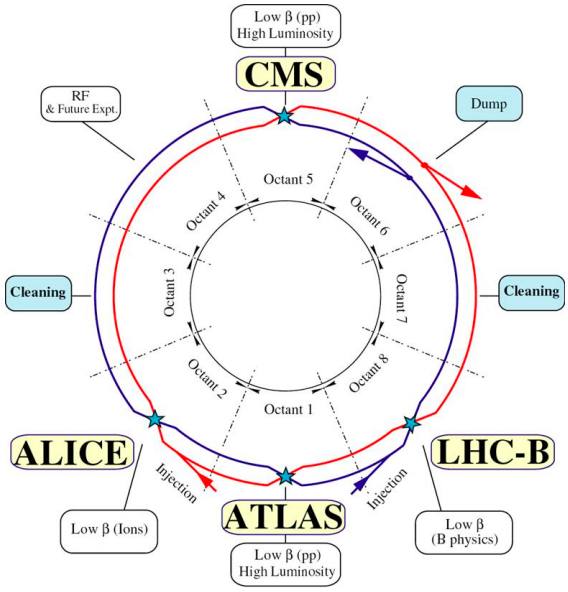

Figure 4.1: The layout of the LHC showing the four collision points [42].

The following sections start from describing the LHC design (4.1) and continue with its actual performance during the 2011 run (4.2). The differences between the design parameters and the parameters of the 2011 run are included in Table 4.1. Pile-up effects are briefly discussed in Section 4.2.1. Reference [42] includes a complete overview of the LHC, while references [29, 30, 27] include the full details of its technical design.

4.1 Design

The LHC is housed in the 27 km long tunnel built between 1984 and 1989 for the LEP ("**L**arge **E**lectron–**P**ositron Collider"). The LEP tunnel had been designed

Table 4.1: LHC design parameters compared to the 2011 operations ones [42].

Parameter	2011 Operation	Design
Beam energy [TeV]	3.5	7
Peak instantaneous luminosity [$\mathrm{cm}^{-2}\ \mathrm{s}^{-1}$]	3.6×10^{33}	10^{34}
Number of filled bunches	1380	2808
Bunch spacing [ns]	50	25
$\beta*$ [m]	1.5	0.55
Crossing angle [μrad]	150–200	286
Transverse width at IP [μm]	30	17

with an internal diameter of 3.7 m. This large size was chosen to take into account the possibility of housing, at a later stage, a hadron machine with superconducting magnets supported by cryogenic equipment [55]. The LEP tunnel lies between 45 m and 170 m below the ground surface, between Geneva airport and the Jura mountains.

The LHC magnets are made with niobium-titaniun (NbTi) cables and they have to be cooled to less than 2 K with superfluid helium in order to reach superconductivity (9.2 K) and to remain superconductive despite the high currents (11,850 A) and large magnetic fields (8.33 T). The large magnetic fields are required to bend the 7 TeV proton beams around the LHC ring ($p[\mathrm{TeV}] = 0.3 \times B[\mathrm{T}] \times r[\mathrm{km}]$). In addition to the dipole magnets used to bend the beam, quadrupole and higher order magnets are used for focusing and correcting the beam, and for steering it into the small area where collisions are produced. Due to the limited space in the tunnel, only a single cryogenic structure fits. Therefore, a *twin-bore* or *two-in-one* design [28] is used, with both proton rings in the same cryostat. The counter circulating proton beams require oppositely oriented magnetic fields in order to be steered along the same circumference. Therefore, the twin-bore structure results in a very complicated design, as the two rings are close enough to influence each other's magnetic field. One

of the LHC twin-bore dipole magnets can be seen in Figure 4.2.

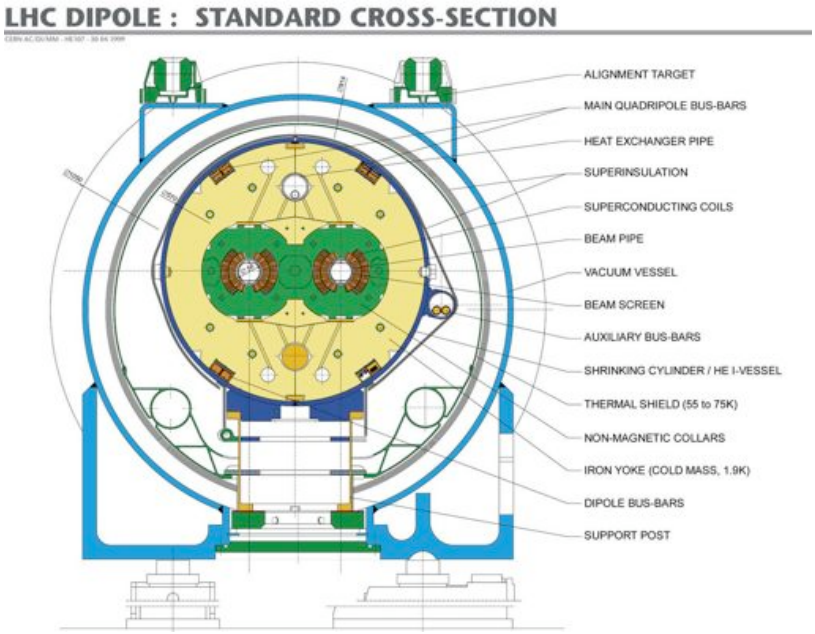

Figure 4.2: An example of an LHC dipole magnet with the twin bore design [26].

The LHC is designed to accelerate protons to an energy of 7 TeV, starting from an initial energy of 450 GeV. The existing CERN accelerators are therefore used to accelerate protons up to 450 GeV, and inject them into the LHC ring. As illustrated in Figure 4.3, 50 MeV protons are initially produced in the LINAC 2 linear accelerator. These protons are accelerated to 1.4 GeV by the Proton Synchrotron Booster (PSB), and consequently reach 25 GeV in the Proton Synchrotron (PS). The Super Proton Synchrotron (SPS) is then used to reach 450 GeV, and inject the protons into the LHC. The CERN accelerator complex was built prior to the LHC, and had to undergo extensive upgrades to handle the luminosity needs of the LHC.

Acceleration within the LHC is provided by electromagnetic fields in eight radio frequency (RF) superconducting cavities per beam. These cavities operate at

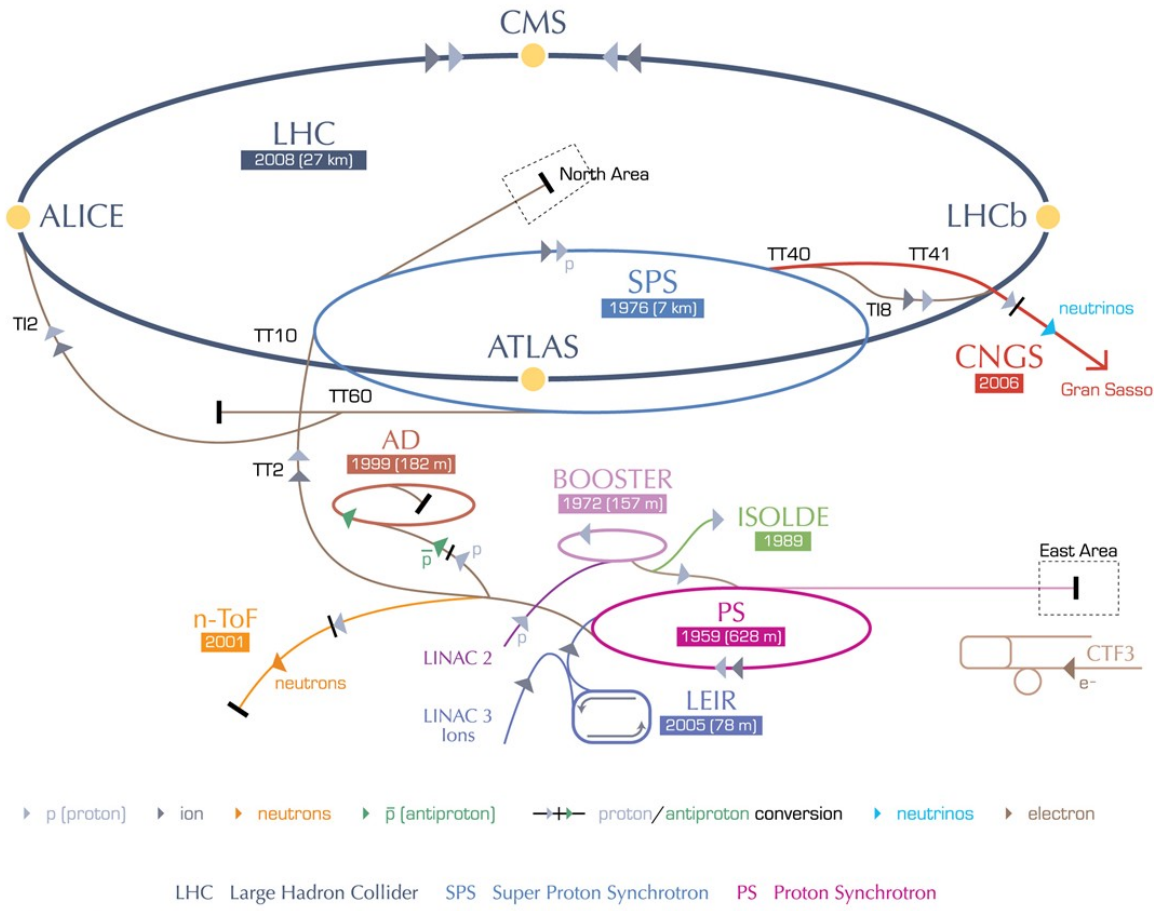

Figure 4.3: The layout of the LHC and the CERN accelerator complex acting as the injector chain for the LHC (© CERN 2008).

400 MHz, with an accelerating gradient of 5 MV/m (2 MV per cavity). Approximately 20 minutes are required to accelerate the beam to its full energy. After the beam has achieved its full energy, the RF cavities also provide small corrections ($\sim$ 7 keV per turn) to account for the energy loss due to synchrotron radiation. The 400 MHz cavities create 35640 RF *buckets* of 2.5 ns length, and each tenth bucket can be filled with a proton *bunch*.

Each beam is injected into the LHC in a series of bunches of 1.15×10^{11} protons. The limit to higher bunch intensities is set by the need to minimize beam-beam interaction experienced by each proton when the bunches collide with each other, which can result in tune shifts (the tune is the number of transverse oscillations of the beam in one full LHC turn). In turn, tune shifts can result in orbit instabilities and radiation losses, which can trigger the heating and subsequent loss of superconductivity (*quenching*) of the magnets. After accounting for injection gaps and abort gaps, each beam is designed to have 2808 circulating proton bunches. The bunches are arranged in *trains* of 72 bunches, with 25 ns spacing within the train, and 12 empty bunches between two trains.

Collisions between counter circulating beams can take place at every *bunch crossing*, resulting in a peak collision rate of 40 MHz (since only each tenth bucket can be filled with a proton bunch). In order to maximize the proton-proton collision rate, the beams are squeezed to a transverse size of $\sim$17 μm at the IP. On both sides of each interaction point (IP), the two beams are brought together in a single beam pipe, for approximately 140 m in each direction. In order to avoid unwanted collisions in the shared beam pipe near the interaction point, the beams are kept on parallel orbits

(*orbit bump*) left and right of the IP. When the parallel beams are brought together at the interaction point, the separation needs to be removed, resulting in a crossing angle of 286 μrad.

4.2 Performance

The LHC construction finished in 2008, but physics data taking only started in 2010. This delay was caused by an incident which took place on September 19th, 2008, only 10 days after the first beams had been circulated in the LHC. During a powering test of the LHC magnets (without beam), the interconnection (*splice*) between two adjacent magnets developed an unexpected resistive heating. This provoked the melting of the material surrounding the splice, and the exposure of superconducting cables resulted in an electric arc. The arc melted the helium pipe in which the cable travels, and the resulting helium expansion caused a very strong pressure wave which damaged 53 consecutive magnets [51].

After the 2008 incident, the damaged magnets were replaced, and all the interconnections were checked. A series of upgrades was planned, including the installation of new relief valves to prevent similar pressure waves, and the extension of the quench protection system (QPS). The upgrades, however, were postponed to the current shutdown (taking place during 2013-2015), and it was determined that the LHC could operate safely at half of its energy (3.5 TeV per beam, for a collision energy of 7 TeV) in order not to further postpone data taking. This energy was reached on March 30th, 2010, and it was maintained during the 2010 and 2011 runs. As a result of further studies of the interconnects, an additional step in energy, up to 4 TeV per beam, was

determined to be safe, and enabled the LHC to provide 8 TeV collisions during the 2012 run.

During the 2010 run, instantaneous luminosities of 2.1×10^{32} cm^{-2} s^{-1} were reached, allowing for the accumulation of an integrated luminosity of approximately 50 pb^{-1}. In 2011, the beam parameters were further tuned based on the experience gathered in 2010, and the instantaneous luminosity reached up to a third of the design luminosity: 3.6×10^{33} cm^{-2} s^{-1}. To obtain such high luminosity, the beams were squeezed at the interaction point to a width of $\sim$30 μm, and a total of 1380 bunches per beam were used. Bunch were organized in trains, each bunch separated by 50 ns from the neighboring ones within the train. The integrated luminosity delivered by the LHC and recorded by the ATLAS detector in 2011 is shown in Figure 4.4.

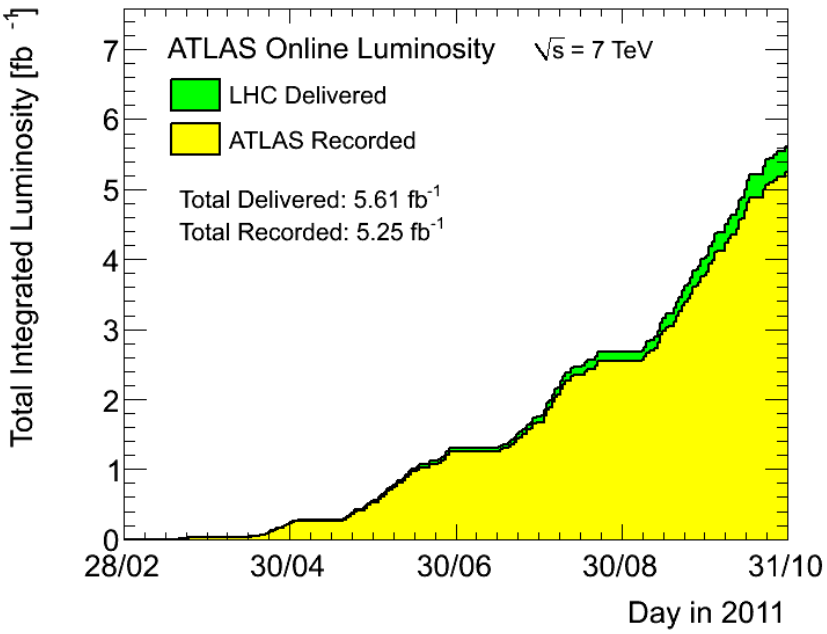

Figure 4.4: Integrated luminosity per day in 2011 as acquired by the ATLAS experiment [11].

4.2.1 Pile-up

This thesis is based on the approximately 5 fb^{-1} of 7 TeV pp collisions collected in 2011. A major side-effect of the large instantaneous luminosity in this dataset is pile-up, both *in-time* and *out-of-time*. Pile-up refers in general to additional proton-proton interactions being recorded by a detector. In-time pile-up consists of additional interactions taking place in the same bunch crossing, and it is a result of the large bunch intensity, and of the narrow squeezing of bunches at the interaction point. Out-of-time pile-up is a result of interactions taking place in preceding or following bunch crossings. These out-of-time interactions can affect the recorded data because of the long read-out window of many of the ATLAS detectors as well as their slow baseline restoration.

In-time and out-of-time pile-up can both be measured in terms of μ, the number of interactions per bunch crossing averaged over a ~ 2 minute period of stable luminosity (*luminosity block*). Out-of-time pile-up only comes into play if the bunch crossings are sufficiently closely spaced in time. Figure 4.5 shows the maximum value of μ delivered by the LHC as a function of day in 2011, and the luminosity recorded by ATLAS as a function of μ. The average μ was approximately 6 in early 2011 running, and increased to approximately 12 when the beam was further squeezed after September 2011, reaching a tail of 24 interactions per bunch crossing. The parameter $\beta*$ in the figure represents the distance along the beam line between the interaction point and the point at which the width of the beam doubles. A stronger focusing will result in a faster widening of the beam, so a smaller $\beta*$ signifies a more focused beam at the interaction point.

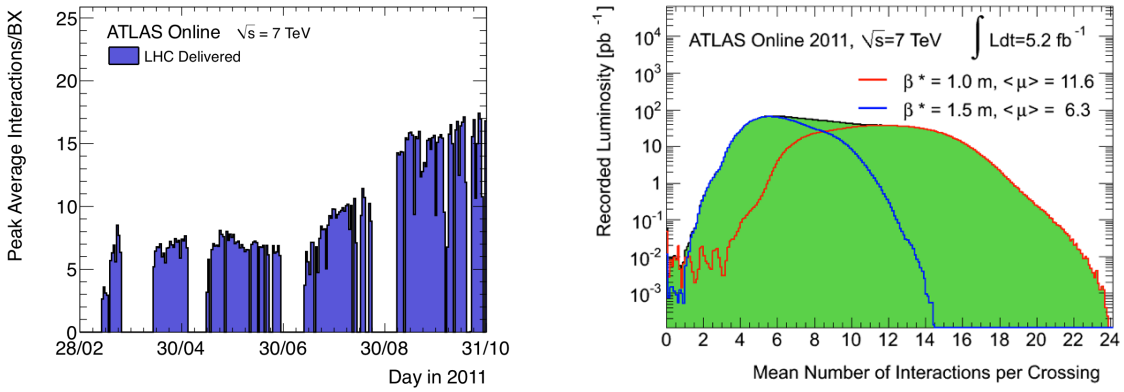

Figure 4.5: (Left) The average number of interactions per bunch crossing as a function of the day in 2011. (Right) The distribution of the average number of interactions per bunch crossing in 2011 [11].

The effects of in-time pile-up on the recorded data are an increase in number of interaction vertices, number of tracks, and energy deposited in each event. As a result, the reconstruction of objects such as vertices, jets and missing energy must take into account the effects of pile-up. The effects of out-of-time pile-up are more subtle, as they can result in signal accumulation but also in threshold shifts. Depending on the detector structure, and on the position of the bunch within the train (at the beginning, middle or end) out-of-time pile-up can thus result in increased or decreased energy recorded. Due to the complex nature of these effects, both in-time and out-of-time pile-up have to be included in any Monte Carlo simulation before comparing it with reconstructed data from the LHC. Moreover, dedicated studies are necessary to estimate and understand these effects, and to validate the simulation. A study of the pile-up effects on the reconstructed jet energy in 2011 data is presented in reference [118], and briefly discussed at the end of Section 6.5. Another effect of the increased instantaneous luminosity is the growing importance of *cavern background*

in the time following a collision. As opposed to out-of-time pile-up, which is related to detector features such as a long readout window and a slow baseline restoration, cavern background is due to low energy photons and neutrons which can result in detector signals long after the collision [49, 39]. The rates expected from cavern background hits are highest in the regions close to the interaction point, reaching approximately 20 Hz/cm^2 at the peak luminosities obtained in the 2011 run [50].

Chapter 5

The ATLAS Detector

The analysis presented in this thesis uses data collected by ATLAS ("**A** **T**oroidal **L**HC **A**pparatu**S**") [20], a general purpose detector experiment located at one of the interaction points of the LHC. The ATLAS detector is designed to study the outcome of proton-proton collisions over a large range of energies in order to extract a wide variety of physics results. It is required to measure physics objects over a large solid angle, while also being able to withstand the harsh environment near the interaction point.

Different technologies are combined to achieve this goal. The structure of the detector is characterized by a series of layers in a cylindrical geometry, building outwards from the beam pipe where the interactions take place. The first three layers consist of silicon pixels, silicon strips, and small drift tubes designed to measure the trajectories of charged particles as they bend inside a 2 T solenoidal magnetic field. Outside the solenoid magnets, calorimeter layers based on liquid argon or scintillator tiles are interleaved with copper, iron or lead. The calorimeters are designed to stop

electrons, photons and hadrons, and to measure their energy. A Muon Spectrometer is placed as the outermost layer of the detector and tasked with providing an additional measurement of the muon tracks. The spectrometer combines four technologies in order to measure muons as they bend inside a toroidal magnetic field: drift tubes, strip chambers, resistive plate chambers and thin gap chambers. The layout of the ATLAS detector can be found in Figure 5.1.

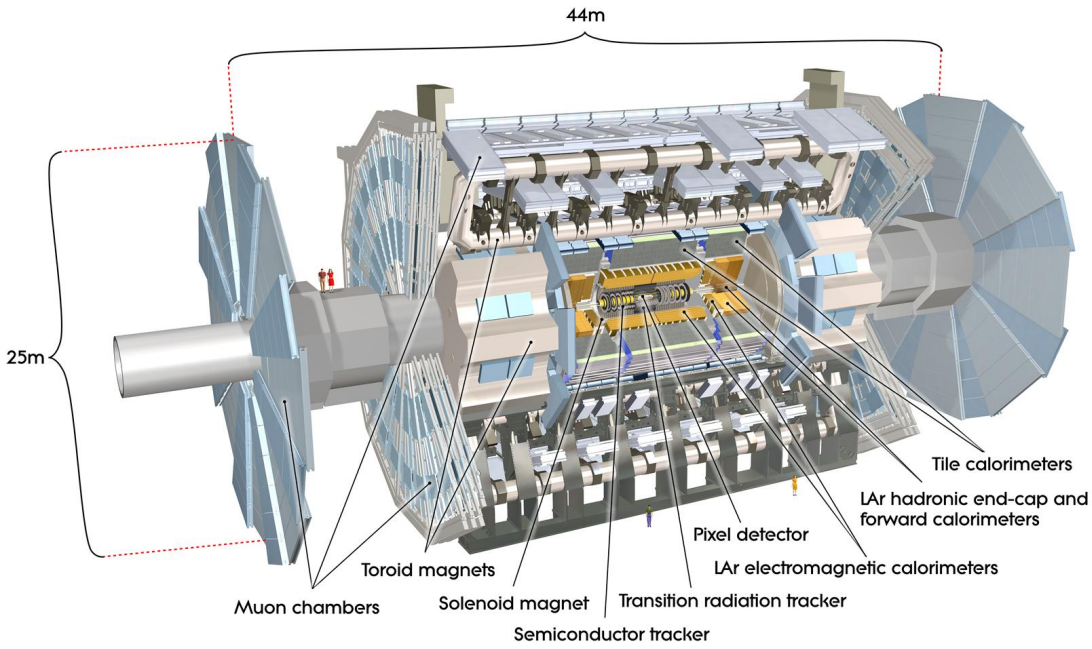

Figure 5.1: A schematic of the ATLAS detector [20].

Before delving into the details of each technology, it is useful to consider the specific performance goals of the ATLAS detector. These goals are dictated by a set of benchmark measurements, such as the different decays of the Higgs boson, which require high resolution measurements of momenta and directions of electrons, muons, photons, taus and b-jets in the $\mathcal{O}(1-100)$ GeV range. Other benchmark

measurements are the searches for new heavy Z' or W' boson with masses up to $\sim$ 7 TeV, which require high resolution lepton measurements up to the TeV range. Similarly, accurate jet measurements up to the TeV range are needed for studying high energy QCD interactions. Accurate missing energy measurements are needed for studying signatures containing neutral particles in the final state, whether they are Standard Model neutrinos or supersymmetric dark matter candidates. Only a small fraction of collisions can be recorded, and very pure and efficient triggers with flexible thresholds are required in order to select these events. A brief summary of the performance goals of the ATLAS detector, in terms of coverage and resolution, are presented in Table 5.1.

Table 5.1: Performance goals specified in the ATLAS detector technical paper [20]. Energy and momentum are listed in GeV and the $\oplus$ sign indicates a sum in quadrature.

Detector	Resolution	Measurement Coverage	Trigger Coverage
Tracking	$\sigma_{p_T}/p_T = 0.05\% p_T \oplus 1\%$	$\|\eta\| < 2.5$	
Electromagnetic Calorimeter (electrons, photons)	$\sigma_E/E = 10\%/\sqrt{E} \oplus 0.7\%$	$\|\eta\| < 3.2$	$\|\eta\| < 2.5$
Hadronic Calorimeter (jets)			
Barrel / End-Cap	$\sigma_E/E = 50\%/\sqrt{E} \oplus 3\%$	$\|\eta\| < 3.2$	$\|\eta\| < 3.2$
Forward	$\sigma_E/E = 100\%/\sqrt{E} \oplus 10\%$	$3.1 < \|\eta\| < 4.9$	$3.1 < \|\eta\| < 4.9$
Muon Spectrometer	$\sigma_{p_T}/p_T = 10\%$ at 1 TeV	$\|\eta\| < 2.7$	$\|\eta\| < 2.4$

This chapter provides an overview of the ATLAS detectors systems, which are described in detail in references [20, 7, 13]. The first section, 5.1, reviews the ATLAS coordinate system, including the definition of track parameters. The magnetic fields of the inner detector and muon spectrometer are described in Section 5.2. Sec-

tions 5.3, 5.4 and 5.5 move outwards from the interaction point to describe respectively the inner detector, calorimeter and muon spectrometer technologies. Finally, the system used to trigger and record events is described in Section 5.6, and the measurement of the integrated luminosity is described in Section 5.7.

5.1 Coordinate System

The coordinates used in ATLAS follow a right-handed Cartesian system with the origin located at the nominal interaction point. The z-axis lies along the beam line, with the positive direction pointing towards the Geneva airport (known as the *A-side*), and the negative direction towards the Jura (known as the *C-side*). The $x-y$ plane is transverse to the beam line, with positive y pointing upward and positive x pointing into the center of the LHC ring. A cylindrical coordinate system is also used, in which r and ϕ denote the radius and the azimuthal angle in the $x-y$ plane, and θ is the polar angle. The two angles, ϕ and θ, are measured respectively from the positive x-axis and from the positive z-axis. The θ angle is often transformed in the pseuro-rapidity, $\eta = -\ln\tan(\theta/2)$, which approaches the rapidity $y = \frac{1}{2}\ln\frac{E+p_z}{E-p_z}$ in the limit where $E >> m$. The pseudo-rapidity is 0 in the transverse plane and infinity along the z axis, with $\eta = 1$ at 45 degrees from the axis. The difference in rapidity between two particles is invariant under boosts along the z axis, and as a result the rapidity and the pseudo-rapidity are natural variables for describing angles in a system where the initial z-momentum is unknown. The angular distance between objects in the ϕ/η plane is a commonly used quantity, defined as $\Delta R = \sqrt{\Delta\eta^2 + \Delta\phi^2}$.

The energy and momentum of outgoing particles, E and p, are often projected

onto the transverse plane. This is because momentum conservation can easily be implemented in the transverse plane, where the initial momentum is known to be zero, but not in the z direction, where the initial momentum is not known. The transverse momentum is then defined as $p_{\mathrm{T}} = \sqrt{p_x^2 + p_y^2}$, and transverse energy as $E_{\mathrm{T}} = E\sin(\theta)$. The momenta and energies of massless particles can be combined in the transverse plane to extract their combined *transverse mass*: $m_T = \sqrt{2E_T^1 E_T^2(1 - \cos(\phi^1 - \phi^2))}$. The transverse mass is used in this thesis for reconstructing $W \to \ell\nu$ decays, where the p_Z component of the neutrino momentum is unknown.

Charged particles in a solenoidal magnetic field follow a helical trajectory, or track, which can be computed at each point in space using 5 parameters: $r,\ z,\ \phi,\ \theta,\ q/p$. The variables $r,\ z,\ \phi$ and θ are the cylindrical coordinates described earlier. The variables q and p are respectively the charge of the track and its momentum, and q/p represent the bending of the track, which is proportional to B/p, and takes opposite directions for positive and negative charges. An alternative parameterization is often used, which focuses on the track parameters closest to the interaction point: $z_0, d_0, \phi, \cot(\theta) = z/r, q/p$. When the track is extrapolated to the point closest to the beam line, d_0 is the transverse distance from the beam line in the (x, y) plane, whereas z_0 is the z position of the track.

5.2 Magnetic Field

The ATLAS detector uses four superconducting magnets to provide the magnetic field for bending charged tracks[1]. The inner detector magnetic field is provided by a solenoid producing a 2 T field in the z-direction. The muon spectrometer magnetic field is provided by three air-core toroid magnets producing fields between 0.5 T and 4 T in the ϕ direction. As a result of the z and ϕ fields, tracks bend in the ϕ direction in the inner detector, and in the η direction in the muon spectrometer. A brief description of the ATLAS magnet system is provided below, while more details can be found in references [20, 62].

Both the solenoid and toroid magnets are made of Al-stabilized NbTi cables cooled to 4.5 K. The magnets are run at a current of 7.7 kA for the solenoid and 20.5 kA for the toroid. To reduce the material thickness and the resulting energy losses of tracks, the solenoid has a thickness of only ~ 0.66 radiation lengths (10 cm), and it is housed in the same cryostat as the electromagnetic calorimeter. For the same reasons, the toroid is built following an air-core design, whereby most muons can traverse the magnetic field without having to cross any of the superconducting coils. The size of the toroid is chosen to provide a large bending volume for muons, resulting in a better lever arm for the muon spectrometer tracking.

Figure 5.2 shows the layout of the magnet system (left) and the field strength in the transverse plane at $z = 0$ (right). The small and partially obscured red cylinder in the center of the left drawing is the solenoid magnet, corresponding to the the

[1]The momentum component of a charged track that is perpendicular to a uniform magnetic field can be estimated by measuring its bending radius R in a magnetic field B: $p[\mathrm{GeV}] = 0.3\ B[\mathrm{T}]\ R[\mathrm{m}]$.

uniform red field in the center of the right plot. The three air-coir toroids are also visible: the large barrel one, whose inhomogeneous field can be seen in the plot, and the two small end-cap ones.

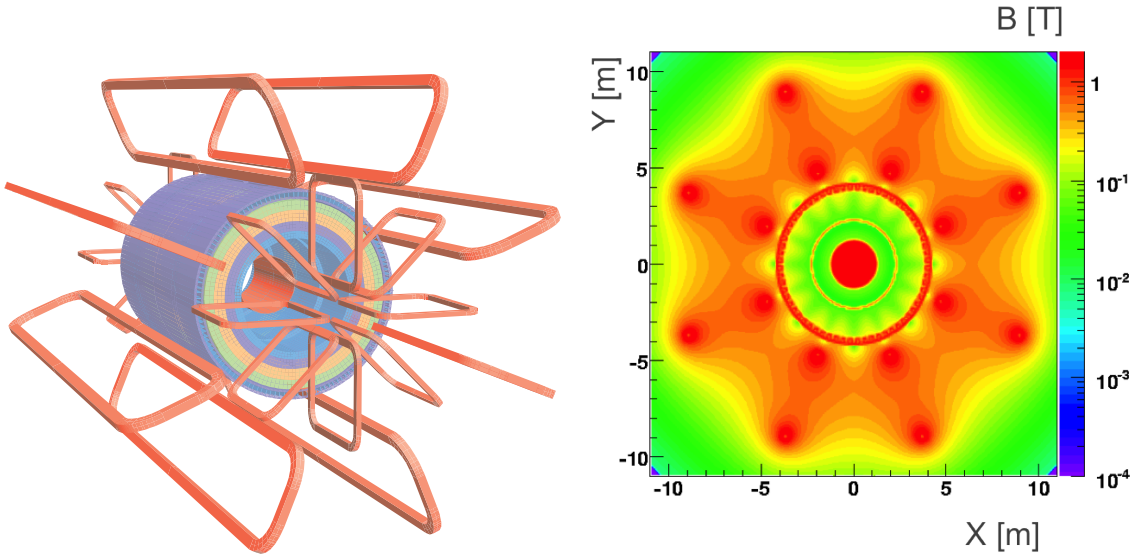

Figure 5.2: (Left) Layout of the ATLAS magnet system. (Right) Cross section view at $z = 0$ of the ATLAS magnetic field strength [20].

As a result of the complex layout of the ATLAS magnet system, the B-field strength affecting each particle has a strong dependence on the particle path. In particular, it is useful to consider the integrated magnetic field affecting a particle on a given trajectory, or $\int B \cdot \mathrm{d}l$, which is also called the bending power. The *sagitta* of a particle track, defined as its distance from a straight path, is proportional to the bending power along its path and inversely proportional to the track momentum in the plane perpendicular to the B field. Therefore, a large bending power is necessary to leads to non-zero sagittas for very high momentum tracks. Figure 5.3 shows the bending power of the ATLAS toroid system as a function of $|\eta|$, in two different ϕ directions. At $\phi = 0$, the barrel field is weaker than the end-cap field, while the

converse is true at $\phi = \pi/8$, due to the position of the toroid coils. It can also be seen that the transition region between the barrel and end-cap is particularly complex, resulting in negative bending power for some (η, ϕ) directions.

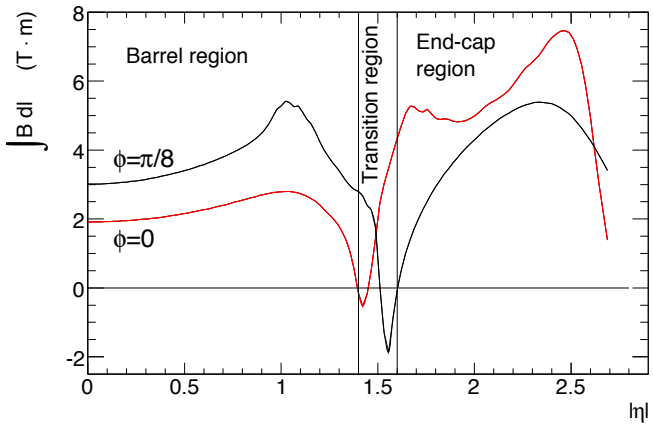

Figure 5.3: Bending power in the ATLAS toroid magnets. [20].

5.3 Inner Detector

The ATLAS inner detector (ID) is designed to reconstruct the paths of charged particles as they traverse a 2 T solenoidal magnetic field. Individual particle tracks are reconstructed using high-resolution position measurements known as hits, and multiple tracks are used in order to reconstruct vertices. The ID is built as a cylinder around the interaction point, with a radius of 1.1 m radius and a length of 7 m. Track hits are measured using three technologies: an innermost Pixel detector composed of silicon pixels, an intermediate silicon strip detector (SCT), and an outermost transition radiation tracker built from small drift tubes (TRT). The three systems are designed to measure respectively three, four, and 36 hits along a track. Figure 5.4

shows a three-dimensional rendering of the ID layout, while Figure 5.5 includes a more detailed schematic.

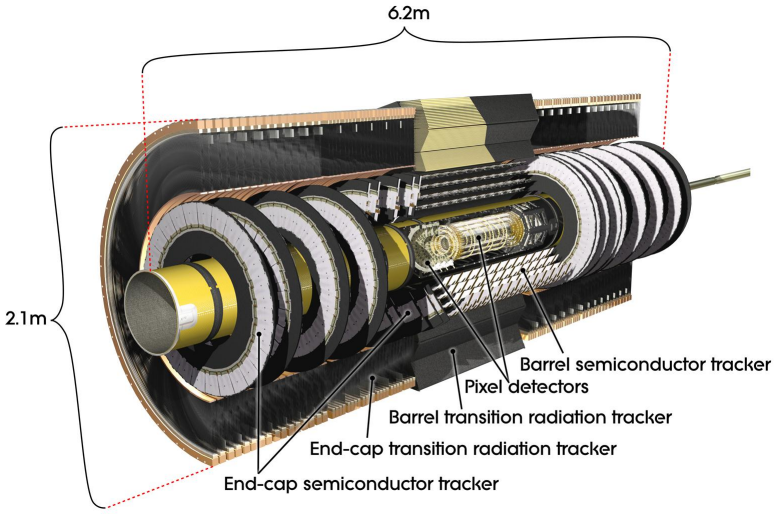

Figure 5.4: Layout of the ATLAS inner detector [20].

The primary goal of the inner detector is to provide accurate and efficient tracking for charged particles with $p_{\mathrm{T}} > 0.5$ GeV within $|\eta| < 2.5$, with a transverse momentum resolution of 1% (5%) for track p_{T} of 0.5 GeV(100 GeV), as specified in Table 5.1. In addition to single track measurements, multiple tracks can be combined to enable the reconstruction of primary vertices from pp collisions and secondary vertices from the decays of long-lived particles. Several challenges are added to these requirements, such as the high occupancy and high radiation environment, and the low material budget required to prevent multiple scattering and energy losses before the calorimeters. At design luminosity, each bunch crossing is expected to generate ~ 40 primary vertices and $\sim$1000 charged particles with $p_{\mathrm{T}} > 0.5$ GeV. The ID design is therefore driven by several constraints, and results in a combination of different technologies. The inner

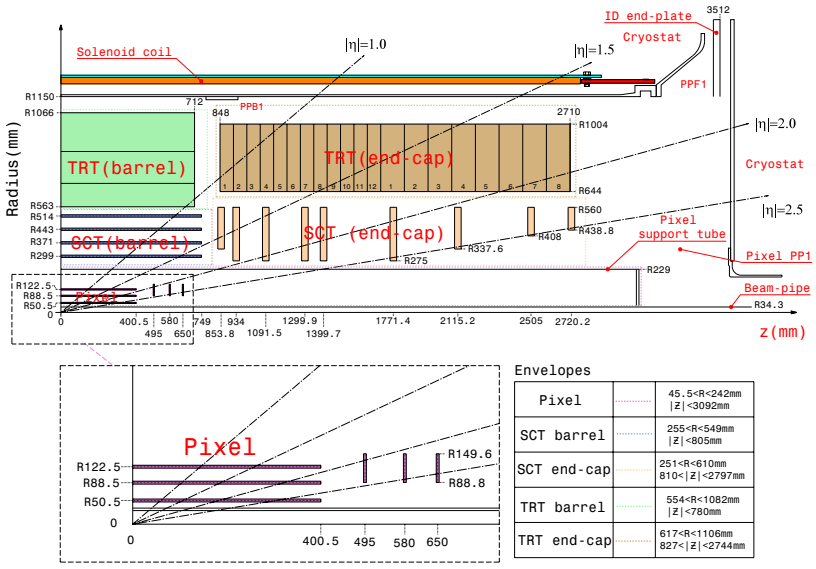

Figure 5.5: Schematic view of the sub-detectors in the ATLAS inner detector [20].

layers are instrumented with dense Pixel and SCT detectors which provide precise measurements of impact parameters (d_0, z_0) and angles (η, ϕ). The outer layers are instrumented with the low-density TRT, providing a large number of individually less precise hits which contribute to the track momentum measurement. A brief overview of the ID detectors is provided below, while more details can be found in references [20, 19, 4, 1].

5.3.1 Silicon Pixel Tracker

The silicon pixel tracker, or Pixel detector [19] is the closest sub-detector to the interaction point, with its innermost layer located at 5 cm from the beam line. In the W+b-jets analysis, the Pixel detector is particularly important for the identification of primary vertices from different pile-up collisions, and for the identification of secondary vertices from long-lived B-hadrons. The detector is organized in three

layers, providing three hits for most tracks within $|\eta| < 2.5$. The size of each pixel is $50 \times 400\mu m$, and the three layers, totaling 80.4 million pixels, allow for a resolution of $\sigma_\phi = 10$ μm in the bending direction (ϕ), and $\sigma_{z,R} = 115$ μm in the z (barrel) or R (end-cap) direction.

5.3.2 Silicon Strip Tracker

The silicon strip tracker, or SemiConductor Tracker (SCT) [4], is located outside the three layers of the Pixel detector, and provides four additional layers of high resolution hits. Each strip is 6.4 cm long, and separated from neighboring strips by 80 μm. Each of the four SCT layers includes two sets of overlapping strips, with a relative rotation angle of 40 mrad to allow for measurements of the second coordinate. The resulting resolution given by the 6.3 million SCT strips is $\sigma_\phi = 17$ μm in the bending direction (ϕ). In the z direction (R for the end-cap), the resolution is only $\sigma_{z,R} = 580$ μm, due to the small rotation angle between SCT layers.

5.3.3 Transition Radiation Tracker

The transition radiation tracker (TRT) [1] is the largest part of the inner detector, and provides $\sim$ 36 additional hits for tracks within $|\eta| < 2.0$. It is a low-density detector, consisting of drift tubes (or straw tubes) embedded in a matrix of $19\mu m$ polypropylene fibers which trigger the transition radiation. Each TRT tube is 4 mm in diameter and 1.4 m long, and it is operated at -1530 V. Charged particles crossing the tube ionize the $Xe/CO_2/O_2$ gas, causing electrons to drift to the central wire. The signal timing is converted to a drift radius, leading to a radial resolution of

$\sim$130 μm within each tube (see Figure 5.12 which describes a drift tube in the muon spectrometer). While this resolution is much larger than that of the silicon layers, the large number of hits and the large large lever arm allow the TRT to contribute significantly to the momentum resolution.

The polypropylene fibers are used as a structure for the tubes, but also as an inhomogeneous material which triggers transition radiation. Charged particles at high-β are susceptible to emitting transition radiation each time they cross a boundary between materials of different dielectric constants. When traversing the thin fibers of the polypropylene matrix, electrons and photons can radiate a large amount of photons, generating high-threshold ($\sim$ 6 keV) hits in the TRT tubes. Slower particles, such as pions, are less likely to emit transition radiation, resulting in low-threshold ($\sim$ 150 eV) hits.

5.4 Calorimeter

The ATLAS calorimeter is designed to provide accurate energy and direction measurements of electromagnetic objects such as electrons and photons, and hadronic objects such as jets. One of the striking features of the ATLAS calorimeter is its large coverage, out to $\eta < 4.9$, which is necessary to measure the missing transverse energy caused by non-interacting particles such as neutrinos. The calorimeter system is composed of an electromagnetic (EM) calorimeter designed to measure electrons and photons, and a hadronic calorimeter designed to measure jets of hadrons. The EM calorimeter is located closer to the beam and covers the region of $|\eta| < 3.2$. Its high segmentation is used to distinguish the shapes of electron and photon showers, and to

associate energy depositions to tracks from the ID. The hadronic calorimeter encloses the EM calorimeters, covering the same region of η. It has a coarser segmentation, and its depth is designed to contain hadronic showers in order to avoid punch-through to the muon spectrometer. In the high pseudorapidity region of $3.1 < |\eta| < 4.9$, a forward calorimeter designed to withstand extremely intense radiation provides both EM and hadronic measurements.

All of the ATLAS calorimeter systems are *sampling* calorimeters, indicating that they alternate layers of absorber material with layers of active medium. Only the active medium is read out, and the total energy of incident particles has to be inferred from the size and distribution of the sampled energy deposits. Two active medium technologies are used, liquid argon (LAr) and plastic scintillator tiles. The LAr is used for all EM calorimeters, and for the end-cap and forward hadronic calorimeters, due to its radiation hardness. The LAr calorimeters require cryogenic cooling to 80 K using liquid nitrogen. The scintillator tiles are used for the barrel and extended-barrel hadronic calorimeter due to their robustness, and their lower cost compared to liquid-argon. Different absorbing materials are used, depending on the radiation and occupancy conditions. These materials are: lead for the EM calorimeters, steel for the barrel hadronic calorimeter, copper for the end-cap hadronic calorimeter, and copper and tungsten for the forward calorimeter. The structure of the sampling also changes in the different calorimeters, from accordion-shaped plates, to parallel plates, tiles, and a tube-embedding matrix. The layout of the calorimeter system can be seen in Figure 5.6, while Figure 5.7 shows the material in the calorimeter systems in terms of radiation and interaction lengths. A brief overview of the calorimeters is provided

below, while more details can be found in references [20, 14, 17].

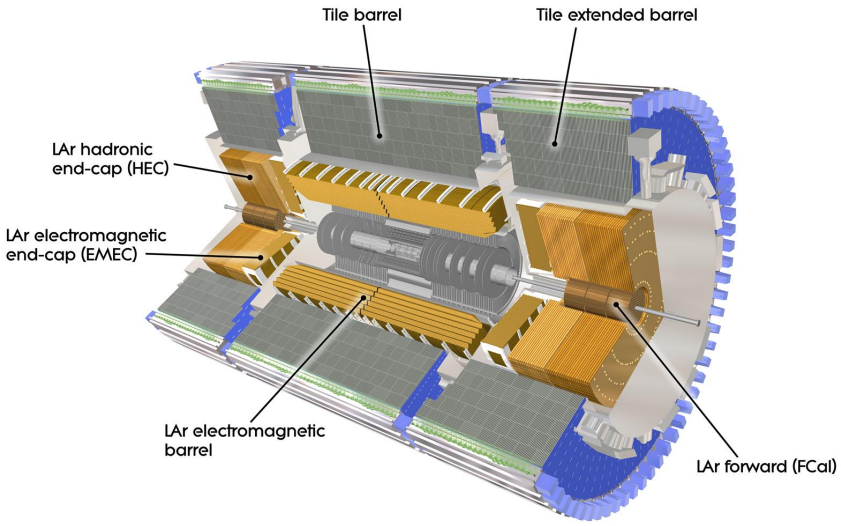

Figure 5.6: Layout of the ATLAS calorimeter system [20].

5.4.1 Liquid Argon Calorimeters

Liquid-argon (LAr) sampling calorimeters in ATLAS use different absorbers and different designs, depending on their locations and tasks, but their signals originate in the same way. A bias voltage is applied across a region filled with liquid argon, so that charged particles entering this gap can ionize the liquid argon and the resulting charge can be read out. The role of the absorber layers is to force electrons, photons and hadrons to produce a shower, and to contain their full shower within the calorimeter in order to achieve a precise energy measurement. The thickness of the absorber layers can be optimized to achieve the desired number of radiation lengths. The read-out segmentation of the active medium can also be optimized to facilitate measurements

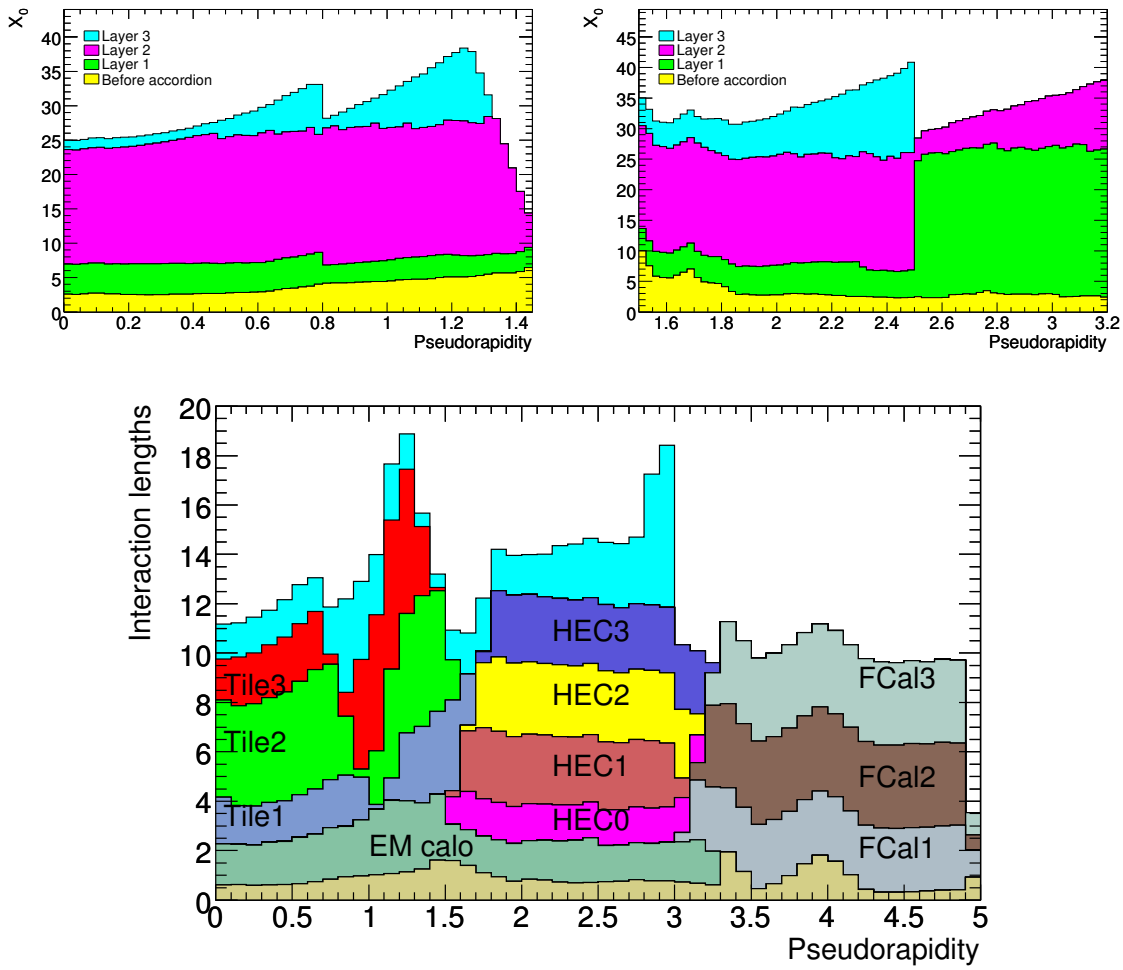

Figure 5.7: Amount of material in terms of radiation lengths X_0 for the EM calorimeter in the barrel and end-cap regions (top). Amount of material in terms of interaction lengths for the the whole ATLAS calorimeter, including EM, hadronic and forward calorimeters (bottom) [20].

of shower direction and shape.

Electromagnetic Calorimeter

The EM calorimeter [14] surrounds the inner detector. Its barrel section shares a cryostat with the solenoid magnet in order to reduce the amount of material in front of the calorimeter. The two end-cap sections are contained in their own cryostat systems. The accordion design, shown in Figure 5.8 (left), is chosen to provide continuous coverage in ϕ, without cracks between adjacent modules. In the photo, the lead absorbers are visible in grey, and the copper sheets used for providing the high voltage and reading out the signal are visible in copper color. The liquid argon is housed in the gaps between these alternating layers, and the gaps are maintained by honeycombed spacers. Figure 5.8 (right) shows a sketch of the EM calorimeter segmentation, starting with a highly segmented first layer used for direction determination and particle discrimination, a deep second layer optimized to contain the largest fraction of the shower energy, and a third layer used to measure the tails in the shower. The radiation lengths of these three layers is plotted in Figure 5.7 (top) for the EM barrel and end-caps.

Hadronic and Forward LAr Calorimeters

The end-cap hadronic calorimeter (HEC) [14] is located beyond the end-cap EM calorimeter, and covers the rapidity region $1.5 < |\eta| < 3.2$. To increase the thickness of the absorbing layer necessary to contain hadronic showers, a parallel-plate geometry is used instead of the accordion one, and copper is chosen as the absorber material.

In the pseudo rapidity region $3.1 < |\eta| < 4.9$, a forward calorimeter (FCAL) [14]

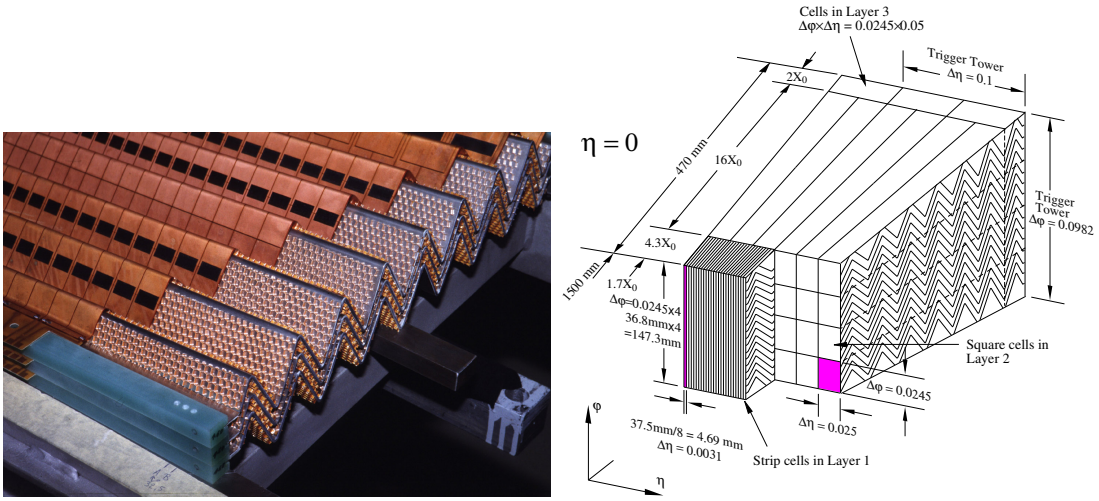

Figure 5.8: A photo showing the accordion design ©1993 CERN (left) and a sketch of the EM calorimeter accordion geometry [20] (right).

is designed to cope with the high radiation and high occupancy environment. The absorbing structure is a metal matrix with regularly spaced holes in which tubes containing liquid nitrogen are embedded. The absorbing material is copper for the EM layer, and tungsten for the two hadronic layers. In the W+b-jets analysis, the primary purpose of the FCAL is to aid in the calculation of the missing transverse energy, by providing a complete picture of the event kinematics even at high pseudorapidity. The interaction lengths of the HEC and FCAL are plotted in Figure 5.7 (bottom).

5.4.2 Plastic Scintillator Calorimeters

The plastic scintillator technology is used in the largest of the ATLAS calorimeters, the barrel hadronic calorimeter (Tile) [17]. With respect to liquid argon calorimeters, the Tile calorimeter has a lower material cost, and does not require cryogenic cooling. The Tile calorimeter uses lead tiles as the absorbing material, alternating with plastic scintillator tiles as the active material. The light from the scintillator tiles is trans-

mitted through optical fibers to photomultiplier tubes, from which the signal is read out. The Tile calorimeter is segmented in three layers to optimize the measurement of hadronic showers. The interaction lengths of the three layers are visible in Figure 5.7 (bottom). The Tile calorimeter energy response can be calibrated between ATLAS runs by circulating a Cesium-137 γ-source throughout the calorimeter.

5.5 Muon Spectrometer

The ATLAS muon spectrometer (MS) [18] uses four different detector technologies to provide accurate direction and momentum measurements for muons with momenta from ∼6 GeV up to a few TeV. It also provides efficient triggering for muons in the same momentum range. The MS is located outside of the calorimeter system and occupies a large fraction of the ATLAS cavern. It relies on the bending power of the barrel and end-cap toroid magnets to bend the muon trajectories over a large distance, and requires a very good hit resolution in order to measure the curved tracks. Figure 5.9 shows the overall layout of the muon spectrometer and the toroid magnets.

The benchmark goal of the MS is a 10% momentum resolution for 1 TeV muon tracks (see Table 5.1). In order to reach this goal, accurate hit resolution and B-field modeling are required, as well as modeling of the material crossed by the muon track. Given the bending power of the toroid magnets, the sagitta of a 1 TeV muon track is $\sim 500\mu$m, so the hit resolution required for a 10% measurement is approximately 50 μm. The hit resolution is determined by the intrinsic resolution of each detector element, and by the alignment, which is the knowledge of the position of that detector

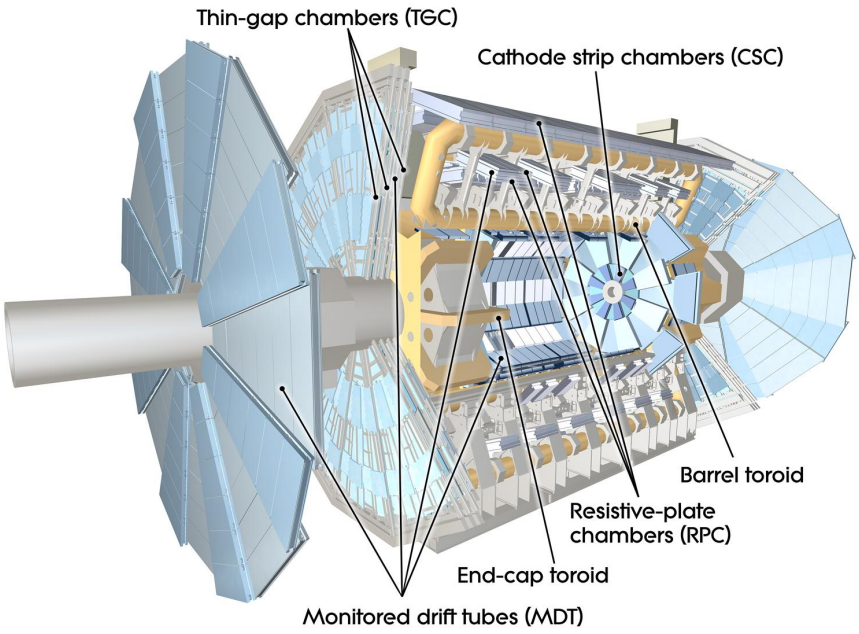

Figure 5.9: A schematic of the ATLAS muon spectrometer [20].

element within ATLAS.

Since the four subsystems of the MS are combined together when reconstructing muon tracks, the B-field monitoring and the alignment monitoring are shared between them. The magnetic field is monitored by almost two thousand Hall probes throughout the MS, which are used to correct B-field modeling software. The alignment is monitored by more than ten thousand optical sensors, which are able to detect position changes at the 20μm level. The expected momentum resolution of the MS is shown in Figure 5.10. At low energies, the resolution is dominated by energy loss in material before the MS, while multiple scattering dominates at medium energies, and alignment and intrinsic detector resolution at high energies.

The four detector technologies used in the MS define four systems. Muon trigger signals, as well as coarse (η, ϕ) hits, are provided by two of them: the Resistive Plate

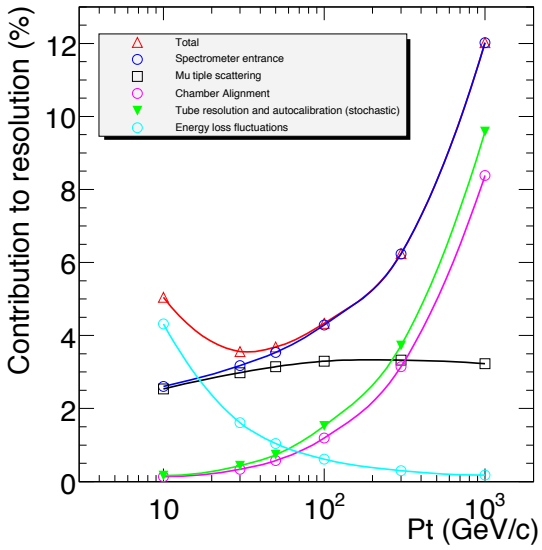

Figure 5.10: Primary contributions to muon stand-alone tracking resolution as described by the ATLAS Monte Carlo simulation [13].

Chambers (RPC) in the barrel region and the Thin Gap Chambers (TGC) in the end-cap region. Both the RPC and TGC are fast tracking detectors with time resolution much smaller than the 25 ns bunch spacing. The high precision measurements in the bending direction (η) is provided by the Monitored Drift Tubes (MDT) over most of the detector acceptance, and by the Cathode Strip Chambers (CSC) in the forward region, where the particle flux is too high for MDT chambers.

The layout of the MS is shown in Figure 5.11. In the upper drawing, the layout of the barrel region can be seen in the transverse plane, showing the sixteen sectors in ϕ (based on the eight-fold symmetry of the toroid), and the three layers of MDT and RPC chambers. The lower drawing shows additionally the three layers of MDT and TGC chambers in the end-cap, and the position of the CSC chambers in the forward region. While the barrel toroid encloses the first two layers of MDT and RPC, in the end-cap region the toroid lies between the first and second MDT layers, and before

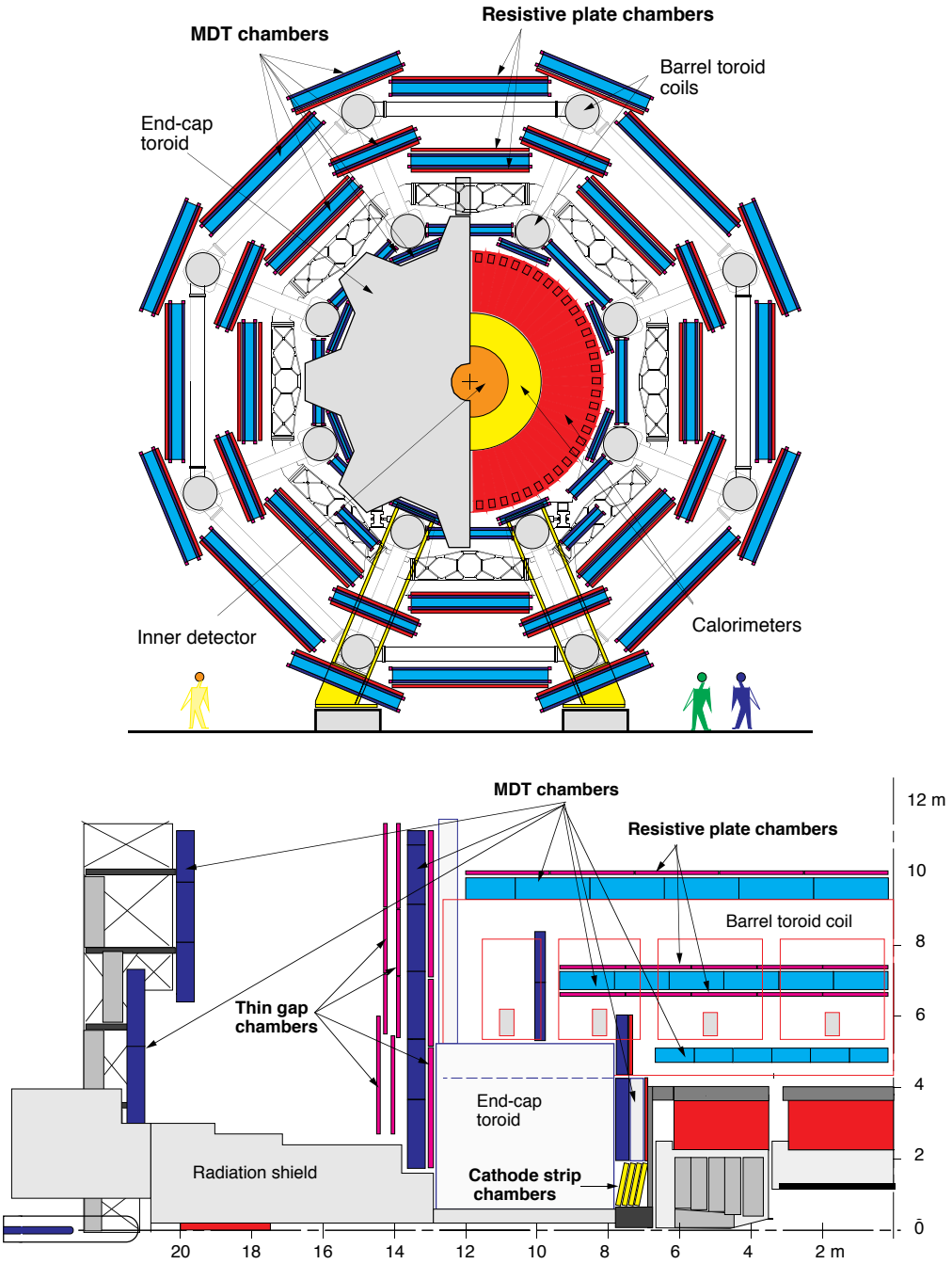

Figure 5.11: The layout of the muon spectrometer in the $x - y$ plane (top) and in the $y - z$ plane (bottom) [18]. The lower drawing only shows a quarter of the $y - z$ plane, with the interaction point located in the lower right corner.

the three TGC layers. An additional (not labeled) TGC layer lies to the right of the innermost MDT end-cap layer. It provides a ϕ-coordinate measurement used in tracking, but it does not participate in the trigger decision. A brief overview of the muon spectrometer systems is provided below, while more details can be found in references [20, 18].

5.5.1 Monitored Drift Tubes

MDT chambers are composed of six or eight layers of drift tubes. Each tube has a 3 cm diameter and a 50 μm thick anode wire at the center. The wire is held at 3080 V while the tube is held at ground, generating a radial electric field. The tubes are filled with a gas mixture of 93% argon, 7% CO_2, and 1 part per million H_2O, held at pressure of 3 bars. The mixture is chosen for its ageing properties, preventing the accumulation of deposits on the anode wires, as well as for its gain of $\sim 2\times10^4$. When a muon passes through an MDT tube, as in Figure 5.12, it ionizes the gas, initiating an avalanche of electrons which drift to the central wire, causing a voltage drop. With this gas mixture, the maximum drift time of electrons in the tubes is approximately 700 ns. When MDT hits are read out, the time of arrival is also recorded, as it can be related to the distance of the muon track from the wire. Using this method, each hit has a resolution of approximately 80 μm on the hit radius, even though the full tube radius is 1.5 cm. The ϕ coordinate (along the tube) is not measured by MDTs, and it is extracted from the RPC and TCC hits.

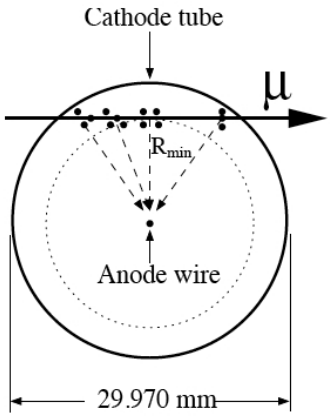

Figure 5.12: A muon traversing the gas of an MDT tube. The muon ionizes the gas mixture, and the first electrons to reach the wire create the hit signal [18].

5.5.2 Cathode Strip Chambers

The CSC chambers cover the forward region of the end-cap inner layer ($2.0 < |\eta| < 2.7$), and they are placed behind the hadronic end-cap calorimeter (see igure 5.11). They are multi-wire proportional chambers. A plane of anode wires is placed between two planes of cathode strips, separated by a 2.5 mm gas gap from both. When a muon ionizes the gas, electrons drift towards the wires, inducing charges on the cathode strips which are read out. One set of strips is oriented parallel to the wires, and one perpendicular, resulting in a two-dimensional measurement. The hit resolution, obtained by interpolating the charge measured in neighboring strips, is 60 μm in η and 5 mm in ϕ. Each CSC chamber is composed of 4 layers of proportional chambers, providing four hits for each muon track.

5.5.3 Resistive Plate Chambers

The RPC chambers provide trigger signals and ϕ-coordinate measurements in the barrel region, and they are placed adjacently to the second and third MDT layers (see Figure 5.11). Due to spatial constraints from support structures and services, the RPC chambers only cover approximately 80% of the barrel region. The RPC chambers are based on two resistive plates, separated by a 2 mm gas gap with a $\sim$ 4.9kV/mm electric field. The gas gap can be seen in Figure 5.13 (left). When a muon ionizes the gas, it creates a charged avalanche. Electrons from the avalanche then drift towards the anode plate, inducing charges on the read out strips that are mounted outside the resistive plates. The strips on the upper and lower plates are oriented in perpendicular directions, providing a two-dimensional measurement. Each RPC chamber includes two gas gaps, shown in Figure 5.13 (right), so a track traversing three RPC chamber layers delivers six measurements in η and ϕ. The distance between RPC strips is approximately 30 mm.

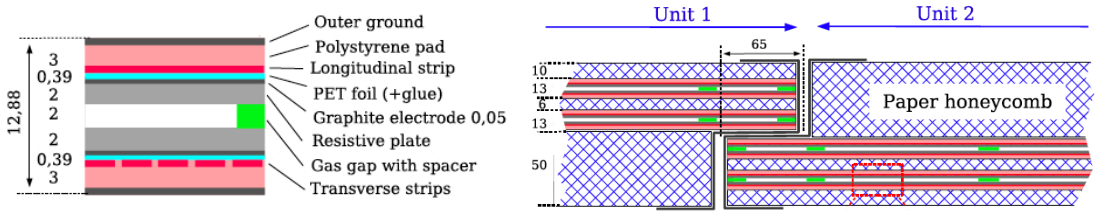

Figure 5.13: The structure of an RPC gas gap (left) and the structure of two adjacent RPC chambers, each consisting of two gas gaps separated by a paper honeycomb layout (left) [18].

5.5.4 Thin Gap Chambers

The TGC chambers provide the triggering and ϕ-coordinate measurements in the end-cap region, and they are placed around the second layer of MDT end-cap chambers. Additional chambers not used for triggering are located on the first layer MDT end-cap chambers. TGC chambers are used in the end-cap due to their higher rate capabilities, their higher granularity, and their radiation resistance. The TGC chambers are multi-wire proportional chambers, like the CSCs, but they have a smaller anode-cathode separation ($\sim$ 1.5mm), resulting in an improved time resolution. Both the anode wires and the strips are read out, providing a measurement of η and ϕ. The wire-to-wire distance is very small, 1.8 mm, and wires can be read out as smaller or larger *groups*, depending on the resolution required in each η region. Each TGC chamber contains two or three gas gaps held together with a honeycomb structure, called doublet and triplet chambers respectively, as seen in Figure 5.14.

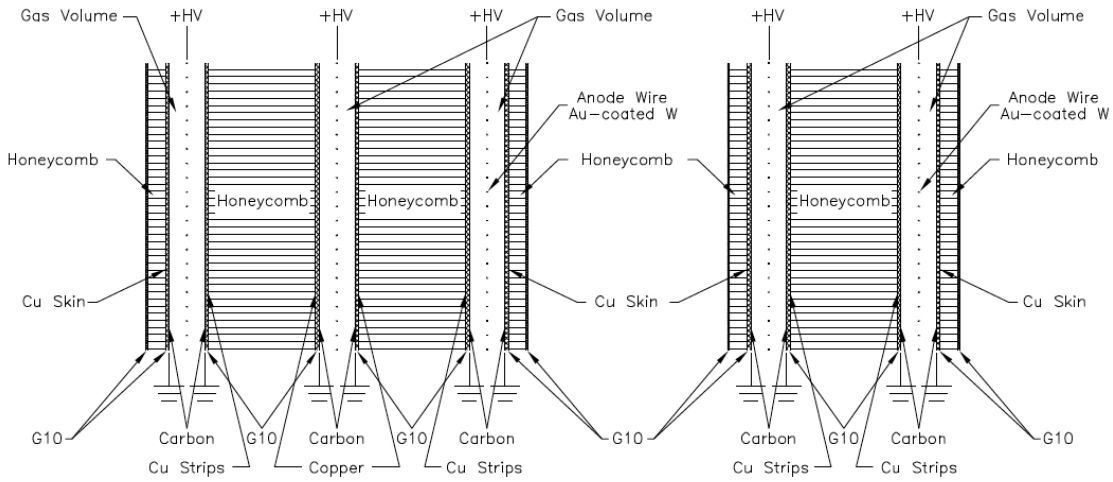

Figure 5.14: The structure of the TGC triplet (left) and doublet (right) chambers [18].

5.6 Trigger and Data Acquisition

The ATLAS trigger and data acquisition (TDAQ) system [20] is designed to identify interesting events, read them out and record them, as well as to configure and synchronize the detector elements. The trigger system is based on analyzing events at three consecutive levels of increasing complexity. The first level (L1) is implemented using custom-made electronics. The second and third level (L2 and Event Filter or EF) form what is called the High Level Trigger (HLT), and they are implemented using off-the-shelf computers and networking equipment. The L1 is designed to cope with the 40 MHz rate of LHC collisions, and perform trigger decisions within 2.5 μs. The L2 can work with an input rate of $\sim$100 kHz (provided by the L1), and perform decisions within 40 ms. The EF analyzes the L2-triggered events at a 3.5 kHz rate, it requires 4 s to analyze an event and it provides an output rate of $\sim$400 Hz. The high input and output rates of the HLT are achieved by analyzing multiple events in parallel. The L2 decision is much faster than the EF one because it only uses the event information located in the specific region where the L1 trigger originated (Region-of-Interest or RoI). The EF, on the other hand, analyzes the entire event.

The Data Acquisition (DAQ) system controls the movement of the data from the detector to the storage disks. When the L1 trigger accepts an event, the DAQ moves the full event data from the detector electronics into the detector-specific Read-Out Drivers (ROD). The RODs encode the data in a common format and transfer it to the common Read-Out System (ROS). The event data then remains in the ROS, and is provided, on request, to the L2 system. If the L2 trigger passes, the event data from different detector regions is merged into a single structure, and provided to the

EF. If the EF trigger passes, the event is sent to an output node and recorded to disk. Monitoring occurs by sampling the data at each stage of the DAQ chain. The ROD data is monitored after the L1 trigger to test low level detector operations. The RoIs are monitored after the L2 trigger, and the fully reconstructed events are monitored after the EF decision.

The W+b-jets analysis uses high p_{T} muon and electron triggers to select $W \to \ell\nu$ events. The following two sections describe briefly the L1 algorithms used in the electron and muon triggers decisions. The L2 and EF algorithms are simplified versions of the offline algorithms described in Chapter 6. A more complete description of the trigger and DAQ system can be found in Reference [20].

Level-1 Muon Trigger

The L1 muon trigger uses on-chamber look-up tables to search for track-like patterns in the hits of the RPC and TGC detectors. The triggering begins with a hit in a reference layer (the middle layer in the RPC and the outermost layer in the TGC), which initiates a search for hits an the other two layers, along predefined search windows, or *roads*. Wider roads correspond to lower momenta (and more curvature), and narrower roads correspond to higher momenta, as shown in Figure 5.15. The association of hits with a road determines which p_{T} threshold is passed. The low-p_{T} triggers, based on hits in two out of the three detector layers, have a threshold range of approximately 6–9 GeV. The high-p_{T} triggers, based on hits in three detector layers, have a threshold range of approximately 9–35 GeV.

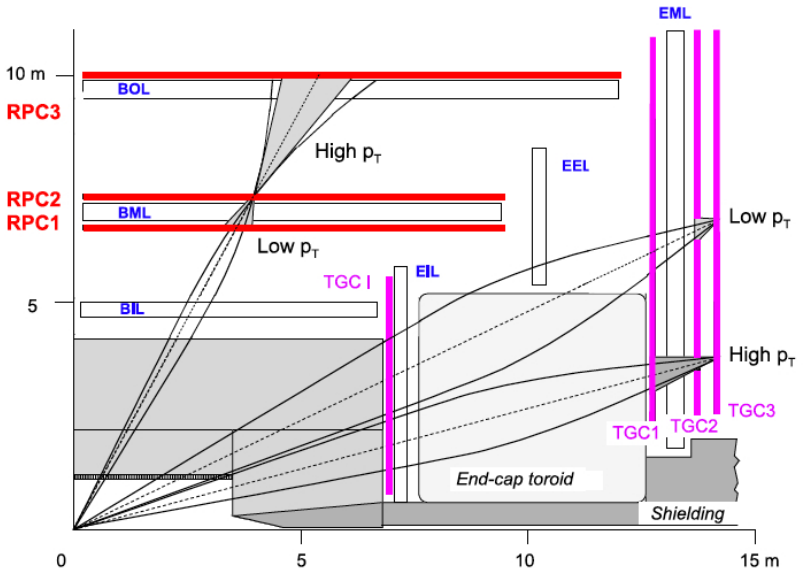

Figure 5.15: The muon L1 trigger logic, showing the high-$p_T$and low-$p_T$roads of the RPC and TGC. The innermost layer of the TGC, at $z \sim 7$m, is not used for triggering. [20].

Level-1 Electron Trigger

The L1 electron trigger decision takes place in the service cavern, where the analog signals from 7000 $\Delta\eta \times \Delta\phi = 0.1 \times 0.1$ towers are sent from both the EM and hadronic calorimeters. These signals are digitized, converted into energy measurements and analyzed by a Cluster Processor (CP) which is used to identify electron-like clusters. The CP algorithm can be described with the aid of Figure 5.16. A 4×4 window is established in which the sum of two of the central (green) towers in the EM calorimeter must pass a programmable lower threshold. To reject jets, programmable upper thresholds are set on the remaining 12 towers in the EM calorimeter, and on the 16 towers in the hadronic calorimeter. The CP is also capable of identifying photon and tau candidates. A separate processor, called the Jet/Energy processor, is used to identify jets, calculate total calorimeter energy, and calculate the missing energy.

The CP and the Jet/Energy processors are both part of the L1 calorimeter (L1Calo) trigger system.

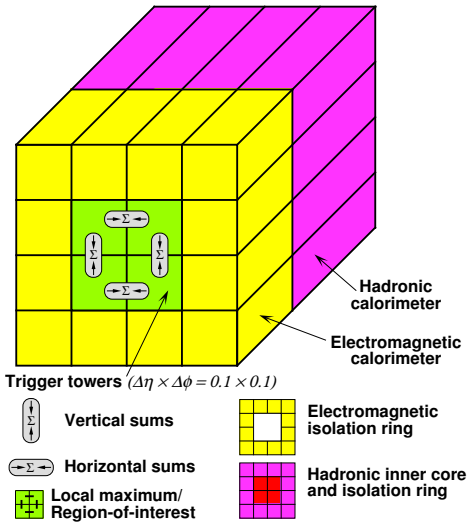

Figure 5.16: Logic of the Level-1 electron trigger [20].

5.7 Luminosity Determination

A precise measurement of the LHC luminosity is necessary for the W+b-jets analysis. Specifically, the luminosity serves as the scaling between the number of observed W+b-jets events and the measured cross-section for the W+b-jets process. The luminosity delivered by the LHC is determined by ATLAS using several detectors, calibrated in dedicated runs. A detailed description of the luminosity determination method used for the 2010 run can be found in reference [22], and the changes adopted for the 2011 run can be found in reference [25]. The following two sections summarize this method, and describe the detectors used to implement it.

5.7.1 Method

The luminosity of a hadron collider, given in units of $\mathrm{cm}^{-2}\ \mathrm{s}^{-1}$, can be expressed both in terms of event rate, and in terms of beam parameters. In terms of event rate, the luminosity is simply the ratio between event rate and cross-section for a specific process. For the *inelastic scattering* process, the luminosity is

$$\mathcal{L} = \frac{R_{inel}}{\sigma_{inel}} = \frac{R_{vis}}{\sigma_{vis}} \tag{5.1}$$

where R_{inel} is the rate of inelastic collisions and σ_{inel} is the inelastic scattering cross-section. The second equation introduces a detector efficiency in both numerator and denominator: $\sigma_{vis} = \epsilon\sigma_{inel}$ and $R_{vis} = \epsilon R_{inel}$. In other words, the visible inelastic cross section, determines the visible event rate.

In terms of beam parameters, the luminosity can be expressed as the number of particles crossing a specific area in a given unit of time,

$$\mathcal{L} = \frac{n_b f_r n_1 n_2}{2\pi\Sigma_x\Sigma_y} \tag{5.2}$$

where n_1 and n_2 are the number of particles in the two colliding bunches and Σ_x and Σ_y are related to the horizontal and vertical widths of the beam overlap profiles. n_b and f_r, the number of bunches and the revolution frequency, are known LHC parameters, while n_1 and n_2 can be estimated by measuring the beam current.

R_{vis} can be measured by ATLAS continuously, as discussed in the next section (5.7.2), while the Σ parameters of equation 5.2 can only be measured in special runs called *van der Meer* scans, in which the separation between the two beams is scanned to determine their profile. The luminosity measurement is thus based on comparing the observed R_{vis} to the reference one measured in the *van der Meer* scans.

The measurement of R_{vis} is based on an *Event Counting* method [22]. This method is complicated by the fact that multiple interactions are expected for each bunch crossing, so $R_{vis} = \mu_{vis} n_b f_r$. μ_{vis} is the number of visible interactions per bunch crossing. The currently used luminosity detectors can count events, but they cannot measured μ_{vis} directly. Poisson statistics is therefore used to convert event counts within a short time period into measurements of μ_{vis}. For example, if N collision events are measured over N_{BC} bunch crossings, this measurement can be converted into an estimate of μ_{vis} using the formula

$$\mu_{vis} = \ln\left(1 - \frac{N}{N_{BC}}\right) \tag{5.3}$$

This formula loses precision at high μ_{vis}, as the number of events N approaches the number of bunch crossings N_{BC}. To prevent this, the definition of *event* can be chosen to be more restrictive, for example requiring a coincidence between two detector elements. However, this choice needs to be made carefully, since the Poisson statistics can only be used if the efficiency for reconstructing single-collision and multi-collision events is the same.

The total uncertainty on the 2011 luminosity measurement was eventually determined to be 1.8% [25], but when the W+b-jets analysis was released, only a preliminary uncertainty of 3.4% was available [15]. The larger uncertainty is therefore used, resulting in a negligible effect given the large statistical and systematic uncertainties of the W+b-jets measurement. The improvement of the new estimate originates from an improved uncertainty on the beam current measurement which determine n_1 and n_2 values of equation 5.2. The beam current measurements have an unknown baseline, $\pm 0.8 \times 10^9$ protons in each beam. This baseline was relevant for the *van*

der Meer scans in early 2011, which were used for the first estimate. As the total circulating currents increased during the 2011 run, this baseline became irrelevant, resulting in much more precise measurements in the later *van der Meer* scans.

5.7.2 Detectors

Measurement of μ_{vis} are performed with different methods in different ATLAS systems, in order to provide a series of cross-checks and estimate the uncertainty on μ_{vis}. In particular, the long term stability of each method is checked, and its bias as a function of μ is corrected. This bias can be caused, for example, by an increased efficiency for selecting events with multiple interactions, which would spoil the basic Poisson behavior.

The primary detectors used for the determination of μ_{vis} by event counting are LUCID and BCM. LUCID (LUminosity measurement using a Chernekov Integrating Detector) is a Cerenkov detector located at $z = \pm 17$m, between the middle and outer MDT stations, and covering the range $5.6 < |\eta| < 5.9$. Each LUCID unit is composed of a ring of twenty aluminum tubes surrounding the beam-pipe, filled with C_4F_{10} gas. The Cherenkov light produced by charged particles in the gas is measured by a photomultiplier tube (PMT).

The BCM (Beam Condition Monitor) is a diamond detector located at $z = \pm 1.84$m, and 5.5 cm away from the beam pipe (in terms of pseudorapidity, $|\eta_{BCM}| = 4.2$). Each BCM unit has four radiation-hard detectors, with very good time resolution ($\sim$ 1ns). The radiation hardness is required to cope with the very intense environment in the forward region close to the interaction point. The time measure-

ment is used to discriminate between collision events, in which particles arrive at each BCM unit simultaneously, from beam incidents originating in one or the other side of the beam pipe.

Further cross-checks are provided by measurements of the readout currents of the Tile and Forward calorimeters. These currents are proportional to the number of particles coming from the interaction point, giving an alternative estimate of μ_{vis} that is not based on Poisson statistics. Finally, another cross-check used in the μ_{vis} estimate is the number of primary vertices measured by the Inner Detector. Figure 5.17 shows the fractional deviations between eight different methods using the BCM, LUCID, Forward (FCal) and Tile (TileCal) calorimeters, in a single LHC fill. The μ_{vis} estimates can be seen to agree within 1%.

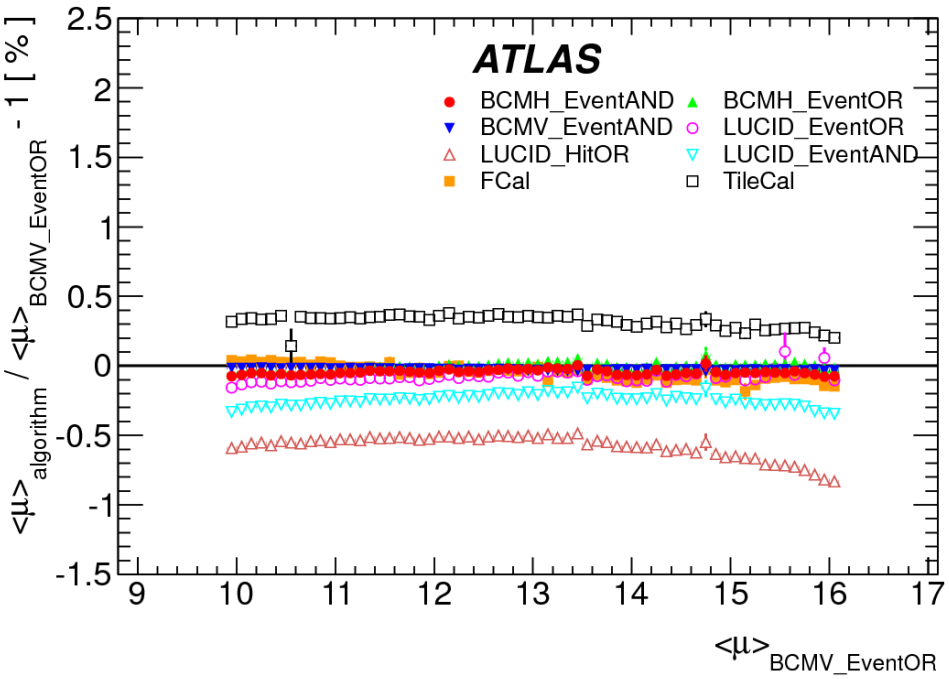

Figure 5.17: Relative deviations of the average number of interactions per bunch crossing $< \mu >$ obtained using different algorithms as a function of $< \mu >$. The μ estimates can be seen to agree within 1%. [25].

Chapter 6

Physics Object Reconstruction

The signals collected with the ATLAS detector are converted into a set of physics objects through a process called *reconstruction*. Reconstruction applies algorithms to the raw data in order to obtain objects such as electrons, muons and jets. The same reconstruction algorithms are used for real data and for simulated data (Monte Carlo), although the respective calibrations can be adjusted to account for known discrepancies.

Events used in the W+b-jets analysis are selected based on leptons (electrons or muons), missing transverse energy, jets and b-tagging. In addition, charged particle tracks in the Inner Detector are used as input for lepton reconstruction and b-tagging, as well as for the reconstruction of primary vertices. The following sections describe the algorithms used for reconstructing ID tracks (6.1), primary vertices (6.2), electrons (6.3), muons (6.4), jets (6.5), b-tagged jets (6.6), and missing transverse energy (6.7). These algorithms are described in detail in references [37, 45, 12, 59, 21, 121, 24], and only an overview is provided here.

6.1 Inner Detector Tracks

Inner detector tracks [37] are reconstructed using space points obtained from the Pixel and SCT hits, and drift circles obtained from the TRT hits. Track reconstruction proceeds in two steps, using an *inside-out* algorithm, followed by an *outside-in* algorithm.

The *inside-out* algorithm associates pairs of hits in two out of the three layers of the Pixel detector, forming track *seeds*. These seeds are extrapolated to the SCT and TRT layers based on a *Kalman Filter* algorithm [44]. The Kalman Filter algorithm starts from the initial track seed, described by a state vector and a covariance matrix. The algorithm takes into account magnetic field, expected energy loss, multiple scattering, and their associated uncertainties in order to extrapolate the track parameters (state vector and covariance matrix) to the next instrumented surface (this is the *prediction* phase of the Kalman Filter algorithm). As new hits consistent with the track parameters are found on the next surface, the Kalman Filter includes them and updates the track description (*filtering* phase). These steps follow iteratively out to the outermost layer. During this whole procedure, in the *smoothing* phase, the updated track information is used to find *outliers* among the hits that are already included in the track. The outlier hits, which contribute most to the track χ^2, are removed and the track parameters are recomputed.

The second step of the ID track reconstruction, the *outside-in* algorithm, is used to recover tracks which were missed by the inside-out algorithm. The inside-out algorithm may fail for a variety of reasons. For example, the track might originate from decays in flight or photon conversions, and they might not have enough pixel

hits to form track seeds. The outside-in algorithm finds TRT track *segments* by transforming the TRT hit patterns into parameters of straight tracks[1] using a Hough transform [41]. For example, in the barrel region, the Hough transform takes as input a 2D histogram of hits in the (r, ϕ) plane. As output, it provides a 2D histogram of parameters of straight segments $(\phi_0, 1/p_{\mathrm{T}})$, where ϕ_0 is the initial position along the ϕ axis and $1/p_{\mathrm{T}}$ is the inverse momentum determining the slope in the (r, ϕ) plane. Each bin in the output histogram is proportional to the number of hits which match the track with the given $(\phi_0, 1/p_{\mathrm{T}})$ parameters, so the largest bins contain the most likely TRT segment candidates. The segments are then fed into a Kalman Filter which extends them backwards into the SCT and Pixels.

6.2 Primary Vertices

The reconstruction of primary vertices (PV) [16] determines an initial vertex *seed* located at the maximum of the z distribution of high quality ID tracks. As nearby tracks are added to this first seed vertex, an iterative fitter [45] progressively updates the vertex information, recomputing its covariance matrix. Tracks that are incompatible with the vertex by more than 7σ are used to generate a new seed, and the process continues until no unassociated tracks remain, or no additional vertices are found. The primary vertex with the highest $\sum p_T^2$ of tracks is considered the hard-scatter primary vertex of the event.

[1] Assuming that tracks originate roughly from the primary interaction region, track segments from tracks with $p_{\mathrm{T}} > 500$ MeV appear as almost straight lines in the $r - \phi$ plane, and straight lines in the (z, ϕ) plane.

6.3 Electrons

Leptons (electrons and muons) are used in this analysis to select $W \to \ell\nu$ decays. Electron reconstruction [12, 23] combines the ID and EM calorimeter information to select electron candidates. Additional criteria are imposed on the electron candidates to ensure that they do not originate from jets.

Electron candidates are reconstructed from an EM cluster matched to an ID track. The cluster is found using a sliding window over the EM calorimeter of $\Delta\eta\times\Delta\phi = 3\times5$ cells, where the dimensions of each cell are $\Delta\eta \times \Delta\phi = 0.125 \times 0.125$. The larger ϕ size of the cluster is chosen to include both the electron track (curving in ϕ) and possible bremsstralung photons which would not be bent by the magnetic field. The EM cluster is then matched to the ID track nearest to its energy-weighted center. If the track points within $\Delta\eta < 0.2$ and $\Delta\phi < 0.1$ of the cluster center, the cluster-track pair forms an electron candidate. To accurately measure the electron energy, additional neighboring cells are added, forming clusters of 3×7 cells in the barrel and 5×5 cells in the end-cap.

The electron candidate is subject to stringent quality requirements designed to reduce the background from multijet events and, to a lesser extent, from photon conversions. The requirements are defined mostly in references [12, 23], with some minor updates included in reference [46]. They are based on three levels, "loose++", "medium++" and "tight++", each inclusive of the previous ones (tight++ includes also the loose++ and medium++ requirements).

The W+b-jets analysis uses tight++ electrons in order to reduce as much as possible the multijet background. It also vetoes second electrons passing the medium++

requirements, in order to reduce the Z+jets background. The medium++ criteria for electron candidates are based on the shower shape in the EM calorimeter, the fraction of energy deposited into the hadronic calorimeter, as well as the ID track quality (number of hits and value of impact parameter), and the track-to-cluster matching. The medium++ electron selection is approximately 85% efficient for electron candidates from $Z \to ee$ decays. The tight++ electron selection uses more strict requirements on the track quality, shower shape and track-to-cluster matching requirements, as well as an additional requirement on the ratio of the cluster energy to the track momentum, resulting in a 78% efficiency for electron candidates from $Z \to ee$ decays.

The electron energy calibration is based on Monte Carlo simulation. The energy in the different EM calorimeter layers of the electron cluster is summed. However, in order to account for energy lost before the calorimeter and for lateral and longitudinal leakage outside the cluster, different weights are applied to the energy measured in each EM calorimeter layer.

Additional corrections derived using $Z \to ee$, $J/\psi \to ee$ and $W \to e\nu$ decays reconstructed in data are applied [109]. Electrons in data are subject to an additional energy correction based on the position of the Z and J/ψ mass peaks. The energy of electrons in Monte Carlo simulation is smeared in order to match the width of the W and Z mass peaks, keeping the electron direction constant. Similarly, the weights of Monte Carlo events are scaled to match the measured identification and reconstruction efficiencies measured in electrons from Z decays.

6.4 Muons

There are currently more than ten types of muon reconstruction algorithms in place in ATLAS, and the "Muon Recopedia" [52] can be very useful for an overview of each. The W+b-jets analysis uses relatively high momentum muons to reconstruct W bosons, and it requires the highest purity available to reduce fake muons and secondary muons from multijet events, and in particular $b\bar{b}$ events. $b\bar{b}$ events can easily be mistaken for W+b-jets events because the two b-hadrons can give rise to a b-jet recoiling against a lepton and $E_{\mathrm{T}}^{\mathrm{miss}}$. The STACO (STAtistical COmbination) Combined (CB) muons are chosen as the best option, given the high purity requirements, and the muon momentum considered[2].

STACO CB muons [20, 59] are reconstructed by combining a track in the Muon Spectrometer and one in the Inner Detector, while energy loss in the calorimeter is taken into account with parameterisations. The combination between two fully independent tracks guarantees the low fake rate, while also improving the momentum resolution. In particular, the STACO algorithm uses the track parameters and covariance matrices of the ID and MS tracks to find a combined ID-MS track with the smallest χ^2 with respect to both. This statistical approach takes full advantage of relative strengths of the ID and the MS, by biasing the combined track to the most precise of the two. For muons with $p_{\mathrm{T}} \lesssim 40$ GeV, the ID track is more precise because the solenoid field is strong enough to significantly bend the track, and because there is little material causing energy loss. In the high momentum $p_{\mathrm{T}} \gtrsim 100$ GeV regime,

[2]An alternative choice, with equivalent performance in terms of reconstruction efficiency and resolution, would have been the MuID algorithm [2], which is not used in this analysis.

the calorimeter energy loss is small in relation to the p_{T} of the muon, and the MS track has a higher resolution because of the long MS lever arm. Thus, the STACO CB track relies on the ID in the low p_{T} regime, on the MS in the high p_{T} regime, and on both ID and MS in the intermediate p_{T} regime.

The Muon Spectrometer tracks used by the STACO CB algorithm are reconstructed with the MUONBOY [59] algorithm. The MUONBOY algorithm is based on combining *track segments* found in at least two of the three MS stations. Segments are reconstructed using trigger hits (with low-resolution η and ϕ coordinates) and precision hits (with precise information in the bending direction, η) to form straight lines through a single MS station. The direction of a segment with respect to the interaction point (IP) is used to estimate its momentum, and to search for segments in nearby MS layers. At the end of the segment search, tracks are refit based on their individual hits. Finally, the MS track parameters are extrapolated to the IP, taking into account the magnetic field as well as the energy lost in the material.

Several additional selections are applied to the ID track used by the STACO CB algorithm in order to reduce fake rates and improve resolution. Specifically, the ID track must have at least one hit in the Pixel B-layer, two in all Pixel layers, six in the SCT, and and less than three holes (missing hits in correspondence with a track) in all silicon layers. For all these hit conditions, dead sensors count as hits observed, not as holes. Finally, a pseudo-rapidity dependent condition on TRT hits and outliers is applied: for $|\eta| < 1.9$, the sum of TRT hits and outliers must be greater than 5, and the number of outliers must be less than 90% of this sum. For $|\eta| > 1.9$, where the TRT layers are fewer, the sum itself has no requirement, and the 90% requirement is

only applied when the sum is greater than 5.

Additional corrections derived using $Z \to \mu\mu$ and $W \to \mu\nu$ decays reconstructed in data are applied [110, 111]. Muons in Monte Carlo simulation are subject to energy correction and smearing to match the position and width of the W and Z mass peaks observed in data. Finally, the weights of Monte Carlo events are scaled to match the measured reconstruction efficiencies measured in muons from Z decays.

6.5 Jets

Jets are heavily used in the W+b-jets analysis, both to define the W+b-jets final state, and to aid in the $E_{\mathrm{T}}^{\mathrm{miss}}$ reconstruction. Jets are reconstructed from topological clusters of calorimeter cells, called *topo-clusters*. The algorithms used to reconstruct topo-clusters and jets are briefly described below, while additional information can be found in references [20, 112, 31, 115].

Topo-clusters [112] are three-dimensional clusters of calorimeter cells, which attempt to encompass a full particle shower, while suppressing noise from electronics and from pile-up. The energy in each calorimeter cell, E_{cell}, is calibrated at the electromagnetic (EM) scale based on test beam results with electrons and photons. The topo-clusters are then constructed using a "4-2-0" clustering scheme, based on the the root-mean-squared noise measured in each cell when triggering on random events, σ_{noise}. In the "4-2-0" scheme, topo-clusters are seeded with calorimeter cells satisfying $|E_{cell}| > 4\sigma_{\mathrm{noise}}$. Then, all neighboring cells with $|E_{cell}| > 2\sigma_{\mathrm{noise}}$ are added to the topo-cluster. The cluster is expanded until all the $|E_{cell}| > 2\sigma_{\mathrm{noise}}$ cells neighboring the cluster are included. Finally, all nearest-neighbor cells (the 0 in 4-2-0) are added

to the cluster. The energy of the topo-cluster is the sum of the energy of the cells in the cluster, and the direction is the energy-weighted sum of the directions of the constituent cells.

Jets are reconstructed by combining topo-clusters using the anti-k_t algorithm [113] with a radius parameter $R = 0.4$. The anti-k_t algorithm is a clustering algorithm based on defining a distance parameter between two clusters:

$$d_{i,j} = \min(p_{\mathrm{T},i}^{-2}, p_{\mathrm{T},j}^{-2}) \frac{\Delta R_{i,j}^2}{R^2} \tag{6.1}$$

The algorithm iterates over all clusters i, starting with the one with highest p_{T}, and attempts to merge i with all remaining clusters j. The object j with the smallest $d_{i,j}$ is merged with i, as long as $d_{i,j}$ is smaller than $d_i = p_{\mathrm{T},i}^{-2}$. For example, j will be merged with i if $p_{\mathrm{T},j} < p_{\mathrm{T},i}$ and $\Delta R_{i,j} < 0.4$. Merging with objects at $\Delta R_{i,j} > 0.4$ requires them to have a larger p_{T}, resulting in a significant shift of the recombined cluster position. When i and j are merged, they are removed from the list of clusters, and replaced with the clustered object. If there are no more clusters j which satisfy this requirement, i is removed from the list of clusters and it is called a *jet*. The clustering then re-starts around the highest p_{T} object among the remaining clusters.

This type of algorithm is chosen by ATLAS because it can be run on both reconstructed quantities (tracks, cells, clusters) and quantities related to theoretical calculations (partons, hadrons). In particular, the anti-k_t algorithm is *safe* with respect to both *collinear* emissions and *soft* emissions. Collinear configurations are caused by a parton splitting in two, or by two small clusters being reconstructed in place of a larger one. Soft emissions are caused by partons produced with very low momentum, or by an additional cluster with a small energy deposition. From the

theoretical perspective, both collinear and soft emissions are non-perturbative effects due to their small scale (see Section 3), and they can lead to divergent amplitudes. From the experimental perspective, cluster-splitting or small clusters should not influence the reconstruction of jets. The anti-k_t algorithm solves both situations, while resulting in jets which are approximately cone-shaped. Other variations of anti-k_t algorithm exist, based on different exponents of each p_{T} term, but they do not result in conical jet-shapes. They are the Cambridge/Aachen algorithm (p_{T}^0) and the k_t algorighm (p_{T}^2).

As mentioned above, the topo-clusters are calibrated to the electromagnetic (EM) scale, so a jet built from topo-clusters is initially calibrated at the EM scale. While this calibration is correct for electrons and photons, it systematically underestimates the energy of hadronic objects, due to the sampling nature of the calorimeters. The jet energy is therefore corrected up to the hadron scale using the response observed in MC simulations [115, 117]. A variety of data-driven techniques are used to improve the accuracy of the jet energy scale, improve the jet energy resolution, and derive systematic uncertainties: jet-photon balance [120], jet-Z balance [119], jet-jet balance [116]. An additional study, to which I contributed, was used to analyze the effects of pile-up on the jet energy scale by studying track-jets [118]. Track-jets are jets constructed from tracks instead of calorimeter objects. By requiring the tracks to originate from the primary vertex, track-jets can be made particularly resistant to pile-up. By comparing track-jet energy to calorimeter-jet energy, this study was used to derive a pile-up correction to the jet energy scale, resulting in a reduction by a factor of two of the jet energy scale uncertainty due to pile-up.

6.6 b-tagging

The W+b-jets analysis focuses on identifying b-jets produced in association with a W boson. b-tagging, the identification of b-jets, is therefore a key aspect of the analysis. b-jets can be defined in different ways, but in general they are jets which contain a b-hadron, or a b-quark. In this analysis, b-jets are defined as jets of final state particles (hadrons) which contain a weakly decaying b-hadron with $p_{\mathrm{T}} > 5$ GeV and within $\Delta R = 0.3$ of the jet axis.

Since B-hadrons can decay weakly and their masses are close to the mass of the b-quark (4.7 GeV), their most important characteristics are a long lifetime (~ 1.5 ps) and a large mass. Due to their long lifetime, coupled with a substantial boost, their decay can take place at a macroscopic distance from the primary vertex (a 50 GeV B-hadron will travel on average a distance of ~ 3 mm) . Due to their large mass, the decay products (which have much smaller masses) can acquire significant angular separation even at large boosts. The long lifetime and large mass therefore result in a displaced *secondary vertex* with tracks that are inconsistent with originating from the primary vertex. In b-tagging, one attempts either to reconstruct the secondary vertex explicitly or to use related variables to identify a jet as originating from a b-hadron.

The b-tagging algorithm used in this analysis is called *JetFitterCombNN* (or simply *CombNN*). It combines the properties measured by two taggers, *IP3D* and *JetFitter* [121, 60]. Both IP3D and JetFitter are based on a custom selection of ID tracks within a ΔR of a jet axis. The ΔR parameter varies with the p_{T} of the jet, to reflect the higher collimation of decay products of high-p_{T} b-hadrons. The track selection is designed to reject fake tracks, tracks from longer-lived particles (K_s mesons, Λ

baryons), and tracks from photon conversions inside detector material.

The IP3D tagger [121] is a 3-dimensional *impact parameter tagger*: it uses the longitudinal and transverse impact parameter of individual tracks in the jet to separate b-jets from light-jets. Specifically, the significances of the impact parameters are used, z_0/σ_{z_0} and d_0/σ_{d_0}, in order to give more weight to well-measured tracks. Tracks which cross the jet axis in front of the primary vertex are assigned a positive sign, while tracks crossing the jet axis behind the primary vertex are assigned a negative sign[3] . Tracks from secondary vertices are expected to be on the positive side, while incorrectly measured tracks are expected to be evenly distributed on both sides. The two-dimensional distributions of impact parameter significances (z_0/σ_{z_0} vs. d_0/σ_{d_0}) for b-jets and light-jets are constructed based on Monte Carlo simulation. Using these distributions as probability distribution functions, the IP3D tagger constructs a likelihood ratio between the b-jet and light-jet hypotheses.

The JetFitter tagger [121, 60] exploits the topological structure of $b \to c \to s$ decays inside a jet, making the assumption that the primary vertex, the b secondary vertex and the c *tertiary vertex* lie on the same line. This assumption was analyzed in Monte Carlo simulated events: for b-jets with an average p_{T} of 60 GeV, the average transverse flight length of b-hadrons was found to be 4.3 mm, and the subsequent transverse flight length of c-hadrons was on average 1.9 mm, with an average lateral displacement of $\sim 30\mu$m. Based on this assumption, a Kalman Filter algorithm is used to find a common line between the primary vertex, the b-hadron vertex and

[3]The procedure used to determine the sign is slightly more complex, since the track and the jet axis are not guaranteed to cross in 3D space. Calling $\vec{t}$ the track, $\vec{j}$ the jet axis (originating at the PV), and $\vec{d}$ the 3D impact parameter of the track with respect to the PV, the sign of the impact parameter is defined as the sign of the dot product $([\vec{t} \times \vec{j}] \cdot [\vec{t} \times \vec{d}])$ [78].

the c-hadron vertex. The algorithm is able to use the common line constraint to reconstruct vertices even if they only have a single associated track. On the other hand, the algorithm does not require the presence of both the b and c vertices, so it can also find events where only a single secondary vertex is reconstructed. This flexibility yields a large set of discriminating variables that can be used to discriminate b-jets from light-jets:

- number of vertices with at least two tracks,
- total number of tracks at these vertices,
- number of additional single-track vertices on the b-hadron flight axis,
- total invariant mass of all tracks associated to the decay chain,
- energy fraction of tracks associated to the decay chain with respect to tracks associated to the entire jet,
- flight length significance of the weighted average position of the displaced vertices.

The JetFitterCombNN algorithm [121] uses the variables produced by the JetFitter tagger in combination with the likelihood ratio produced by the IP3D tagger, as well as the jet p_{T} and η. It feeds these variables into a Neural Network which produces three output variables: a b-jet-probability (p_b), a c-jet probability (p_c) and a light-jet probability (p_l). The b and light probabilities are combined to form the CombNN variable: CombNN $= \ln(p_b/p_l)$. Given the large c-jet background in the $W+b$-jets analysis, the possibility to use another variable, $\ln(p_b/p_c)$, was investigated,

but it was found to yield a lower overall statistical separation between the signal and background.

Scale factors are used to reweight Monte Carlo events with b-, c- and light-jets in order to reproduce the jet tagging efficiencies measured in data [122, 123, 124]. The scale factors applied to b-, c- and light-jets in this analysis are shown in Figure 6.1 as a function of p_{T}. They correspond to the tightest calibrated CombNN working point, with a b-jet efficiency ranging from 40% to 60% and c-jet and light-jet efficiencies of 10% and 0.1%, respectively. In these plots, the b-jet efficiency uncertainty ranges from 2% to 10%, the c-jet uncertainty is stable at about 15%, and the light-jet uncertainty is at most 5%. An additional feature visible in these plots is the large p_{T} dependence of the scale factors. This can be particularly problematic in combination with the jet energy scale uncertainty, which can move between neighboring scale factor bins, and cause their weight to be modified. To aid in this situation, the p_{T} bins of the differential W+b-jets measurement are chosen to match the bins of the light-jet and c-jet scale factors, which show the largest bin-to-bin variations.

6.7 Missing Transverse Energy

The missing transverse energy ($E_{\mathrm{T}}^{\mathrm{miss}}$) represents the momentum in the transverse plane which was not reconstructed by any of the detector elements. It is a very useful quantity, assuming that any imbalance observed in the transverse plane (whose initial momentum was zero) must be caused by an unobserved object, such as a neutrino or a more exotic particle. However, $E_{\mathrm{T}}^{\mathrm{miss}}$ can also be the result of one or more mismeasured objects, or one or more "gaps" in the detector. As such, its reconstruction requires

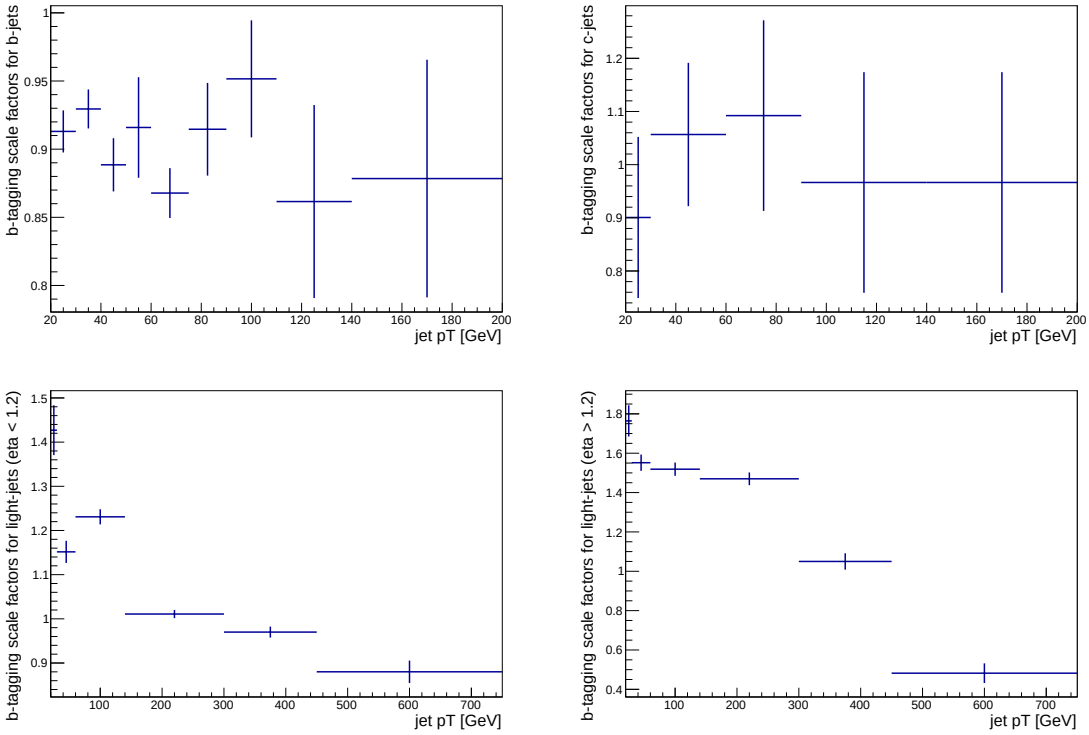

Figure 6.1: b-tagging Scale Factors as a function of jet p_{T} for b-jets (top left), c-jets (top right) and light-jets (bottom left and right), corresponding to the tightest (57%) working point of the CombNN tagger.

good knowledge of all objects considered for the vectorial sum. In initial ATLAS analyses, the $E_{\mathrm{T}}^{\mathrm{miss}}$ reconstruction was based on summing all the energy in calorimeter clusters [126], together with the momentum of muons in the MS.

In later analyses, including the W+b-jets analysis, the $E_{\mathrm{T}}^{\mathrm{miss}}$ algorithm [125] started to make use of jets and electrons to take advantage of their precise calibration. Calorimeter cells which are associated with jets or electrons are therefore removed from the calculations, and replaced with the corresponding physics objects[4].

[4]The $E_{\mathrm{T}}^{\mathrm{miss}}$algorithm is designed to also use photons and hadronically decaying taus to replace calorimeter cells. These are however not expected to play a significant role in the W+b-jets final state.

For the purposes of this analysis, the $E_{\mathrm{T}}^{\mathrm{miss}}$ can thus be defined as:

$$\vec{E}_{\mathrm{T}}^{\mathrm{miss}} = -\sum_{electrons} \vec{E}_{\mathrm{T}}^{e} - \sum_{muons} \vec{p}_{\mathrm{T}}^{\mu} - \sum_{jets} \vec{p}_{\mathrm{T}}^{jet} - \sum_{clusters} \vec{E}_{\mathrm{T}}^{cluster} \tag{6.2}$$

Chapter 7

$W+b$-jets analysis

7.1 Overview

The production of $W+b$-jets events has been discussed in detail in Chapter 3. The leading-order diagram with the $q\bar{q}'$ initial state, shown in Figure 7.1 (left), is only a part of the $W+b$-jets production. A large role at the LHC is played by the gq initial state (middle), which can also be interpreted as a bq initial state by absorbing the gluon splitting ($g \to b\bar{b}$) into the PDF (right). Additionally, double-parton-scattering events can also result in a $W+b$-jets final state.

The criteria used to select $W+b$-jets events from the ATLAS data are based on the reconstruction of a leptonically decaying W boson and a b-tagged jet. Specifically, events are required to be consistent with the decay of a W boson to the $\ell\nu$ ($\ell = \mu, e$) final state, and to contain either one or two jets, of which exactly one must be b-tagged. The exclusion of events with three or more jets and with two or more b-tagged jets is motivated by the large backgrounds in these final states.

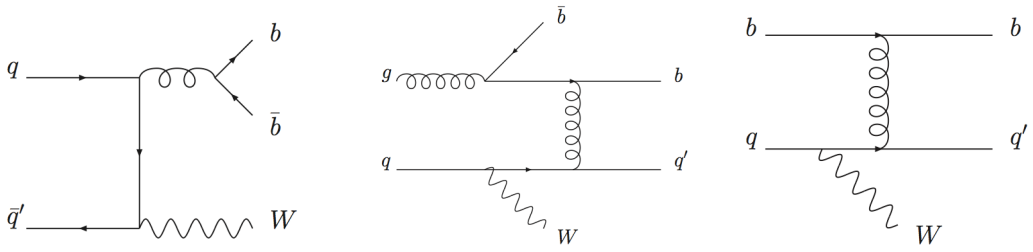

Figure 7.1: A subset of W+b-jets production processes: $q\bar{q}' \to Wb\bar{b}$ (left), $qg \to Wb\bar{b}\bar{q}'$ (center), $bq \to Wb\bar{q}'$ (right).

The W+b-jets selection defines four analysis regions, based on the lepton flavor and the number of jets: Electron 1-jet, Muon 1-jet, Electron 2-jet, Muon 2-jet. For the differential measurement, each analysis region is split into four bins, based on the transverse momentum of the b-tagged jet: 25–30 GeV, 30–40 GeV, 40–60 GeV, 60–140 GeV. The bins are chosen to contain approximately the same number of signal events, and the region above 140 GeV is not used due to the large background contributions.

Different processes can result in events with final states that are similar to the W+b-jets one. These background processes are reduced using specific selection criteria, and their remaining contribution is estimated using theoretical estimates as well as data-driven methods. The main background sources are events with a fake W boson (Multijet), a fake b-jet (W+c-jets, W+light-jets), or a real W and b-jet coming from a $t \to Wb$ decay (single-top, $t\bar{t}$). Smaller backgrounds sources are Z+jets and Diboson (WW and WZ) events.

The impact of W+c-jets and W+light-jets events is reduced using tight b-tagging requirement. The Multijet background is reduced by tightening the lepton identification and the W transverse mass requirements. Single-top and $t\bar{t}$ contributions

are unaffected by these criteria, so their contribution is reduced by selecting events with few jets and b-tags, as mentioned above. The Diboson background is very small, and the Z+jets background is reduced by vetoing events with a second reconstructed lepton. Except for the Z+jets and Diboson backgrounds, all other contributions are estimated using data-driven methods. Specifically, binned maximum likelihood fits to detector-level distributions are used to estimate the multijet, $t\bar{t}$, single-top, W+c-jets and W+light-jets backgrounds. These estimates are handled in sequence, so that the results of a fit can be used in the following fits.

The background estimation results in a measurement of the W+b-jets yield, in terms of observed events. This yield is affected by reconstruction effects (efficiency, acceptance), and it does not correspond to the number of generated W+b-jets events. An unfolding procedure is therefore used to account for all reconstruction effects and to calculate the number of generated $pp \rightarrow W$+b-jets events in a restricted fiducial region. This estimate is then divided by the measured luminosity to obtain a fiducial cross-section of the W+b-jets process. An additional estimate is made, using similar techniques, of the combined W+b-jets plus single-top process.

The following two sub-sections, 7.1.1 and 7.1.2, are relevant to the full W+b-jets analysis. Section 7.1.1 gives an ordered overview of the full analysis, pointing to the sections in which each part is described. Section 7.1.2 describes the implementation of maximum likelihood fitting, which is used to estimate all of the main backgrounds and the W+b-jets yield.

7.1.1 Analysis Strategy

The strategy of the W+b-jets analysis, described in detail in the following chapters, is essentially very simple. The W+b-jets sample is selected, the backgrounds are estimated to measure a W+b-jets yield, and the yield is converted to a cross-section (or unfolded). The backgrounds are estimated independently in the electron and muon channel, but the W+b-jets yield can be unfolded both independently and in combination.

The order in which background contributions are estimated is based on practical concerns. The multijet background is estimated first, since no Monte Carlo simulation is available for it. The $t\bar{t}$ background comes next, because it can be estimated in a very high purity control region, allowing for large uncertainties to be placed on all the other processes. The single-top background estimate requires good knowledge of the multijet and $t\bar{t}$ backgrounds, but it is independent of the relative fraction of b-jets, c-jets and light-jets in the W sample. So the single-top background is estimated after the multijet and $t\bar{t}$ fits, but before the flavor content (CombNN) fit. The CombNN fit, where the W+b-jets yield is measured, makes use of all the knowledge acquired in the previous steps.

1. Events compatible with the production of a W boson and exactly 1 jet or exactly 2 jets are selected. Exactly 1 jet is required to be b-tagged. The two sub-samples created are referred to as *1-jet* and *2-jet* , respectively. Details of the event selection are described in Section 7.4.

2. Backgrounds are modeled using the Monte Carlo samples described in Section 7.3 with the exception of the multijet background, for which templates are

extracted from data.

3. The multijet contribution is estimated by fitting the $E_{\mathrm{T}}^{\mathrm{miss}}$ distribution in each analysis region, as described in Section 7.5.1.

4. The normalization of the $t\bar{t}$ background is estimated in the *at least 4 jets 1-b-tag* control region. It is then extrapolated to the 1-jet and 2-jet analysis regions using Monte Carlo, as described in Section 7.5.2

5. Single-top estimations are treated differently in the two analysis regions. In the 1-jet region, the Monte Carlo prediction is used, and a significant uncertainty is assigned to the single-top normalization. In the 2-jet bin, the single-top contribution is estimated by fitting kinematic distributions. Details of this can be found in Section 7.5.3.

6. The number of W+b-jets events is estimated in data by fitting the b-tagging weight distribution in the 1-jet and 2-jet analysis regions, as described in Section 7.5.4. The previous background estimations are propagated into the fit via Gaussian constraints, as described in detail in Section 7.1.2. The fit results are presented in Section 7.6.

7. The detector level yields are unfolded into an event-level fiducial cross-section, as described in Section 7.7. An iterative Bayesian algorithm is used to unfold the p_{T} differential measurement.

8. Systematic uncertainties on the unfolded results are discussed in Section 7.8

9. Theoretical prediction are computed for the specific fiducial region chosen.

When necessary, they are multiplied by correction factors to account for underlying event and hadronization. Similarly, the contribution from double-parton-scattering can be added. Details of the theoretical predictions can be found in Section 7.9.

10. Finally, the unfolded results are presented in Section 7.10, and compared to the theoretical predictions.

7.1.2 Maximum Likelihood fits

Maximum likelihood (ML) fits are used in many of the steps defined above (3, 4, 5, 6) in order to estimate backgrounds directly from data, and to reduce the uncertainties on their normalization.

Specifically, a sequence of binned ML fits is performed. In each fit, a binned distribution (histogram) measured in data is described by a linear combination of templates representing each contributing process. The normalization of the measured process is allowed to float freely, while other processes can be constrained by Gaussian terms in the likelihood. For a constrained process, the mean of the corresponding Gaussian constraint is fixed to the expected number of events, while the width is fixed to the associated uncertainty. Depending on the process, the width of the Gaussian constraint is derived either from the results of a previous fit or from theoretical uncertainties.

Each fit therefore measures one *signal normalization* parameter, and various *nuisance* parameters, corresponding to the normalizations of the remaining processes. The uncertainties on the nuisance parameters contribute to the uncertainty on the signal normalization, and the Gaussian constraints help in reducing this additional

contribution. For example, in the CombNN fit, the uncertainty on the W+b-jets component would be much larger than 100% if all the backgrounds containing b-jets (multijet, $t\bar{t}$, single-top) were completely free to float. Thanks to the Gaussian constraints applied to these backgrounds, the W+b-jets uncertainty is reduced to 10–15%, as shown in the first row of Table 7.1. The second row of this table shows the W+b-jets uncertainty for fits in which the constraints are infinitely tight. The uncertainty on the W+b-jets normalization becomes 5–7%, representing the statistical separation of the W+b-jets signal from the two free-floating backgrounds (W+c-jets and W+light-jets).

Table 7.1: Statistical uncertainties on the number of W+b-jets events as estimated with pseudo experiments: the Gaussian constraints used in the analysis are applied (top row); only W+b-jets, W+c-jets and W+light-jets are free to float and the other backgrounds are fixed to the corresponding expectation (bottom row).

Stat. Uncertainty	μ 1-jet	e 1-jet	μ 2-jet	e 2-jet
Central Fit	± 14%	± 16%	± 10%	± 13%
Fixed Backgrounds	± 5%	± 6%	± 6%	± 7%

Fit implementation

Fits are implemented by defining a binned likelihood function which encodes the shape and normalization information for each of the samples considered, as well as the number of observed events in each bin. The negative logarithm of the likelihood is then minimized using the MINUIT program[1]. The only movable parameters estimated in the minimization are the scale factors for the normalization of each sample. The binned likelihood function is described below.

[1]Minimizing $(-\ln \mathcal{L})$ is equivalent to maximizing $\mathcal{L}$.

In each bin i, the number of events n_i is assumed to be distributed according to a Poisson probability density function $\mathcal{P}(n_i|\mu_i)$; μ_i represents the total expected number of events in bin i and is expressed as:

$$\mu_i = \sum_j \beta_j \, \mu_{ij} \ , \tag{7.1}$$

where the index j runs on the number of components (which can be signal or background). The μ_{ij}'s are the expected number of events in each bin i from each component j. The β_j's are the fit parameters: for a given component j, β_j represents a fitted scale factor to be applied to the corresponding expected number of events as determined by the fit to the data.

At this point, the likelihood characterizing a distribution is a sum of Poissonian distributions, one for each bin i:

$$\mathcal{L} = \prod_i \mathcal{P}(n_i|\mu_i) = \prod_i \frac{\mu_i^{n_i} e^{-\mu_i}}{n_i!} \tag{7.2}$$

The logarithm of a Poissonian is

$$\ln\left(\frac{\mu^n e^{-\mu}}{n!}\right) = n\ln(\mu) - \mu - \ln(n!) \tag{7.3}$$

Since the last term is not a function of μ, it can be ignored in a minimization process. The negative log likelihood of the distribution is then:

$$-\ln(\mathcal{L}) = -\ \ln\ (\ \prod_{\mathrm{i}} \mathcal{P}(\mathrm{n_i}|\mu_\mathrm{i})\ )\ =\ \sum_{\mathrm{i}}[-\ \mathrm{n_i}\ \ln\ (\mu_\mathrm{i}) + \mu_\mathrm{i}] \tag{7.4}$$

Including explicitly the scale factors β_j for each component, the log likelihood reads:

$$-\ln(\mathcal{L}) = \ \sum_{\mathrm{i}}[-\ \mathrm{n_i}\ \ln\ \left(\sum_{\mathrm{j}}\ \beta_\mathrm{j}\ \mu_\mathrm{ij}\right) + \sum_{\mathrm{j}}\ \beta_\mathrm{j}\ \mu_\mathrm{ij}] \tag{7.5}$$

where the index i runs on the number of bins, and j on the number of components.

The Gaussian terms, added to the likelihood fit to constrain the background normalizations, are applied to the β_j terms. Each Gaussian term, constraining β_j within σ_j of 1, is of the form:

$$G\left(\beta_j|\sigma_j\right) = \frac{1}{\sigma_j\sqrt{2\pi}}\,\exp\left(-\frac{1}{2}\frac{(\beta_j-1)^2}{\sigma_j^2}\right) \tag{7.6}$$

$$\ln(G\left(\beta_j|\sigma_j\right)) = -\frac{(\beta_j-1)^2}{2\sigma_j^2} + C \tag{7.7}$$

The resulting negative log likelihood, including the Gaussian terms, is:

$$-\ln(\mathcal{L}) = \sum_{\mathrm{i}}[-\ \mathrm{n_i}\ \ln\left(\sum_{\mathrm{j}}\ \beta_{\mathrm{j}}\ \mu_{\mathrm{ij}}\right) + \sum_{\mathrm{j}}\ \beta_{\mathrm{j}}\ \mu_{\mathrm{ij}}]\ +\ \sum_{\mathrm{j}}\frac{(\beta_{\mathrm{j}}-1)^2}{2\sigma_{\mathrm{j}}^2} \tag{7.8}$$

For example, in the CombNN fit in the 1-jet region, the W+b-jets, W+c-jets and W+light-jets components are free to float independently in the fit, while Gaussian terms are applied to the likelihood to constrain the other backgrounds. The Multijet background is constrained to the results of the $E_{\mathrm{T}}^{\mathrm{miss}}$ fits with an uncertainty of 50%. The single-top contribution in the 1-jet region is constrained to the Monte Carlo expectation with an uncertainty of 50%. In the 2-jet region, the single-top is constrained to the result of a fit to the $m(Wb)$ distribution with an uncertainty of 20%. The $t\bar{t}$ is constrained to the number of events extrapolated from the corresponding control region with an uncertainty of 10%. Finally, WW+WZ and Z+jets are constrained to the MC expectation with an uncertainty of 10%. These constraints are motivated in Section 7.5.

Validation of fit procedure and uncertainty

This section describes the behavior and properties of the CombNN fit from which the number of W+b-jets events is extracted. Pseudo-experiments are used to study the fit. The primary goal of the study is to determine whether the fitted scale factors for W+b-jets, β_{fit}, are systematically biased above or below their true value. Additionally, the distribution $(\beta_{\text{generated}} - \beta_{\text{fit}})$ is studied, to determine whether it can be described as a Gaussian distribution with a width corresponding to the fit uncertainty (σ_{fit}). The study finds that the distributions are Gaussian and unbiased, but that the fit uncertainty is overestimated.

In a pseudo-experiment, the distribution formed by the signal and background templates, normalized to the results of the fit to data, is Poisson-varied to generate a pseudo-data sample. This procedure is preferred to the Poisson-variation of data points, as it removes the statistical effects coming from the data sample. The pseudo-data sample is then fitted using the same templates and constraints as in the fit to data, with the same initial normalization as the generated pseudo-data. This process, which defines a pseudo-experiment, is repeated 10,000 times, by generating and fitting 10,000 pseudo-data samples.

For each pseudo-experiment, the *residual* and the *pull* the can be studied to determine whether the estimator for the scale factor, β, is unbiased and whether its uncertainty is Gaussian. The residual is the difference between the generated and fitted scale factor $(\beta_{\text{generated}} - \beta_{\text{fit}})$, and the pull is the same quantity divided by σ_{fit}, the uncertainty on β_{fit} estimated by the fitting program.

As shown in Figure 7.2, the residual distributions of the W+b-jets estimator in

each analysis region have a Gaussian shape, with a mean consistent with 0, indicating that the fit is well behaved and unbiased. The $W+b$-jets estimator is also found to be unbiased for different number of generated $W+b$-jets events, as shown in Figure 7.3.

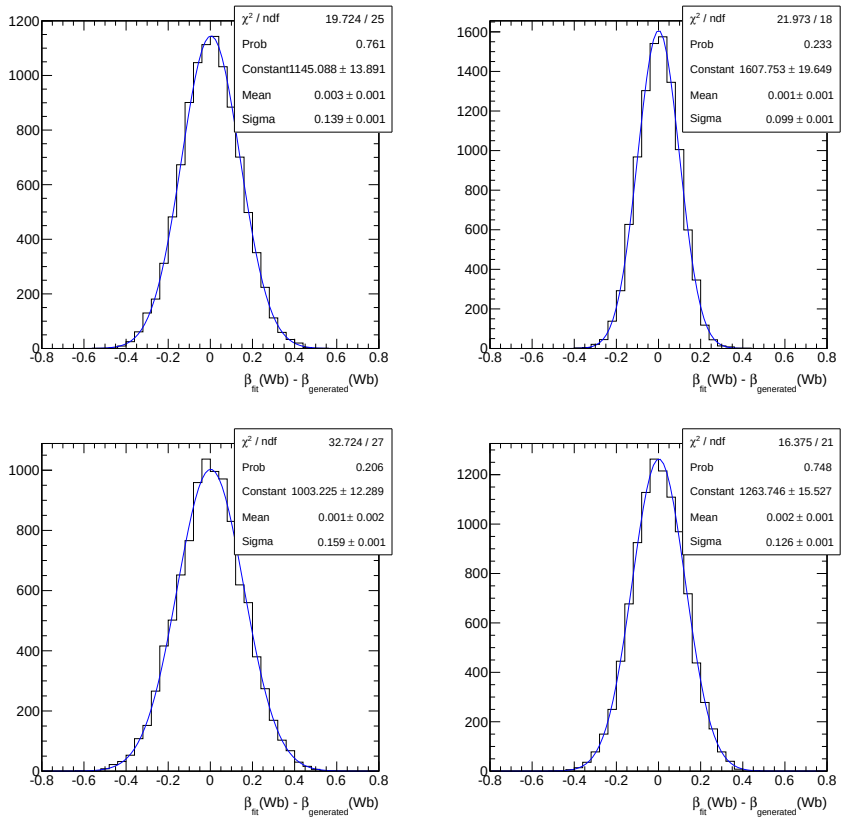

Figure 7.2: Residual distribution of the β_{W+b} estimators in the four analysis regions: muons 1-jet (top left), muons 2-jet (top right), electrons 1-jet (bottom left), electrons 2-jet (bottom right). The residuals are Gaussian, with a mean centered at 0.

The pull distributions, shown in Figure 7.4, are also Gaussian, however their width is significantly smaller than one. This behavior indicates that the statistical uncertainty of the $W+b$-jets content provided by the fit is over-estimated[2]. For this

[2]The $W+c$-jets and $W+$light-jets estimators were found to be unbiassed and the corresponding

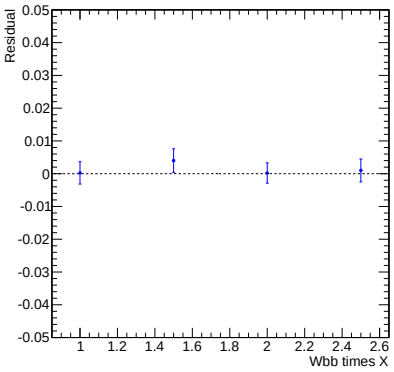

Figure 7.3: Mean of the residual distribution as a function of the generated number of $W+b$-jets events (a value 1 corresponds to the number of $W+b$-jets events estimated in the fit to data). The mean is consistent with 0, meaning that the fit is unbiased.

reason, the uncertainties reported in the analysis for the $W+b$-jets estimators are those extracted from the pseudo-experiments distributions, instead of those produced by the fit.

The over-estimation of the $W+b$-jets uncertainties calculated by the fitting code-was studied in depth. New pseudo-experiments were produced, simulating data sets collected with 1, 5, 10, 15, 25, 50 and 100 times the integrated luminosity available. As shown in Figure 7.5 (left) the width of the pulls asymptotically converged to one as the number of total events events increased. Another set of pseudo-experiments was produced, in which the Gaussian constraints were tightened, and the backgrounds were effectively fixed to their generated cross-sections. In this configuration, the resulting β_{W+b} pull was found to have width compatible with 1 for any simulated integrated luminosity, including the one of the data set used in the measurement,

statistical uncertainty estimated by the MINUIT program was found to be in agreement with the one estimated using pseudo. The same is true for the Gaussian-constrained components.

Figure 7.5 (right). Thus, the Gaussian constraints, together with the low statistics, were found to be the cause of the over-estimated uncertainties.

In conclusion, the fit was found to be unbiased in each analysis region; but the uncertainty returned by MINUIT for the W+b-jets estimator is not correct. For these reasons, the statistical uncertainty quoted in each analysis region and differential bin is estimated using pseudo-experiments, by taking the width of the residual distribution of the W+b-jets estimator. The uncertainties for the W+b-jets normalization in the four analysis region are shown in Table 7.1 for both the standard configuration and for a configuration where the $t\bar{t}$, single-top, multijet backgrounds are completely fixed.

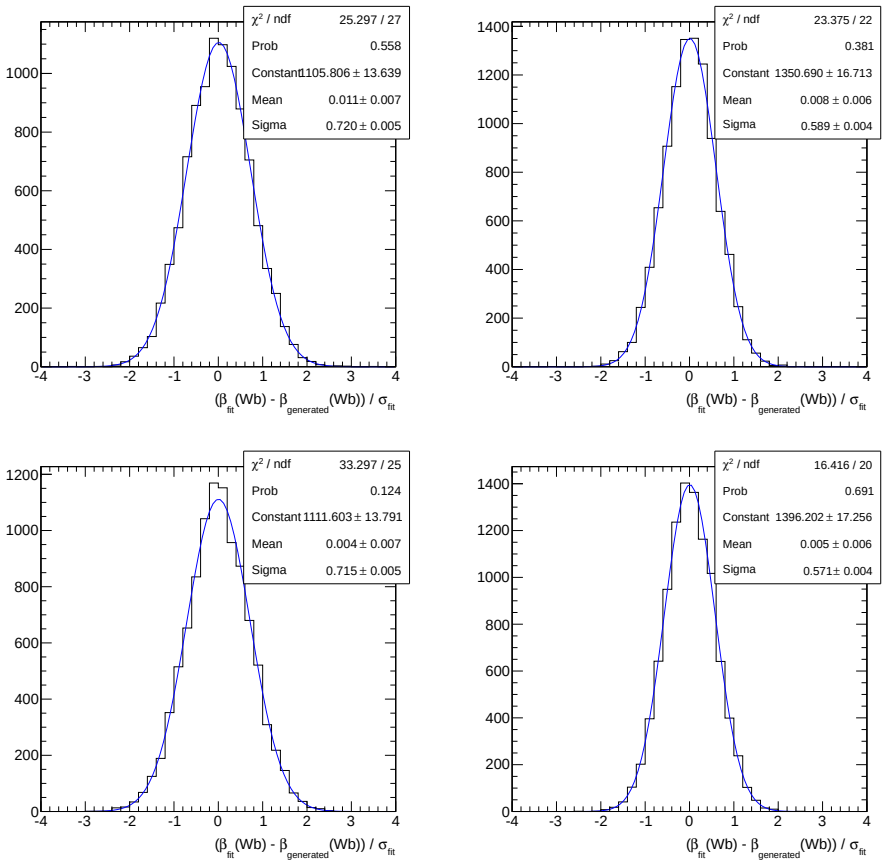

Figure 7.4: Pull distribution of the β_{W+b} estimators in the four analysis regions: muons 1-jet (top left), muons 2-jet (top right), electrons 1-jet (middle left), electrons 2-jet (middle right). The Sigma of the Gaussians are significantly smaller than 1, indicating that the fit uncertainties, σ_{fit}, are over-estimated.

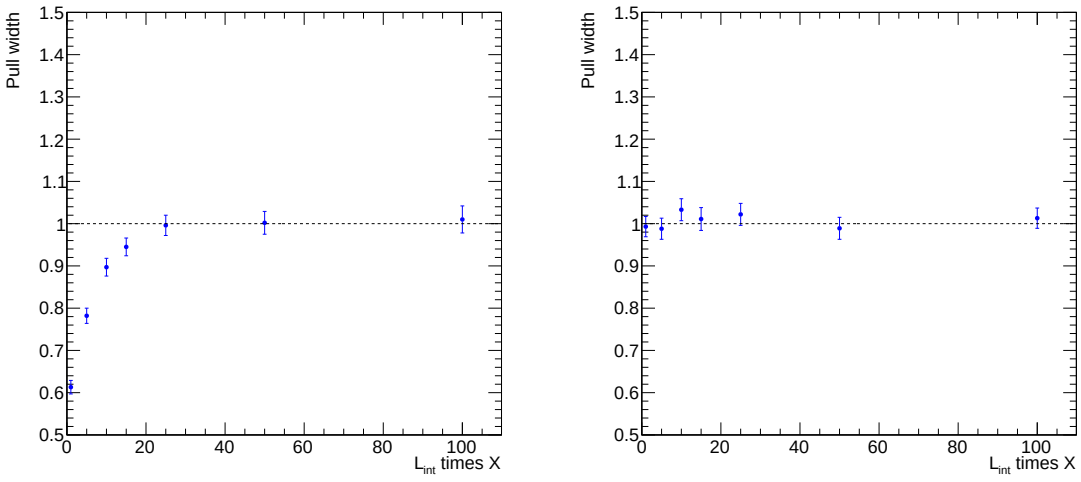

Figure 7.5: Left: Pull width of the β_{W+b} scale factor as a function of the simulated integrated luminosity when the standard Gaussian constraints are applied. Right: Pull width of the β_{W+b} estimator as a function of the simulated integrated luminosity when the corresponding backgrounds are fixed to the expectation.

Fits in Bins of b-tagged jet p_{T}

The fits used for the differential $p_{\mathrm{T}}^{b-\mathrm{jet}}$ measurement are studied using the same methods as the inclusive fits in the four analysis regions (muon 1-jet, muon 2-jet, electron 1-jet, electron 2-jet). The inclusive studies are described in the previous section.

In the differential $p_{\mathrm{T}}^{b-\mathrm{jet}}$ measurement, a separate fit to the CombNN distribution is performed in each analysis region in four intervals of b-tagged jet p_{T}: 25–30 GeV, 30–40 GeV, 40–60 GeV and 60–140 GeV. The background contributions are extrapolated to each p_{T} interval from the inclusive measurements, and the same Gaussian constraints as those of the inclusive fits are used. These Gaussian constraints are listed in the "Fit implementation" section above, and motivated in Section 7.5. For the multijet background, this extrapolation is based on the b-tagged jet p_{T} spectrum found in the multijet templates extracted from data. For all other backgrounds, the extrapolation is based on Monte Carlo simulation.

As in the inclusive fits described in the previous section, the uncertainty on the scale factor β_{W+b} is over-estimated in the p_{T}-binned fits. This behavior, as in the inclusive measurement, disappears when a higher integrated luminosity is simulated, or when the Gaussian constraints are removed from the background normalizations. To correct for this effect, the strategy of the inclusive measurement is used. The widths of the residual distributions obtained using pseudo-experiments are quoted as the statistical uncertainties associated with the fits. The resulting statistical uncertainties in each p_{T} bin and in each analysis region are summarized in Table 7.2. The uncertainties are expressed as % of the fitted scale factor β_{W+b}.

Table 7.2: Statistical uncertainties on the number of W+b-jets events estimated using pseudo experiments in each b-tagged jet p_{T}bin.

p_T range (GeV)	μ 1-jet	e 1-jet	μ 2-jet	e 2-jet
25-30	± 9%	± 13%	± 11%	± 15%
30-40	± 8%	± 10%	± 11%	± 14%
40-60	± 13%	± 17%	± 18%	± 20%
60-140	± 22%	± 26%	± 30%	± 33%

Two interesting effects can be observed: the first is that the statistical uncertainties associated with the first two p_{T} bins are smaller than the statistical uncertainty of the corresponding inclusive measurement; this is due to the very low contribution of single-top and $t\bar{t}$ in these two bins, in particular for the 1-jet region. The second effect is the loss of precision in the highest p_{T} bins due to both the decrease in the number of events in the data and the increase of the relative contribution from single-top and $t\bar{t}$.

In Figure 7.6 the mean value of the scale factor β_{W+b} residual distribution are shown as a function of the p_{T} bin, both in the muon and electron samples. The residual mean is mostly centered at zero, indicating that the fits are unbiased. Some bias is observed in the high p_{T} bins, but this bias is not corrected as it is small compared to its statistical uncertainty.

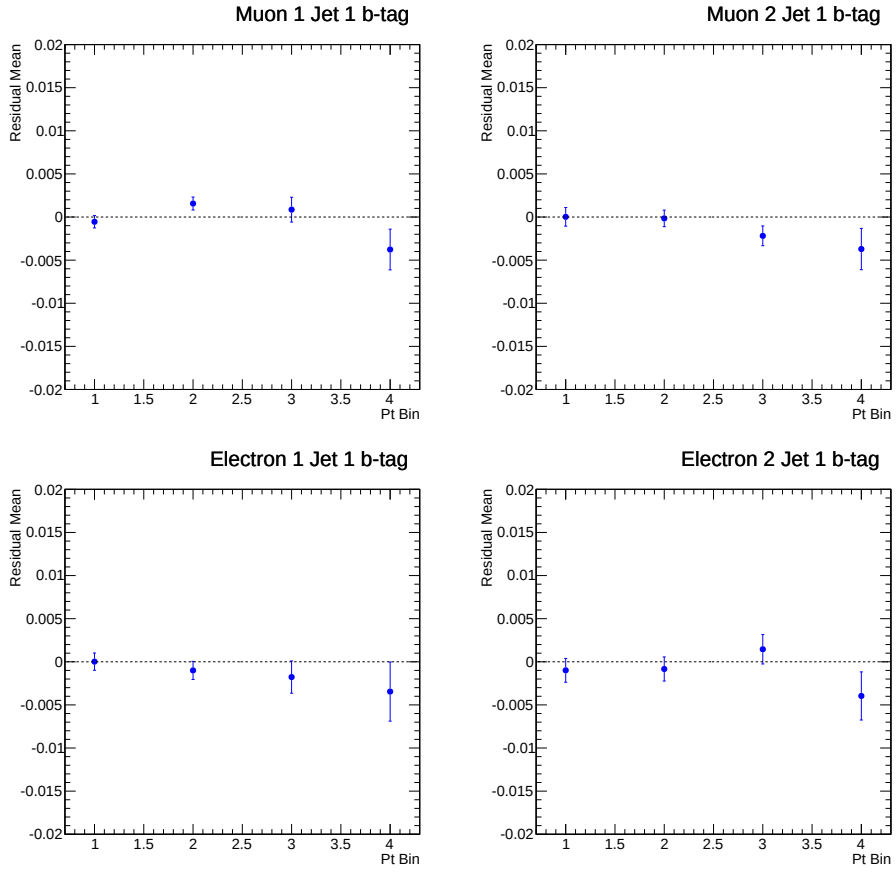

Figure 7.6: Mean of the scale factor β_{W+b} residual distribution as a function of the p_T bin number in the four analysis regions: muons 1-jet (top left), muons 2-jet (top right), electrons 1-jet (middle left), electrons 2-jet (middle right). The bias (difference from zero) is found to be small compared to the statistical uncertainty on the mean, and it is not corrected for in the analysis.

7.2 Data sample

The analysis considers data recorded in 2011 during periods with stable pp collisions at $\sqrt{s} = 7$ TeV, and where all relevant parts of the detector were operating normally. The resulting data set corresponds to 4.6 fb^{-1} of integrated luminosity, with an uncertainty of 3.9%. The luminosity determination is described briefly in Section 5.7, while details are presented in references [107] and [108]. Events are collected using single-muon or single-electron triggers, which are described briefly in Sections 5.6 and 5.6, and in reference [20] in detail. The p_{T} threshold of the muon trigger was 18 GeV, while the transverse energy (E_{T}) threshold used for the electron trigger was initially 20 GeV and was later raised to 22 GeV to cope with the increasing LHC instantaneous luminosity. The pile-up conditions of the 2011 data, discussed in Section 4.2.1, are characterized by an average of 9 proton-proton interaction per bunch-crossing.

7.3 Monte Carlo samples

Monte Carlo simulated samples are used to model the reconstructed W+b-jets signal and most of its background contributions, as well as to extract a fiducial cross-section from the measured W+b-jets yield.

The processes of W boson production in association with b-jets, c-jets and light-jets are simulated separately using the Alpgen 2.13 [95] generator, interfaced to Herwig 6.510 [96] for parton showers and hadronization, and Jimmy 4.31 [97] for the underlying-event simulation. Exclusive samples with zero to four additional partons

and an inclusive sample with five or more additional partons are used. The MLM matching scheme [98], as implemented in ALPGEN, is used to remove overlaps between samples with the same parton multiplicity originating from the matrix element (ME) and the parton shower (PS). The MLM matching results in accurate description of the W+jets and Z+jets kinematics at the LHC, as seen in references [34, 35].

In addition to the overlaps in number of partons, overlaps in heavy-flavor production are also considered. This is because the $g \to b\bar{b}$ and $g \to c\bar{c}$ processes are accounted for by the ALPGEN matrix element simulation as well as by the HERWIG parton shower simulations. To remove this overlap, a dedicated "heavy-flavor overlap removal" (HFOR) tool has been developed. This tool works under the hypothesis that ALPGEN provides a better description of heavy-flavour production at large angles, while the HERWIG parton shower provides a better description at small angles. Events containing heavy-flavor quarks produced from gluon splitting in the parton shower are therefore kept only if the quarks are produced at small angles ($\Delta R_{b,\bar{b}} < 0.4$ or $\Delta R_{c,\bar{c}} < 0.4$). Events containing heavy flavor quarks produced from gluon splitting at the matrix element level are kept only if the quarks are produced with $\Delta R_{b,\bar{b}} > 0.4$ or $\Delta R_{c,\bar{c}} > 0.4$. The HFOR tool can also be modified so as to provide two variations, which are used to estimate systematic uncertainties. In one variation only the parton shower is used, for all ΔR values, and in the other variation only the matrix element is used. These configurations are summarized in Table 7.3.

The Z+jets background is simulated with ALPGEN interfaced to HERWIG and JIMMY, using the same configuration as for W+jets. The diboson (WW, WZ, ZZ) background is simulated with HERWIG. The t-channel, s-channel and Wt-channel

Table 7.3: Monte Carlo samples used to produce heavy-flavor configuration resulting from a gluon splitting ($g \to b\bar{b}$ and $g \to c\bar{c}$). ΔR is the angle between the two b or c quarks. In the standard configuration, HERWIG is used for small angles and ALPGEN for large angles.

	$\Delta R < 0.4$	$\Delta R > 0.4$
Standard HFOR	HERWIG	ALPGEN
Full parton shower	HERWIG	HERWIG
Full matrix element	ALPGEN	ALPGEN

single-top processes are simulated with AcerMC 3.7 [100] interfaced to PYTHIA. The $t\bar{t}$ background is simulated with POWHEG [82] interfaced to PYTHIA.

The total cross-sections of the W+jets and Z+jets samples are normalized to the inclusive NNLO predictions [101], while other backgrounds are normalized to NLO predictions [102, 103, 104]. The $t\bar{t}$ contribution in the 1-jet and 2-jet analysis regions, and the single-top contribution in the 2-jet analysis region, are estimated from data.

The detector simulation [105] is based on the GEANT4 program [106]. For all the processes modeled, multiple interactions per bunch crossing (pile-up) are accounted for by overlaying minimum-bias events simulated with PYTHIA onto the generated hard process. The MC simulation is divided into four periods to reflect data-taking conditions as closely as possible. The fraction of total data represented by different periods is 3.2% for periods B – D, 17.4% for periods E –H, 25.8% for periods I – K and 53.5% for periods L – M. The bunch spacing is 50 ns and the distribution of the average number of interactions per bunch crossing varies in each period. A pile-up reweighting tool that applies weights to MC events, depending on their period and instantaneous luminosity, is used to correct for any residual difference due to the data taking conditions [10].

Additional Monte Carlo samples are used to study backgrounds, estimate sys-

tematic uncertainties, and simulate the b-tagging properties of jets. The fragmentation and decay properties characteristic of light and heavy-flavor jets within the W+jets sample are simulated using PYTHIA: specifically, the large PYTHIA dijet and POWHEG+PYTHIA W+bb samples are used to extract templates for all the W+jets samples, and the small ALPGEN +PYTHIA test samples are used to cross-check these templates. To study the properties of heavy-flavor jets in $t\bar{t}$ events, the standard POWHEG+PYTHIA $t\bar{t}$ sample is compared with samples generated with MC@NLO +HERWIG and POWHEG+HERWIG. Lepton-filtered[3] PYTHIA simulations of the $b\bar{b}$ and $c\bar{c}$ processes are used to develop the methods for the data-driven estimate of the multijet background. Finally, additional samples are generated to evaluate the initial-state and final-state radiation (ISR/FSR) uncertainties in the $t\bar{t}$ and single-top processes. These effects are evaluated using the ACERMC generator interfaced to PYTHIA, and by varying the parameters controlling ISR and FSR in PYTHIA in a range consistent with data collected in the 2010 LHC run [133]. The samples used are summarized in Table 7.4.

The uncertainty related to the ALPGEN W+b-jets fiducial acceptance modeling is estimated using modified W+b-jets samples, generated using different settings. Specifically, the set of parton distribution functions (PDF) is changed from CTEQ6L1 [134] to MRST2002LO [135]; the minimum jet p_{T} used in the MLM matching is decreased (increased) to 15 (25) GeV, from the reference value of 20 GeV. Additionally, the renormalization and factorization scales, usually taken to be $\mu_R^2 = \mu_F^2 = m_W^2 + p_{\mathrm{T},W}^2$, are halved, doubled, and their functional form is changed first to

[3]A generation level filter selects events with at least a truth lepton with $p_{\mathrm{T}} > 10$ GeV.

$\mu_R^2 = \mu_F^2 = m_W^2$ and then to $\mu_R^2 = \mu_F^2 = m_W^2 + \sum_{partons}(m_{part.}^2 + p_{\mathrm{T},part.}^2)$.

Table 7.4: Simulated event samples used in this analysis, including the production cross-section (multiplied by the relevant branching ratio, BR).

Physics process	Generator	Parton Shower	$\sigma \cdot$ BR (nb)	
$W \to \ell\nu$ + jets	ALPGEN	Herwig	10.46	NNLO
$Z \to \ell\ell$ + jets	ALPGEN	Herwig	1.07	NNLO
$t\bar{t}$	Powheg	Pythia	89.7×10^{-3}	approx. NNLO
Single-top (s-channel)	AcerMC	Pythia	4.3×10^{-4}	NLO
Single-top (t-channel)	AcerMC	Pythia	6.34×10^{-3}	NLO
Single-top (Wt)	AcerMC	Pythia	13.1×10^{-3}	NLO
WW	HERWIG	-	44.9×10^{-3}	NLO
WZ	HERWIG	-	18.5×10^{-3}	NLO
ZZ	HERWIG	-	5.96×10^{-3}	NLO
Samples used for cross-checks, systematics, b-tagging properties				
$W \to \ell\nu$ + jets	ALPGEN	Pythia	10.46	NNLO
$Z \to \ell\ell$ + jets	ALPGEN	Pythia	1.07	NNLO
$W + b\bar{b}$	ALPGEN	Herwig+Evtgen	[normalized]	
$W + b\bar{b}$	ALPGEN	Pythia+Evtgen	[normalized]	
$W + b\bar{b}$	Powheg	Pythia	42.8×10^{-3}	NNLO
$t\bar{t}$	MC@NLO	Herwig	89.7×10^{-3}	approx. NNLO
$t\bar{t}$	Powheg	Herwig	89.7×10^{-3}	approx. NNLO
Single-top (s-channel)	MC@NLO	Herwig	$\times10^{-4}$	NLO
Single-top (t-channel)	MC@NLO	Herwig	$\times10^{-3}$	NLO
Single-top (Wt)	MC@NLO	Herwig	13.1×10^{-3}	NLO
$c\bar{c}$ (lepton-filtered)	Pythia	-	[normalized]	
$b\bar{b}$ (lepton-filtered)	Pythia	-	[normalized]	
Dijet	Pythia	-	[normalized]	

7.4 Event Selection

Candidate W+b-jets events are required to have exactly one high-p_{T} electron or muon, missing transverse momentum ($E_{\mathrm{T}}^{\mathrm{miss}}$) consistent with a neutrino from a W boson, and one or two reconstructed jets, exactly one of which must be b-tagged.

The event selection is optimized to reduce the large backgrounds present in the lepton plus b-tagged jet data sample. In particular, backgrounds containing b-jets ($t\bar{t}$, single-top, multijet) cannot be separated from the W+b-jets signal using the CombNN variable. The choice of applying a veto on any third jet and on any second b-tagged jet is made in order to reject the top background.

After discussing initial requirements such as trigger and event cleaning (7.4.1), the sections below cover the selections of the basic objects, such as muons (7.4.2), electrons (7.4.3), jets (7.4.4), b-jets (7.4.5), $E_{\mathrm{T}}^{\mathrm{miss}}$(7.4.6). An overview of the techniques used to reconstruct these basic objects can be found in Section 6. The selection criteria are driven by considerations of high efficiency, low fake rate, and small systematic uncertainties. They usually follow the recommendations of the ATLAS Combined Performance groups, except for the lepton isolation and W transverse mass selection, which are discussed in Section 7.4.7 in relation to the multijet background. Finally, Section 7.4.8 presents comparisons of distributions from data and Monte Carlo simulation after the full event selection.

The selected events fall into four *analysis regions*, defined by the lepton flavor and the number of jets: muon 1-jet, electron 1-jet, muon 2-jet, electron 2-jet. For the differential measurement as a function of $p_{\mathrm{T}}^{b-\mathrm{jet}}$, four bins of b-tagged jet p_{T} are defined: 25–30 GeV, 30–40 GeV, 40–60 GeV and 60–140 GeV. This binning choice

is found to maintain similar statistics in each bin. The specific bin boundaries are chosen based on those of the b-tagging scale factors, in order to minimize their effect in shaping the p_{T} distribution.

7.4.1 Trigger, vertex, event cleaning

Events are selected in data from a set of ~ 2 minutes intervals called *luminosity blocks* during which the LHC was delivering stable beams, and each ATLAS sub-detector was recording good data with more than 90% of its channels. This set of luminosity blocks defines a *Good Runs List* [4].

Within the Good Run List, collision events are selected by requiring the existence of at least one reconstructed vertex formed by the intersection of at least three tracks with $p_{\mathrm{T}} > 400$ MeV. In events with multiple vertices, the vertex with the largest sum of squared p_{T} of the associated tracks is taken to be the primary hard-scatter vertex (PV).

For each data-taking period, the lowest p_{T} single-electron or single-muon trigger that was fully active during the corresponding run period is used. For the electrons, these triggers are `EF_e20_medium` for periods D–I, `EF_e22_medium` for period K, and `EF_e22vh_medium1` for periods L–M. For the muons, the triggers are `EF_mu18_MG` for periods D–I and `EF_mu18_MG_medium` for periods J–M. Events with two selected leptons are removed, to prevent event duplication and to reduce the Z+jets background. In order to account for the trigger efficiency correctly, muon events are kept only if they originate in the "Muons" stream (meaning that they were selected by a muon trigger),

[4]The Good Run List used to select events is included in the file `data11_7TeV.periodAllYear_DetStatus-v36-pro10_CoolRunQuery-00-04-08_WZjets_allchannels_DtoM.xml`

and electron events if they originate in the "Egamma" stream (electron trigger).

Finally, *event cleaning* cuts are applied, which are the same in both electron and muon channel; they remove a small fraction of the events (less than 1%) and are for the most part applied to both data and Monte Carlo.

- *LAr Flag:* Events with a Liquid Argon Calorimeter noise warning flag (larError!=0) are removed (data only).

- *LAr Hole:* Events with a jet reconstructed within the η-ϕ hole defined as the area of $-0.1 < \eta < 1.5$ and $-0.9 < \phi < -0.5$ are removed if the p_{T} of the jet (corrected to compensate for the jet energy lost in the hole) is larger than 25 GeV[5]. This cut is only applied in the approximately 17% of events which are affected by the Liquid Argon Hole: periods E-H in data and Run 103003 in Monte Carlo [9].

- $E_{\mathrm{T}}^{\mathrm{miss}}$ *cleaning or Bad Jet Removal:* Jets with $\mathrm{p}_T > 20$ GeV which do not overlap ($\Delta R > 0.3$) with a selected lepton (see sections 7.4.2 and 7.4.3) are tested for the `Looser` [9] bad jet criteria, which tests for noise spikes, non-collision backgrounds and coherent noise. The full event is discarded if one or more jet falls into this category, since a bad jet would affect the $E_{\mathrm{T}}^{\mathrm{miss}}$ calculation.

7.4.2 Muon Selection

The muons used in this analysis are STACO Combined muons (CM). Their reconstruction is described in Section 6.4. Combined muons are selected with $p_{\mathrm{T}} > 25$ GeV

[5]The correction for lost energy is based on the energy in neighboring cells and on the jet shapes in Monte Carlo simulation.

and $|\eta| < 2.4$. The 25 GeV cut is chosen to reduce the multijet background, and to simplify the comparison between the electron and muon channels, even though only 20 GeV are required to be on the plateau of the trigger efficiency.

In order to reject cosmic muons and secondary muons from decays in flight, the muon candidate track is required to have an absolute z_0 of less than 10 mm with respect to the primary vertex and d_0 significance less than 3.

In order to reduce the large background from multijet production, muon candidates are required to be isolated from neighbouring tracks within $\Delta R = 0.4$ of their direction, as well as from other calorimeter energy depositions, corrected for pile-up contributions, within $\Delta R = 0.2$. Specifically, the the sum of transverse momenta of neighbouring tracks must be less than 2 GeV, while the sum of the calorimeter transverse energies must be less than 1 GeV.

To be considered for a second lepton veto, muons are subject to a looser selection than the standard one: the p_{T} and η requirements are loosened, respectively to 20 GeV and $\eta < 2.5$.

7.4.3 Electron Selection

The electrons used in this analysis are "Tight++" electrons. Their reconstruction is described in Section 6.3. To select central electrons and to avoid the transition region between the calorimeters, electrons must have a cluster $|\eta| < 1.37$ or $1.52 < |\eta| < 2.47$. The electron transverse energy (E_{T}) is calculated from the cluster energy and the track direction. The candidate electrons are required to have $E_{\mathrm{T}} > 25$ GeV. To avoid problems with the liquid argon calorimeter, such as dead front-end boards

or masked cells, electron candidates are required to pass an object quality cut [6].

To ensure that the candidates come from the primary vertex, the absolute z_0 must be less than 10 mm with respect to the primary vertex and the d_0 significance must be less than 10. The d_0 significance distribution is wider for signal electrons than for signal muons, requiring a looser selection in this variable (for muons the d_0 significance is required to be less than 3). The lower resolution is due to the larger amount of bremsstrahlung and to the lack of the Muon Spectrometer hits in the track fit.

The isolation condition is imposed on two variables. One, the calorimeter isolation, is the sum of the calorimeter energy in a cone of $\Delta R = 0.2$ around the electron candidate cluster. The calorimeter isolation is corrected to account for additional energy leaking from the electron cluster into the surrounding cone, and for additional energy due to pile-up contributions, as described in reference [6]. The other variable, the track isolation, is the sum of inner detector tracks in a cone of $\Delta R = 0.4$ around the electron candidate track. The isolation requirement is implemented through p_{T} and η dependent cuts for both calorimeter and tracking isolation, resulting in a constant efficiency on signal electrons across all detector regions and energy ranges, as measured in Monte Carlo events.

To be considered for a second lepton veto, electrons are subject to a looser selection than the standard one: the p_{T} and "Tight++" requirements are loosened, respectively to 20 GeV and "Medium++".

[6] This requirement is implemented by requiring that the "OQ" (object quality) variable satisfies the bitwise condition: OQ AND 1446 == 0.

7.4.4 Jet Selection

The jets used in this analysis are anti-k_{T} jets with a distance parameter $R = 0.4$. Their reconstruction is described in Section 6.5. Jets are required to have a fully calibrated transverse momentum $p_{\mathrm{T}} > 25$ GeV and, in order for the full jet to be reconstructed in the tracking region, their absolute rapidity $|y|$ is required to be smaller 2.1. Jets originating in pile-up interactions are suppressed by requiring that at least 75% of the total transverse momentum of tracks associated with each jet point to the PV [8]. Jets within a distance $\Delta R = 0.5$ of the lepton candidate are removed, and jets arising from detector noise or cosmic rays are also rejected [114].

7.4.5 b-tagging

The CombNN tagger (described in Section 6.6) is used both to select a sample enriched with b-jets, as well as to discriminate between b-jets, c-jets and light-jets within the enriched sample. The working point used for the selection (CombNN $>$ 2.2) corresponds to a b-tagging efficiency of about 40% at low p_{T}, increasing to a plateau of 57% for b-jets of p_{T} above 60 GeV, with rejection rates of about 10 for c-jets and 1000 for light-jets. The CombNN distribution in the b-tagged sample is then used to separate statistically the remaining c-jet and light-jet contributions from the W+b-jets signal.

7.4.6 Missing transverse energy

The measurement of the missing transverse energy is based on the METRefFinal algorithm, described in Section 6.7. To be consistent with a W boson decay, and to

reduce the multijet background, the $E_{\mathrm{T}}^{\mathrm{miss}}$ is required to be larger than 25 GeV, and the W boson transverse mass $m_T(W) = \sqrt{2p_{\mathrm{T}}^{\ell}p_{\mathrm{T}}^{\nu}(1-\cos(\phi^{\ell}-\phi^{\nu}))}$ is required to be larger than 60 GeV.

7.4.7 Multijet background reduction: isolation and $m_{\mathrm{T}}(W)$

The first step in reducing the multijet background was to tighten the lepton isolation for both the electron and muon channels. Absolute and relative isolation cuts were studied, using all the available cone sizes, and the following selection was chosen:

- Muons: $p_{\mathrm{T}}^{\mathrm{cone40}} < 2$ GeV, $E_{\mathrm{T}}^{\mathrm{cone20}} < 1$ GeV.
- Electrons: 90% efficiency working point for $p_{\mathrm{T}}^{\mathrm{cone40}}$ and $E_{\mathrm{T}}^{\mathrm{cone20}}$.

The efficiency of these cuts on signal leptons is between 80 and 90%. Measurements of this efficiency based on the tag and probe technique were performed on both data and Monte Carlo events, resulting in scale factors very close to unity.

After the tightened isolation requirements, the multijet background was found to be at a level of 7% in the Muon channel and 12% in the Electron channel in the 1-jet region. The remaining reduction, down to the final 3% and 6.5% level of table 7.6, was achieved by tightening the kinematic selection. The two variables most sensitive to the multijet background, $E_{\mathrm{T}}^{\mathrm{miss}}$ and $m_T(W)$, were studied. Figure 7.7 includes two sets of plots, for $E_{\mathrm{T}}^{\mathrm{miss}}$ (top) and $m_T(W)$(bottom), in the electron (left) and muon (right) channels. Each set of plots include normalized kinematic distributions of the $W+b\bar{b}$ process (simulated in Monte Carlo) and the multijet background (estimated in data, see Section 7.5.1). Under each kinematic distribution, a plot of signal ($W+b\bar{b}$)

vs. background (multijet) efficiency is shown. The efficiencies are calculated with respect to a nominal cut ($E_{\mathrm{T}}^{\mathrm{miss}} > 25$ GeV and $m_T(W) > 40$ GeV) for which the signal and background efficiencies are defined to be 1 (SignalEff = 1 and 1 − BkgEff = 0 point). For tighter cuts, the signal and background efficiencies became smaller than 1. Each point, starting from the [1,0] point and moving towards the left, defines a tighter cut on the $E_{\mathrm{T}}^{\mathrm{miss}}$ or the $m_T(W)$. The efficiency plot corresponding to the $m_T(W)$distribution is steeper, indicating a larger gain in background rejection (1 − BkgEff) for a similar signal efficiency. As a result of this study, the $m_T(W)$ cut was moved from 40 to 60 GeV.

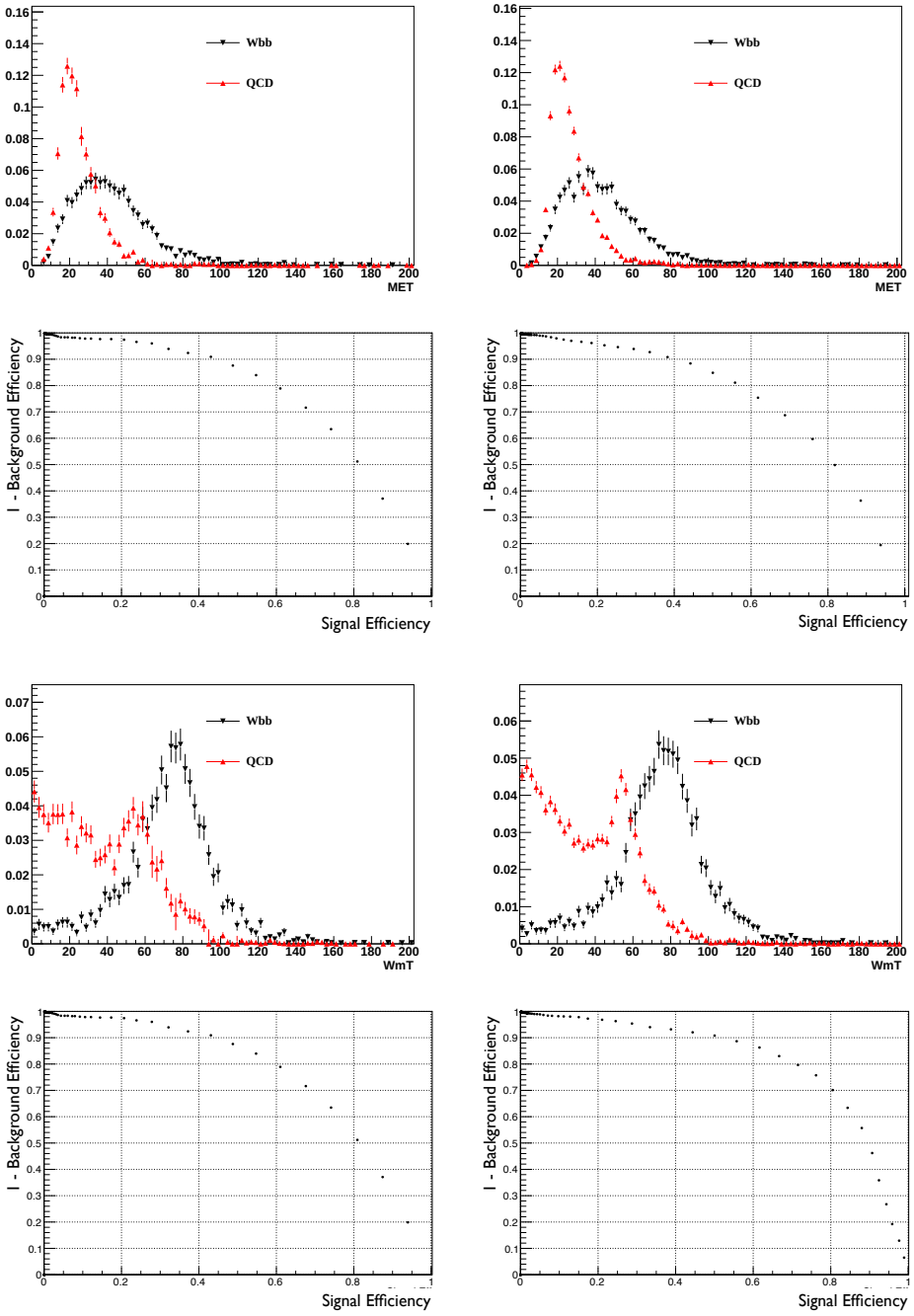

Figure 7.7: Missing transverse energy (first row) and transverse W mass (third row) distribution in W+b-jets and multijet events for electrons (right) and muons (left) in the 1-jet analysis region.Corresponding signal efficiency and background rejection (second and fourth rows) obtained by applying cuts in steps of 2.5 GeV. The lower right corner, SignalEff $= 1$ and $1 -$ BkgEff $= 0$, corresponds to the nominal cuts ($E_{\mathrm{T}}^{\mathrm{miss}} > 25$ GeV and $m_T(W) > 40$ GeV).

7.4.8 Selection Plots

In this section we compare data and Monte Carlo distributions after the multijet background normalization has been determined, but before performing the fits for $t\bar{t}$, single-top, and flavor content. The multijet background and W+jets normalizations are estimated using the method described in Section 7.5.1. In the "at least 4 jets 1-b-tag" $t\bar{t}$ control region plots, the signal plus background is normalized to the data in order to facilitate shape comparison. This normalization corresponds to the 10% correction measured when fitting the $t\bar{t}$ control region.

The first distributions shown are the jet multiplicity distributions for the electron and muon channel, in Figure 7.8. All requirements on electron, muon, b-tagged jet, $E_{\mathrm{T}}^{\mathrm{miss}}$, $m_T(W)$ described in Section 7.4 are applied, except for the requirement on the number of jets (1 or 2 jets). The jet multiplicity distribution gives an overall idea of the composition of the four analysis region (1-jet electron, 2-jet electron, 1-jet muon, 2-jet muon), as well as the $t\bar{t}$ control region (at least 4 jets 1-b-tag, electron and muon).

The following figures show the main kinematic distributions for the analysis and control regions: 1-jet electron (Figure 7.9), 1-jet muon (Figure 7.10), 2-jet electron (Figure 7.11), 2-jet muon (Figure 7.12), "at least 4 jets 1-b-tag" electron (Figure 7.13), "at least 4 jets 1-b-tag" muon (Figure 7.14). In each of these figures, the top left plot is the CombNN distribution, top right is the b-tagged jet p_{T}, middle left is the H_{T}, middle right is the lepton p_{T}, bottom left is the $E_{\mathrm{T}}^{\mathrm{miss}}$, bottom right is the $m_T(W)$. Only the statistical uncertainties of the data are shown, and no systematic effects are included. All plots are shown after the selection (CombNN > 2.2, $p_{\mathrm{T}}^{jet} > 25$ GeV,

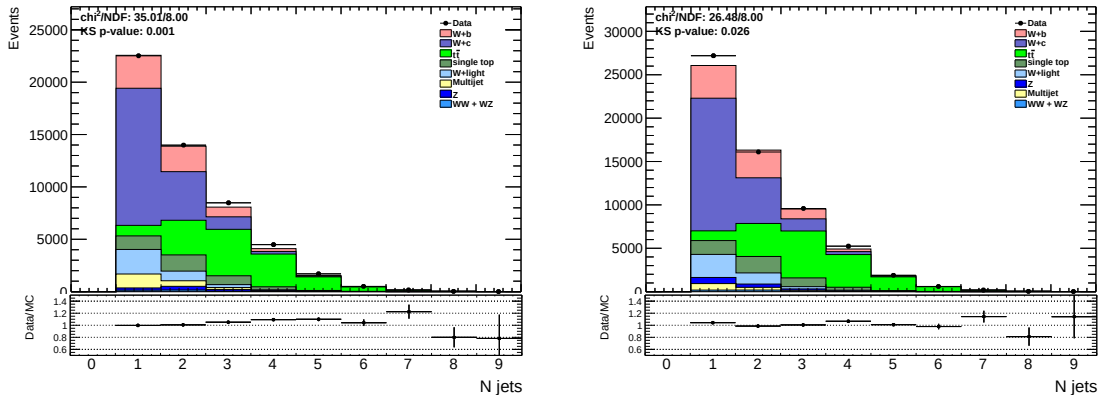

Figure 7.8: Jet multiplicity in the selected sample. The requirements applied to electron, muon, b-tagged jet, $E_{\mathrm{T}}^{\mathrm{miss}}$, $m_T(W)$ are described in Section 7.4. The requirement of exactly 1 or 2 jet is not applied. The electron channel is shown on the left, the muon channel on the right.

$p_{\mathrm{T}}^{\ell} > 25$ GeV). The $E_{\mathrm{T}}^{\mathrm{miss}}$ and $m_T(W)$ distribution are shown for the full region in which the multijet background is estimated ($E_{\mathrm{T}}^{\mathrm{miss}} > 0$ GeV and $m_T(W)>$ 40 GeV). The cuts used on $E_{\mathrm{T}}^{\mathrm{miss}}$ and $m_T(W)$ in the analysis regions, as implemented in all other plots, are $E_{\mathrm{T}}^{\mathrm{miss}} > 25$ GeV and $m_T(W)>$ 60 GeV.

The disagreement in the CombNN distribution in the four analysis regions is expected, since the flavor fraction has not been fitted. The b-tagged jet p_{T}, H_{T}, lepton p_{T}, $E_{\mathrm{T}}^{\mathrm{miss}}$, $m_T(W)$ distributions show good agreement between data and the sum of signal and background expectation in all analysis regions. Even though these distributions don't include the correction factors to the $t\bar{t}$, single-top, W+b-jets, W+c-jets and W+light-jets processes, the agreement at this level is not surprising. This is because the $t\bar{t}$ and single-top correction factors are only of the order of 10–15%, and because the kinematics of the W+b-jets, W+c-jets and W+light-jets are similar, hence their relative fraction does not strongly affect the overall kinematics.

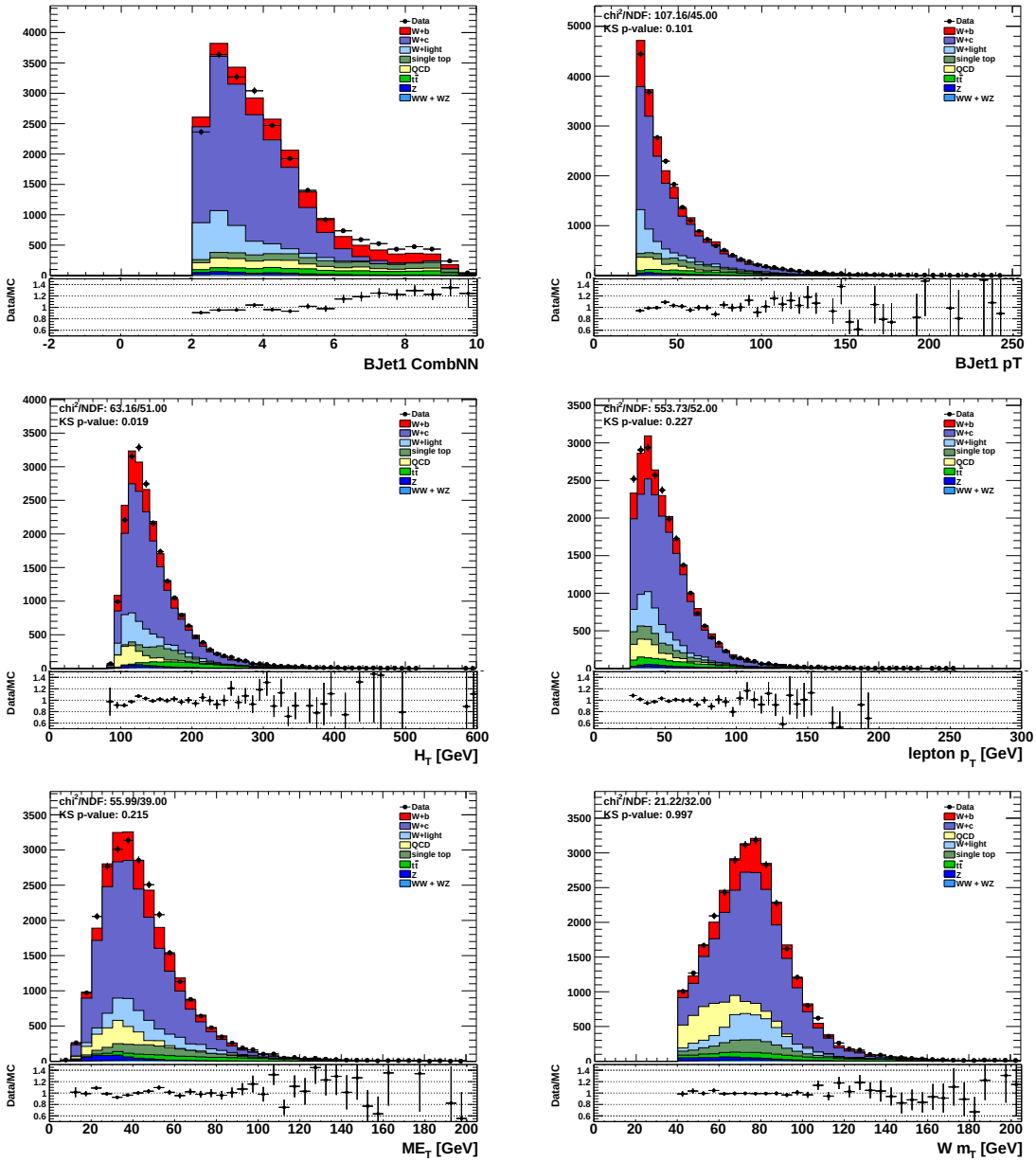

Figure 7.9: Kinematic and flavor content distributions in the 1-jet electron channel. The $E_{\mathrm{T}}^{\mathrm{miss}} > 25$ GeV cut is applied in all distributions except the $E_{\mathrm{T}}^{\mathrm{miss}}$ one, and similarly the $m_T(W) > 60$ GeV cut is applied in all distributions except the $m_T(W)$ one. The other main cuts are CombNN > 2.2, $p_{\mathrm{T}}^{jet} > 25$ GeV and $p_{\mathrm{T}}^{\ell} > 25$ GeV.

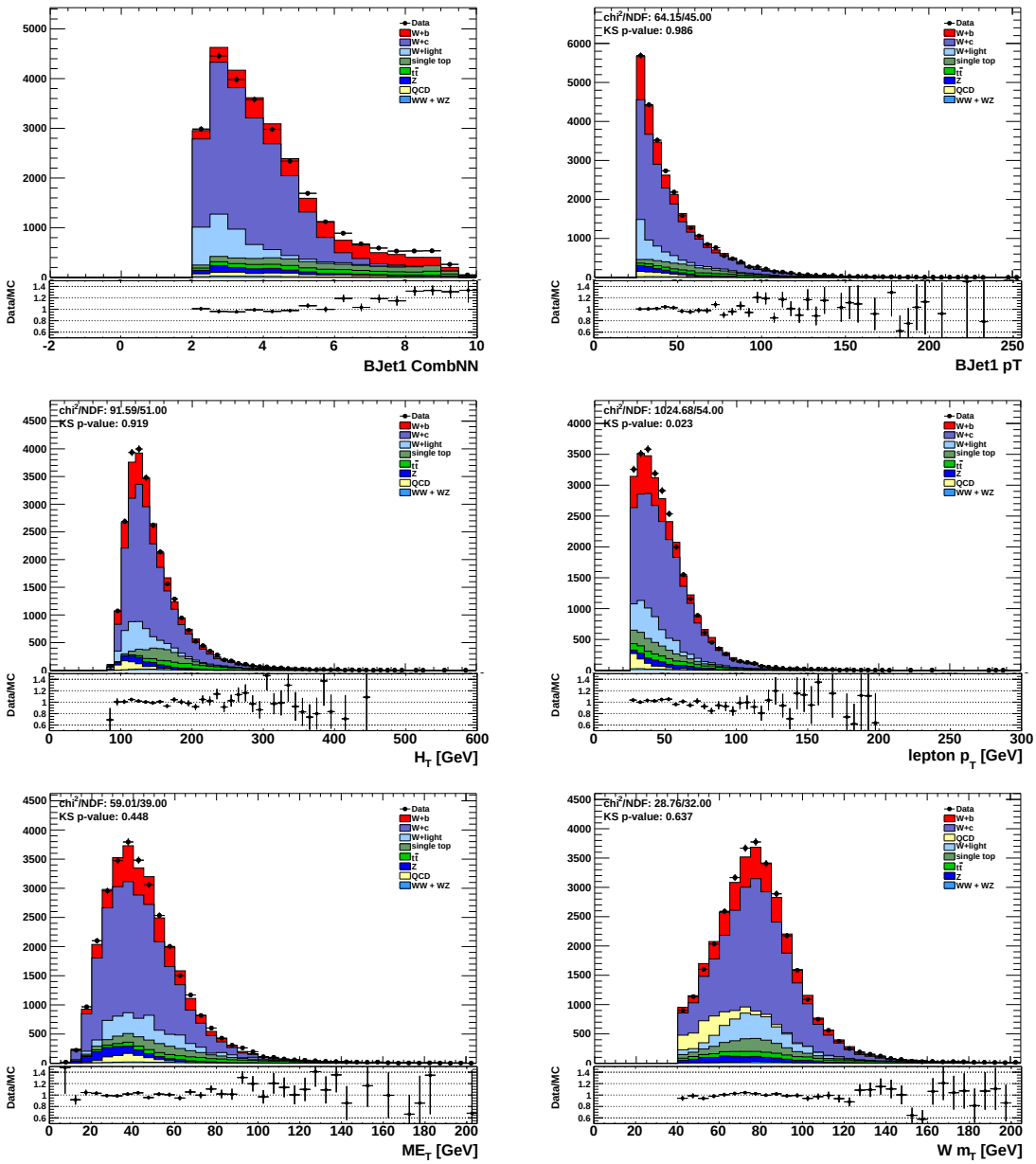

Figure 7.10: Kinematic and flavor content distributions in the 1-jet muon channel. The $E_{\mathrm{T}}^{\mathrm{miss}} > 25$ GeV cut is applied in all distributions except the $E_{\mathrm{T}}^{\mathrm{miss}}$ one, and similarly the $m_T(W) > 60$ GeV cut is applied in all distributions except the $m_T(W)$ one. The other main cuts are CombNN > 2.2, $p_{\mathrm{T}}^{jet} > 25$ GeV and $p_{\mathrm{T}}^{\ell} > 25$ GeV.

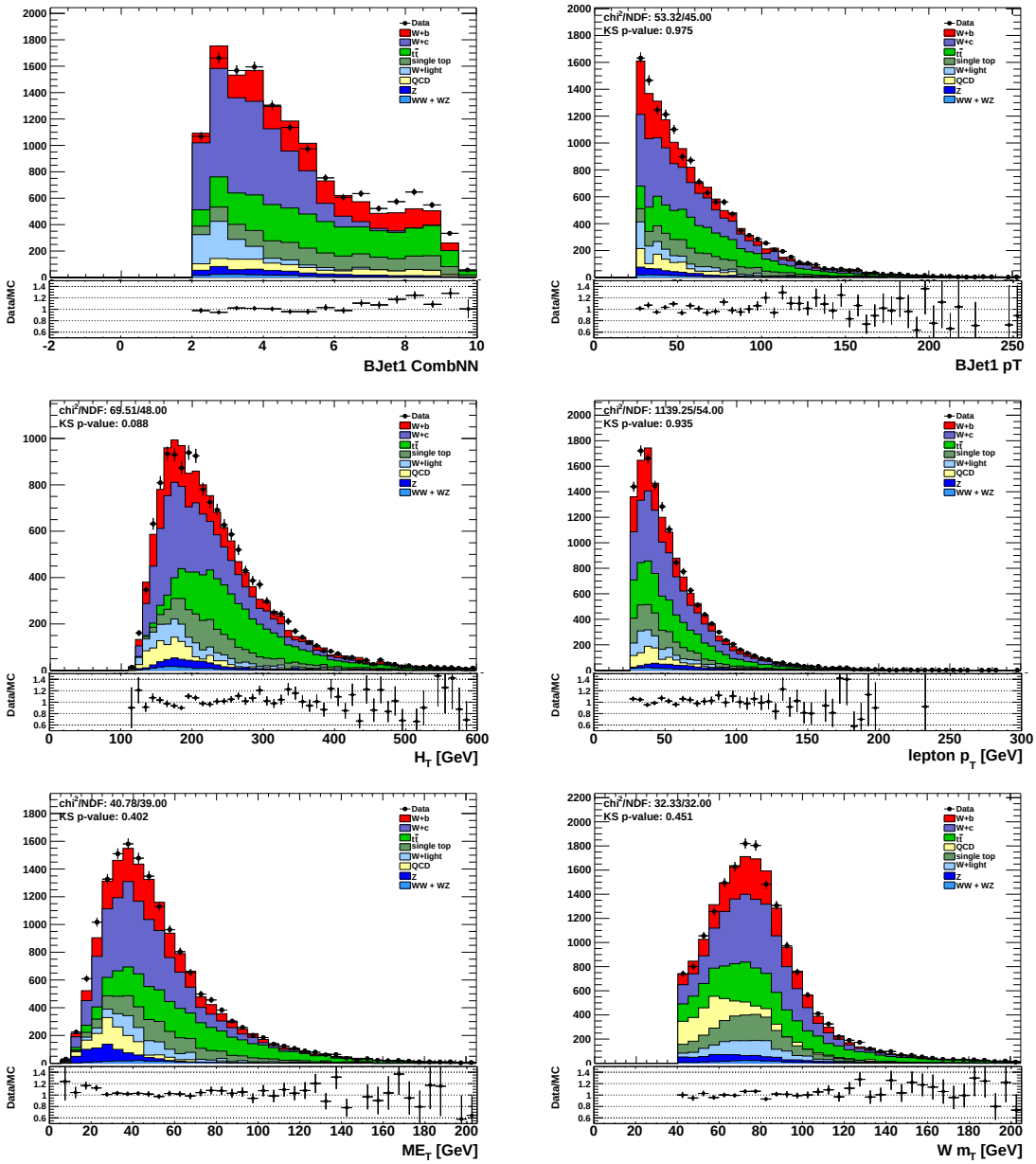

Figure 7.11: Kinematic and flavor content distributions in the 2-jet electron channel. The $E_{\mathrm{T}}^{\mathrm{miss}} > 25$ GeV cut is applied in all distributions except the $E_{\mathrm{T}}^{\mathrm{miss}}$ one, and similarly the $m_T(W) > 60$ GeV cut is applied in all distributions except the $m_T(W)$ one. The other main cuts are CombNN > 2.2, $p_{\mathrm{T}}^{jet} > 25$ GeV and $p_{\mathrm{T}}^{\ell} > 25$ GeV.

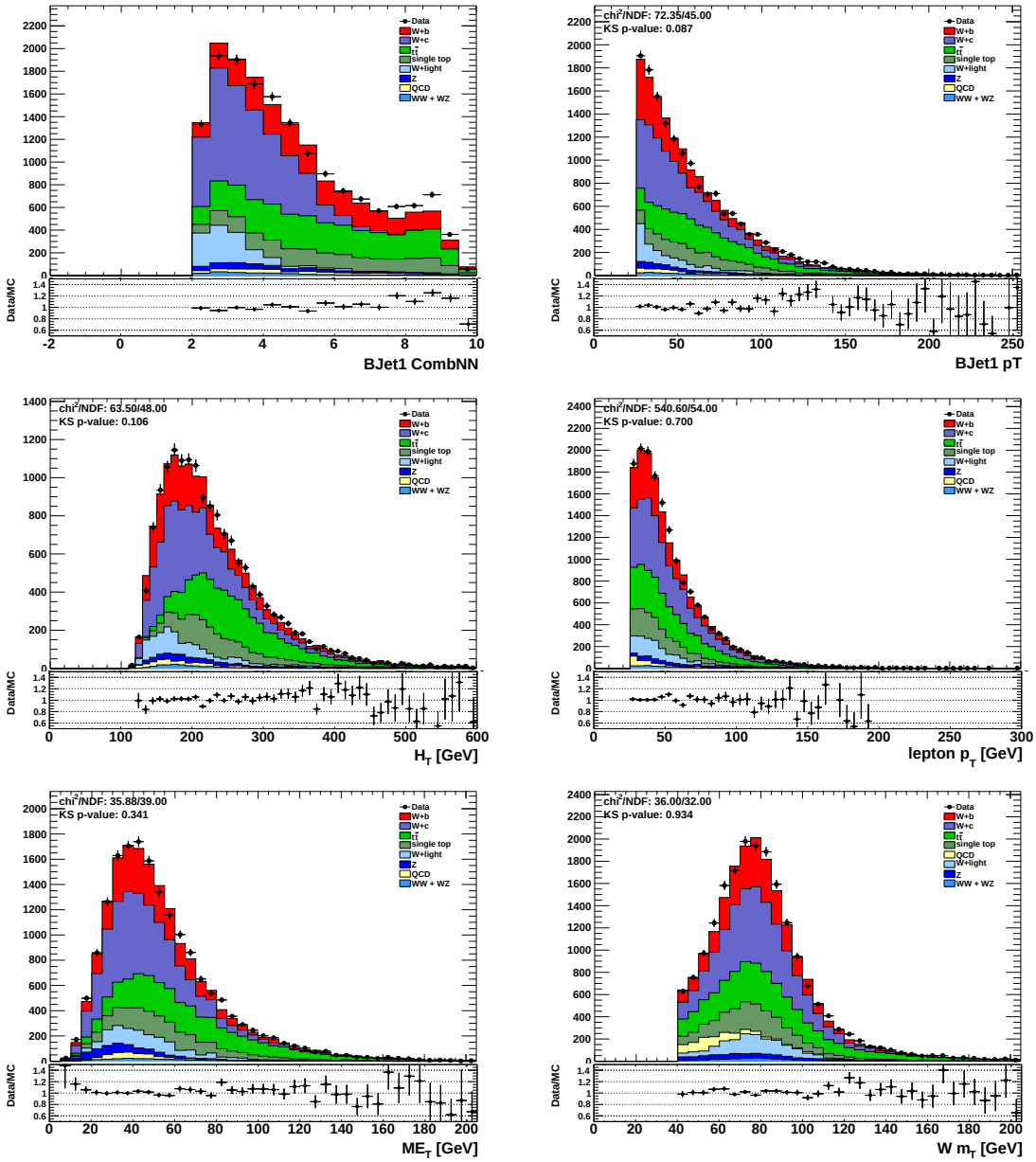

Figure 7.12: Kinematic and flavor content distributions in the 2-jet muon channel. The $E_{\mathrm{T}}^{\mathrm{miss}} > 25$ GeV cut is applied in all distributions except the $E_{\mathrm{T}}^{\mathrm{miss}}$ one, and similarly the $m_T(W) > 60$ GeV cut is applied in all distributions except the $m_T(W)$ one. The other main cuts are CombNN > 2.2, $p_{\mathrm{T}}^{jet} > 25$ GeV and $p_{\mathrm{T}}^{\ell} > 25$ GeV.

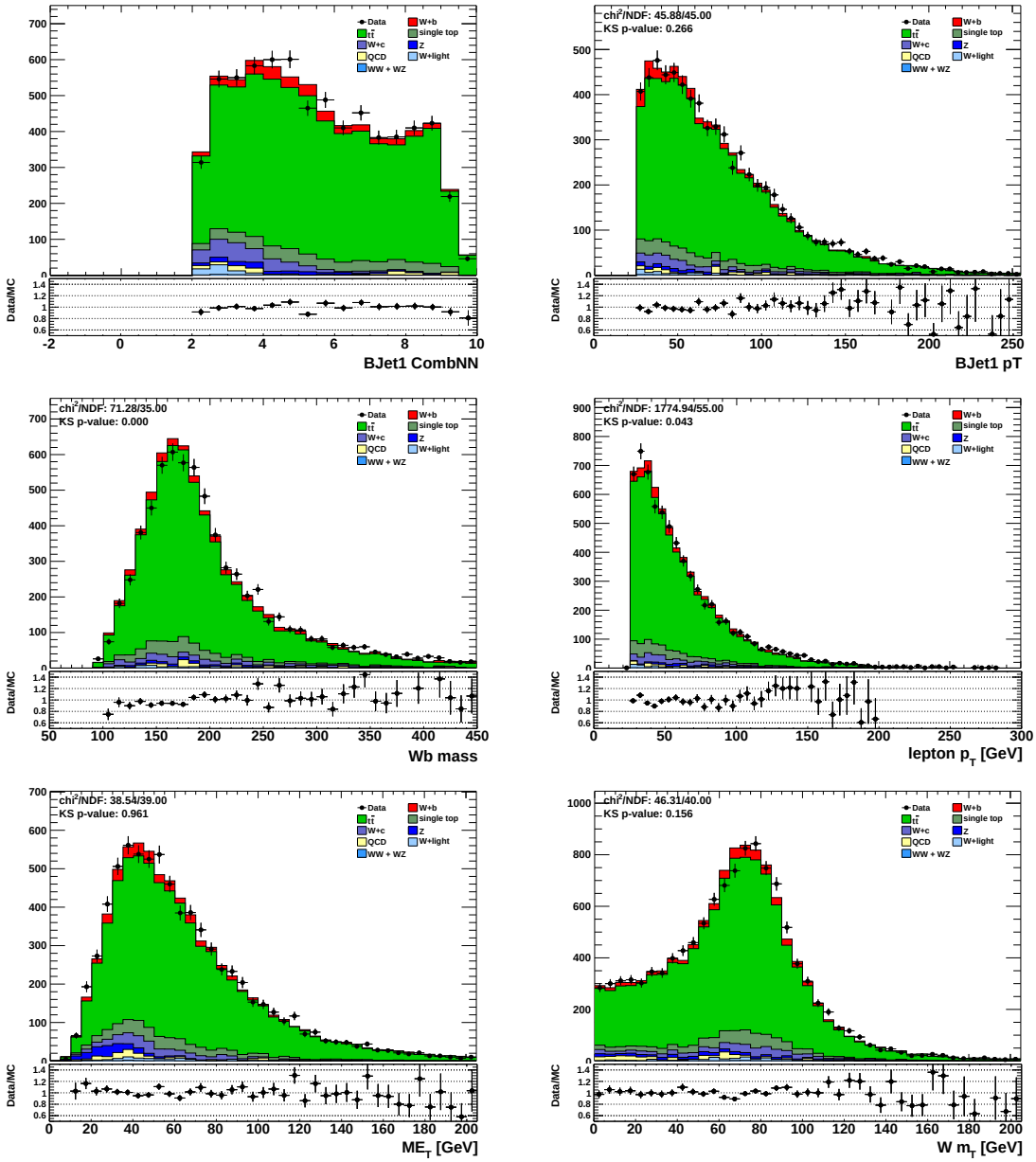

Figure 7.13: Kinematic and flavor content distributions in the at least 4 jets 1-b-tag electron channel. The $E_{\mathrm{T}}^{\mathrm{miss}} > 25$ GeV cut is applied in all distributions except the $E_{\mathrm{T}}^{\mathrm{miss}}$ one, and similarly the $m_T(W) > 60$ GeV cut is applied in all distributions except the $m_T(W)$ one. The other main cuts are CombNN > 2.2, $p_{\mathrm{T}}^{jet} > 25$ GeV and $p_{\mathrm{T}}^{\ell} > 25$ GeV.

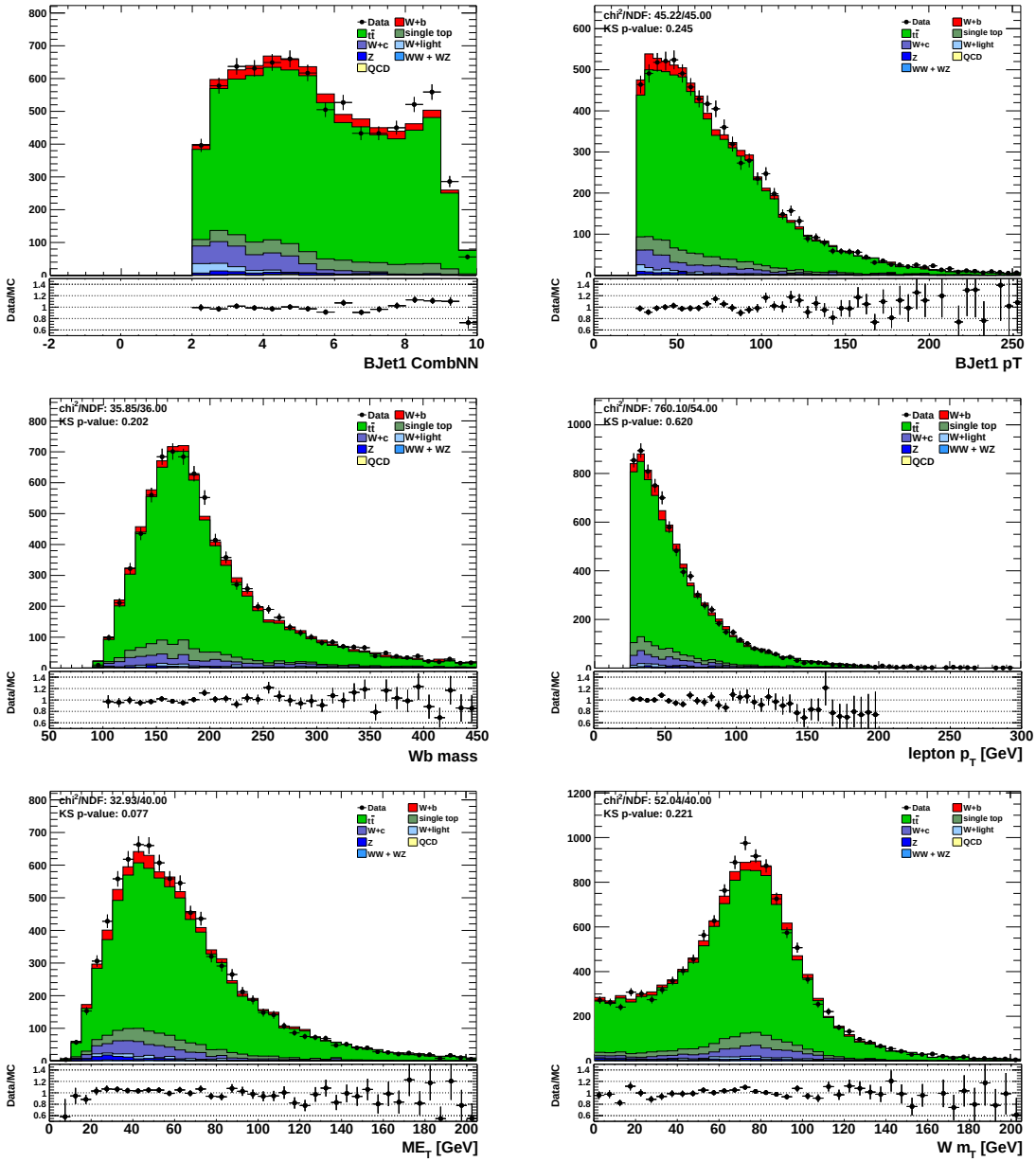

Figure 7.14: Kinematic and flavor content distributions in the at least 4 jets 1-b-tag muon channel. The $E_{\mathrm{T}}^{\mathrm{miss}} > 25$ GeV cut is applied in all distributions except the $E_{\mathrm{T}}^{\mathrm{miss}}$ one, and similarly the $m_T(W) > 60$ GeV cut is applied in all distributions except the $m_T(W)$ one. The other main cuts are CombNN > 2.2, $p_{\mathrm{T}}^{jet} > 25$ GeV and $p_{\mathrm{T}}^{\ell} > 25$ GeV.

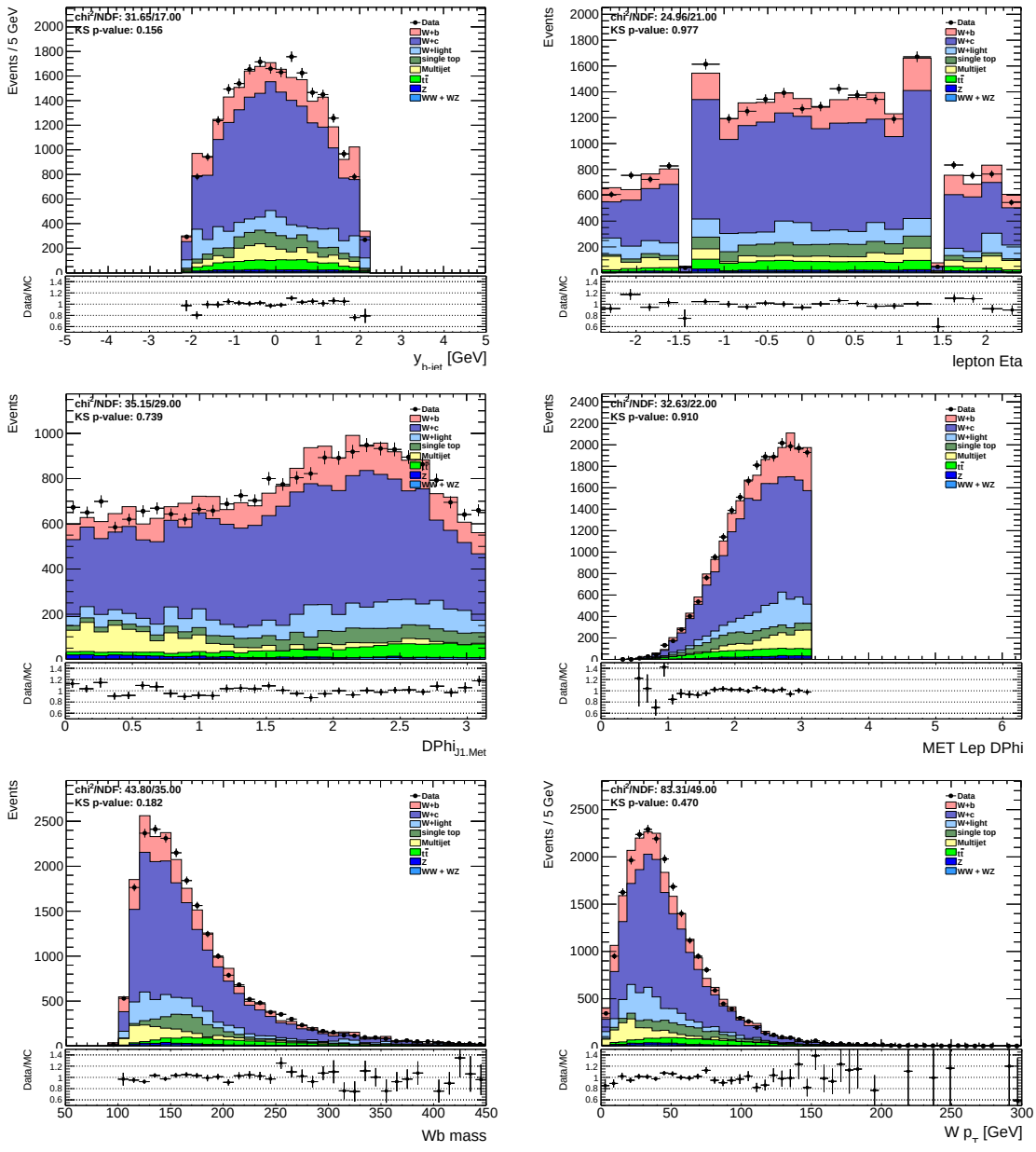

Figure 7.15: Additional plots in the 1-jet electron channel.

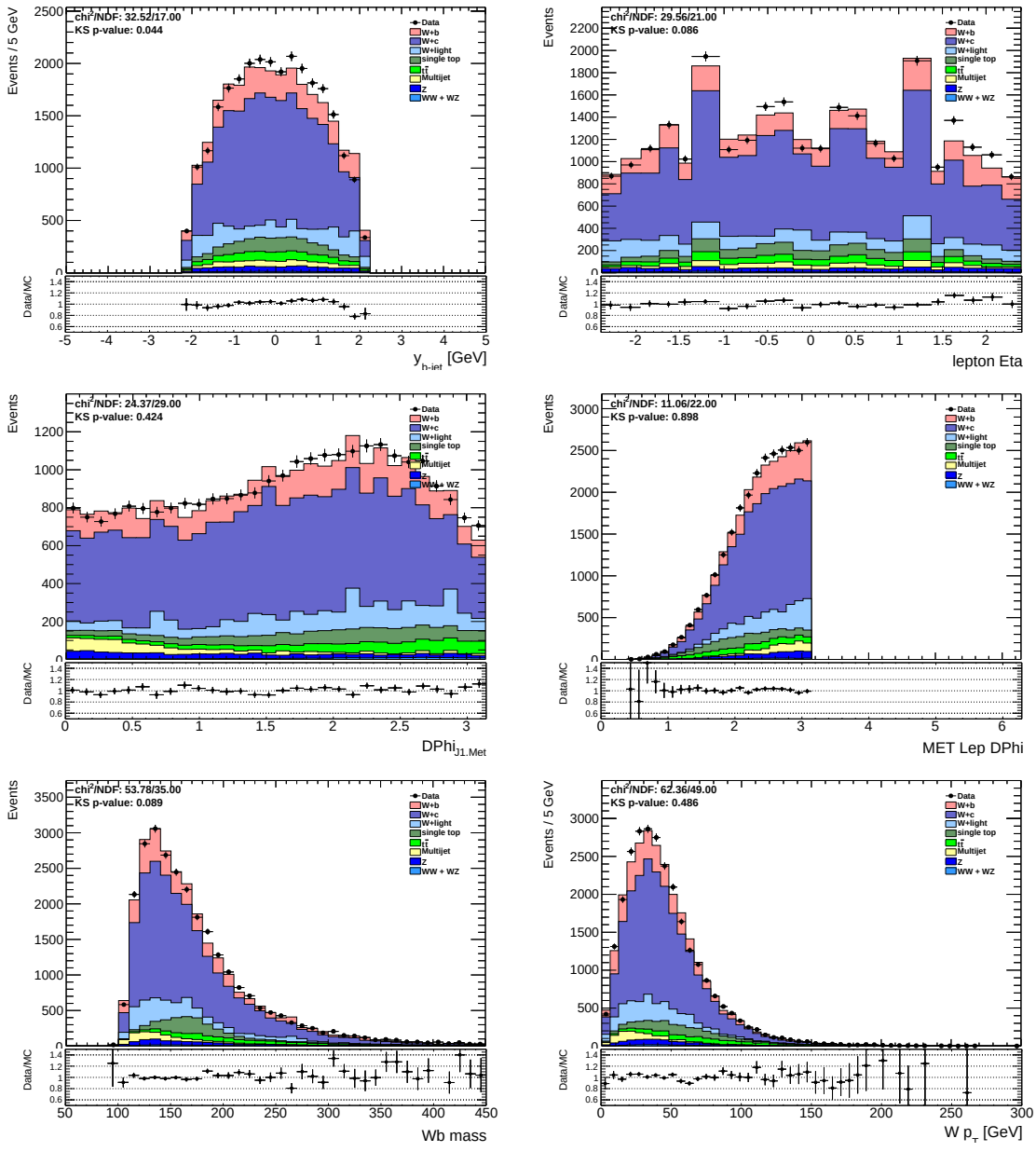

Figure 7.16: Additional plots in the 1-jet muon channel.

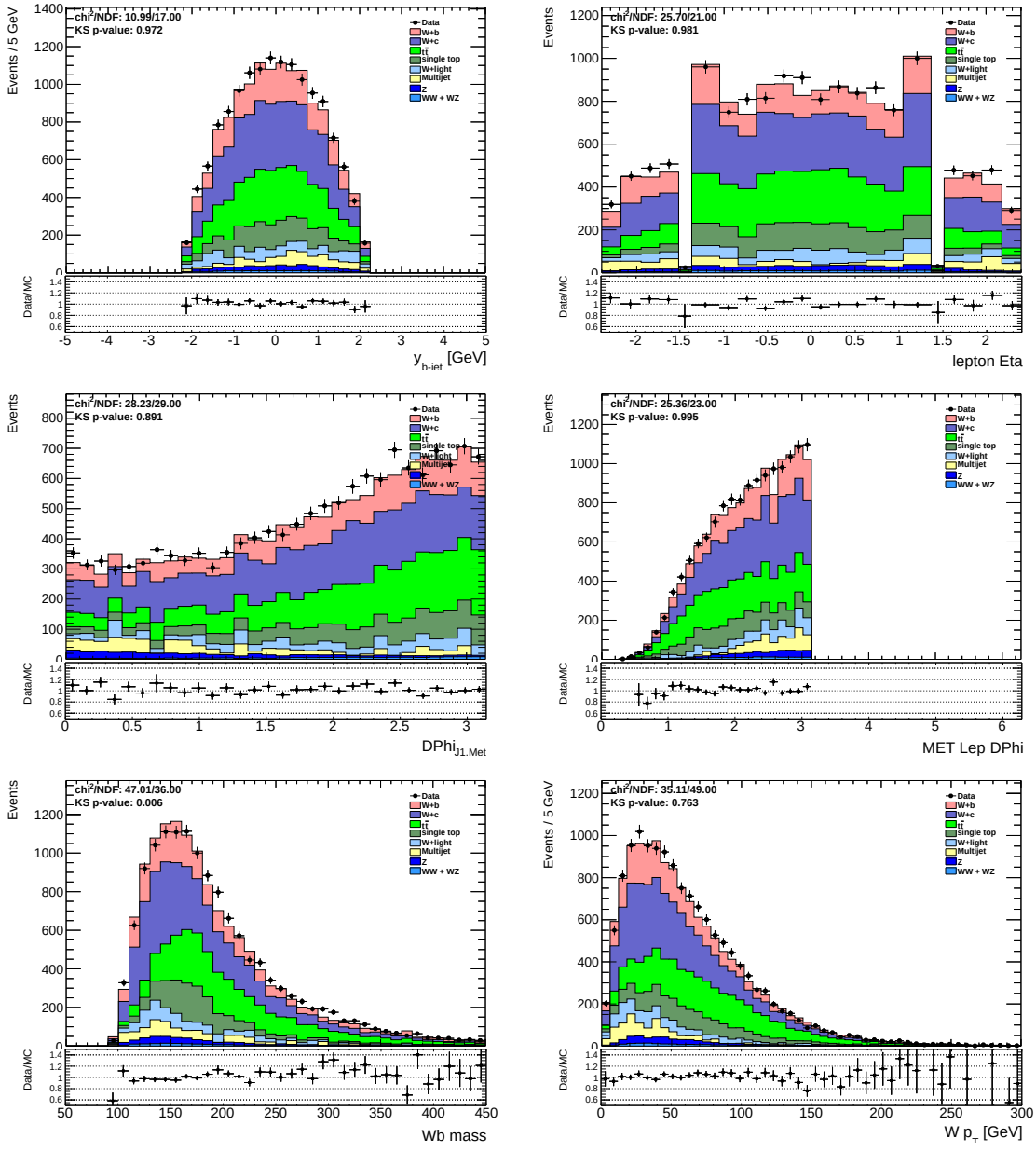

Figure 7.17: Additional plots in the 2-jet electron channel.

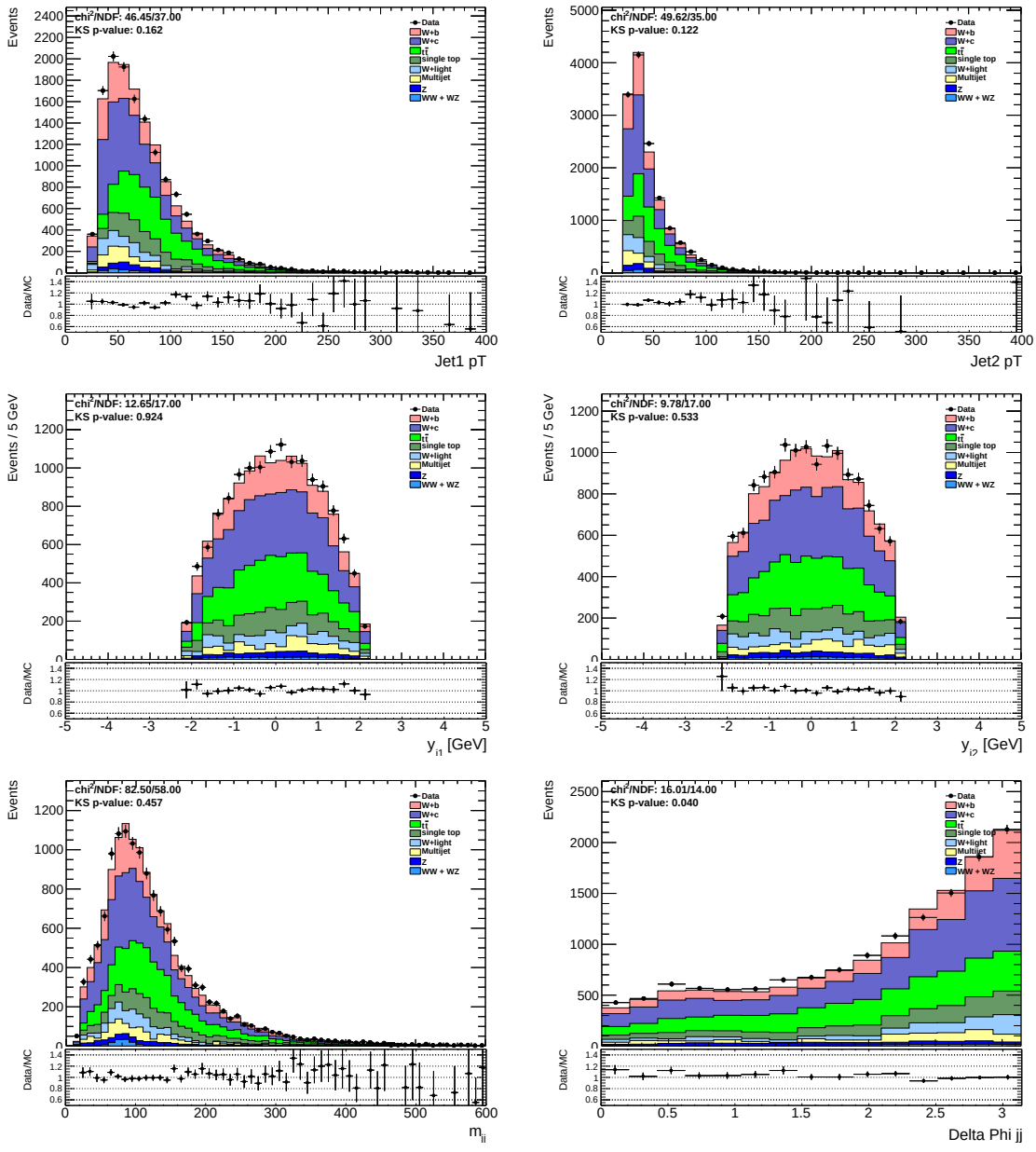

Figure 7.18: Additional plots in the 2-jet electron channel.

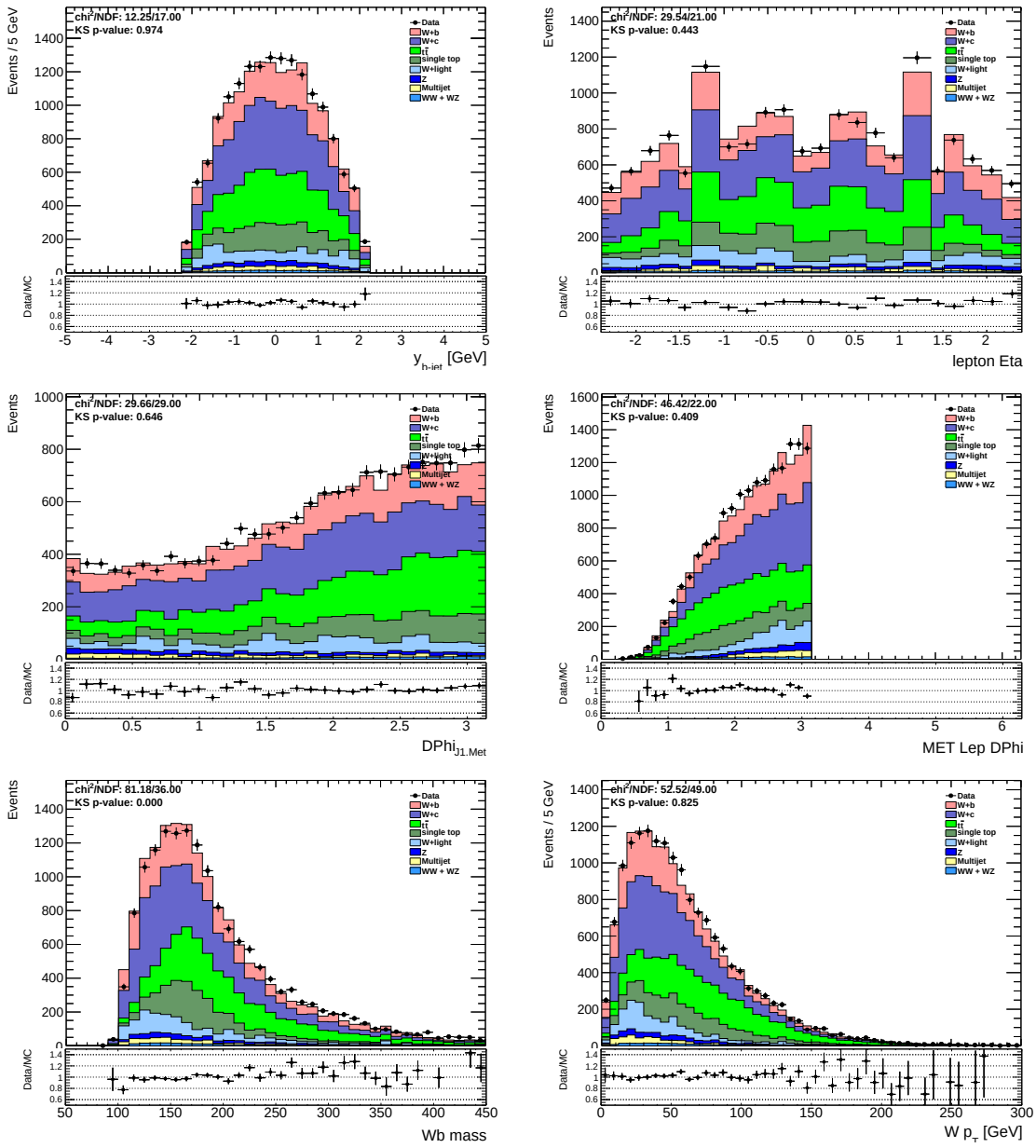

Figure 7.19: Additional plots in the 2-jet muon channel.

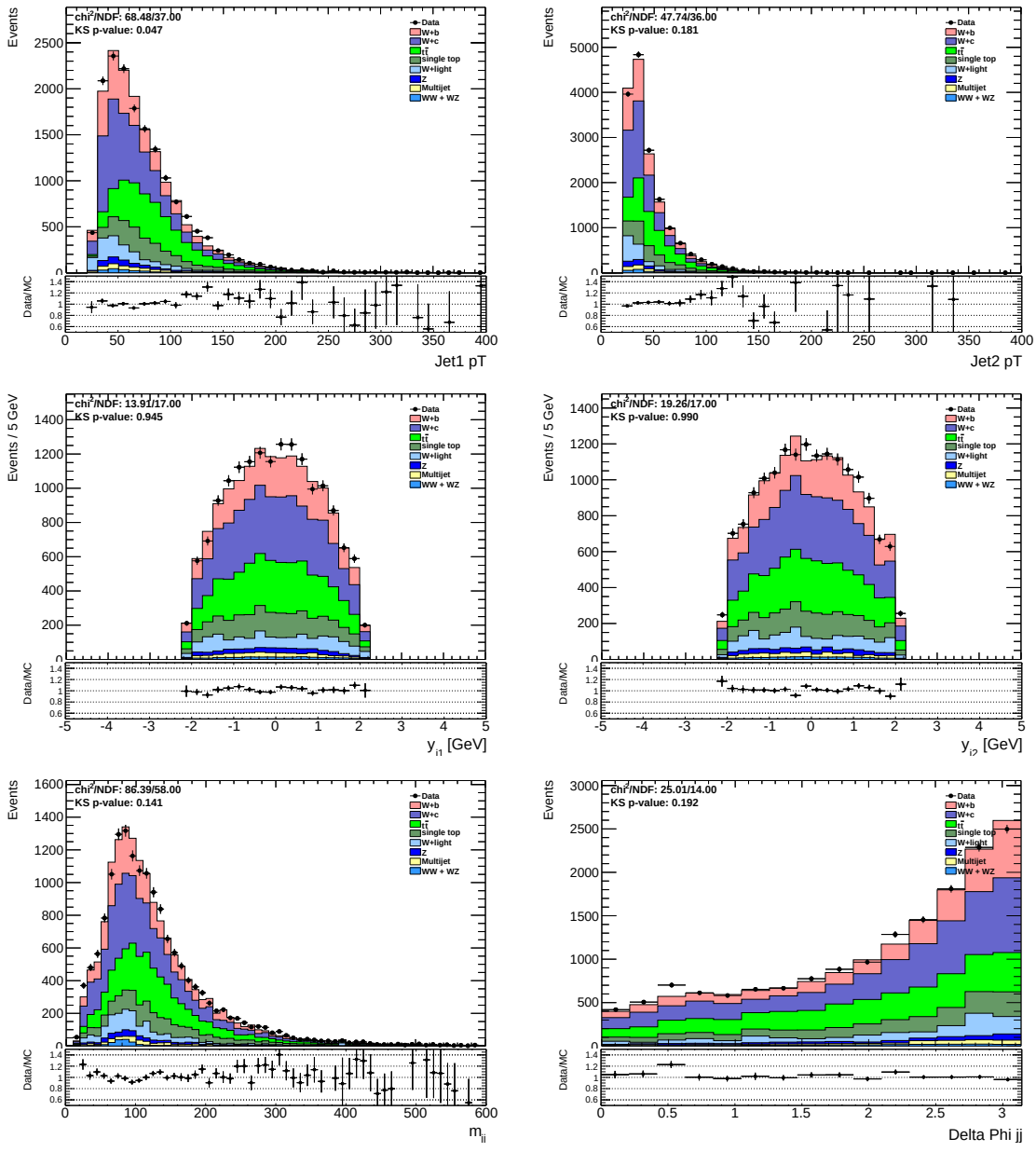

Figure 7.20: Additional plots in the 2-jet muon channel.

7.5 Backgrounds

Several processes contribute to the overall background for the W+b-jets signal, accounting for more than 85% of the selected sample. Some of the backgrounds, such as single-top, $t\bar{t}$ and multijet, are characterized by different kinematics from W+b-jets, but they have real b-jets in their final state and show similar b-tagging response. Others, W+c-jets and W+light-jets, have kinematic properties similar to the signal, but they can be statistically separated by studying the characteristics of b-tagged jets. The remaining backgrounds, diboson (WW and WZ) and Z+jets, contribute less than 5% of the selected sample.

The single-top, $t\bar{t}$ and multijet contributions are estimated either in background-enriched control regions or using kinematic distributions directly in the signal regions. These event selections used in the different background control regions are listed in Table 7.5.

Table 7.5: Event selection and distributions used to estimate the multijet, $t\bar{t}$ and single-top background normalizations and their uncertainties. The signal region (s.r.) selection is presented in the last row for comparison.

Process	N_{jets}	$N_{b-\text{tag}}$	$E_{\text{T}}^{\text{miss}}$ [GeV]	$m_T(W)$[GeV]	Distribution
Multijet	s.r.	s.r.	> 0	> 40	$E_{\text{T}}^{\text{miss}}$
$t\bar{t}$	> 4	s.r.	s.r.	s.r.	CombNN
Single-top	2	s.r.	s.r.	s.r.	$m(W, b)$
Cross-checks and systematics					
Multijet	s.r.	s.r.	> 0	> 40	$m_T(W)$
Multijet	s.r.	s.r.	> 0	> 40	p_{T}^{ℓ}
$t\bar{t}$	> 3	s.r.	s.r.	s.r.	CombNN
$t\bar{t}$	> 4	s.r.	s.r.	s.r.	N_{jets}
$t\bar{t}$	> 1	s.r.	s.r.	s.r.	N_{jets}
Single-top	2	s.r.	s.r.	s.r.	H_{T}
Signal region (s.r.)					
	1 or 2	1	> 25	> 60	

The W+b-jets, W+c-jets and W+light-jets contributions are then statistically separated, and the number of W+b-jets events is extracted, by fitting the CombNN weight distribution of b-tagged jets observed in data in each analysis region. Example CombNN templates for the muon 1-jet sample are shown in Figure 7.21. In this figure, W+b-jets template reaches very high values of the CombNN variable, while the W+c-jets and W+light-jets have a steeply falling distribution.

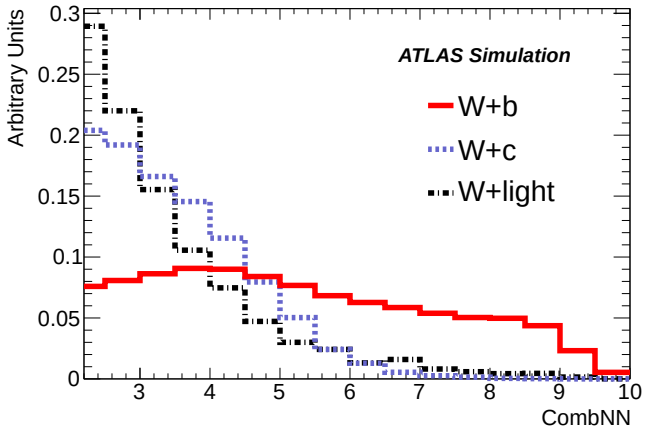

Figure 7.21: Overlay of the W+b-jets, W+c-jets and W+light-jets CombNN distributions in the muon 1-jet analysis region.

The following sections discuss the estimation of each background contribution. The number of events expected from Monte Carlo simulation for each process is summarized[7] in Table 7.6. In this table, the very tight identification and isolation requirements used to reduce the multijet contribution in electron events result in a lower efficiency for the electron channels with respect to the muon channels. Additionally, an interesting behavior can be observed in the Z+jets background when comparing

[7]Note that the W+b-jets, W+c-jets and W+light-jets in this table are not scaled by the results of the $E_{\mathrm{T}}^{\mathrm{miss}}$ fit discussed in section 7.5.1. Similarly, $t\bar{t}$ and single top are not scaled by the results of the fits in sections 7.5.2 and 7.5.3.

electron and muon channels. The difference in the predictions in these channels is due to the different properties of $Z \to ee$ and $Z \to \mu\mu$ events in which one lepton is not identified. Specifically, an un-identified second electron can be mistaken for an additional jet, while an un-identified second muon can give rise to missing energy.

Table 7.6: Expected number of events in each analysis region before any fit (except for the multijet background, for which the normalization is estimated according to section 7.5.1).

Process	μ 1-jet	e 1-jet	μ 2-jet	e 2-jet
W+b-jets	3173	2422	2632	1908
W+c-jets	12741	10290	4447	3642
W+light-jets	2301	1877	1017	737
$t\bar{t}$	1232	1105	4180	3638
Single top	1594	1334	2261	1795
Multijet [fit]	702	1252	313	683
Diboson	181	139	185	154
Z+jet	769	258	397	366

7.5.1 Multijet background

Multijet events from QCD production processes in which one of the jets is either misidentified as a lepton, or contains a real lepton originating from a heavy-quark decay, can enter the selected sample. Various selection criteria on the leptons are used to reduce this contamination, such as identification, isolation and impact parameter. Additionally, the event-level $E_{\mathrm{T}}^{\mathrm{miss}}$ and $m_T(W)$ requirements mentioned in Section 7.4 are also used to reduce the multijet background. To estimate the remaining multijet contribution, complementary data samples highly enriched in multijet events are created by requiring that some of these criteria are not fulfilled. The normalization of these samples is then obtained by fitting the $E_{\mathrm{T}}^{\mathrm{miss}}$ distribution in data.

Specifically, the multijet background shape is obtained in the muon channel by inverting the tracking isolation requirement. In the electron channel, the multijet shape is obtained by inverting some of identification requirements and waiving the calorimeter isolation requirement. The motivation and details for the selection used to form the multijet template from data are discussed in Section A.1.1. An additional section, A.1.2, is devoted to the development of a technique to estimate the shape uncertainty on the multijet template.

The normalization of the multijet template is assessed, in each analysis region, by performing a fit to the $E_{\mathrm{T}}^{\mathrm{miss}}$ distribution in data after relaxing the $m_T(W)$ requirement from 60 GeV to 40 GeV, and removing the $E_{\mathrm{T}}^{\mathrm{miss}} > 25$ GeV requirement. The templates used in this fit for the W/Z+jets, $t\bar{t}$, single-top and diboson processes are based on Monte Carlo simulation. The multijet and the W+jets template normalizations are free parameters of the fit, while those of the other components are fixed to their expected cross-sections. The $E_{\mathrm{T}}^{\mathrm{miss}}$ distributions, normalized to the results of the fit, are presented in Figure A.6 for the 1-jet and 2-jet regions in the muon and electron channels. The multijet background, in yellow, is visibly larger in the electron channel, and concentrated at low $E_{\mathrm{T}}^{\mathrm{miss}}$ values.

To estimate the uncertainty of the multijet background normalization, the $E_{\mathrm{T}}^{\mathrm{miss}}$ fit results are compared in each analysis region with the results obtained by fitting the $m_T(W)$ and lepton p_{T} distributions. The results of these fits are presented in Table A.2 of Section A.1.3. As a result of the comparison, an uncertainty of 50%, applied as a Gaussian constraint in subsequent ML fits, is assigned to the multijet background normalization in the 1-jet and 2-jet regions. In the 4-jet region used to

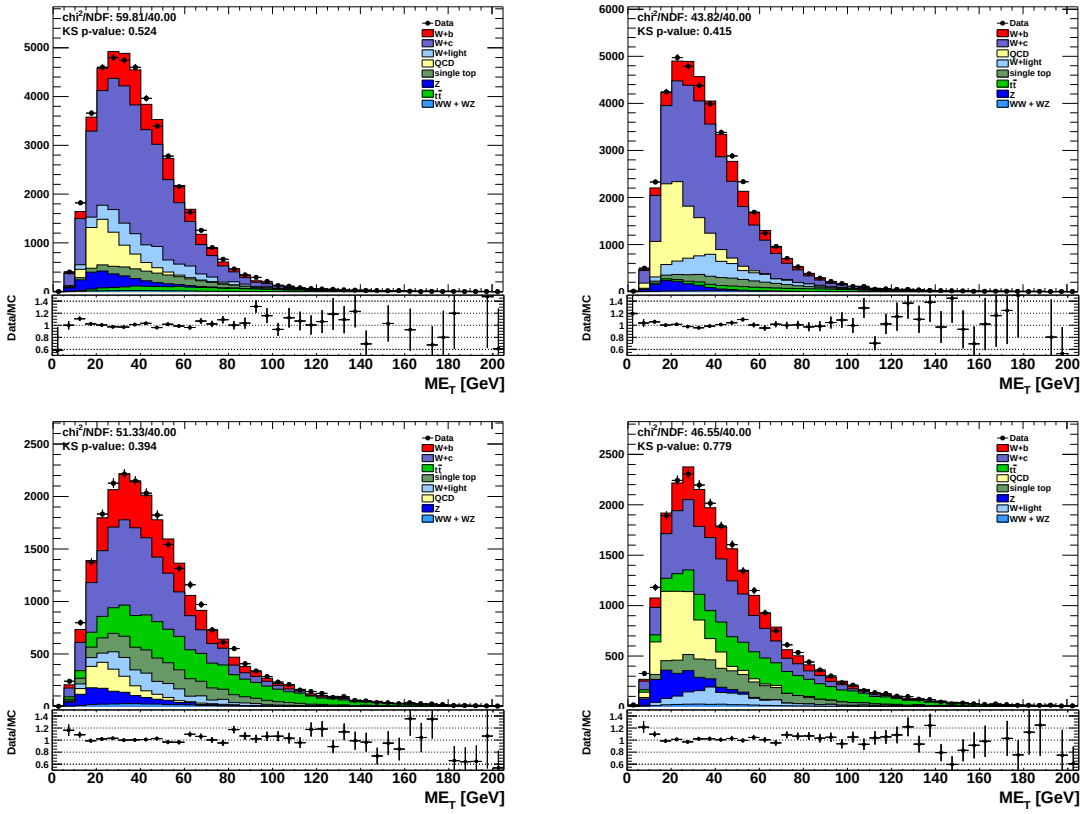

Figure 7.22: $E_{\mathrm{T}}^{\mathrm{miss}}$ distribution in data and MC simulation in the 1-jet (top) and 2-jet (bottom) analysis regions, in the muon (left) and electron (right) channels. MC samples are normalized to the results of the multijet background fit. To enhance the multijet contribution in the fitted region, the $m_T(W)$ selection is loosened from 60 GeV to 40 GeV.

estimate the $t\bar{t}$ background, this uncertainty is estimated from the different fit results to be 100%. In the differential measurement, the multijet background normalization is extrapolated from the inclusive estimates, and the same 50% uncertainty is applied as an independent Gaussian constraint in each $p_{\mathrm{T}}^{b-\mathrm{jet}}$ bin.

7.5.2 $t\bar{t}$ background

$t\bar{t}$ is an irreducible background for W+b-jets due to the presence of real W bosons and real b-jets in its decay products. In particular, the CombNN weight distributions for W+b-jets and $t\bar{t}$ events are very similar, so an accurate and reliable estimation of the $t\bar{t}$ contribution represents one of the most important ingredients of this analysis.

The $t\bar{t}$ background is estimated in a data control region constructed by selecting events with at least four jets, of which exactly one must be b-tagged[8]. In this control region, which is dominated by top events with only a small W+jets contribution, the $t\bar{t}$ normalization is estimated by fitting the CombNN distribution. The $t\bar{t}$ Monte Carlo simulation is then used to extrapolate the measured normalization into the 1-jet and 2-jet analysis regions. Due to the choice of control region, this extrapolation is only weakly dependent on the b-tagging scale factor uncertainties, while the jet energy scale and resolution uncertainties have a larger impact.

The $t\bar{t}$ template normalization is a free parameter of the CombNN fit in the $t\bar{t}$ control region, while all other templates are constrained by Gaussian terms in the likelihood. The sum of the W+b-jets, W+c-jets and W+light-jets MC templates is normalized to the NNLO W inclusive cross-section while their relative contributions are taken from the Alpgen Monte Carlo prediction. An uncertainty of 100% is applied independently to the W+b-jets, W+c-jets and W+light-jets normalizations. Similarly, the single-top template is assigned a 50% uncertainty that reflects the maximum uncertainty on the single-top normalization discussed in section 7.5.3. The multijet

[8] Requiring two b-tagged jets would significantly increase the $t\bar{t}$ sample purity, however it would also reduce the number of events in the control region and, more importantly, it would increase the impact of systematic uncertainties in the extrapolation of the $t\bar{t}$ content to the analysis regions. This tighter (2 b-tag) selection is used in section A.4.2 for validating the shapes of b-tagging variables.

background is estimated using the technique described in section 7.5.1 and assigned a normalization uncertainty of 100%, based on the fits to the different distributions ($E_{\mathrm{T}}^{\mathrm{miss}}$, $m_T(W)$, lepton p_{T}). The Z+jets contribution is assigned a 10% normalization uncertainty based on theoretical calculations and previous measurements [127, 128]. Finally, the diboson contribution is assigned a 10% normalization uncertainty that is twice the uncertainty of the corresponding NLO calculations [129, 130].

The $t\bar{t}$ normalization scale factors estimated by the fit, and applied to the $t\bar{t}$ Monte Carlo in the 1-jet and 2-jet analysis regions, are 1.09 ± 0.06 for the muon channel and 1.08 ± 0.07 for the electron channel. The corresponding fit projections in the CombNN variable are shown in Figure 7.23. Good agreement is found between the electron and the muon $t\bar{t}$ normalization scale factor, and an uncertainty of 10% is assigned in both channels. This uncertainty is applied through a Gaussian constraint to the $t\bar{t}$ template in subsequent ML fits. Additional cross-checks for the $t\bar{t}$ normalization estimate are described in Section A.2.

7.5.3 Single-top background

Single-top events containing a W boson and at least one b-jet are, like $t\bar{t}$ events, an irreducible background for the W+b-jets signal. However, it is difficult to define a high purity single-top control region such as for the $t\bar{t}$ background, since the majority of single-top events fall in the 1-jet and 2-jet analysis regions. Therefore, the single-top contribution is estimated directly in the 1-jet and 2-jet analysis regions by studying kinematic observables.

The kinematics of single-top events are expected to be characterized by more

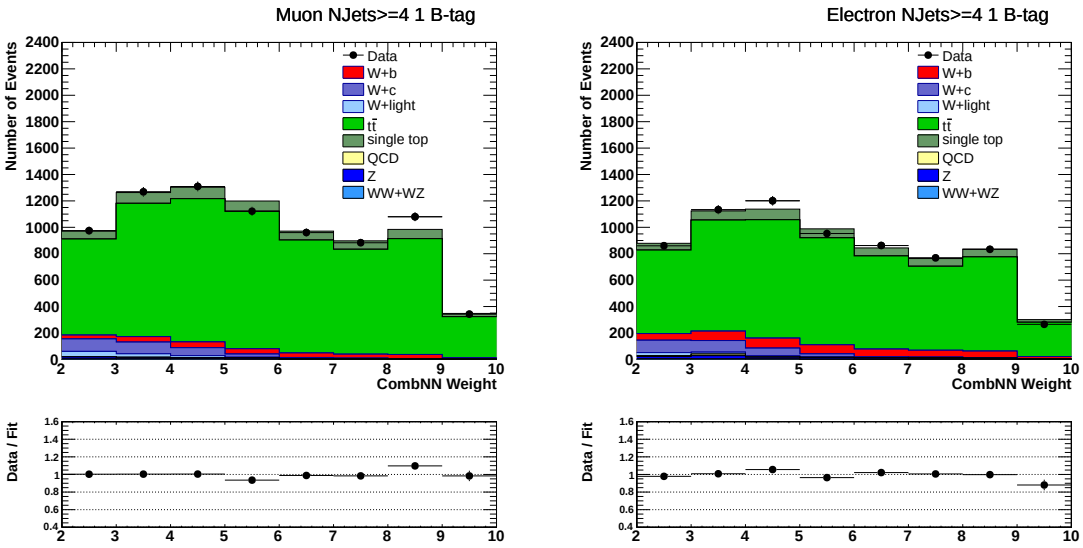

Figure 7.23: Fitted CombNN distribution in the at least 4 jets 1-b-tag control region for the muon (left) and electron (right) samples. MC samples are normalized to the results of the fit. The $t\bar{t}$ normalization scale factor obtained in the fit is used to estimate the $t\bar{t}$ contribution in the analysis regions (1-jet, 2-jet).

high p_{T}emissions than those of W+jets events. Hence a good candidate variable to disentangle single-top from the other processes is the $H_{\mathrm{T}} = p_{\mathrm{T}}^{\ell} + E_{\mathrm{T}}^{\mathrm{miss}} + \sum_{i=1}^{n} p_{\mathrm{T}}^{\mathrm{jet}_i}$. Another variable used is the invariant mass of the W boson and the b-tagged jet[9], $m(Wb)$. In this variable, the single-top contribution is expected to form a narrow peak centered at the top mass.

In the fits to the H_{T} and $m(Wb)$ distributions, the W+b-jets, W+c-jets and W+light-jets processes are found to have similar distributions in Monte Carlo, so they are merged to form a single W+jets template. For the single-top template, the t-channel, s-channel and Wt processes simulated with the AcerMC Monte Carlo

[9] The p_z of the neutrino is computed by imposing the W mass to be equal to the world average of 80.399 GeV [131]. In case of complex solutions, only the real part is considered. In case of two real solutions, the smaller p_z is used.

are combined, with their relative normalizations fixed to the Monte Carlo expectation. The W+jets and single-top template normalizations are free parameters of the fit, while Gaussian constraints are applied to the multijet, $t\bar{t}$, Z+jets, and diboson backgrounds as described above. The resulting templates are shown superimposed in Figure 7.24. The results of the fits to the H_{T} and $m(Wb)$ distributions are shown in Figures 7.25 and 7.26, and the single-top normalization scale factors obtained are summarized in Table 7.7. Detailed fit results can be found in section B.

Table 7.7: Single-top normalization scale factors estimated by fitting the H_{T} and the $m(Wb)$ distributions in the 1-jet and 2-jet analysis regions. The 2-jet scale factors based on the $m(Wb)$ distribution are applied in the 2-jet region. The 1-jet scale factors are not used, as described below. The AcerMC single-top Monte Carlo simulation is used for these estimates.

Observable	μ 1-jet	e 1-jet	μ 2-jet	e 2-jet
H_{T}	0.66 ± 0.17	0.77 ± 0.14	1.12 ± 0.11	1.17 ± 0.17
$m(Wb)$	1.02 ± 0.20	1.76 ± 0.25	1.09 ± 0.13	1.13 ± 0.15

In the 1-jet region, the single-top normalization scale factors resulting from the fits to the H_{T} distribution are not consistent with those resulting from the $m(Wb)$ distribution, as can be seen in Table 7.7. In addition, differences on the order of 30% are observed when comparing predictions obtained from the AcerMC and MC@NLO simulations, as discussed in Section A.3. Given these discrepancies, the AcerMC prediction is used, and a large uncertainty of 50% is applied to the single-top normalization in the 1-jet region. This uncertainty results in a larger uncertainty for the W+b-jets component in the CombNN fit, since the single-top and W+b-jets templates have similar CombNN shapes. Fortunately, the single-top contribution in the 1-jet region is smaller than in the 2-jet region, so the large uncertainty in the 1-jet region does not strongly impact the measurement.

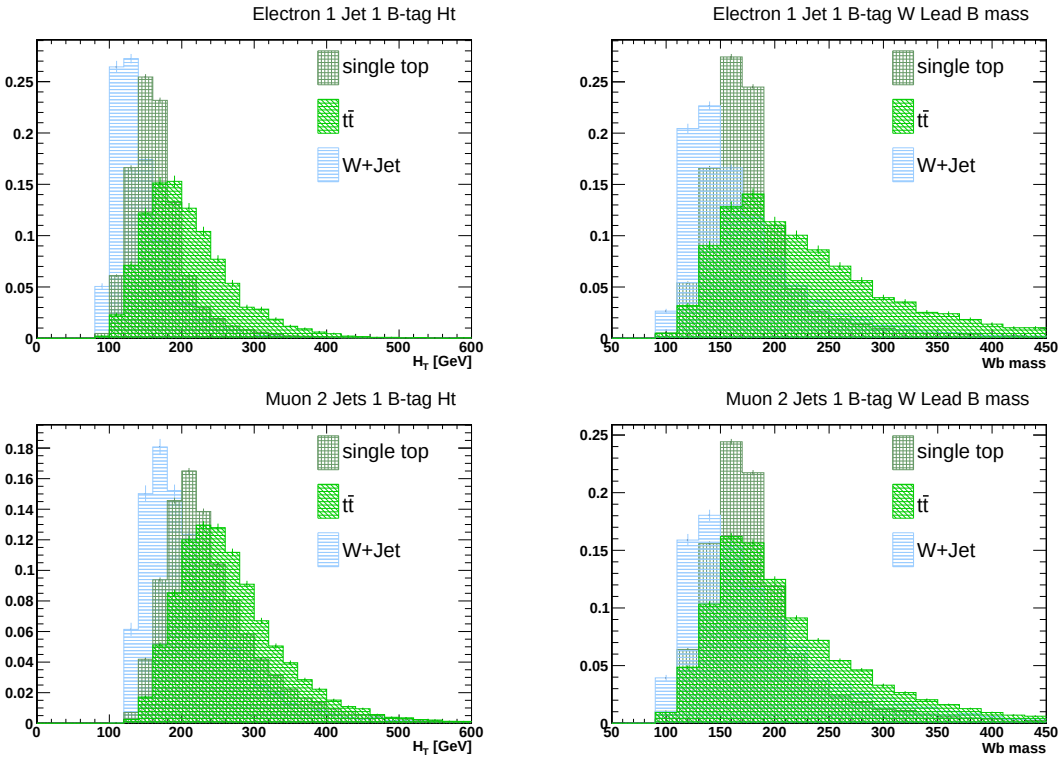

Figure 7.24: W+jets, single-top and $t\bar{t}$ H_T (left column) and $m(Wb)$ distributions (right column). Each Monte Carlo distribution is normalized to unit area in the 1-jet (upper row) and 2-jet (lower row) analysis regions.

In the 2-jet region, the single-top normalization scale factors estimated using the H_{T} and the $m(Wb)$ distributions are in very good agreement with each other. Moreover, AcerMC and MC@NLO provide consistent expectations. Given this consistent picture, the scale factor measured in the $m(Wb)$ fit is applied to the AcerMC prediction, and an uncertainty of 20% is assigned to the single-top normalization in the 2-jet region. It is this smaller uncertainty which makes it possible to have a comparable precision for the W+b-jets measurement in the 1-jet and 2-jet regions, despite the different background compositions.

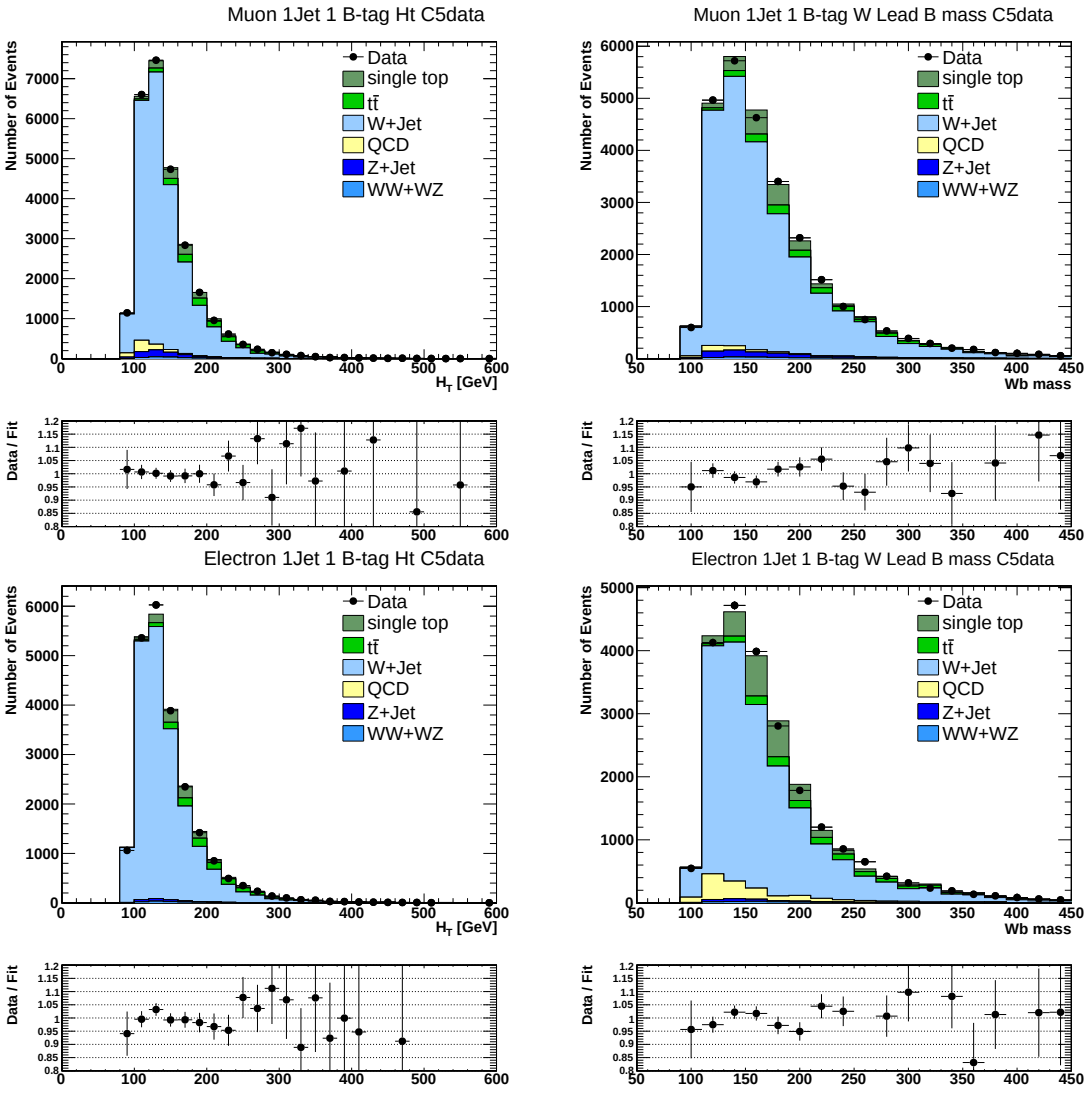

Figure 7.25: Fitted H_T (left) and $m(Wb)$ distributions in the muon (top) and electron (bottom) channels for the 1-jet analysis region. MC samples are normalized to the results of the fit. The single-top normalization scale factors obtained in the fit are included in Table 7.7, but they are not used in the analysis.

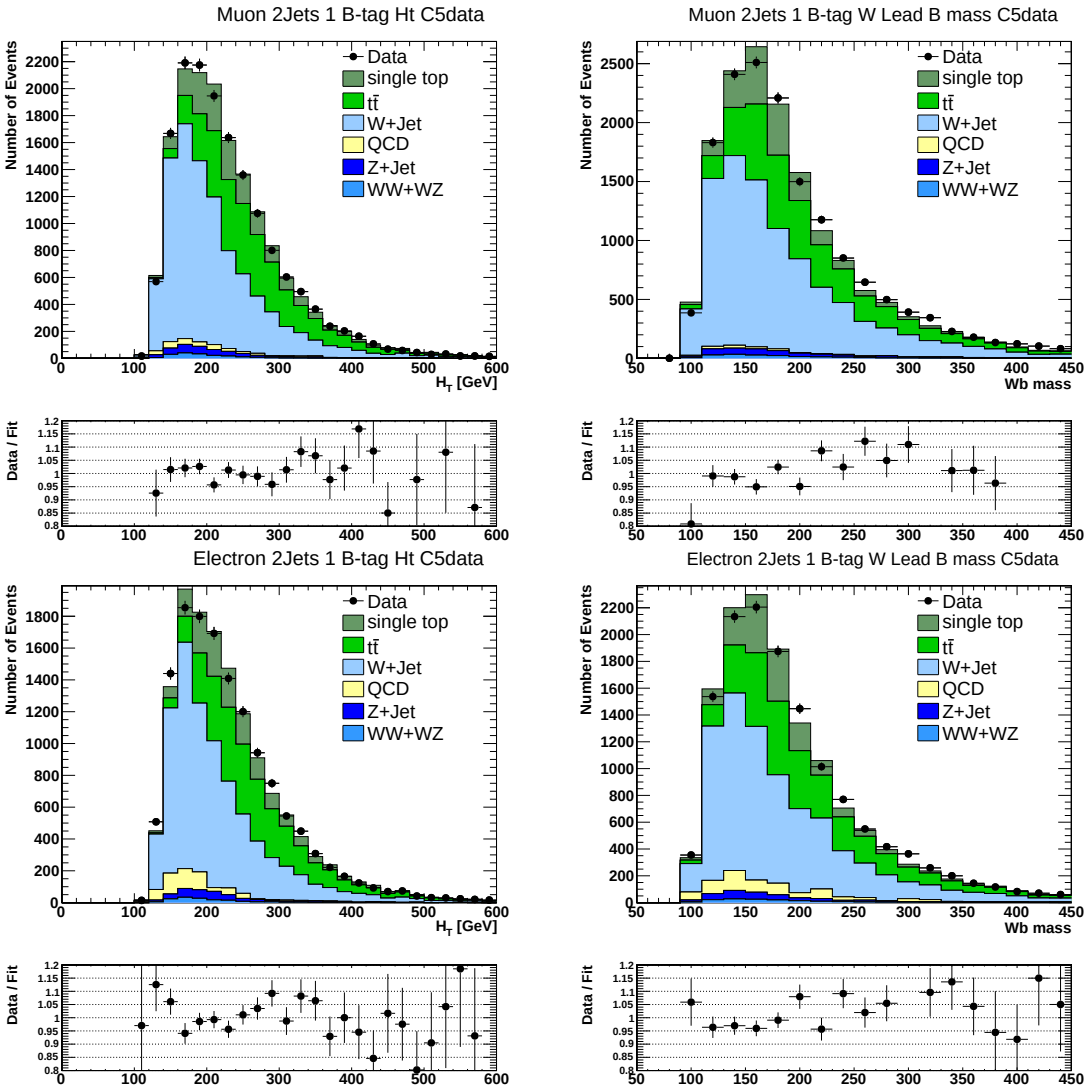

Figure 7.26: Fitted H_T (left) and $m(Wb)$ distributions in the muon (top) and electron (bottom) channels for the 2-jet analysis region. MC samples are normalized to the results of the fit. The single-top normalization scale factors obtained in the fit are included in Table 7.7, and they are used to estimate the single-top contribution in the 2-jet region.

7.5.4 W+c-jets and W+light-jets backgrounds

The W+b-jets signal is separated statistically from the W+c-jets and W+light-jets backgrounds in each analysis region, and in each bin of the differential measurement, with a fit to the b-tagging weight (CombNN) distribution. The W+b-jets, W+c-jets and W+light-jets normalizations are free parameters of the fit, while Gaussian constraints are applied to all other processes. In addition to the Gaussian constraints discussed above for the multijet, $t\bar{t}$ and single-top background normalizations, 10% uncertainties are assigned to the diboson and Z+jets backgrounds.

The CombNN template shapes for the multijet component are extracted from data, while those from the other non-W processes are extracted from their respective MC samples. For W+b-jets, W+c-jets and W+light-jets, the corresponding templates are prepared in each analysis region using large Pythia-generated samples.

The Pythia-generated samples are used because of their large statistics, and because it was found that the Alpgen/Herwig samples were not correctly modeling B-hadron decays. This procedure was validated in $t\bar{t}$ events, and–with lower statistics–in W+jets events. The details of the comparison between Herwig and Pythia, as well as the recipe used to reweight the Pythia samples to the Alpgen/Herwig W+jets ones, are discussed in Section A.4.

The results of the CombNN fits, including the estimate of the number of W+b-jets events observed in the full 2011 data sample, are presented in Section 7.6.

7.6 Fit results

The CombNN distribution is fitted to determine the number of W+b-jets events, and the fit is performed independently in each channel of the 1-jet and 2-jet measurements and in each bin of the differential measurements. The W+b-jets, W+c-jets and W+light-jets components are free to float in the fit, while Gaussian terms are applied to the likelihood to constrain the other backgrounds. For a given background, the mean of the corresponding Gaussian constraint is fixed to the expected number of events, while the width is fixed to the associated uncertainty. As such, background normalization uncertainties are accounted for in the uncertainty on the number of W+b-jets events estimated by the fit.

The first of the following two sections (7.6.1) describes the fit result in the inclusive (1-jet, 2-jet, electron, muon) regions, and divided in bins of $p_{\mathrm{T}}^{b-\mathrm{jet}}$. In the second section (7.6.2), the CombNN fit is repeated, but the W+b-jets and single-top templates are merged to form a single template, and the number of "W+b-jets + single-top" events is estimated.

7.6.1 W+b-jets

The CombNN distributions normalized to the fit results are shown in Figure 7.27, and the number of W+b-jets and background events estimated by the fits, along with their statistical uncertainties, are summarized in Table 7.8. Table 7.9 shows the scale factors estimated by the fit to the data compared to the prediction for each process.

The first three rows of the table refer to the unconstrained components (W+b-jets, W+c-jets, W+light-jets), while the last 5 components are constrained to MC

(diboson, Z+jets, single-top 1-jet) or previous fits ($t\bar{t}$, single-top 2-jet). When looking at Table 7.9, the fitted scale factors for the constrained components are expected to be close to one, and their uncertainty is not expected to be larger than the width of the Gaussian constraint. These expectations are generally satisfied, except for the multijet background which occasionally moves by more than 1 σ (e 2-jet).

While the electron and the muon sample backgrounds are treated as completely uncorrelated, the estimated background levels are found to be in good agreement across the channels. Exception are found in the multijet component, which is not expected to be the correlated for electrons and muons, and in the W+light-jets component. The behavior of the W+light-jets is understood based on its strong (90%) correlation with the dominant background, the W+c-jets. As a result of this correlation, the W+light-jets component can be impacted significantly by small relative changes of the W+c-jets background. This behavior, however, does not impact the W+b-jets estimate, since the W+light-jets and W+b-jets estimators have only a 15% correlation. As an additional test, the W+light-jets normalization was fixed to the expected cross-section, and the W+b-jets yield was found to be consistent with the nominal fit.

The differential measurement is made by dividing each analysis region in four samples based to the b-tagged jet p_{T}: 25–30 GeV, 30–40 GeV, 40–60 GeV and 60–140 GeV. The resulting fit projections are shown in Figure 7.28 and Figure 7.29 for the 1-jet and the 2-jet regions, respectively. In addition, Tables B.6-B.21 in Section B summarize the fit results in the muon and electron samples, in each jet and p_{T} bin, and Tables B.22-B.25 summarize the systematic and total uncertainties on the W+b-jets

Table 7.8: Fitted event yields for the eight contributions to the four analysis regions, including the statistical uncertainty from the binned maximum likelihood fit to the CombNN distribution.

Process	μ 1-jet	e 1-jet	μ 2-jet	e 2-jet
W+b-jets	5300 ± 400	4800 ± 400	3000 ± 260	2220 ± 250
W+c-jets	15600 ± 600	13300 ± 500	4600 ± 400	4000 ± 400
W+light-jets	1600 ± 500	500 ± 500	1170 ± 330	490 ± 320
$t\bar{t}$	1230 ± 120	1100 ± 110	4300 ± 400	3690 ± 350
Single-top	1700 ± 500	1400 ± 500	2300 ± 400	1810 ± 350
Diboson	181 ± 18	139 ± 14	185 ± 18	155 ± 15
Z+jets	770 ± 70	258 ± 26	397 ± 40	365 ± 37
Multijet	780 ± 330	1000 ± 500	210 ± 150	1220 ± 290

Table 7.9: Normalization scale factors estimated by the fit to the CombNN distribution for each process in the four analysis regions, including the statistical uncertainty. The multijet, $t\bar{t}$ and 2-jet single-top factors are given with respect to their previous data-driven estimates (7.5.1, 7.5.2 and 7.5.3). The remaining factors are given with respect to the Monte Carlo expectations normalized to the NLO (single-top 1-jet, diboson) and inclusive NNLO (W/Z+jets) cross-sections.

Process	μ 1-jet	e 1-jet	μ 2-jet	e 2-jet
W+b-jets	1.68 ± 0.14	1.98 ± 0.16	1.14 ± 0.10	1.16 ± 0.13
W+c-jets	1.22 ± 0.04	1.30 ± 0.05	1.04 ± 0.09	1.10 ± 0.10
W+light-jets	0.70 ± 0.22	0.28 ± 0.25	1.15 ± 0.33	0.67 ± 0.44
$t\bar{t}$	1.00 ± 0.10	1.00 ± 0.10	1.02 ± 0.10	1.01 ± 0.10
Single-top	1.07 ± 0.34	1.02 ± 0.36	1.08 ± 0.19	1.01 ± 0.19
Diboson	1.00 ± 0.10	1.00 ± 0.10	1.00 ± 0.10	1.00 ± 0.10
Z+jets	1.00 ± 0.10	1.00 ± 0.10	1.00 ± 0.10	1.00 ± 0.10
Multijet	1.12 ± 0.47	0.80 ± 0.40	0.67 ± 0.49	1.79 ± 0.42

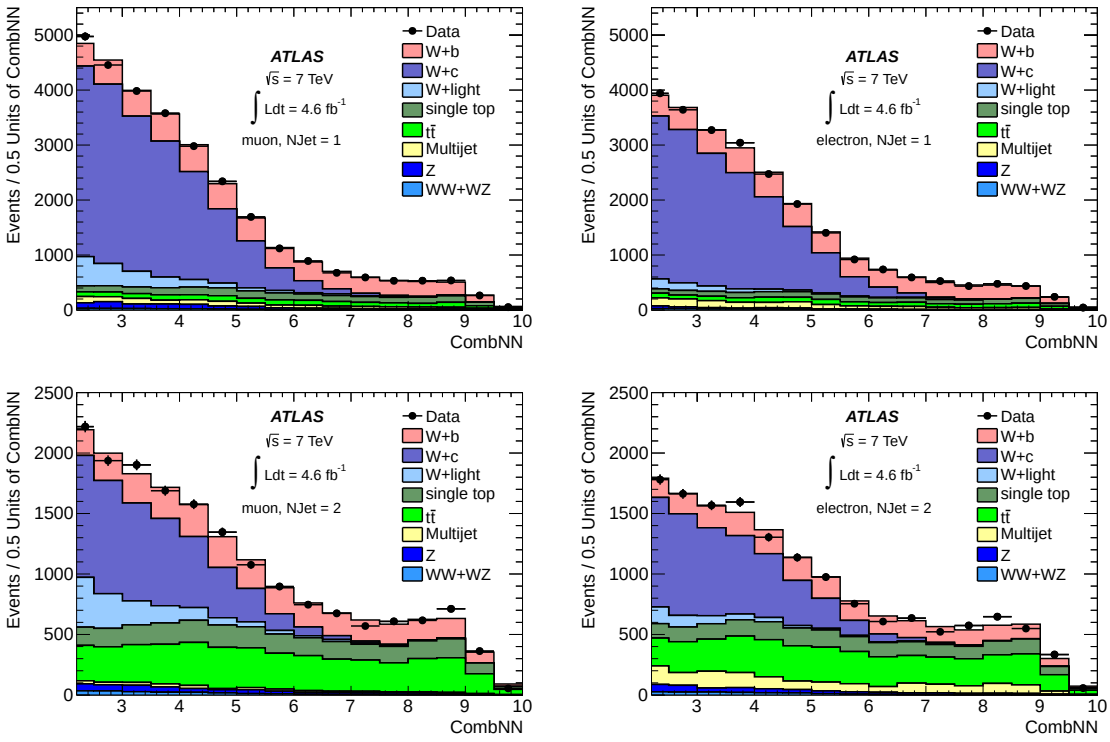

Figure 7.27: CombNN distribution for the b-tagged jet in data and MC simulation, where the MC samples are normalized to the results of the maximum likelihood fit, for the 1-jet (top) and 2-jet (bottom) analysis regions, in the muon (left) and electron (right) channels.

estimate in each $p_{\mathrm{T}}^{b-\mathrm{jet}}$ bin.

Finally, in Figure 7.30, the measured detector level differential distributions are compared to the ALPGEN reconstruction-level predictions. For comparisons with the MCFM particle-level predictions (including NLO terms and the contributions from the 5 flavor number scheme), the fitted number of $W+b$-jets events must be unfolded to a fiducial cross-section, as discussed in Section 7.7.

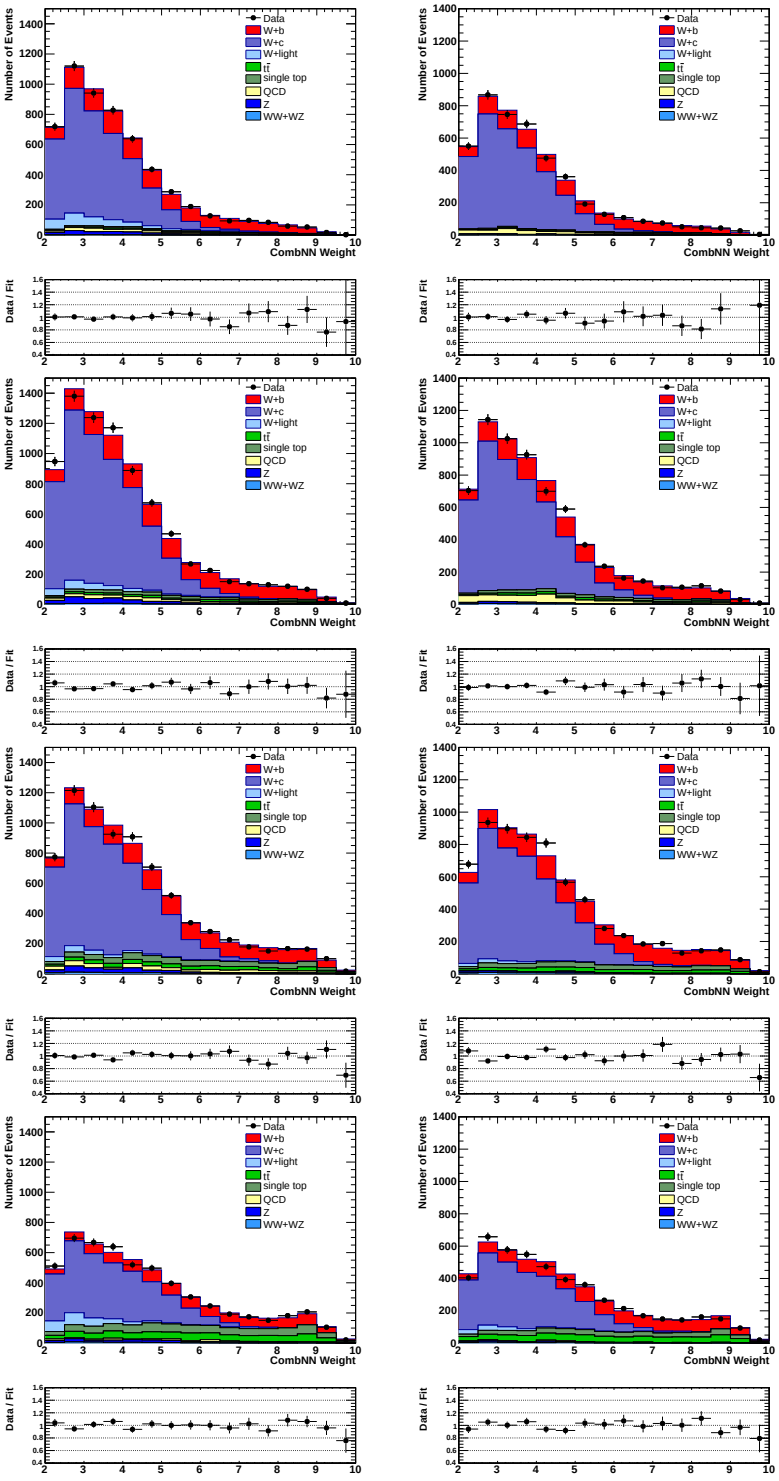

Figure 7.28: CombNN weight distribution of the b-tagged jet for the 1-jet region, in the muons (left) and electrons (right) channels. Each row represents a different p_{T} bin: 25-30, 30-40, 40-60, 60-140 GeV. Each process is normalized according to the corresponding fit result.

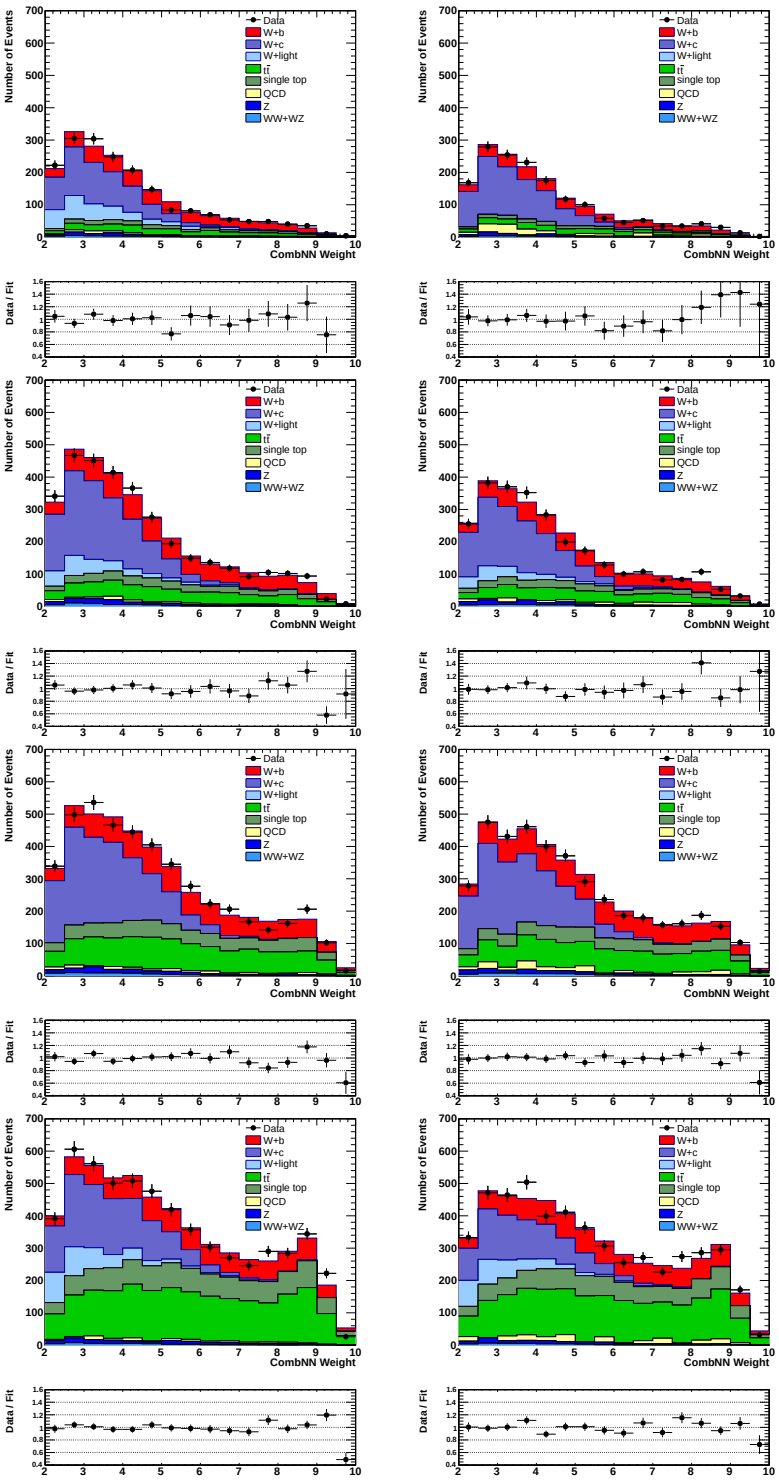

Figure 7.29: CombNN weight distribution of the b-tagged jet for the 2-jet region, in the muons (left) and electrons (right) channels. Each row represents a different p_{T} bin: 25-30, 30-40, 40-60, 60-140 GeV. Each process is normalized according to the corresponding fit result.

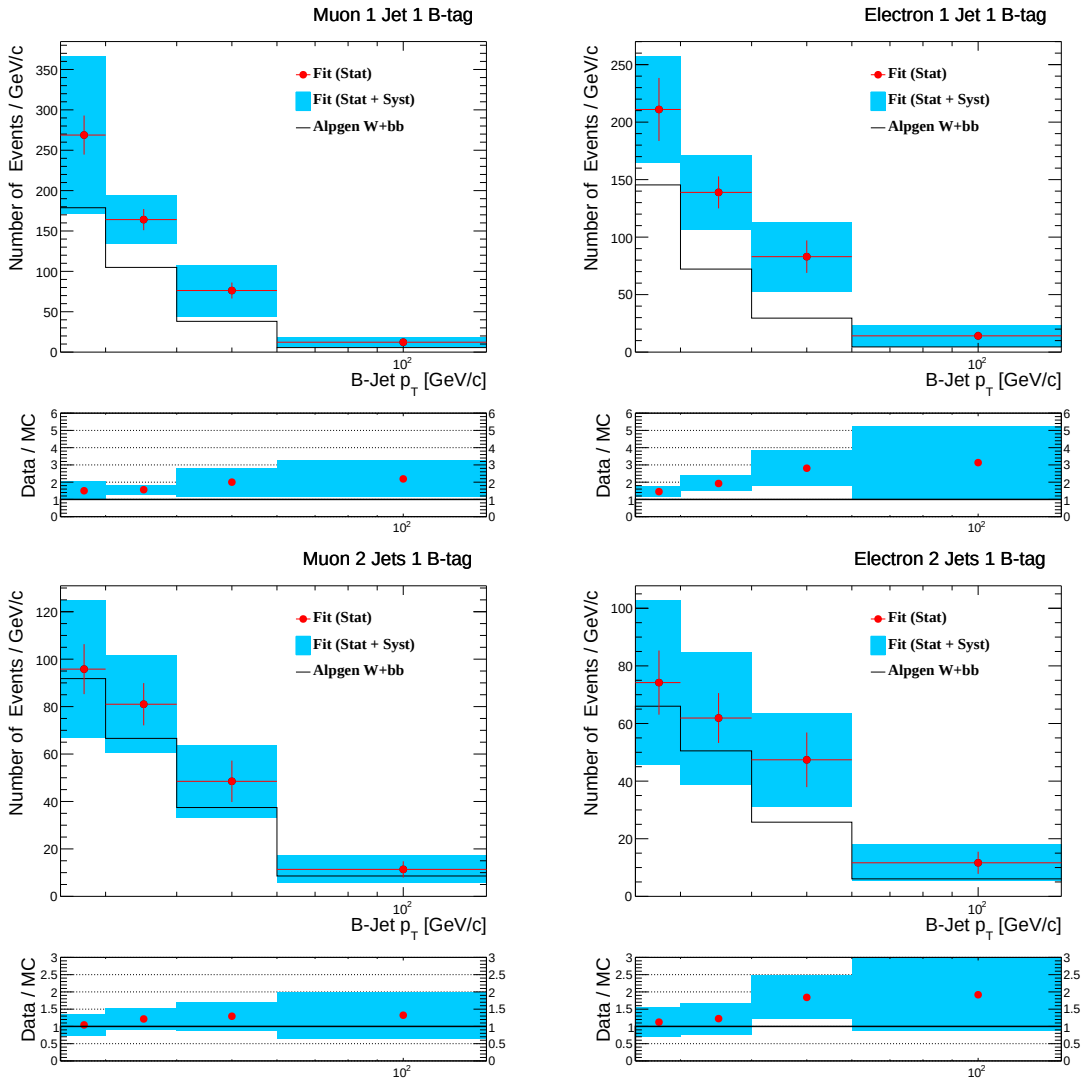

Figure 7.30: Summary of the fitted W+b-jet yields, including statistical and systematic uncertainties, in all p_{T} bins in the 1-jet (top) and 2-jet (bottom) analysis regions, in the muons (left) and electrons (right) channels. Systematic uncertainties are symmetrized by taking the largest contribution in absolute value. The ALPGEN detector-level predictions are shown in black for comparison. They are not necessarily expected to agree with the estimated number of $W+b$-jets events, since ALPGEN is only leading-order and does not include the 5 flavor number scheme contribution.

7.6.2 W+b-jets plus single-top

The W+b-jets yield is also measured including the contribution of the single-top process. For each analysis region and $p_{\mathrm{T}}^{b-\mathrm{jet}}$ bin, the same maximum likelihood fit as the W+b-jets measurement is used, as well as the same estimates and constraints for the multijet, $t\bar{t}$, Z+jets and diboson backgrounds. In the fit to the CombNN distribution, the W+b-jets and single-top templates are merged accounting for their respective predicted cross-sections, and they form a single template whose normalization is estimated. As a consequence of the single-top process being considered as part of the signal, the single-top normalization uncertainty is removed, thereby increasing the statistical precision of the fit.

In Figure 7.31 the fit projections are shown for the inclusive fits, while Figures 7.32 and 7.33 include the differential fits. The number of "W+b-jets plus single-top" and the number of background events estimated by the inclusive fits, along with their statistical uncertainties, are summarized in Table 7.10. Table 7.11 shows the scale factors estimated by the fit compared to the prediction for each process. Tables B.26 to B.29 in Section B include the detailed fit results.

As in the W+b-jets fits of the previous section (7.6), the backgrounds are uncorrelated in each analysis region. The background estimates in Tables 7.10 and 7.11 are in good agreement with those of the previous section, indicating that merging the W+b-jets and single-top templates does not affect the overall fit. The uncertainties of the measured component, W+b-jets plus single-top, are much smaller that the uncertainties found in the previous section when measuring the W+b-jets and single-top templates separately.

When looking at the first row of Table 7.11, and comparing it with the corresponding row of Table 7.9, it is important to keep in mind that an initial normalization scale factor of $\sim$ 15% was applied to the single-top background in the 2-jet region in Table 7.9. This scale factor is not applied in the current section, as the initial single-top normalization is taken directly from Monte Carlo simulation. Therefore it is not surprising to see that, when comparing the two tables, the numbers in the first column are smaller for the first two rows (1-jet region) and larger for the last two rows (2-jet region).

Overall, these fits point to a normalization scale factor for "W+b-jets +single-top" of $\sim$ 60% in the 1-jet region and $\sim$ 25% in the 2-jet region, as opposed to the W+b-jets scale factors of $\sim$ 80% in the 1-jet region and $\sim$ 15% in the 2-jet region measured in the previous section

Table 7.10: Fitted event yields for the seven contributions to the four analysis regions, including the statistical uncertainty from the binned maximum likelihood fit to the CombNN distribution. The W+b-jets and single-top templates are merged and treated as a single component.

Process	μ 1-jet	e 1-jet	μ 2-jet	e 2-jet
W+b-jets + single-top	5300 ± 130	6030 ± 170	5370 ± 170	4050 ± 160
W+c-jets	15700 ± 500	13500 ± 500	4600 ± 400	4000 ± 400
W+light-jets	1600 ± 500	500 ± 500	1190 ± 340	510 ± 310
$t\bar{t}$	1230 ± 120	1100 ± 110	4200 ± 400	3700 ± 400
Diboson	181 ± 18	139 ± 14	185 ± 19	155 ± 15
Z+jets	770 ± 70	257 ± 26	397 ± 40	365 ± 37
Multijet	790 ± 320	1000 ± 500	200 ± 150	1220 ± 290

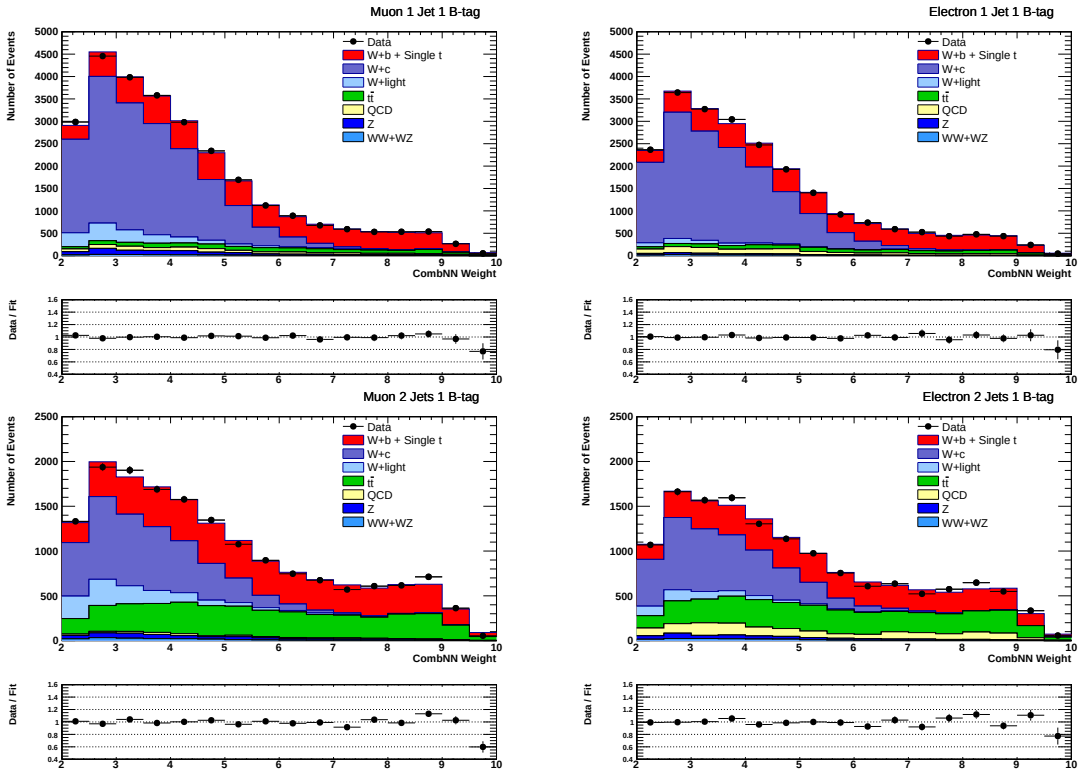

Figure 7.31: CombNN weight distribution of the b-tagged jet for the 1-jet (top) and 2-jet (bottom) analysis regions, in the muons (left) and electrons (right) channels. Each process is normalized according to the fit results. The W+b-jets and single-top templates are merged to form a single template (red).

Table 7.11: Normalization scale factors estimated by the fit to the CombNN distribution for each process in the four analysis regions, including the statistical uncertainty. The multijet and $t\bar{t}$ are given with respect to their previous data-driven estimates (7.5.1, 7.5.2). The remaining factors are given with respect to the Monte Carlo expectations normalized to the NLO (single-top, diboson) and inclusive NNLO (W/Z+jets) cross-sections. The W+b-jets and single-top templates are merged and treated as a single component.

Process	μ 1-jet	e 1-jet	μ 2-jet	e 2-jet
W+b-jets + single-top	1.57 ± 0.03	1.74 ± 0.05	1.25 ± 0.04	1.25 ± 0.05
W+c-jets	1.23 ± 0.04	1.31 ± 0.05	1.03 ± 0.09	1.10 ± 0.10
W+light-jets	0.69 ± 0.22	0.24 ± 0.24	1.17 ± 0.33	0.69 ± 0.42
$t\bar{t}$	1.00 ± 0.10	0.99 ± 0.10	1.00 ± 0.10	1.01 ± 0.10
Diboson	1.00 ± 0.10	1.00 ± 0.10	1.00 ± 0.10	1.00 ± 0.10
Z+jets	1.00 ± 0.10	1.00 ± 0.10	1.00 ± 0.10	1.00 ± 0.10
Multijet	1.12 ± 0.45	0.85 ± 0.37	0.64 ± 0.48	1.78 ± 0.42

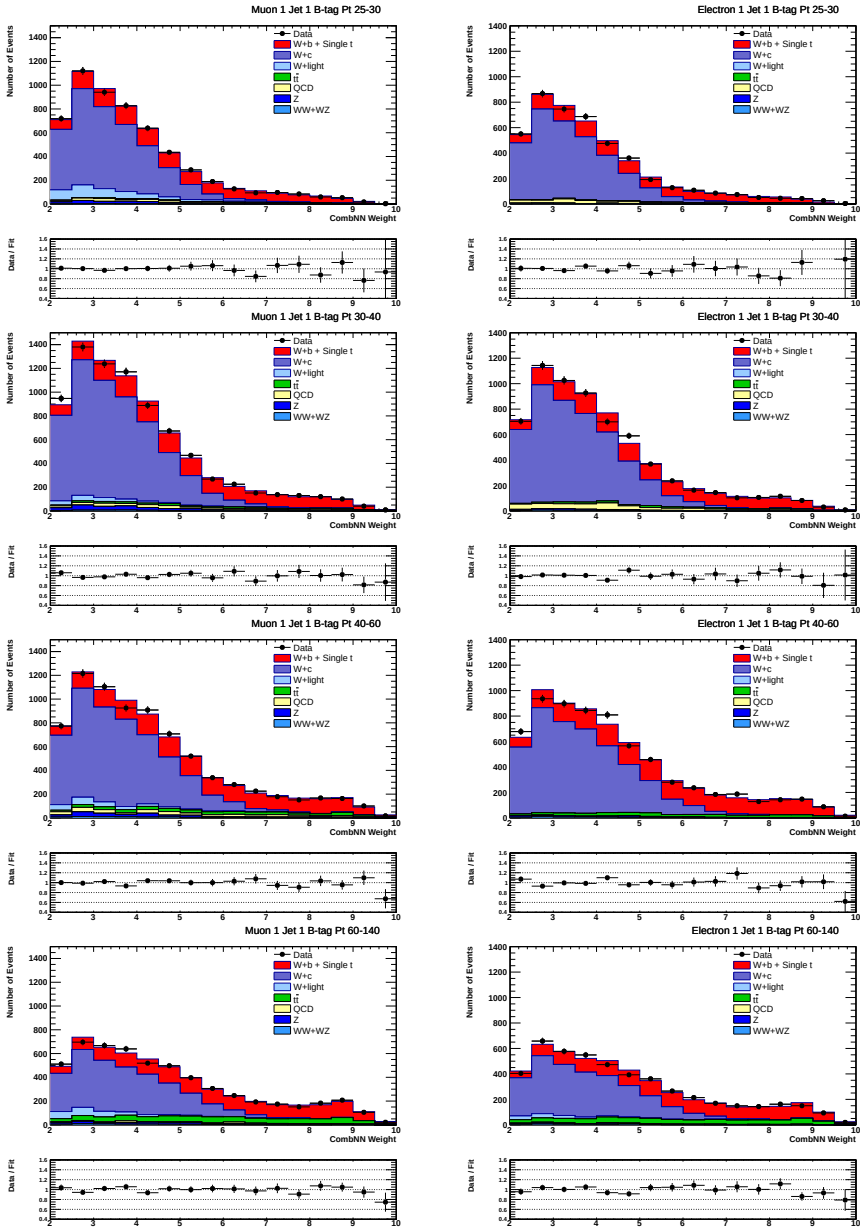

Figure 7.32: CombNN weight distribution of the b-tagged jet for the 1-jet region, in the muons (left) and electrons (right) channels. Each row represents a different p_{T} bin: 25-30, 30-40, 40-60, 60-140 GeV. Each process is normalized according to the corresponding fit result. The W+b-jets and single-top templates are merged to form a single template (red).

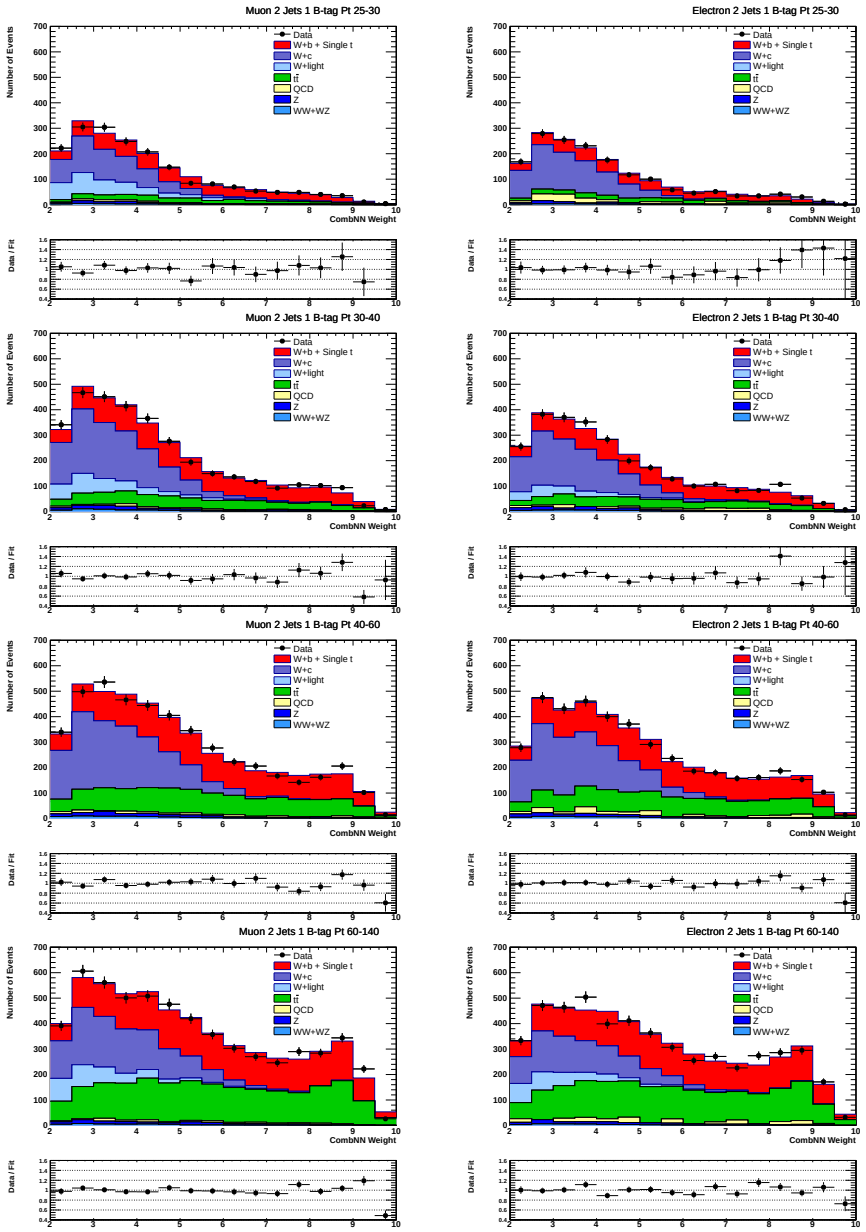

Figure 7.33: CombNN weight distribution of the b-tagged jet for the 2-jet region, in the muons (left) and electrons (right) channels. Each row represents a different p_{T} bin: 25-30, 30-40, 40-60, 60-140 GeV. Each process is normalized according to the corresponding fit result. The $W+b$-jets and single-top templates are merged to form a single template (red).

7.7 Extraction of the fiducial cross-section

The $W+b$-jets event yields obtained from the CombNN fits are converted, using Monte Carlo simulation, to a cross-section for $W+b$-jets times the branching ratio for each $W \to \ell\nu$ decay channel ($\ell = e, \mu$). The $W+b$-jets final state is produced with energy and angular distributions which span all the available phase space, while the detector has a limited *acceptance*: it can only measure particles that fall into the instrumented regions, within a limited range of energies. Moreover, due to the limited *efficiency* for triggering and reconstruction, not all the $W+b$-jets events that can be observed by the detector are in fact observed.

Monte Carlo simulation can be used to account for both acceptance and efficiency effects, as well as for through a procedure called *unfolding*. With respect to efficiency, the MC simulation is validated and corrected using systematically modified data samples for each of the reconstructed objects (leptons, jets, b-tagged jets). With respect to the geometrical acceptance, however, validating the MC simulation would require a knowledge of the $W+b$-jets kinematics in regions not covered by the detector. For this reason, instead of correcting for the acceptance effects with respect to the full phase space of possible $W+b$-jets events, the acceptance is only calculated with respect to a *fiducial region* of phase space.

The fiducial region is designed to be as similar as possible to the phase space of $W+b$-jets events observed in the detector. As opposed to the detector-level selection, the fiducial region is defined in terms of final state particles (particles with a proper lifetime longer than 10 ps, such as electrons, muons, hadrons). This allows for theoretical calculations to provide results which can be compared directly to the

measured cross-section, without needing to simulate the ATLAS detector.

In W+b-jets differential measurement as a function of b-jet p_{T}, the unfolding procedure is used to convert the event yields of each individual p_{T} bin into a corresponding cross-section. In addition, the unfolding procedure combines the knowledge of the Monte Carlo response with information from all available bins, in order to correct for migrations of reconstructed events between neighboring b-jet p_{T} bins.

The following sections describe the fiducial region chosen for the measurement (7.7.1), and the unfolding procedure used to convert the observed W+b-jets yield into a fiducial cross-section for W+b-jets (7.7.2).

7.7.1 Fiducial region definition

The W+b-jets cross-section is measured in a restricted fiducial region defined at the *particle level*, meaning that it is defined in terms of final state particles (with a proper lifetime longer than 10 ps). To enter the fiducial region, events are required to contain an electron or muon and a neutrino originating from a W boson decay, and one or two hadron-level jets. Hadron-level jets are built by clustering final state particles, including leptons from decaying hadrons, but not including leptons from W boson decays. At least one of the jets is required to be a b-jet, defined by the presence of a weakly decaying B-hadron with $p_{\mathrm{T}} > 5$ GeV and within $\Delta R = 0.3$ of the jet axis. Details of the fiducial selection are given in Table 7.12.

It is apparent from Table 7.12 that the fiducial selection is very similar to the reconstructed-level selection. One notable exception is the b-jet multiplicity. Given the fiducial region definition and the reconstruction-level selection, the measurement

Table 7.12: Definition of the phase space for the fiducial region. The W transverse mass is defined as $m_{\mathrm{T}}(W) = \sqrt{2p_{\mathrm{T}}^{\ell}p_{\mathrm{T}}^{\nu}(1-\cos(\phi^{\ell}-\phi^{\nu}))}$.

Requirement	1+2 jet region	1 jet region	2 jet region
Lepton transverse momentum	$p_{\mathrm{T}}^{\ell} > 25$ GeV	-	-
Lepton pseudorapidity	$\lvert\eta^{\ell}\rvert < 2.5$	-	-
Neutrino transverse momentum	$p_{\mathrm{T}}^{\nu} > 25$ GeV	-	-
W transverse mass	$m_{\mathrm{T}}(W) > 60$ GeV	-	-
Jet transverse momentum	$p_{\mathrm{T}}^{j} > 25$ GeV	-	-
Jet rapidity	$\lvert y^{j}\rvert < 2.1$	-	-
Jet multiplicity	$n \leq 2$	$n = 1$	$n = 2$
b-jet multiplicity	$n_b \leq 2$	$n_b = 1$	$n_b \leq 2$
Jet-lepton separation	$\Delta R(\ell, \mathrm{jet}) > 0.5$	-	-

is performed using reconstructed events containing a single b-tagged jet, but it is unfolded to a fiducial region with one or more b-jets. The unfolding process therefore requires an extrapolation to account for W+b-jets events with a second b-jet which satisfies the fiducial selection. Such $W + b\bar{b}$ events are expected to represent 10% of the 2-jet fiducial region[10].

The fiducial region is divided, according to the number of particle-level jets, in the 1-jet and 2-jet fiducial regions. For the differential measurement as a function of $p_{\mathrm{T}}^{b-\mathrm{jet}}$, the W+b-jets cross-section is estimated separately in four bins of b-jet p_{T}[11]: 25–30 GeV, 30–40 GeV, 40–60 GeV and 60–140 GeV. This binning choice is found to maintain similar statistics in each bin, and the specific bin boundaries are chosen based on those of the b-tagging scale factors, to minimize their effect in shaping the p_{T} distribution. The p_{T} region above 140 GeV is completely dominated by $t\bar{t}$ and

[10]More than half of these $W + b\bar{b}$ events are expected to have exactly one b-tagged jet (due to the $\sim 50\%$ b-tagging working point), and they are included at the reconstruction level. The extrapolation therefore has to account for the $\sim 25\%$ of $W + b\bar{b}$ events with 0 b-tagged jets and the $\sim 25\%$ of $W + b\bar{b}$ events with 2 b-tagged jets. This is quite similar to the extrapolation needed for $W + b + j$ events, which has to account for the $\sim 50\%$ of $W + b + j$ events with 0 b-tagged jets.

[11]In $W + b\bar{b}$ events, the p_{T} of the leading b-jet is used.

single-top, with a very minor W+b-jets contribution. For this reason the differential measurement does not extend to b-jets with $p_{\mathrm{T}} > 140$ GeV.

7.7.2 Unfolding Procedure

The unfolding procedure is defined with respect to the fiducial region introduced in Table 7.12. It accounts for trigger and object reconstruction efficiencies (including the b-jet identification efficiency) and includes corrections for all known detector effects, including dead regions within the fiducial region. It also account for the small contribution (less than 5%) from $W \to \tau\nu$, where the τ decays to an electron or a muon. $W \to \tau\nu$ events are not included in the fiducial region, so the unfolding process effectively subtracts their expected contribution.

The Alpgen Monte Carlo simulation is used to produce unfolding factors to account for two effects: events passing the fiducial selection which fail the reconstructed-level selection (mostly due to efficiency effects), and events which pass the reconstructed-level selection but originate from outside the fiducial region (due to effects such as momentum smearing). These unfolding factors are then applied to the W+b-jets yields in each analysis region to obtain a fiducial cross-section.

The differential cross-section is extracted, in the 1-jet and 2-jet regions, as a function of the transverse momentum of the leading b-jet, $p_{\mathrm{T}}^{b-\mathrm{jet}}$, using the same bins as the CombNN differential fits. The measured quantity is therefore $\mathrm{d}\sigma_{\mathrm{fiducial}}/\mathrm{d}p_{\mathrm{T}}^{b-\mathrm{jet}}$. For the differential cross-section, the unfolding procedure is similar, but it also accounts for in migrations between neighboring bins, which can be the result of differences between the reconstructed and particle-level p_{T} of jets. As a first step, the unfolding

factors mentioned above are produced for each $p_{\mathrm{T}}^{b-\mathrm{jet}}$ bin. In addition, Monte Carlo events which pass both reconstruction and fiducial selections are used to fill a 2-dimensional histogram, with the axes representing the reconstructed b-tagged jet p_{T} and the particle-level $p_{\mathrm{T}}^{b-\mathrm{jet}}$. This histogram, treated as a matrix and normalized by column, is called "response matrix", and it is shown in Figure 7.34 for the 1-jet and 2-jet regions in the muon channel.

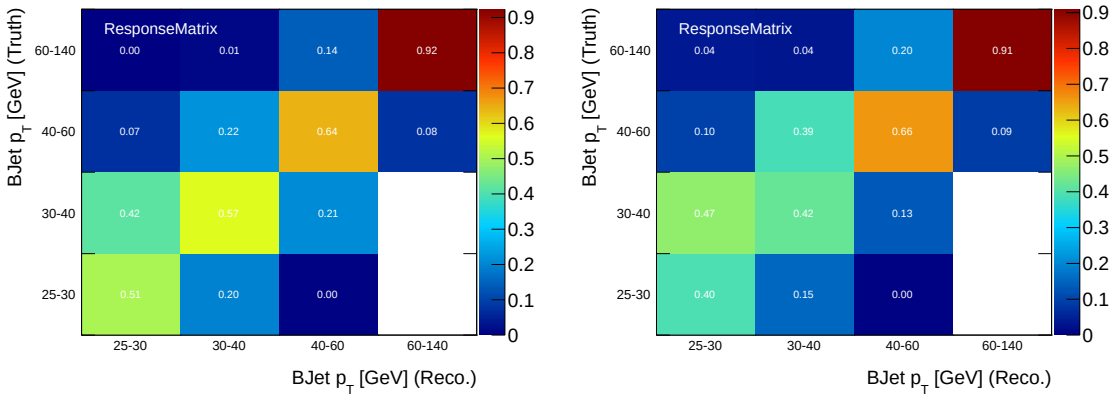

Figure 7.34: Response matrices for the $p_{\mathrm{T}}^{b-\mathrm{jet}}$ distribution in the 1-jet (left) and 2-jet (right) muon channels.

The response matrix is applied through an iterative Bayesian technique [132], in which the MC prediction is used as the initial prior, and three successive iterations are performed to remove the bias from the initial distribution. A higher number of iteration was found to increase the statistical uncertainty of the unfolded results. For a detailed overview of the method used to implement Bayesian unfolding in this analysis, see Appendix G of reference [69].

The stability of the unfolding procedure is tested by comparing the unfolded spectra after three iterations with those obtained after two and four iterations. The

largest differences from the nominal results, found when using 2 iterations, are then quoted as systematic uncertainties of the unfolding process. The bias introduced by the choice of prior is tested, as shown in Figure 7.35, by creating a biased sample (yellow)[12], and unfolding it using the nominal response matrix (green). After three iterations, the unfolded distribution (black) is significantly different from the initial prior given by the response matrix, and reproduces correctly the biased generated distribution.

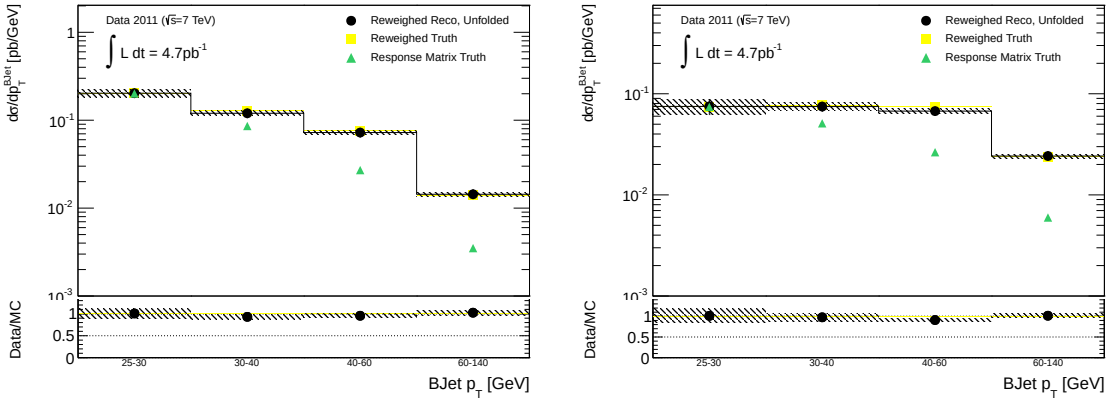

Figure 7.35: Result of bias test for unfolding in the 1-jet (left) and 2-jet (right) electron channels. Reweighed MC (yellow) is used as input for the $p_{\mathrm{T}}^{b-\mathrm{jet}}$ distribution, and the nominal response matrix (green) is used for unfolding. After three iteration, the unfolded distribution (black) is not biased by the response matrix.

During the unfolding process, different jet bins and lepton flavour channels can be combined to yield more precise measurements of the $W+b$-jets cross-section. In order not to introduce new assumptions on the background normalizations, the $W+b$-jets yields are added after the CombNN fit, and their sum is unfolded using correction factors and response matrices obtained from Monte Carlo simulated events in the

[12]The biased samples are generated by applying weights {1, 1.5, 2.8, 4} to Monte Carlo events depending on their truth $p_{\mathrm{T}}^{b-\mathrm{jet}}$ bin.

combined channels. This procedure is performed for each systematic variation and, in order to take into account the correlation of systematic uncertainties, correlated uncertainties are varied simultaneously in the samples being combined.

The statistical uncertainty of the unfolding procedure is evaluated using pseudo-experiments. The $W+b$-jets yield in each bin is fluctuated according to the statistical uncertainty of the CombNN fit, and the r.m.s. of the unfolded results from each pseudo-experiment is taken as the statistical uncertainty.

7.8 Systematic Uncertainties

Several sources of systematic uncertainties on the measured $W+b$-jets cross-section are considered. Each source may affect the background estimation in the control regions, the results of the CombNN fits, and the unfolding factors and response matrices. The strategy described here is used in all the jet multiplicity regions and b-jet p_{T} intervals.

7.8.1 Evaluating fit systematics

The effect of each systematic uncertainty on the estimated number of $W+b$-jets events is quantified using pseudo-experiments, similar to those used in Section 7.1.2 to calculate the fit statistical uncertainty. For a given systematic variation, a new set of signal and background templates is prepared which may differ in both shape and normalization from the reference set used in the fit to data. The modified templates are used to generate pseudo-data samples that are fitted using the reference templates. In these pseudo-experiments, background constraints are applied as in the fit to data.

Finally, the quoted fractional systematic uncertainty associated with a given source is defined as the ratio $(\bar{N}_{\text{fit}} - \mu_{\text{gen}})$ / μ_{gen}, where $\bar{N}_{\text{fit}}$ is the mean of the estimator of the number of W+b-jets events and μ_{gen} is the number of W+b-jets events used in the pseudo-data generation.

The full analysis procedure is repeated for each systematic variation: the multijet, $t\bar{t}$ and single-top contributions are estimated in the corresponding control sample or distribution, and the fit to the CombNN distribution is performed in the analysis regions after propagating the new background estimates.

7.8.2 Evaluating unfolding systematics

Systematic uncertainties in the unfolding process are accounted for by using each systematically varied signal Monte Carlo sample to generate a modified response matrix and a modified set of unfolding factors. The difference in fiducial cross-section obtained when using the modified Monte Carlo in place of the default one is quoted as the systematic uncertainty in the measurement. For systematic uncertainties that are split into an upwards and downwards variation, the unfolding is performed twice, and only the largest of the two resulting variations is taken as a symmetric uncertainty.

Most of the systematic effects influence both the fitting and unfolding steps. In these cases, the systematic effects are propagated coherently and for a given systematic uncertainty the corresponding estimated W+b-jets yields are unfolded using the corresponding response matrix.

To account for errors introduced by the unfolding process itself, an additional uncertainty is added. The Bayesian unfolding procedure is performed using 2 or 4

iterations, instead of the standard 3 iterations. The largest differences from the nominal results, found when using 2 iterations, are then quoted as systematic uncertainties of the unfolding process.

7.8.3 Special case: background normalizations

Background normalizations (W+c-jets, W+light-jets, multijet, $t\bar{t}$, single-top, diboson and Z+jets) are allowed to float in the CombNN maximum likelihood fits, using Gaussian constraints. As such, background normalization uncertainties are accounted for in the uncertainty on the number of W+b-jets events estimated by the fit. The statistical uncertainty of the unfolded results is then evaluated using pseudo-experiments based on the uncertainty on the number of W+b-jets events estimated by the fit. In the 1-jet region, the Gaussian constraints are set to 50% for the multijet background, 10% for $t\bar{t}$, 50% for single-top, and 10% for diboson and Z+jets. In the 2-jet region, the single-top uncertainty is lowered to 20%, while the others remain the same. The W+c-jets and W+light-jets backgrounds are not constrained.

7.8.4 Description of individual uncertainties

In this section, individual systematic uncertainties are discussed. They are categorized into detector uncertainties (on electrons, muons, jets), and process uncertainties (on template shapes, Monte Carlo assumptions).

Detector uncertainties

Common software packages maintained by the Combined Performance groups are used to evaluate uncertainties on objects such as electrons, muons, jets, $E_{\mathrm{T}}^{\mathrm{miss}}$, and on b-tagging. These uncertainties are applied as additional scale factors at the event-level, or as modification in the smearing and scaling of individual objects, based on variations by $\pm 1\sigma$ from the properties measured by the Combined Performance groups. These variations are applied to both signal and background Monte Carlo samples.

Leptons. Uncertainties related to the lepton trigger and reconstruction efficiencies are evaluated using tag-and-probe measurements in $Z \to \mu\mu$ and $Z \to ee$ events [111, 109]. Similarly, the Z-mass peak is used to determine the lepton momentum scales and resolutions and the corresponding uncertainties [110, 109]. For the muons, these uncertainties result in a total of 6 variations, counting *up* and *down* separately: trigger scale factors, reconstruction scale factors, and amount of smearing applied to the muon momenta. For the electrons, identification scale factors are also applied, resulting in 8 variations. The effect of these sources of uncertainties on the $W+b$-jets cross-section is between 1% and 2%.

Jets. The uncertainty on the jet energy scale (JES) is derived from data and from Monte Carlo simulation [115, 116, 117, 118, 119, 120], and varies between $\sigma_E/E \sim 3\%$ and 14% depending on the jet p_{T} and pseudorapidity. This uncertainty includes effects arising from the dependence of the jet response on the pile-up conditions. It also accounts for differences between the calorimeter responses to light-quark-, gluon-, and heavy-quark-initiated jets, as measured in Monte Carlo simulation, and

for additional low-momentum jets found within $\Delta R = 0.8$ of each jet considered. Uncertainties related to the jet energy resolution (JER) are derived from the jet response asymmetry measured in dijet events in data [115, 117].

The effects of the JES and JER uncertainties are quantified using modified signal and background Monte Carlo templates in which the jet energy is modified by $\pm 1\sigma$ or smeared, respectively. They represent the dominant sources of systematic uncertainties on the measured W+b-jets fiducial cross-sections and are found to be in the range 10–50%, depending on the jet multiplicity and p_{T} interval considered.

Missing Transverse Energy. Since the $E_{\mathrm{T}}^{\mathrm{miss}}$ is based on all high p_{T} objects in the event, the scale and resolution uncertainties of electrons, muons and jets have a direct impact on the $E_{\mathrm{T}}^{\mathrm{miss}}$ value. For this reason, when evaluating the systematics on these objects, the event $E_{\mathrm{T}}^{\mathrm{miss}}$ is recalculated with the object systematic uncertainties taken into account.

Two additional uncertainties (resulting in four variations) are considered: *topological cluster energy scale*, accounting for uncertainties on the energy measurement of low-momentum jets and calorimeter cells that are not associated with high-momentum objects, and *pile-up modeling*. Their combined effect is estimated to be in the range 2–6%.

***b*-tagging.** The calibration of the b-tagging efficiency is performed using control samples in data [122]. Uncertainties on these calibrations are estimated separately for light-jets, c-jets and b-jets as a function of the p_{T} and η of each jet [123, 124]. Since each variation of the scale factors is treated independently, this process results in 6 variations of the event-level scale factors. Due to their p_{T} dependence, and the

correlation of CombNN weight and jet p_{T}, these uncertainties affect not only signal and background selection efficiencies, but also template shapes. The corresponding impact on the measured cross-section is estimated to be in the range 1–8%.

Signal and background modeling uncertainties

All of the detector uncertainties mentioned in the previous section affect the template shapes used in maximum likelihood fits, as they influence the kinematics of events in the Monte Carlo simulation. An additional set of uncertainties is used to estimate the effects of a possible mismodeling of the signal and background templates. These can be based on modified Monte Carlo models, or on the ratio of data to Monte Carlo obtained in control regions. When using control regions, the assumption is made that the discrepancies observed in a control region also apply to the corresponding analysis region.

Multijet background CombNN shape. The systematic uncertainty on the multijet template shape is assessed using a control region defined by $E_{\mathrm{T}}^{\mathrm{miss}} < 25$ GeV and $m_T(W) < 40$ GeV. As discussed in detail in Section A.1.2, any mismodeling observed in this region is used to generate modified multijet shapes in the signal region, both in the electron and muon samples. The corresponding effect on the measured cross-section is larger in the electron sample where it is in the range 1–10% depending on the jet multiplicity and p_{T} interval considered.

Initial-state and final-state radiation (ISR/FSR). Uncertainties on ISR and FSR affect the extrapolation of the $t\bar{t}$ contribution in the analysis regions, as well the single-top Monte Carlo expectation in the 1-jet region and the data-driven single-top

estimate in the 2-jet region. These effects are evaluated using Monte Carlo samples generated with AcerMC interfaced to Pythia (see Section 7.3). Their effects on the final cross-section measurements depend strongly on the jet p_{T} interval and vary between 2% and 30%.

Signal p_{T} spectrum. Because of the dependence of the CombNN template shape on the jet p_{T}, an additional systematic uncertainty is estimated by changing the implementation of the heavy flavor overlap removal (HFOR) tool described in Section 7.3. In the default HFOR implementation, the parton shower is used to model events where the b-quarks are produced at small angles ($\Delta R_{b,\bar{b}} < 0.4$), while the matrix element is used to model events where b-quarks are produced at large angles ($\Delta R_{b,\bar{b}} > 0.4$). A similar distinction is made for c-quarks. Modified signal samples are generated by using either the full parton shower sample or the full matrix element sample, instead of the default mixture. This choice is made because the c-jets and b-jets spectra are found to be softer in the full parton shower samples than in the full matrix element samples.

To evaluate whether the HFOR variation is a reasonable estimate of the p_{T} spectrum uncertainty, additional W+b-jets samples with modified generation parameters are used, as described in Section 7.3. These samples are generated only at truth level, since their full simulation would require significant resources, and the assumption is made that the difference observed with the nominal sample would be the same at truth and reconstructed level.

These two types of variation, based on HFOR implementation and based on generator parameters used, are compared in Figure 7.36. With respect to the nominal

MC sample, the HFOR varied samples (black) are found to result in a larger difference, except for the difference obtained when the jet p_{T} matching parameter is increased to 25 GeV (blue), giving a result comparable to the HFOR variation. As a result, the HFOR variations are used to cover the range of variations observed in the modified ALPGEN samples. The resulting systematic uncertainties on the measured cross-section are in the range 2–8%.

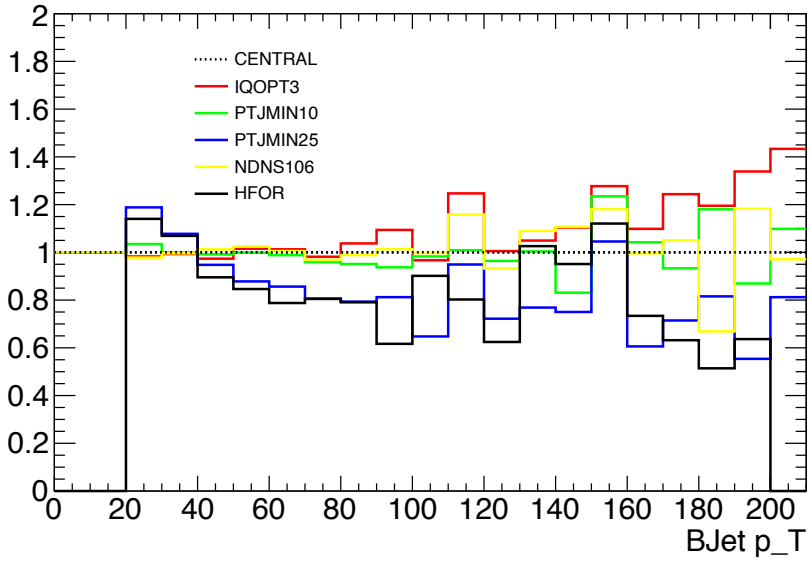

Figure 7.36: Comparison of the fractional change of the ALPGEN b-jet p_{T} spectrum due to theoretical uncertaintes. Modified W+b-jets samples generated with modified parameters are compared at truth level to the nominal sample. Superimposed (black solid line) is the difference in b-jet p_{T} spectrum between the ME+PS and full PS case at the reconstruction level. This difference is used to estimate part of the HFOR uncertainties.

***b*-jets CombNN weight**. The systematic uncertainty associated with the b-jet CombNN shape is estimated using data. Events with at least four jets, two of which

must be b-tagged, are selected. These events form a sample of $t\bar{t}$ candidates whose leading jet is a real b-jet approximately 95% of the time, as estimated in Monte Carlo simulation. This clean sample of b-jet candidates is used to compute the ratio of the corresponding CombNN distribution in data to that in MC simulation. To increase the statistical power, the electron and the muon samples are combined before computing the ratio, and the ratio is fitted using a second order polynomial. The second order polynomial is applied to all the b-jet templates used in the CombNN fit and the new set of templates is used to assess the corresponding systematic uncertainty. The effects of these variations on the final cross-section measurements range between 2% and 8%

c-jets CombNN weight. It is not possible to select an unbiased sample of c-jets with the same level of purity and statistics as the b-jet samples extracted from $t\bar{t}$ events. A first qualitative check of the c-jet template is made using the techniques of the ongoing W+c-jet measurement. A quantitative estimate of the systematic uncertainty is then obtained by preparing modified templates based on Monte Carlo simulation.

The W+c-jet production cross-section measurement [77] uses a Soft Muon Tagger to select jets containing low p_{T} muons. It then exploits the charge correlation of the W boson and the selected soft muon which is expected to be of opposite sign (OS) in real W+c events ($s \to W^- + c$ or $\bar{s} \to W^+ + \bar{c}$). In non-$W$+$c$ events, no charge correlation is expected and the same sign (SS) and OS yields should be equal except for detector effects. Finally, by considering the difference OS - SS it is possible to extract rather clean kinematic distributions of c-jets. In Figure 7.37, the OS - SS

CombNN distribution is compared between data and MC after subtracting the small remaining background. Within statistical uncertainties, the MC distribution agrees very well with the data, and the ratio between the two can be fitted by a first order polynomial as shown in Figure 7.37, right. Using the fitted linear function to modify the c-jet templates used in the $W+b$-jets extraction yields to differences of $\sim 2\%$ on the number of $W+b$-jets events. The remarkable agreement between data and MC gives confidence on the c-jet template. However, the Soft Muon Tagger biases the c-jet sample to be only a partial representation of one selected in the $W+b$-jets analysis. Therefore, the c-jet CombNN shape uncertainty cannot be estimated directly from this sample.

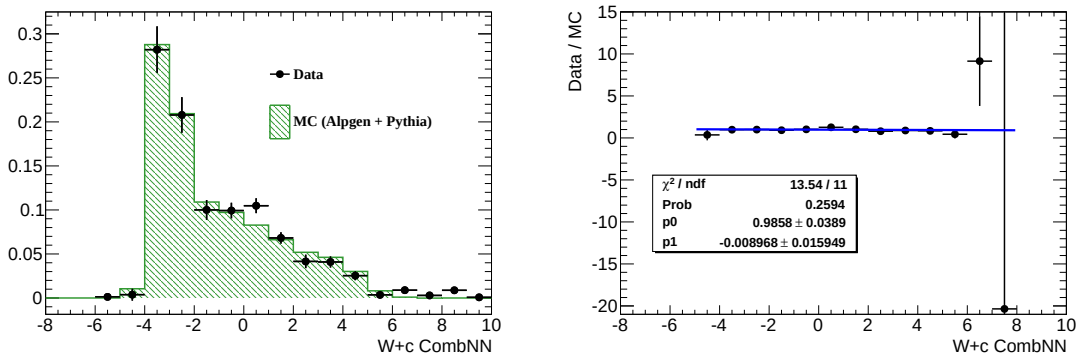

Figure 7.37: Comparison of the OS - SS CombNN weight distribution between Alpgen +Pythia and data for jets tagged by the SMT (left); the corresponding ratio with a first order polynomial fit is shown on the right.

Another approach, that of comparing $W+c$-jets MC showered with Pythia and Herwig, is also not viable. Although these two MC result in different CombNN shapes, these differences disappear once the Herwig distribution of number of tracks associated to secondary vertices is reweighted to match the Pythia one. This is

interpreted as an indication that the difference is related to different decay tables, which are outdated for the HERWIG case.

Given that the PYTHIA/HERWIG variation is too conservative (since the HERWIG decay tables are outdated), the c-jet shape uncertainty is estimated by varying the MC simulation within a more reasonable set of assumptions. Specifically, modified c-jet templates are obtained by reweighting events as a function of the track multiplicity associated with secondary vertices. Variations of +10% are considered in each track multiplicity bin, consistent with the relevant uncertainties in the c-hadron branching ratios. The results of these variations on the CombNN distribution are shown in Figure 7.38. The largest effects are observed when modifying by +10% the number of events with 4 tracks, which are the most similar to B-decays. The effects of these variations on the final cross-section measurements range between 1% and 5%.

Light-jets CombNN weight. In the case of the light jet CombNN distribution, the systematic uncertainty is estimated by using the HERWIG templates instead of PYTHIA ones. The outdated heavy flavor decay tables in HERWIG are not relevant for light jets, while differences in the fragmentation scheme of the two showers may produce differences in the fake rate for each value of the CombNN distribution. The resulting effect on the final cross-section measurements is only of a few percentage points.

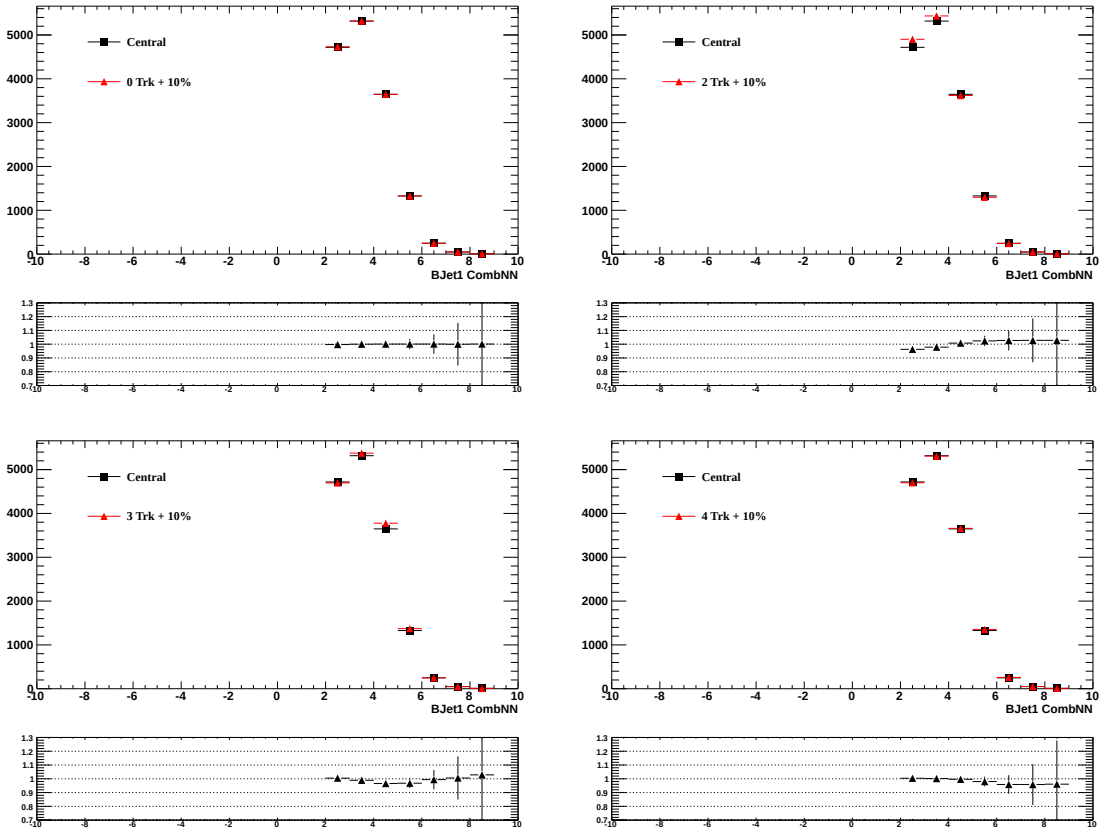

Figure 7.38: Comparison between the central $W+c$-jets CombNN template and several modified templates when the number N of secondary vertex tracks is increased by 10%: N=0 top left; N=2 top right; N=3 bottom left; N=4 bottom right. Note how higher secondary vertex track multiplicity variations correspond to higher values of the CombNN weight variations.

7.9 Theoretical predictions

The particle-level (see Section 7.7.1) measurement of W+b-jets can be compared to leading-order and next-to-leading-order calculations. The leading-order calculation used throughout this paper is that provided by ALPGEN, described in Section 3.3. This calculation is enhanced using HERWIG and JIMMY to account for the non-perturbative effects of hadronization and underlying event (UE), respectively. ALPGEN W+light-jets events in which the HERWIG parton shower results in a collimated $b\bar{b}$ pair ($\Delta R < 0.4$) are included in the calculation, and used in place of the corresponding ALPGEN $W + b\bar{b}$ events (see Section 7.3). ALPGEN/HERWIG W+0-jets events in which the JIMMY underlying event produces additional b-jets through a double parton scattering (DPS) are also included in the calculation (see Section 3.5). As a result, the ALPGEN/HERWIG/JIMMY calculation is very complete, even though it features large dependence on the renormalization and factorization scales. For this reason, the predictions from ALPGEN/HERWIG/JIMMY remain widely used in analyses to estimate the W+b-jets contribution, making their comparison to data relevant.

The W+b-jets measurement is also compared to two NLO calculations (see sections 3.4 and 3.4.1). The POWHEG calculation, described in detail in reference [82], considers massive b-quarks but it does not implement a b-quark PDF to describe the initial state. On the other hand, the MCFM calculation, described in references [84, 85], implements the 5 flavor number scheme including the b-quark PDF.

7.9.1 Scale choice and uncertainty

The NLO predictions of MCFM and POWHEG are evaluated using the MSTW2008 [137] NLO PDF, and the following dynamic renormalization and factorization scales (μ_R and μ_F)[13]:

$$\mu_F^2 = \mu_R^2 = m_{\ell\nu}^2 + p_{\mathrm{T}}^2(\ell\nu) + \frac{m_b^2 + p_{\mathrm{T}}^2(b)}{2} + \frac{m_{\bar{b}}^2 + p_{\mathrm{T}}^2(\bar{b})}{2}. \tag{7.9}$$

The uncertainty on the choice of PDF is calculated by varying the MSTW2008 PDFs using the Hessian procedure described in reference [137]. The dependence of the result on the choice of scale, which dominates the theoretical uncertainty, is evaluated by varying μ_R and μ_F up and down by a factor of four, as in reference [84]. These variations are used to calculate an asymmetric systematic uncertainty on the inclusive cross-sections (without vetoes on additional jets). For the exclusive cross-sections (1-jet, 2-jet 1+2-jet), the effect of the jet veto is taken into account by adding in quadrature the uncertainty of the inclusive and the vetoed processes, following the procedure outlined by Stewart and Tackmann in reference [138]:

$$\delta_\sigma^{1-\text{jet excl}} = \sqrt{(\delta_\sigma^{1-\text{jet incl}})^2 + (\delta_\sigma^{2-\text{jet incl}})^2}. \tag{7.10}$$

As a direct result of this procedure, the relative uncertainty estimated in the 1-jet region is larger than the relative uncertainty of the inclusive 1+2-jet region.

[13] In the 5-flavour number scheme, the production of one b-jet in the final state with an associated light jet can occur. In those cases, one of the two last terms in eqn. 7.9 is omitted.

7.9.2 Double-parton scattering correction for MCFM and Powheg

The double-parton scattering (DPS) production of W+b-jets events (Section 3.5), where the b-jet and the W arise from two separate parton-parton interactions within the same proton-proton collision, is an important contribution to the total W+b-jets cross-section. This process is accounted for in the Alpgen/Herwig/Jimmy calculation, but not in the Powheg and MCFM ones, which have to be corrected to include it. As discussed in Section 3.5, the ATLAS measurement of σ_{eff} in the W+2-jets sample [141] has shown the DPS contribution in Alpgen/Herwig/Jimmy to be accurate at least with regard to light-jet production in association with a W boson. The strategy used in this analysis is thus to correct the Powheg and MCFM calculation using the Alpgen/Herwig/Jimmy prediction, and to assign as an uncertainty on this correction the uncertainty of the σ_{eff} measurement: $^{+39}_{-28}\%$.

The DPS contribution estimated using Alpgen/Herwig/Jimmy is shown in Figure 7.39 for the inclusive measurement, and in Figure 7.40 in bins of $p_{\text{T}}^{b-\text{jet}}$. In these figures, the total fiducial cross-section estimated with Alpgen is shown (solid line), together with the DPS contribution (dashed line, labelled DPI for "double-parton interactions") and the main $W + b\bar{b}$ contribution estimated by the Alpgen matrix element for $\Delta R(b, \bar{b}) > 0.4$ (dotted line, labelled ME). The additional W+light-jets contribution, in which the Herwig parton shower results in a collimated $b\bar{b}$ pair with $\Delta R(b, \bar{b}) < 0.4$, is included in the total cross-section, but not shown as a separate histogram due to its small size. The contribution from DPS to the total cross-section reaches up to 60% of the total prediction, and it is concentrated in the lowest end of

the $p_{\mathrm{T}}^{b-\mathrm{jet}}$ spectrum, in the 1-jet bin. This behavior is expected, since the jets in DPS events follow the p_{T} spectrum of inclusive jet production, which is much steeper than that of jets in $W+b$-jets production.

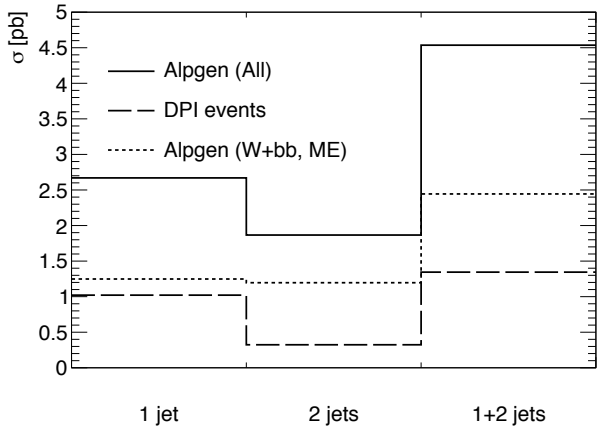

Figure 7.39: Fiducial cross-section as a function of jet multiplicity in the electron channel showing the two main contributions: that from DPS events (dashed line) and that from $W + b\bar{b}$ events in which the two b-jets are well separated (dotted line).

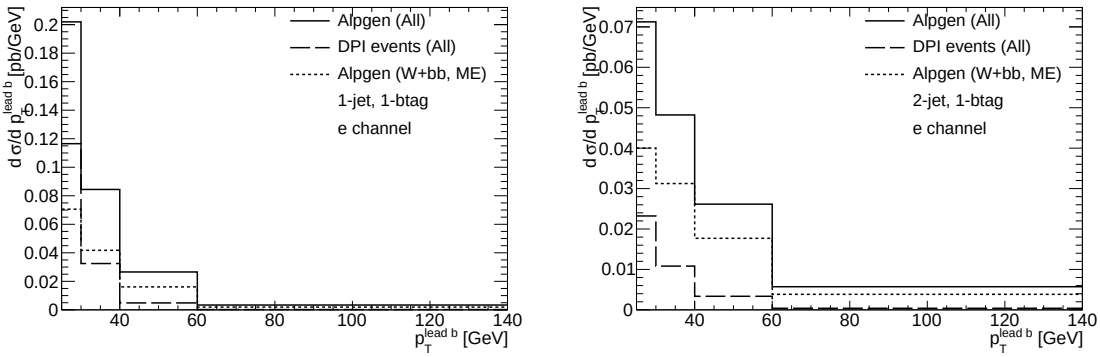

Figure 7.40: Fiducial cross-section as a function of leading b-jet p_{T} in the 1-jet/1-b-jet bin in the electron channel showing the two main contributions: that from DPS events (dashed line) and that from $W + b\bar{b}$ events in which the two b-jets are well separated (dotted line).

7.9.3 Correction for non-perturbative effects in MCFM

The POWHEG calculation is enhanced using PYTHIA to model the hadronization and underlying event, allowing for a particle-level prediction, while the MCFM calculation is only provided at the parton level. The MCFM prediction is therefore corrected to account for these two effects. To calculate the correction, a special POWHEG sample is generated without underlying event, and jets in this sample are reconstructed using partons before the hadronization. The fiducial cross-section estimated in this sample is compared to the standard particle-level results in order to calculate a correction that accounts simultaneously for the two effects.

The correction for non-perturbative effects is shown in Figure 7.41 for the different analysis multiplicity bins and in Figure 7.42 as a function of the p_{T} of the b-jet in the 1-jet and 2-jet regions. In both figures, the systematic uncertainties on the effect of hadronization, estimated using HERWIG instead of PYTHIA to describe the POWHEG parton shower, are shown on the left. The systematic uncertainties on the effect of the underlying event, estimated using the the Perugia2011 PYTHIA tune instead of the AUET2B one, are shown on the right. These two uncertainties are added in quadrature and assigned to the non-perturbative correction.

7.9.4 Corrected predictions for Alpgen, MCFM and Powheg

Table 7.13 summarizes the fully corrected theoretical predictions for the $W+b$-jets cross section in different jet multiplicity bins for ALPGEN, POWHEG and MCFM. The DPS and non-perturbative corrections are also shown. The differential cross-section and its uncertainties, as calculated with MCFM, are shown in Table 7.14 in

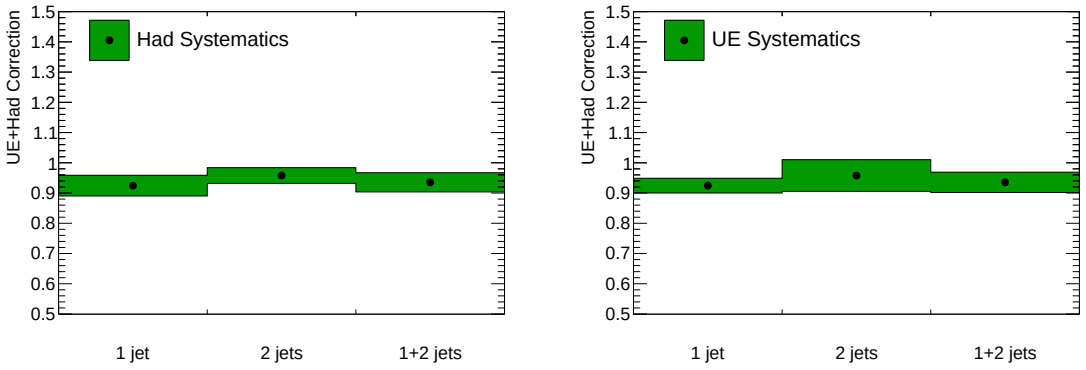

Figure 7.41: Correction for non-perturbative effects for the different multiplicity bins used in the analysis. The systematic uncertainties related to hadronization (left) and underlying event (right) are shown as green error bands around the correction.

bins of $p_{\mathrm{T}}^{b-\mathrm{jet}}$, for each exclusive jet multiplicity bin.

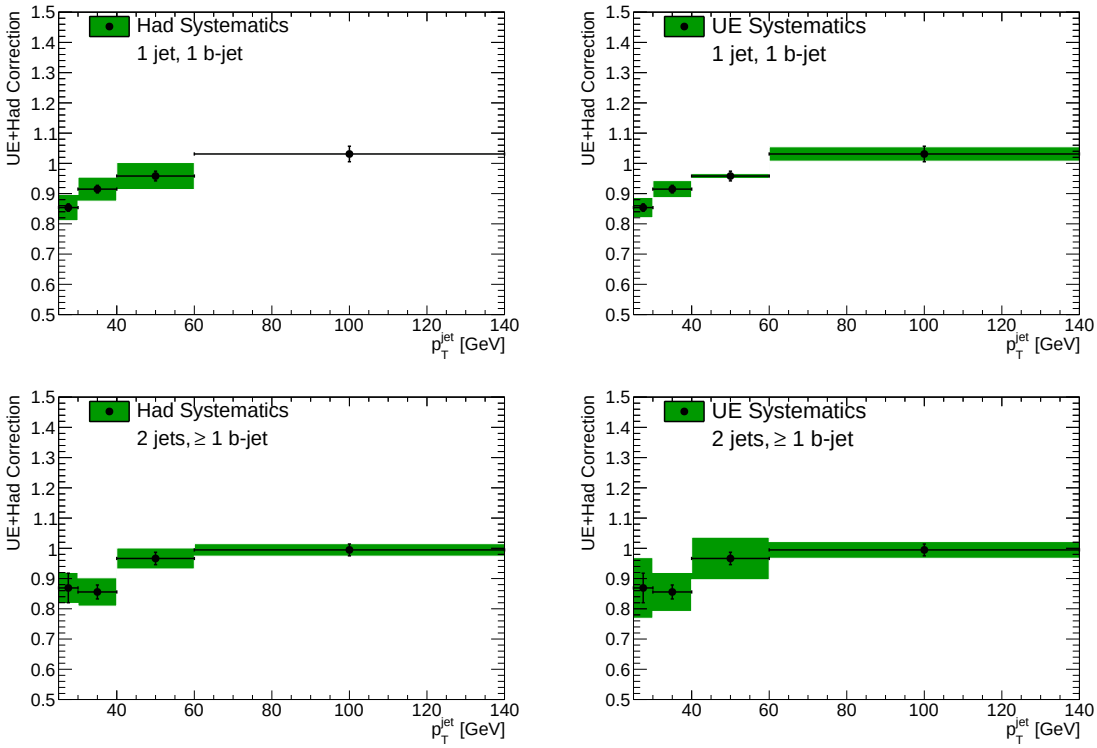

Figure 7.42: Correction for non-perturbative effects as a function of leading b-jet p_{T} in the 1-jet (top) and 2-jet (bottom) bins. The systematic uncertainties related to hadronization (left) and underlying event (right) are shown as green error bands around the correction.

Table 7.13: Production cross-sections in the different exclusive jet multiplicity bins used in the analysis and corresponding uncertainties. The MCFM and the POWHEG results are shown after all corrections. The value of the non-perturbative multiplicative correction (applied to the MCFM calculation) and the additive correction for double parton scattering (applied to the MCFM and the POWHEG calculations) are also shown.

σ_{fiducial} [pb]	1 jet	2 jet	1+2 jet
ALPGEN	2.70 ± 0.05 (stat.)	1.96 ± 0.03 (stat.)	4.66 ± 0.06 (stat.)
POWHEG	2.82 ± 0.01 (stat.) ± 0.28 (DPS)	1.33 ± 0.01 (stat.) ± 0.09 (DPS)	4.15 ± 0.01 (stat.) ± 0.37 (DPS)
MCFM	3.01 ± 0.07 (stat.) $^{+0.72}_{-0.54}$ (scale) ± 0.04 (pdf) ± 0.08 (non-pert) ± 0.28 (DPS)	1.69 ± 0.06 (stat.) $^{+0.40}_{-0.23}$ (scale) ± 0.04 (pdf) ± 0.08 (non-pert) ± 0.09 (DPS)	4.70 ± 0.09 (stat.) $^{+0.60}_{-0.49}$ (scale) ± 0.06 (pdf) ± 0.16 (non-pert) ± 0.37 (DPS)
Correction	1 jet	2 jet	1+2 jet
Double-parton scattering [pb]	1.02 ± 0.05 (stat.) $^{+0.28}_{-0.21}$ (syst.)	0.32 ± 0.02 (stat.) $^{+0.09}_{-0.07}$ (syst.)	1.34 ± 0.05 (stat.) $^{+0.36}_{-0.28}$ (syst.)
Non-perturbative (multiplicative)	0.92 ± 0.02 (had.) ± 0.03 (UE)	0.96 ± 0.05 (had.) ± 0.03 (UE)	0.94 ± 0.03 (had.) ± 0.03 (UE)

Table 7.14: Cross-sections for W+b-jets production in the b-jet p_{T} and jet multiplicity bins used in the analysis, as calculated with MCFM after all corrections. Uncertainties for Monte Carlo statistics, renormalization/factorization scale, PDF choice, non-perturbative corrections and double-parton-scattering corrections are shown.

b-jet p_{T} [GeV]	MCFM cross-section after corrections, 1-jet [pb]
25 - 30	$1.19 \pm 0.05\ (\mathrm{stat})\ ^{+0.18}_{-0.15}\ (\mathrm{scale})\ ^{+0.08}_{-0.09}\ (\mathrm{pdf})\ \pm 0.04\ (\mathrm{non\text{-}pert}) \pm 0.17\ (\mathrm{DPI})$
30 - 40	$0.99 \pm 0.027\ (\mathrm{stat})\ ^{+0.23}_{-0.17}\ (\mathrm{scale})\ ^{+0.07}_{-0.06}\ (\mathrm{pdf})\ \pm 0.04\ (\mathrm{non\text{-}pert}) \pm 0.09\ (\mathrm{DPI})$
40 - 60	$0.56 \pm 0.03\ (\mathrm{stat})\ ^{+0.20}_{-0.14}\ (\mathrm{scale})\ ^{+0.02}_{-0.03}\ (\mathrm{pdf})\ \pm 0.02\ (\mathrm{non\text{-}pert}) \pm 0.03\ (\mathrm{DPI})$
60 - 140	$0.24 \pm 0.01\ (\mathrm{stat})\ ^{+0.11}_{-0.08}\ (\mathrm{scale})\ ^{+0.05}_{-0.05}\ (\mathrm{pdf}) \pm 0.00\ (\mathrm{non\text{-}pert}) \pm 0.01\ (\mathrm{DPI})$
b-jet p_{T} [GeV]	MCFM cross-section after corrections, 2-jet [pb]
25 - 30	$0.32 \pm 0.02\ (\mathrm{stat})\ ^{+0.09}_{-0.05}\ (\mathrm{scale})\ ^{+0.02}_{-0.02}\ (\mathrm{pdf}) \pm 0.03\ (\mathrm{non\text{-}pert}) \pm 0.04\ (\mathrm{DPI})$
30 - 40	$0.41 \pm 0.04\ (\mathrm{stat})\ ^{+0.13}_{-0.07}\ (\mathrm{scale})\ ^{+0.04}_{-0.04}\ (\mathrm{pdf}) \pm 0.03\ (\mathrm{non\text{-}pert}) \pm 0.03\ (\mathrm{DPI})$
40 - 60	$0.49 \pm 0.03\ (\mathrm{stat})\ ^{+0.12}_{-0.07}\ (\mathrm{scale})\ ^{+0.03}_{-0.02}\ (\mathrm{pdf}) \pm 0.03\ (\mathrm{non\text{-}pert}) \pm 0.02\ (\mathrm{DPI})$
60 - 140	$0.41 \pm 0.02\ (\mathrm{stat})\ ^{+0.08}_{-0.04}\ (\mathrm{scale})\ ^{+0.04}_{-0.04}\ (\mathrm{pdf}) \pm 0.01\ (\mathrm{non\text{-}pert}) \pm 0.01\ (\mathrm{DPI})$

7.10 Results

The unfolded result for the fiducial W+b-jets cross-section is presented in Figure 7.43, while the measured differential $\mathrm{d}\sigma/\mathrm{d}p_{\mathrm{T}}^{b-\mathrm{jet}}$ distributions are shown in Figure 7.44. The numerical values corresponding to the combination of electron and muon channels are shown in Tables 7.15–7.17, where details of the systematic uncertainties and correlation matrices for the statistical and systematic uncertainties are also presented. Additionally, tables in Section C include separate results for the electron and muon channels.

The measured cross-sections for the 1-jet, 2-jet and 1+2-jet fiducial regions defined in Table 7.12 are:

σ_{fid} (1 jet) $= 5.0 \pm 0.5$ (stat) ± 1.2 (syst) pb,

σ_{fid} (2 jet) $= 2.2 \pm 0.2$ (stat) ± 0.5 (syst) pb,

σ_{fid} (1+2 jet) $= 7.1 \pm 0.5$ (stat) ± 1.4 (syst) pb.

The results are compared to the NLO predictions of MCFM and Powheg, and to the Alpgen predictions scaled by the NNLO normalization factor for the inclusive W cross-section [101]. Both the Alpgen and Powheg predictions implement a 4-flavour number scheme (4FNS) calculation, while the MCFM prediction, following the calculation described in ref. [85], includes terms which use the 5-flavour number scheme (5FNS) to account for the presence of b-quarks in the initial state originating from parton distribution functions.

The inclusive results in the 1-jet, 2-jet and 1+2-jet regions, in Figure 7.43, show various interesting properties. With respect to the theoretical calculation, corrected for non-perturbative effects and for the double-parton-scattering contribution, it is

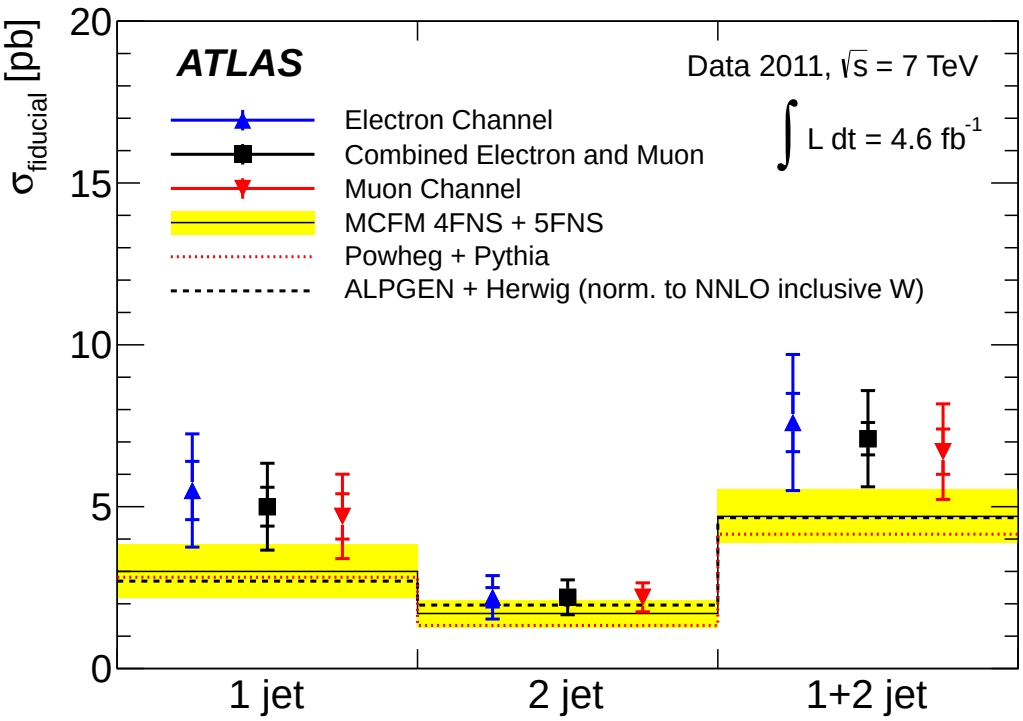

Figure 7.43: Measured fiducial cross-sections with the statistical (inner error bar) and statistical plus systematic (outer error bar) uncertainties in the electron, muon, and combined electron and muon channels. The cross-sections are given in the 1-jet, 2-jet, and 1+2-jet fiducial regions. The measurements are compared with the MCFM NLO predictions [85] corrected for the effects of hadronization and double-parton scattering (DPS). The yellow bands represent the total uncertainty on the prediction. It is obtained by combining in quadrature the uncertainties resulting from variations of the renormalization and factorization scales, the PDF set, the DPS model and non-perturbative corrections. The NLO prediction from POWHEG interfaced to PYTHIA, corrected for DPS effects, and the prediction from ALPGEN interfaced to HERWIG and JIMMY and scaled by the NNLO inclusive W normalization factor are also shown.

surprising to see that the LO order ALPGEN calculation (scaled by the NNLO inclusive W normalization factor of 1.2) and the NLO 4FNS POWHEG calculation reach very similar results to those of the NLO 5FNS MCFM calculation. The difference between the 4FNS and 5FNS NLO calculation is along the lines of the one found in Table 3.4. The differences between the LO and NLO calculations seem to be very well accounted for by the 1.2 scale factor for inclusive W production. The theoretical uncertainties on the MCFM calculation are mostly due to the scale variations and the double-parton-scattering corrections.

With respect to the measured cross-section, the compatibility between the muon and electron measurements gives confidence in the result. This compatibility was already visible at the fit stage in Table 7.9, before the systematic uncertainties (which are for the most part correlated between the two channels) had been calculated. The combined measurements agree very well with the predictions in the 2-jet bin, while they are found to be about 1σ higher than the predictions in the 1-jet bin. When combining the two bins to reach the smallest uncertainty, the measurement in the 1+2-jet bin is found to be higher than the central value of the MCFM prediction, but compatible when considering the uncertainties assigned both to the measurement and to the prediction.

The uncertainty of the inclusive measurement is broken down into its components in Table 7.15. The statistical uncertainty includes the effect of the floating background templates in the CombNN fit. The systematic uncertainties affect the data-driven background normalizations, the template shapes, and the unfolding procedure. The leading uncertainties are the jet energy scale and resolution, due to their effects on

all three aspects. The ISR/FSR affect the top background normalization, while the b-jet efficiency affects the unfolding process. All the uncertainties in the table are described in Section 7.8.

Table 7.15: Measured fiducial W+b-jets cross-sections for the combination of the electron and muon channels with statistical and systematic uncertainties and breakdown of relative systematic uncertainties per jet multiplicity, and combined across jet bins.

Fiducial cross-section [pb]			
	1 jet	2 jet	1+2 jet
σ_{fid}	5.0	2.2	7.1
Statistical uncertainty	0.5	0.2	0.5
Systematic uncertainty	1.2	0.5	1.4
Breakdown of systematic uncertainty [%]			
Jet energy scale	15	15	15
Jet energy resolution	14	4	8
b-jet efficiency	6	4	5
c-jet efficiency	1	1	0
light-jet efficiency	1	3	2
ISR/FSR	4	8	3
MC modelling	8	4	6
Lepton resolution	1	1	0
Trigger efficiency	1	2	2
Lepton efficiency	1	2	1
$E_{\text{T}}^{\text{miss}}$ scale	3	6	2
$E_{\text{T}}^{\text{miss}}$ pile-up	2	2	2
b-jet template	3	5	4
c-jet template	4	2	3
light-jet template	0	0	0
Multijet template	2	2	2
Total syst. uncertainty	24	23	20

With respect to the differential measurement, presented in Figure 7.44 and Tables 7.16–7.17, the conclusions are similar to those of the inclusive measurement. The agreement between MCFM and Alpgen continues to be surprising, and the disagreement between the measurement and the prediction continues to be concentrated in

the 1-jet bin. It is worth mentioning that the sum of the differential measurement is consistent with the inclusive measurement in both the 1-jet and 2-jet bin, and that the differential measurements in the electron and muon channels are consistent.

The 1-jet region can be studied to understand the apparent disagreement found in the inclusive measurement. The precision of the differential measurement does not allow us to draw any definite conclusions, but it is interesting to see that the disagreement seems to not be concentrated at low-$p_{\mathrm{T}}^{b-\mathrm{jet}}$ (where the DPS component dominates), but at high-$p_{\mathrm{T}}^{b-\mathrm{jet}}$ (where the top backgrounds are largest). The discrepancy between the central measured and predicted values (not considering uncertainties) reaches a factor of 3.5 in the highest $p_{\mathrm{T}}^{b-\mathrm{jet}}$ bin (60 GeV–140 GeV). This interesting behavior at high-$p_{\mathrm{T}}^{b-\mathrm{jet}}$ is one of the main motivations for trying to explore the "W+b-jets plus single-top" measurement in an attempt to reduce uncertainties.

Table 7.16: Measured fiducial W+b-jets cross-section in the 1-jet region with statistical and systematic uncertainties and their correlations in bins of $p_{\mathrm{T}}^{b-\mathrm{jet}}$.

Fiducial cross-section, 1 jet				
$p_{\mathrm{T}}^{b-\mathrm{jet}}$ [GeV]	[25, 30]	[30, 40]	[40, 60]	[60, 140]
$\mathrm{d}\sigma/\mathrm{d}p_{\mathrm{T}}^{b-\mathrm{jet}}$ [nb/GeV]	259	143	65	10.3
Statistical Uncertainty (%)	9	6	12	18
Systematic Uncertainty (%)	24	19	33	54
Correlation coefficients of statistical uncertainties	1	0.415 1	−0.38 −0.01 1	−0.02 −0.17 −0.14 1
Correlation coefficients of systematic uncertainties	1	0.893 1	0.740 0.887 1	0.582 0.750 0.875 1

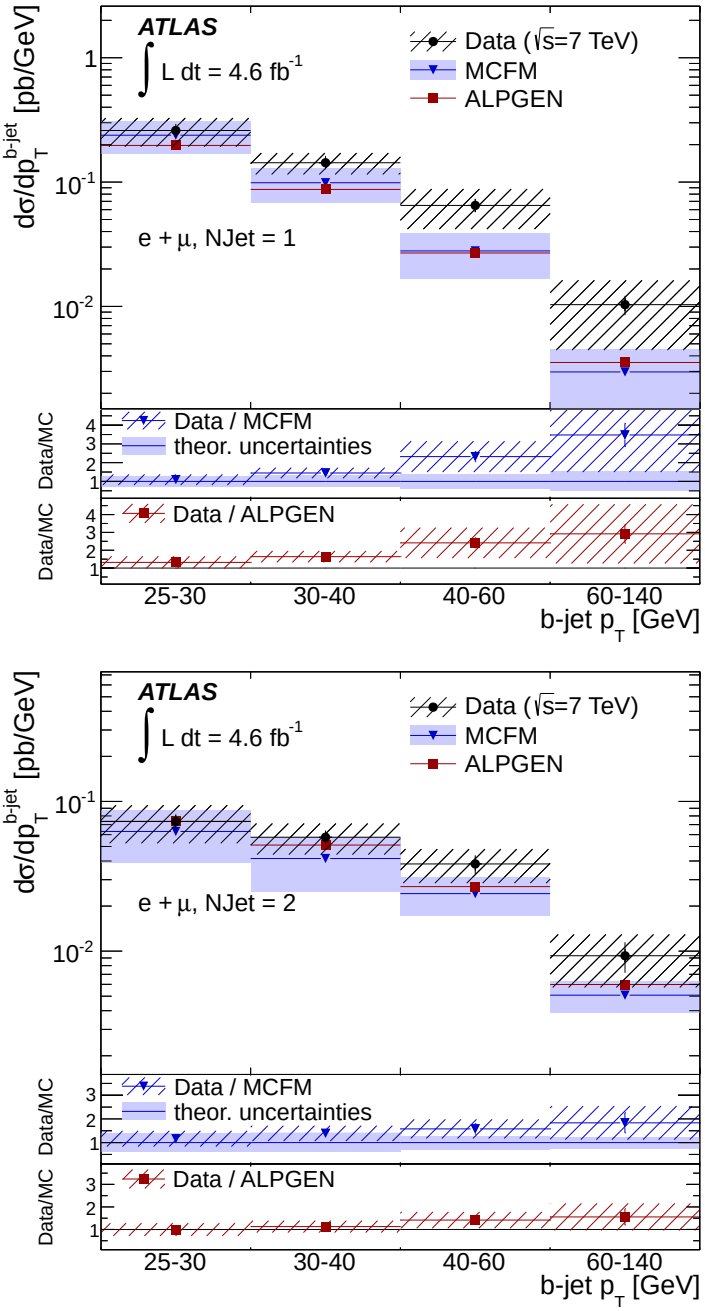

Figure 7.44: Measured differential W+b-jets cross-sections with the statistical plus systematic uncertainties as a function of $p_{\mathrm{T}}^{b-\mathrm{jet}}$ in the 1-jet (left) and 2-jet (right) fiducial regions, obtained by combining the muon and electron channel results. The measurements are compared to the MCFM predictions and to the ALPGEN predictions interfaced to HERWIG and JIMMY and scaled by the NNLO inclusive W normalization factor. The ratios between measured and predicted cross-sections are also shown.

Table 7.17: Measured fiducial W+b-jets cross-section in the 2-jet region with statistical and systematic uncertainties and their correlations in bins of $p_{\mathrm{T}}^{b-\mathrm{jet}}$.

Fiducial cross-section, 2 jets				
$p_{\mathrm{T}}^{b-\mathrm{jet}}$ [GeV]	[25, 30]	[30, 40]	[40, 60]	[60, 140]
$\mathrm{d}\sigma/\mathrm{d}p_{\mathrm{T}}^{b-\mathrm{jet}}$ [nb/GeV]	73	58	38	9.3
Statistical Uncertainty (%)	12	8	14	23
Systematic Uncertainty (%)	26	22	21	31
Correlation coefficients of	1	0.585	−0.45	−0.08
statistical uncertainties		1	0.069	−0.29
			1	−0.20
				1
Correlation coefficients of	1	0.900	0.550	0.544
systematic uncertainties		1	0.795	0.719
			1	0.775
				1

7.10.1 W+b-jets plus single-top

The W+b-jets cross-section is also measured including the contribution of the single-top process. These measurements provide a complementary perspective on the W+b-tagged-jet sample, and they have a higher statistical precision than the single-top subtracted ones, especially at high $p_{\mathrm{T}}^{b-\mathrm{jet}}$.

The number of estimated "W+b-jets + single-top" events estimated in the CombNN fit is unfolded to a common fiducial region, identical to the W+b-jets fiducial region. The unfolding is performed using correction factors and a response matrix built from the sum of the two Monte Carlo samples.

The systematic uncertainties from the fit and unfolding steps are accounted for using the same methods as for the standard measurement. Since the efficiency of the two processes (W+b-jets and single-top) is different, an additional uncertainty is introduced to account for their relative normalization. Modified samples, in which the amounts of W+b-jets and single-top are doubled in turn, are used to perform the unfolding. The largest deviation obtained with respect to the nominal result, approximately 5%, is then quoted as a separate systematic uncertainty.

Combining the electron and muon channels, the fiducial cross-sections for W+b-jets plus single-top in the regions defined in Table 7.12 are:

σ_{fid} (1 jet) $= 5.9 \pm 0.2$ (stat) ± 1.3 (syst) pb,

σ_{fid} (2 jet) $= 3.7 \pm 0.1$ (stat) ± 0.8 (syst) pb,

σ_{fid} (1+2 jet) $= 9.6 \pm 0.2$ (stat) ± 1.7 (syst) pb.

The corresponding expected cross-sections, calculated for the W+b-jets process using Alpgen interfaced to Herwig and Jimmy and scaled by the NNLO inclusive

W normalization factor and for the single-top processes using AcerMC interfaced to Pythia and scaled to NLO, are 3.6 pb, 3.0 pb and 6.6 pb, respectively. The differential results as a function of $p_{\mathrm{T}}^{b-\mathrm{jet}}$ are presented in Figure 7.45 and Tables 7.18 and 7.19.

The improved precision of the "W+b-jets + single-top" results, especially at high-$p_{\mathrm{T}}^{b-\mathrm{jet}}$, allows us to draw some additional conclusions with respect to the W+b-jets results. In particular, focusing on the 1-jet region, it is interesting to note that the disagreement at high-$p_{\mathrm{T}}^{b-\mathrm{jet}}$ becomes significant, even though the ratio of measurement to prediction decreases to ~ 1.9 from the ~ 3.5 of the W+b-jets measurement. This could indicate that the single-top measurement is in agreement with its prediction (based AcerMC scaled to the NLO inclusive cross-section for single-top), and that including single-top in the signal causes the discrepancy to decrease. More importantly, it indicates that the 50% constraint, which is applied to the single-top background in the standard W+b-jets measurement, is not forcing the single-top normalization to a local minimum.

Table 7.18: Measured fiducial W+b-jets cross-section without single-top subtraction in the 1-jet region, with statistical and systematic uncertainties and their correlations in bins of $p_{\mathrm{T}}^{b-\mathrm{jet}}$.

Fiducial cross-section of W+b-jets + single-top, 1 jet				
$p_{\mathrm{T}}^{b-\mathrm{jet}}$ [GeV]	[25, 30]	[30, 40]	[40, 60]	[60, 140]
$\mathrm{d}\sigma/\mathrm{d}p_{\mathrm{T}}^{b-\mathrm{jet}}$ [nb/GeV]	278	156	80	15.7
Statistical Uncertainty (%)	6	4	5	5
Systematic Uncertainty (%)	23	15	15	16
Correlation coefficients of	1	0.401	−0.31	−0.03
statistical uncertainties		1	0.00	−0.13
			1	−0.05
				1
Correlation coefficients of	1	0.840	0.682	0.866
systematic uncertainties		1	0.935	0.875
			1	0.861
				1

Table 7.19: Measured fiducial W+b-jets cross-section without single-top subtraction in the 2-jet region, with statistical and systematic uncertainties and their correlations in bins of $p_{\mathrm{T}}^{b-\mathrm{jet}}$.

Fiducial cross-section of W+b-jets + single-top, 2 jets				
$p_{\mathrm{T}}^{b-\mathrm{jet}}$ [GeV]	[25, 30]	[30, 40]	[40, 60]	[60, 140]
$\mathrm{d}\sigma/\mathrm{d}p_{\mathrm{T}}^{b-\mathrm{jet}}$ [nb/GeV]	88	73	56.5	18.8
Statistical Uncertainty (%)	8	5	6	5
Systematic Uncertainty (%)	20	18	16	19
Correlation coefficients of	1	0.602	−0.27	−0.08
statistical uncertainties		1	0.125	−0.18
			1	−0.12
				1
Correlation coefficients of	1	0.905	0.723	0.792
systematic uncertainties		1	0.925	0.940
			1	0.885
				1

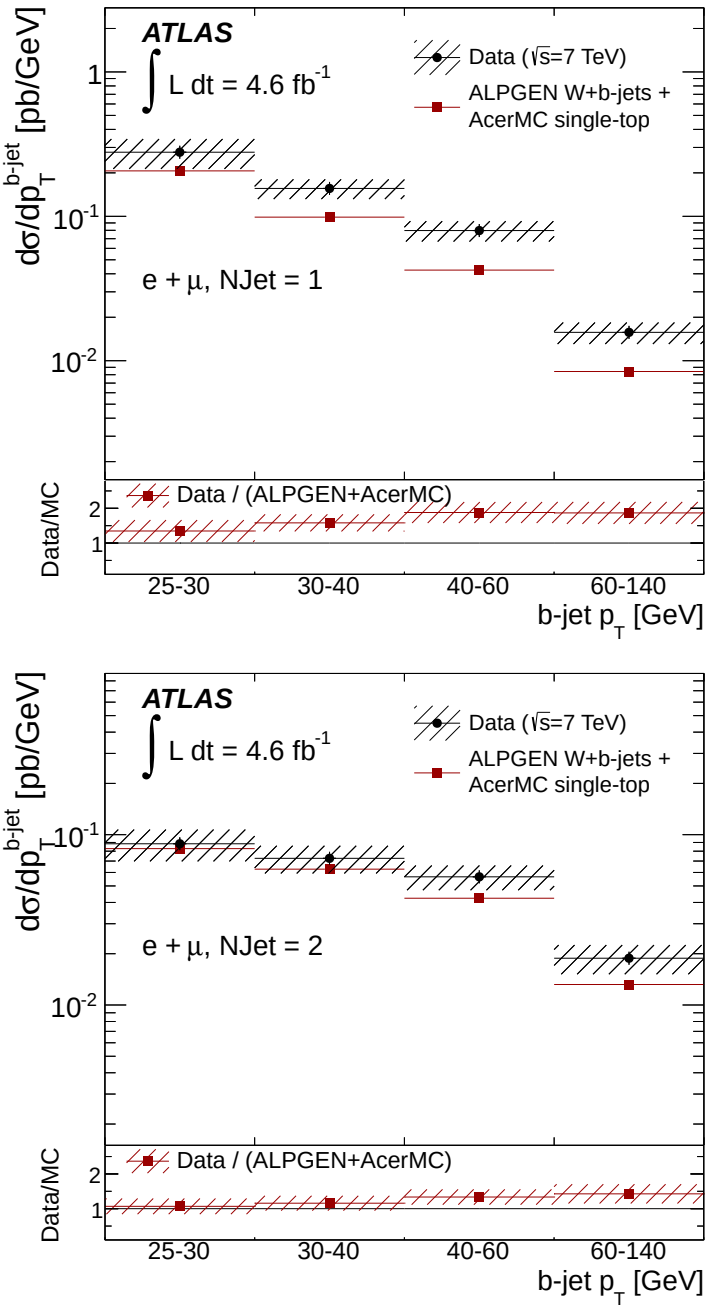

Figure 7.45: Measured differential W+b-jets cross-section without single-top subtraction as a function of $p_{\mathrm{T}}^{b-\mathrm{jet}}$ in the 1-jet (left) and 2-jet (right) samples, obtained by combining the electron and muon channels. The measurements are compared to the W+b-jets plus single-top predictions obtained using ALPGEN interfaced to HERWIG and JIMMY and scaled by the NNLO inclusive W normalization factor plus ACERMC interfaced to PYTHIA and scaled to the NLO single-top cross-section. The ratios between measured and predicted cross-sections are also shown.

Chapter 8

Conclusion

This thesis presents a set of measurements of the W+b-jets process in proton-proton collisions at $\sqrt{s} = 7$ TeV at the LHC. The measurements are made using data collected with the ATLAS detector, corresponding to an integrated luminosity of 4.6 fb^{-1}. Measurements of the W+b-jets process are relevant for searches for physics beyond the Standard Model, as well as for measurements of the single top-quark process ($t \to Wb$) and measurements of the Higgs coupling to b-quarks in the $WH \to Wb\bar{b}$ process. From the theoretical point of view, the W+b-jets process at the LHC represent an interesting combination of perturbative QCD, non-perturbative b-quark PDFs, and non-perturbative double-parton scattering (DPS).

The W+b-jets cross-section is measured in the fiducial region defined by a high p_{T} lepton and neutrino, one or two high p_{T} jets, of which at least one b-jet. The measured cross-section is found to be higher than the predicted one by $\sim 1\sigma$ in the 1-jet region, while very good agreement is observed in the 2-jet region. In the inclusive 1+2-jet region the measured cross-section is 7.1 ± 0.5 (stat) $\pm$ 1.4 (syst) pb, while

the MCFM prediction corrected for non-perturbative effects and the contribution of double-parton scattering is 4.70 ± 0.09 (stat) $^{+0.60}_{-0.49}$ (scale) ± 0.06 (PDF) ± 0.16 (non-pert) $^{+0.52}_{-0.38}$ (DPS).

For the first time, the differential W+b-jets cross-section as a function of b-jet p_{T} is also measured, taking advantage of the large data sample. The differential cross-section demonstrates an overall agreement in the 2-jet region, while the 1σ excess observed in the inclusive measurement seems to be concentrated at high $p_{\mathrm{T}}^{b-\mathrm{jet}}$ in the 1-jet region.

Since one of the largest sources of uncertainties, especially at high $p_{\mathrm{T}}^{b-\mathrm{jet}}$, is the uncertainty on the single-top background kinematics and normalization, an additional measurement is made for the combined "W+b-jets plus single-top" process. This combined measurement sheds some light on the high $p_{\mathrm{T}}^{b-\mathrm{jet}}$ excess. Specifically, the high $p_{\mathrm{T}}^{b-\mathrm{jet}}$ excess in the 1-jet region is reduced (possibly diluted by the presence of the correctly-modeled single-top component), but it becomes more significant.

It is not straightforward to interpret this measurement in terms of the different W+b-jets processes. In the 1-jet region, the majority of W+b-jets events are $pp \to W$+b single-parton-scattering events, but there is also a large contribution from double-parton scattering. In both single-parton and double-parton scattering events, there is a non-negligible fraction of $W + (b\bar{b})$ events where the $(b\bar{b})$ pair is reconstructed within a single jet. Therefore, further studies are needed to separate these categories of events. In the 2-jet region, the majority of W+b-jets events are $pp \to W$+b+X events (where X is a light-flavour jet), and the fraction of $pp \to W$+$b\bar{b}$ events is expected to be around 10%. Agreement in this region is an indication of

a possible agreement of the $pp \to W + b\bar{b}$ process, but a dedicated study with two b-tagged jets is needed to add further clarification.

Future studies of the W+b-jets process at the LHC, using the 8 TeV dataset collected in 2012 and the 13-14 TeV dataset expected for 2015, will have multiple goals. The reduction of systematic uncertainties will certainly be the main goal, starting from the jet related uncertainties (jet energy scale and resolution). The jet-related uncertainties on the W+b-jets cross-section have a particularly large role in this measurement, due to their effect on the data-driven estimates of the $t\bar{t}$ and single-top backgrounds. So they can be tackled both directly (studying jets) and indirectly (studying the top backgrounds). For a quantitative estimate of the uncertainty reduction that could be obtained from a precise knowledge of the single-top background, one can simply take the difference in uncertainty between the "W+b-jets plus single-top" measurement and the W+b-jets measurement.

Another goal in any future study would be to analyze the other final states of the W+b-jets process, and to distinguish the different underlying processes. A study of events with two b-tagged jets would give access to the perturbative QCD region. On the other hand, studying events with double-tagged jets (with two b-hadrons in the same jet), or using track-based tagging without requiring jets, would give access to the collinear final state. Finally, given precise estimates of the kinematic distributions expected from single-parton and double-parton scattering, it would be also interesting to measure the fraction of DPS events. A measurement of DPS in the W+b-jets final state could be compared to previous measurements in other final states, leading to further testing of the effective cross-section model for double-parton scattering.

Bibliography

[1] E. Abat et al. The ATLAS Transition Radiation Tracker (TRT) proportional drift tube: design and performance. *JINST*, 3:P02013, 2008.

[2] D. Adams et al. Track reconstruction in the ATLAS Muon Spectrometer with MOORE 007. ATLAS Technical Report ATL-SOFT-2003-007, 2003.

[3] S. Agostinelli et al. GEANT4: A simulation toolkit. *Nucl. Instrum. Meth.*, A506:250–303, 2003.

[4] A. Ahmad et al. The silicon microstrip sensors of the ATLAS semiconductor tracker. *NIM A*, 578:98, 2007.

[5] ALICE Collaboration. The ALICE Experiment at the CERN Large Hadron Collider. *JINST*, 3:S08002, 2008.

[6] ATLAS Collaboration. ATLAS Calorimeter Isolation Correction Internal Webpage. `https://twiki.cern.ch/twiki/bin/viewauth/AtlasProtected/CaloIsolationCorrections`.

[7] ATLAS Collaboration. ATLAS Detector and Physics Performance Technical Design Report. `http://atlas.web.cern.ch/Atlas/GROUPS/PHYSICS/TDR/access.html`.

[8] ATLAS Collaboration. ATLAS Jet Vertex Fraction Tool Internal Webpage. `https://twiki.cern.ch/twiki/bin/viewauth/AtlasProtected/JetVertexFraction`.

[9] ATLAS Collaboration. ATLAS Liquid Argon Hole Internal Webpage. `https://twiki.cern.ch/twiki/bin/viewauth/AtlasProtected/HowToCleanJets2011`.

[10] ATLAS Collaboration. ATLAS Pileup Reweighting Internal Webpage. `https://twiki.cern.ch/twiki/bin/viewauth/AtlasProtected/ExtendedPileupReweighting`.

[11] ATLAS Collaboration. ATLAS Public Luminosity Plots. `https://twiki.cern.ch/twiki/bin/view/AtlasPublic/LuminosityPublicResults`.

[12] ATLAS Collaboration. Electron and photon reconstruction and identification in ATLAS: expected performance at high energy and results at 900 GeV. ATLAS conference note: ATLAS-CONF-2010-005, `https://atlas.web.cern.ch/Atlas/GROUPS/PHYSICS/CONFNOTES/ATLAS-CONF-2010-005/`.

[13] ATLAS Collaboration. Expected Performance of the ATLAS Experiment - Detector, Trigger and Physics. arXiv:0901.0512 [hep-ex].

[14] ATLAS Collaboration. Liquid argon calorimeter technical design report. CERN-LHCC-96-041, `http://cdsweb.cern.ch/record/331061`.

[15] ATLAS Collaboration. Luminosity Determination in pp Collisions at $\sqrt{s} = 7$ TeV using the ATLAS Detector in 2011. ATLAS conference note: ATLAS-CONF-2011-116 `https://cdsweb.cern.ch/record/1376384?ln=en`.

[16] ATLAS Collaboration. Performance of primary vertex reconstruction in proton-proton collisions at $\sqrt{s} = 7$ tev in the atlas experiment. ATLAS Conference Note: ATLAS-CONF-2010-069, `https://cdsweb.cern.ch/record/1281344?ln=en`.

[17] ATLAS Collaboration. Tile calorimeter technical design report. CERN-LHCC-96-042, `http://cdsweb.cern.ch/record/331062`.

[18] ATLAS Collaboration. *ATLAS Muon Spectrometer Technical Design Report*. CERN, Geneva, 1997.

[19] ATLAS Collaboration. ATLAS Pixel Detector Electronics and Sensors. *JINST*, 3(07):P07007, 2008.

[20] ATLAS Collaboration. The ATLAS Experiment at the CERN Large Hadron Collider. *JINST*, 3:S08003, 2008.

[21] ATLAS Collaboration. Jet energy measurement with the ATLAS detector in proton-proton collisions at $\sqrt{s} = 7$ TeV. arXiv:1112.6426 [hep-ex], 2011.

[22] ATLAS Collaboration. Luminosity Determination in pp Collisions at $\sqrt{s} = 7$ TeV using the ATLAS Detector at the LHC. *European Physics Journal C*, 71:1630, 2011.

[23] ATLAS Collaboration. Electron performance measurements with the ATLAS detector using the 2010 LHC proton-proton collision data. *Eur. Phys. J. C*, 72:1909, 2012.

[24] ATLAS Collaboration. Performance of Missing Transverse Momentum Reconstruction in Proton-Proton Collisions at $\sqrt{s}$ = 7 TeV with ATLAS. *Eur.Phys.J.C*, 72:1844, 2012.

[25] ATLAS Collaboration. Improved luminosity determination in pp collisions at sqrt(s) = 7 TeV using the ATLAS detector at the LHC. *Sumbmitted to European Physics Journal C*, 2013.

[26] ATLAS Experiment @ 2011 CERN. ATLAS Photos. `http://www.atlas.ch/photos/index.html`.

[27] M. Benedikt and others (eds.). The LHC design report v.3 : the LHC Injector Chain. CERN-2004-003-V-3, `http://cdsweb.cern.ch/record/823808`.

[28] J.P. Blewett. 200 gev intersecting storage accelerators. Proceedings of the 8th International Conference on High-Energy Accelerators, CERN, Geneva Switzerland (1971).

[29] O.S. Bruning and others (eds.). The LHC design report v.1 : the LHC Main Ring. CERN-2004-003-V-1, `http://cdsweb.cern.ch/record/782076`.

[30] O.S. Bruning and others (eds.). The LHC design report v.2 : the LHC Infrastructure and General Services. CERN-2004-003-V-2, `http://cdsweb.cern.ch/record/815187`.

[31] M. Cacciari, G. P. Salam, and G. Soyez. The anti-kt jet clustering algorithm. *JHEP*, 04:063, 2008.

[32] J.M. Campbell et al. Next-to-leading order QCD predictions for W + 2jet and Z + 2jet production at the CERN LHC. *Phys. Rev.*, D68:094021, 2003.

[33] CMS Collaboration. The CMS Experiment at the CERN Large Hadron Collider. *JINST*, 3:S08004, 2008.

[34] ATLAS Collaboration. Measurement of the production cross section for Z/gamma* in association with jets in *pp* collisions at $\sqrt{s}$ = 7 TeV with the ATLAS detector. *Phys.Rev.*, D85:032009, 2012.

[35] ATLAS Collaboration. Study of jets produced in association with a W boson in *pp* collisions at $\sqrt{s} = 7$ TeV with the ATLAS detector. *Phys.Rev.*, D85:092002, 2012.

[36] G. Corcella et al. HERWIG 6: an event generator for Hadron Emission Reactions With Interfering Gluons. *JHEP*, 010:0101, 2001.

[37] T Cornelissen et al. Concepts, design and implementation of the atlas new tracking (newt). ATLAS Technical Report ATL-SOFT-PUB-2007-007, `https://cdsweb.cern.ch/record/1020106`, 2007.

[38] G. D'Agostini. Improved Iterative Bayesian Unfolding. arXiv:1010.0632 [physics.data-an].

[39] A. Dell'Acqua, C. Maiani, Z. Marshall, and J. Penwell. The simulation of cavern background in ATLAS using Geant4. ATLAS Internal Communication ATL-COM-SOFT-2011-010 (2011).

[40] S. D. Drell and T. Yan. Partons and their applications at high energies. *Ann. Phys.*, 66:578623, 1971.

[41] R. Duda and P. Hart. Use of the Hough Transformation to Detect Lines and Curves in Pictures. *Comm. ACM*, 15, 1972.

[42] L. Evans and P. Bryant. LHC Machine. *JINST*, 3:S08001, 2008.

[43] S. Frixione, P. Nason, and C. Oleari. Matching NLO QCD computations with Parton Shower simulations: the POWHEG method. *JHEP*, 11:070, 2007.

[44] R. Fruhwirth et al. Application of Kalman Filtering to Track and Vertex Fitting. *Nucl. Inst. Meth. A*, 262, 1987.

[45] R. Fruhwirth, W. Waltenberger, and P. Vanlaer. Adaptive vertex fitting. *J. Phys. G*, 34, 2007.

[46] The ATLAS Egamma Group. isEM Identification. https://twiki.cern.ch/twiki/bin/view/AtlasProtected/ IsEMIdentification.

[47] The ATLAS Jet/EtMiss Group. How To Clean Jets. https://twiki.cern.ch/twiki/bin/view/AtlasProtected/HowToCleanJets.

[48] S.W. Herb, D.C. Hom, L.M. Lederman, J.C. Sens, H.D. Snyder, et al. Observation of a Dimuon Resonance at 9.5-GeV in 400-GeV Proton-Nucleus Collisions. *Phys.Rev.Lett.*, 39:252–255, 1977.

[49] L. Jeanty, M. Franklin, and G. Zevi Della Porta. MDT Cavern Background Studies in 7 TeV Collision Data. ATLAS Internal Communication ATL-COM-MUON-2010-029 (2011).

[50] L. Jeanty and S. Sun. Private communication, 2013.

[51] M. Lamont. LHC: Status and commissioning plans. arXiv:0906.0347 [physics.acc-ph], 2009.

[52] D. Levin. Muonrecpedia.
`https://twiki.cern.ch/twiki/bin/view/AtlasProtected/MuonRecoPedia`.

[53] LHCb Collaboration. The LHCb Detector at the LHC. *JINST*, 3:S08005, 2008.

[54] LHCf Collaboration. The LHCf detector at the CERN Large Hadron Collider. *JINST*, 3:S08006, 2008.

[55] L. Maiani. *A caccia del bosone di Higgs. Magneti, governi, scienziati e particelle nell'impresa scientifica del secolo.* Mondadori, 2013.

[56] M.L. Mangano et al. ALPGEN, a generator for hard multiparton processes in hadronic collisions. *JHEP*, 07:001, 2003.

[57] A.D. Martin et al. Parton distributions for the LHC. arXiv:0901.0002 [hep-ph].

[58] K. Nakamura et al. Review of Particle Physics. *Journal of Physics G*, 37, 2010.

[59] R Nicolaidou, L Chevalier, S Hassani, J F Laporte, E Le Menedeu, and A Ouraou. Muon identification procedure for the ATLAS detector at the LHC using Muonboy reconstruction package and tests of its performance using cosmic rays and single beam data. *Journal of Physics: Conference Series*, 219(3):032052, 2010.

[60] Giacinto Piacquadio and Christian Weiser. A new inclusive secondary vertex algorithm for b-jet tagging in ATLAS. *J.Phys.Conf.Ser.*, 119:032032, 2008.

[61] TOTEM Collaboration. The TOTEM Experiment at the CERN Large Hadron Collider. *JINST*, 3:S08007, 2008.

[62] A. Yamamoto et al. Progress in ATLAS central solenoid magnet. *IEEE T. Appl. Supercond.*, 10:353, 2000.

[63] M. L. Mangano, *Production of W plus heavy quark pairs in hadronic collisions*, Nucl. Phys. B 405, 536 (1993).

[64] M. L. Mangano, M. Moretti and R. Pittau, *Multijet matrix elements and shower evolution in hadronic collisions: $Wb\bar{b}$ + n jets as a case study*, Nucl. Phys. B 632, 343 (2002) [hep-ph/0108069].

[65] F. Caravaglios, M. L. Mangano, M. Moretti and R. Pittau, *A New approach to multijet calculations in hadron collisions*, Nucl. Phys. B 539, 215 (1999) [hep-ph/9807570].

[66] F. Febres Cordero, L. Reina and D. Wackeroth, *NLO QCD corrections to W boson production with a massive b-quark jet pair at the Tevatron p anti-p collider*, Phys. Rev. D 74, 034007 (2006) [hep-ph/0606102].

[67] J. M. Campbell, R. K. Ellis, F. Maltoni and S. Willenbrock, *Production of a W boson and two jets with one b^- quark tag*, Phys. Rev. D 75, 054015 (2007) [hep-ph/0611348].

[68] J. M. Campbell, *Overview of the theory of W/Z + jets and heavy flavor*, arXiv:0808.3517 [hep-ph].

[69] P. Catastini, M. Franklin, J. Huth, D. Lopez Mateos, A. Messina, and G. Zevi Della Porta. Measurement of the cross section for the production of a W boson in association with b-jets in 4.64 fb^{-1}of pp collisions at $\sqrt{s} = 7$ TeV, ATLAS Internal Communication ATL-COM-PHYS-2012-828 (2012).

[70] M.E. Peskin and D. V. Schroeder *An Introduction to Quantum Field Theory*, Westview Press (1995).

[71] UA1 Collaboration, *Experimental Observation of Isolated Large Transverse Energy Electrons with Associated Missing Energy at s**(1/2) = 540-GeV*, Phys. Lett. B 122 103 (1983) .

[72] UA2 Collaboration, *Observation of Single Isolated Electrons of High Transverse Momentum in Events with Missing Transverse Energy at the CERN anti-p p Collider*, Phys. Lett. B 122, 476 (1983).

[73] M. Kobayashi and T. Maskawa, *CP Violation in the Renormalizable Theory of Weak Interaction*, Prog. Theor. Phys. 49, 652 (1973).

[74] J. H. Christenson, J. W. Cronin, V. L. Fitch and R. Turlay, *Evidence for the 2 pi Decay of the k(2)0 Meson*, Phys. Rev. Lett. 13, 138 (1964).

[75] CDF Collaboration, *Observation of top quark production in $\bar{p}p$ collisions*, Phys. Rev. Lett. 74, 2626 (1995) [hep-ex/9503002].

[76] D0 Collaboration, *Observation of the top quark*, Phys. Rev. Lett. 74, 2632 (1995) [hep-ex/9503003].

[77] G. Aad, H. Arnold, L. Cerrito, K. Lohwasser, G. Snidero, M. Vanadia and W. Weiser, *Measurement of the production cross-section of a W boson in association with a charm jet using 4.5 fb-1 of data at sort(s)=7 TeV*, ATLAS Internal Communication ATL-COM-PHYS-2012-1403 (2012).

[78] G. Piacquadio, *Identification of b-jets and investigation of the discovery potential of a Higgs boson in the $WH \to \ell\nu bb$ channel with the ATLAS experiment*, PhD thesis, Albert Ludwig University of Freiburg, 2010, CERN-THESIS-2010-027.

[79] P. Bartalini, E. L. Berger, B. Blok, G. Calucci, R. Corke, M. Diehl, Y. .Dokshitzer and L. Fano *et al.*, *Multi-Parton Interactions at the LHC*, arXiv:1111.0469 [hep-ph].

[80] Axial Field Spectrometer Collaboration, *Double parton scattering in pp collisions at sqrt(s) = 63 GeV*, Z. Phys. C 34, 163 (1987).

[81] J. M. Campbell and R. Ellis, *MCFM for the Tevatron and the LHC*, *Nucl. Phys. Proc. Suppl.* 205-206 (2010) 10.

[82] S. Alioli, P. Nason, C. Oleari, and E. Re, *A general framework for implementing NLO calculations in shower Monte Carlo programs: the POWHEG BOX*, *JHEP* 1006 (2010) 043 [arXiv:1002.2581];
C. Oleari and L. Reina, *W +- b $\bar{b}$ production in POWHEG*, JHEP 1108, 061 (2011) [arXiv:1105.4488 [hep-ph]].

[83] S. Frixione and B. R. Webber, *Matching NLO QCD computations and parton shower simulations*, *JHEP* 06 (2002) 029 [hep-ph/0204244];
S. Frixione, P. Nason and B. R. Webber, *Matching NLO QCD and parton showers in heavy flavour production*, *JHEP* 08 (2003) 007 [hep-ph/0305252];
S. Frixione, E. Laenen and P. Motylinski, *Single-top production in MC@NLO*, *JHEP* 03 (2006) 092 [hep-ph/0512250].

[84] S. Badger, J. M. Campbell and R. K. Ellis, *QCD corrections to the hadronic production of a heavy quark pair and a W-boson including decay correlations*, *JHEP* 1103 (2011) 027 [arXiv:1011.6647];
F. F. Cordero, L. Reina and D. Wackeroth, *Associated production of a W or Z boson with bottom quarks at the Tevatron and the LHC*, *PoS* RADCOR2009 (2010) 055 [arXiv:1001.3362];
J. M. Campbell, R. K. Ellis, F. Febres Cordero, F. Maltoni, L. Reina, D. Wackeroth and S. Willenbrock, *Associated Production of a W Boson and One b Jet, Phys. Rev.* D 79 (2009) 034023 [arXiv:0809.3003].

[85] J. M. Campbell, F. Caola, F. Febres Cordero, L. Reina and D. Wackeroth, *NLO QCD predictions for $W + 1$ jet and $W + 2$ jet production with at least one b jet at the 7 TeV LHC, Phys. Rev.* D 86 (2012) 034021 [arXiv:1107.3714].

[86] E. L. Berger, C. B. Jackson, S. Quackenbush and G. Shaughnessy, *Calculation of $Wb\bar{b}$ Production via Double Parton Scattering at the LHC, Phys. Rev.* D 84 (2011) 074021 [arXiv:1107.3150].

[87] ATLAS Collaboration, *Search for the Standard Model Higgs boson produced in association with a vector boson and decaying to a b-quark pair with the ATLAS detector*, *Phys. Lett.* B 718 (2012) 369 [arXiv:1207.0210].

[88] ATLAS Collaboration, *Observation of a new particle in the search for the Standard Model Higgs boson with the ATLAS detector at the LHC, Phys. Lett.* B 716 (2012) 1 [arXiv:1207.7214].

[89] ATLAS Collaboration, *Search for light top squark pair production in final states with leptons and b-jets with the ATLAS detector in $\sqrt{s} = 7$ TeV proton-proton collisions*, submitted to *Phys. Lett.* B (2012) [arXiv:1209.2102].

[90] ATLAS Collaboration, *Measurement of the t-channel single top-quark production cross section in pp collisions at $\sqrt{s} = 7$ TeV with the ATLAS detector*, *Phys. Lett.* B 717 (2012) 330 [arXiv:1205.3130].

[91] CDF Collaboration, T. Aaltonen et al, *First Measurement of the b-jet Cross Section in Events with a W Boson in $p\bar{p}$ Collisions at $\sqrt{s} = 1.96$ TeV*, *Phys. Rev. Lett.* 104 (2010) 131801 [arXiv:0909.1505].

[92] D0 Collaboration, V. Abazov et al, *Measurement of the $p\bar{p} \to W+b+X$ production cross section at $\sqrt{s}$ =1.96 TeV* [arXiv:1210.0627].

[93] ATLAS Collaboration, *Measurement of the cross section for the production of a W boson in association with b-jets in pp collisions at $\sqrt{s} = 7$ TeV with the ATLAS detector*, *Phys. Lett.* B 707 (2012) 418 [arXiv:1109.1470].

[94] ATLAS Collaboration, *The ATLAS Experiment at the CERN Large Hadron Collider*, *JINST* 3 (2008) S08003.

[95] M. L. Mangano, M. Moretti, F. Piccinini, R. Pittau and A. D. Polosa, *ALPGEN, a generator for hard multiparton processes in hadronic collisions*, *JHEP* 07 (2003) 001.

[96] G. Corcella et al., *HERWIG 6.5: an event generator for Hadron Emission Reactions With Interfering Gluons (including supersymmetric processes)*, *JHEP* 01 (2001) 010;
G. Corcella et al., *HERWIG 6.5 release notes* [hep-ph/0210213].

[97] J. M. Butterworth, J. R. Forshaw, and M. H. Seymour, *Multiparton Interactions in Photoproduction at HERA*, *Z. Phys.* C 72 (1996) 637 [hep-ph/9601371].

[98] M. L. Mangano and R. Pittau, *Multijet matrix elements and shower evolution in hadronic collisions: Wbb + n jets as a case study*, *Nucl. Phys.* B 632 (2002) 343 [hep-ph/0108069].

[99] T. Sjostrand, S. Mrenna, and P. Z. Skands, *PYTHIA 6.4 Physics and Manual*, *JHEP* 0605 (2006) 026 [hep-ph/0603175].

[100] B.P. Kersevan and E. Richter-Was, *The Monte Carlo event generator AcerMC version 2.0 with interfaces to PYTHIA 6.2 and HERWIG 6.5* [hep-ph/0405247].

[101] C. Anastasiou, L. Dixon, K. Melnikov and F. Petriello, *High-precision QCD at hadron colliders: electroweak gauge boson rapidity distributions at NNLO*, *Phys. Rev.* D 69 (2004) 094008 [hep-ph/0312266].

[102] J. M. Campbell, R. K. Ellis and C. Williams, *Vector boson pair production at the LHC*, *JHEP* 1107 (2011) 018 [arXiv:1105.0020].

[103] J. M. Campbell, R. K. Ellis and F. Tramontano, *Single top production and decay at next-to-leading order*, *Phys. Rev.* D 70 (2004) 094012 [hep-ph/0408158].

[104] M. Aliev, H. Lacker, U. Langenfeld, S. Moch, P. Uwer and M. Wiedermann, *HATHOR: HAdronic Top and Heavy quarks crOss section calculatoR*, *Comput. Phys. Commun.* 182 (2011) 1034 [arXiv:1007.1327].

[105] ATLAS Collaboration, *The ATLAS Simulation Infrastructure*, *Eur. Phys. J.* C 70 (2010) 823 [arXiv:1005.4568].

[106] S. Agostinelli et. al., *GEANT4: A simulation toolkit*, *Nucl. Instrum. Meth.* A 506 (2003) 250.

[107] ATLAS Collaboration, *Luminosity determination in pp collisions at* $\sqrt{s} = 7$ *TeV using the ATLAS detector at the LHC*, *Eur. Phys. J.* C 71 (2011) 1630 [arXiv:1101.2185].

[108] ATLAS Collaboration, *Luminosity Determination in pp Collisions at* $\sqrt{s} = 7$ *TeV using the ATLAS Detector in 2011*, ATLAS-CONF-2011-116.

[109] ATLAS Collaboration, *Electron performance measurements with the ATLAS detector using the 2010 LHC proton-proton collision data*, *Eur. Phys. J.* C 72 (2012) 1909 [arXiv:1110.3174].

[110] ATLAS Collaboration, *Muon reconstruction efficiency in reprocessed 2010 LHC proton-proton collision data recorded with the ATLAS detector*, ATLAS-CONF-2011-063.

[111] ATLAS Collaboration, *ATLAS muon momentum resolution in the first pass reconstruction of the 2010 pp Collision Data at* $\sqrt{s} = 7$ TeV, ATLAS-CONF-2011-046.

[112] W. Lampl et al., *Calorimeter clustering algorithms: description and performance*, ATL-LARG-PUB-2008-002.

[113] M. Cacciari, G. P. Salam, and G. Soyez, *The anti-k_t jet clustering algorithm*, *JHEP* 04 (2008) 063 [arXiv:0802.1189].

[114] ATLAS Collaboration, *Selection of jets produced in proton-proton collisions with the ATLAS detector using 2011 data*, ATLAS-CONF-2012-020.

[115] ATLAS Collaboration, *Jet energy measurement with the ATLAS detector in proton-proton collisions at $\sqrt{s} = 7$ TeV* , submitted to *Eur. Phys. J.* [arXiv:1112.6426].

[116] ATLAS Collaboration, *In situ jet pseudorapidity intercalibration of the ATLAS detector using dijet events in $\sqrt{s} = 7$ TeV proton-proton 2011 data*, ATLAS-CONF-2012-124.

[117] ATLAS Collaboration, *Light-quark and Gluon Jets: Calorimeter Response, Jet Energy Scale Systematics and Properties*, ATLAS-CONF-2012-138.

[118] ATLAS Collaboration, *Pile-up corrections for jets from proton-proton collisions at $\sqrt{s} = 7$ TeV in ATLAS in 2011*, ATLAS-CONF-2012-064.

[119] ATLAS Collaboration, *Probing the measurement of jet energies with the ATLAS detector using Z+jet events from proton-proton collisions at $\sqrt{s} = 7$ TeV*, ATLAS-CONF-2012-053.

[120] ATLAS Collaboration, *Probing the measurement of jet energies with the ATLAS detector using photon+jet events in proton-proton collisions at $\sqrt{s} = 7$ TeV*, ATLAS-CONF-2012-063.

[121] The ATLAS collaboration, *Commissioning of the ATLAS high-performance b-tagging algorithms in the 7 TeV collision data*, ATLAS-CONF-2011-102.

[122] ATLAS Collaboration, *Measurement of the b-tag Efficiency in a Sample of Jets Containing Muons with 5 fb^{-1} of Data from the ATLAS Detector*, ATLAS-CONF-2012-043.

[123] ATLAS Collaboration, *b-jet tagging calibration on c-jets containing D^{*+} mesons*, ATLAS-CONF-2012-039.

[124] ATLAS Collaboration, *Measurement of the Mistag Rate with 5 fb^{-1} of Data Collected by the ATLAS Detector*, ATLAS-CONF-2012-040.

[125] ATLAS Collaboration, *Reconstruction and Calibration of Missing Transverse Energy and Performance in Z and W events in ATLAS Proton-Proton Collisions at 7 TeV*, ATLAS-CONF-2011-080.

[126] T. Barillari et al., *Local hadronic calibration*, ATL-LARG-PUB-2009-001.

[127] K. Melnikov, F. Petriello, *Electroweak gauge boson production at hadron colliders through $O(\alpha_s^2)$*, *Phys. Rev.* D 74 (2006) 114017 [hep-ph/0609070].

[128] ATLAS Collaboration, *Measurement of the production cross section for Z/γ^* in association with jets in pp collisions at $\sqrt{s} = 7$ TeV with the ATLAS detector*, *Phys. Rev.* D 85 (2012) 032009 [arXiv:1111.2690].

[129] K. Hagiwara, S. Ishihara, R. Szalapski, and D. Zeppenfeld, *Low energy effects of new interactions in the electroweak boson sector*, *Phys. Rev.* D 48 (1993) 2182.

[130] J. M. Campbell and R. K. Ellis, *An update on vector boson pair production at hadron colliders*, *Phys. Rev.* D 60 (1999) 113006.

[131] J. Beringer et al. (Particle Data Group), *The Review of Particle Physics*, *Phys. Rev.* D 86 (2012) 010001.

[132] G. D'Agostini, *Improved Iterative Bayesian Unfolding* [arXiv:1010.0632].

[133] P. Skands, *Tuning Monte Carlo generators: The Perugia tunes*, *Phys. Rev.* D 82 (2010) 074018 [arXiv:1005.3457].

[134] J. Pumplin, D. R. Stump, J. Huston, H. L. Lai, P. M. Nadolsky and W. K. Tung, *New generation of parton distributions with uncertainties from global QCD analysis*, *JHEP* 0207 (2002) 012 [hep-ph/0201195].

[135] A. D. Martin, R. G. Roberts, W. J. Stirling and R. S. Thorne, *Uncertainties of predictions from parton distributions. 1: Experimental errors*, *Eur. Phys. J.* C 28 (2003) 455 [hep-ph/0211080].

[136] ATLAS Collaboration, *Performance of Missing Transverse Momentum Reconstruction in ATLAS with 2011 Proton-Proton Collisions at $\sqrt{s} = 7$ TeV*, ATLAS-CONF-2012-101.

[137] A. Sherstnev and R. S. Thorne, *Parton distributions for LO generators*, *Eur. Phys. J.* C 55 (2008) 553 [arXiv:0711.2473].

[138] I. W. Stewart and F. J. Tackmann, *Theory Uncertainties for Higgs and Other Searches Using Jet Bins*, *Phys. Rev.* D 85 (2012) 034011 [arXiv:1107.2117].

[139] ATLAS Collaboration, *New ATLAS event generator tunes to 2010 data*, ATL-PHYS-PUB-2011-008.

[140] ATLAS Collaboration, *ATLAS tunes of PYTHIA 6 and Pythia 8 for MC11*, ATL-PHYS-PUB-2011-009.

[141] ATLAS Collaboration, *Measurement of hard double-parton interactions in* $W \to \ell\nu$ *+ 2 jet events at* $\sqrt{s} = 7$ TeV *with the ATLAS detector*, submitted to *NPJ* (2013) [arXiv:1301.6872].

Appendix A

Background estimates

A.1 Multijet background estimate

In the following sections, details of the multijet background estimate are presented. Section A.1.1 describes the motivation and details for the selection used to form the multijet template from data. Section A.1.2 describes the method used to estimate shape uncertainties on the multijet template. Section A.1.3 includes the fit result for the $E_{\mathrm{T}}^{\mathrm{miss}}$, $m_T(W)$and lepton p_{T} distributions.

A.1.1 Multijet Background Template Choice

The data-driven templates used to model the multijet background are chosen based on the need to minimize kinematic biases with respect to the standard signal selection, while maintaining the large number of events required to obtain smooth templates. Large lepton-filtered $b\bar{b}$ and $c\bar{c}$ dijet samples, combined according to their expected cross-sections, are used to determine how to vary the leptonic selection to

obtain the best templates.

Very few events from the $b\bar{b}$ and $c\bar{c}$ samples pass the full analysis selection, so a relaxed set of requirements is used in place of the standard one. Specifically, in the studies below, the $E_{\mathrm{T}}^{\mathrm{miss}}$ and $m_T(W)$ requirements are inverted ($E_{\mathrm{T}}^{\mathrm{miss}} < 25$ GeV and $m_T(W) < 40$ GeV), forming a multijet control region which can be used when comparing templates with data. Even in this control region, very few $b\bar{b}$ and $c\bar{c}$ events have both a selected lepton and a b-tagged jet, as can be seen in Figure A.1, making this sample unsuitable to study the bias in the CombNN variable. To further increase the number of events, a b-tagged jet is therefore not required in the following.

It is clear that the sample resulting from this modified selection is kinematically biased with respect to the standard selection. As shown in Figure A.2, even the b-tagging requirement affects the event kinematics. However, this sample can be used as a testing ground for the influence of modified leptonic selections on the kinematics of dijet events.

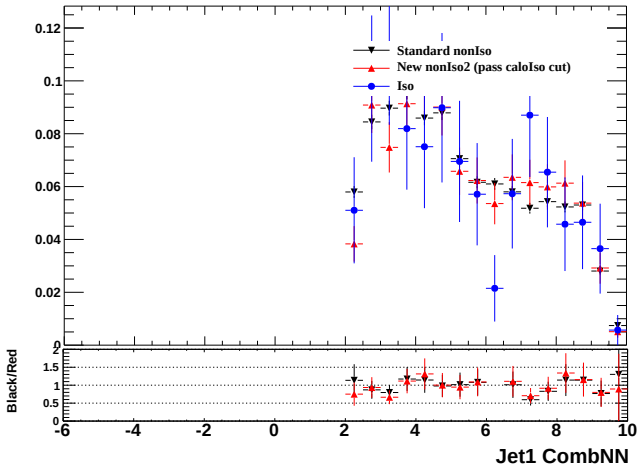

Figure A.1: CombNN distribution for b-tagged jets in the multijet control region ($E_{\mathrm{T}}^{\mathrm{miss}} < 25$ GeV and $m_T(W) < 40$ GeV) in $b\bar{b}$ and $c\bar{c}$ events. The number of events in the sample which satisfies the standard leptonic selection ("Iso") is very small.

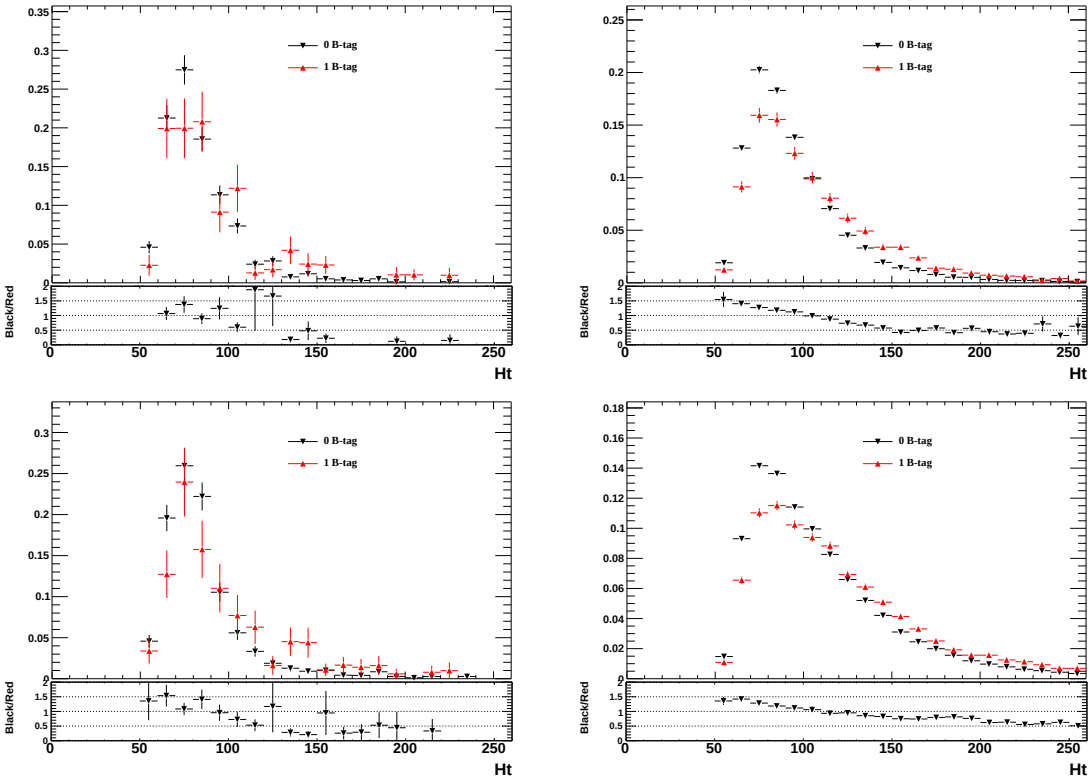

Figure A.2: H_{T} distribution in the electron (top) and muon (bottom) channels, with and without a b-tag requirement in $b\bar{b}$ and $c\bar{c}$ events in the multijet control region. The standard leptonic selection is used in the left plots, while in the right plots the isolation requirements are inverted. In these plots, it is clear that the b-tagging requirement affects the kinematic of selected events, indicating that the untagged shapes cannot be used as a model of the tagged shapes.

The modified leptonic selections are based on inverting cuts. For muons, three cuts are considered and combined to form five separate templates. The same is done for electrons. The cuts considered are the two isolation requirements (calorimetric and tracking) for both electrons and muons (AntiIsolated), the impact parameter (d_0) cut for the muons (Anti-d_0), and the Tight++ selection for the electrons (AntiElectrons)[1]. The definition of the templates resulting from these combination are shown in Table A.1, for the muon and electron selection. The first entry in the table defines the standard selection used for the signal leptons.

Table A.1: Modified leptonic selections used to generate data-driven templates for the multijet background. The templates chosen to represent the multijet background are marked with (*).

Modified muon selection for multijet templates			
Selection name	Calorimeter Isolation	Track Isolation	d_0 significance
Iso (standard selection)	Pass	Pass	< 3
Standard nonIso	Fail	Fail	< 3
New nonIso	Fail	Pass	< 3
New nonIso2 (*)	Pass	Fail	< 3
Standard antiD0	Pass	Pass	> 3
New antiD0	Pass OR Fail	Pass	> 3
Modified electron selection for multijet templates			
Selection name	Calorimeter Isolation	Track Isolation	Tight++
Iso (standard selection)	Pass	Pass	Pass
Standard nonIso	Fail	Fail	Pass
New nonIso	Pass	Fail	Pass
New nonIso2	Fail	Pass	Pass
Standard antiEle	Pass	Pass	Fail
New antiEle (*)	Pass OR Fail	Pass	Fail

The templates resulting from applying the standard and modified leptonic selec-

[1]Since the trigger used in the electron channel is based on the Medium++ requirements, the AntiElectrons used in the multijet template are required to be of Medium++ quality. AntiElectrons are therefore defined as electrons passing the Medium++ requirements but failing at least 2 of the Tight++ cuts. These cuts are: ConversionMatch, TrackMatchPhi, TrackMatchEoverP, TrackTRThits.

tions to dijet events are shown in Figure A.3 for the muon and electron channels. In the muon case, the least biased sample with respect to the standard selection is found to be the AntiIsolated option where only the tracking isolation cut is required to fail: "New nonIso2" in Figure A.3, middle left. For the electron channel, all the pure AntiIsolated templates show large biases, and the best performance with reasonable statistics is achieved by the AntiElectron selection where the Calorimeter Isolation cut is not required: "New antiEle" in Figure. A.3, bottom right. The increase in H_{T} with increasing AntiIsolation should be expected in dijet events: the larger is the energy in a cone around the selected lepton, the larger will be the jet recoiling against it.

As a result of these studies in the pre-tag, low-$E_{\mathrm{T}}^{\mathrm{miss}}$ and low-$m_T(W)$ region, the "New nonIso2" and "New antiEle" selections are chosen to produce multijet templates for the W+b-jets analysis regions. The following sections describe the method used to assign shape uncertainties to these templates in the W+b-jets analysis regions, and to estimate their normalization

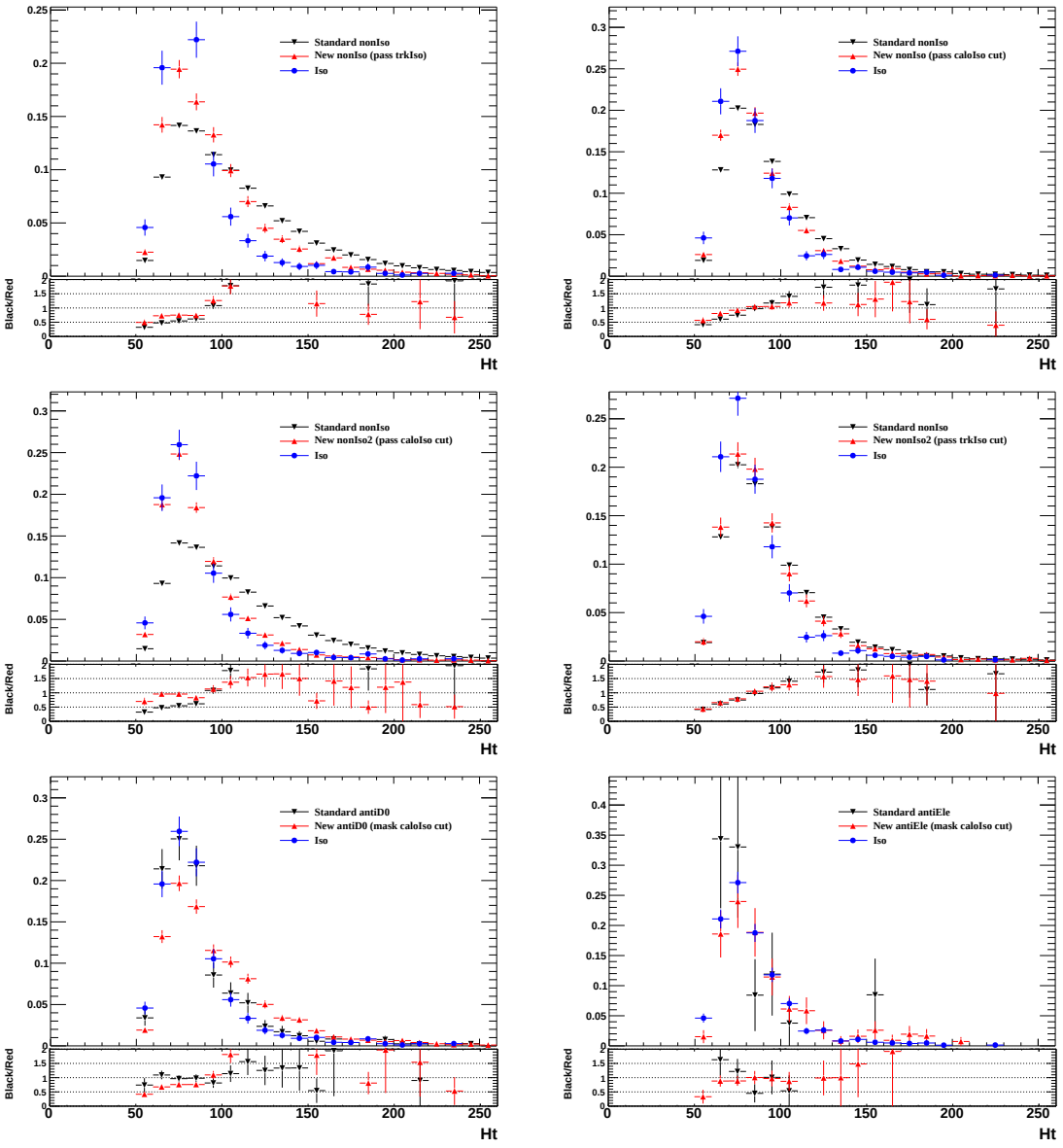

Figure A.3: Comparisons between various modified leptonic selections with the standard one in $b\bar{b}$ and $c\bar{c}$ events for the muon (left) and electron (right) channels. The selection chosen for the multijet template in the muon channel is the one labeled "New nonIso2" (middle left). The one chosen in the electron channel is labeled "New antiEle" (bottom right).

A.1.2 Multijet Background Shape Uncertainty

The systematic uncertainty on the multijet template shape is assessed using the multijet control region defined by requiring $E_{\mathrm{T}}^{\mathrm{miss}} < 25$ GeV and $m_T(W) < 40$ GeV, based on the following strategy.

Using the modified leptonic selection defined above, multijet templates are obtained for this control region for all the fitted kinematic and b-tagging distributions. These templates are compared to data, as in Figures A.4 (electron) and A.5 (muon), after accounting for the non-multijet contributions based on Monte Carlo simulation. Figures A.4 and A.5 include distribution of the CombNN, H_{T}, and $m_T(W)$ variables in the 1-jet and 2-jet regions. The overall agreement between data and the total signal plus background model is in large part due to the accurate choice of template discussed in the previous section.

Small disagreements between the data and the model can be attributed to flaws in the multijet background template, assuming that all other components are correctly modeled by Monte Carlo. For example, looking at the CombNN distribution in the electron 1-jet region (Figure A.4, top left), one could argue that the electron multijet template slightly underestimates the fraction of heavy-flavor (high CombNN weight) events. The corresponding distribution in the muon channel (Figure A.5, top left) indicates an opposite behavior: the muon multijet template overestimates the fraction of heavy-flavor events. These discrepancies are not used to correct the multijet templates in the signal region, but to produce modified multijet templates. These modified templates are then used instead of the nominal one to determine a systematic uncertainty on the multijet shape.

Each modified multijet background template is produced by scaling the nominal one by the histogram ratio [(Data - non-multijet)/Multijet] obtained in the multijet control region. The difference between using the nominal and the modified templates is then used to establish a shape systematic. The corresponding effect on the measured cross-section is larger in the electron sample and it is in the range 1-10% depending on the jet multiplicity and p_{T} interval considered.

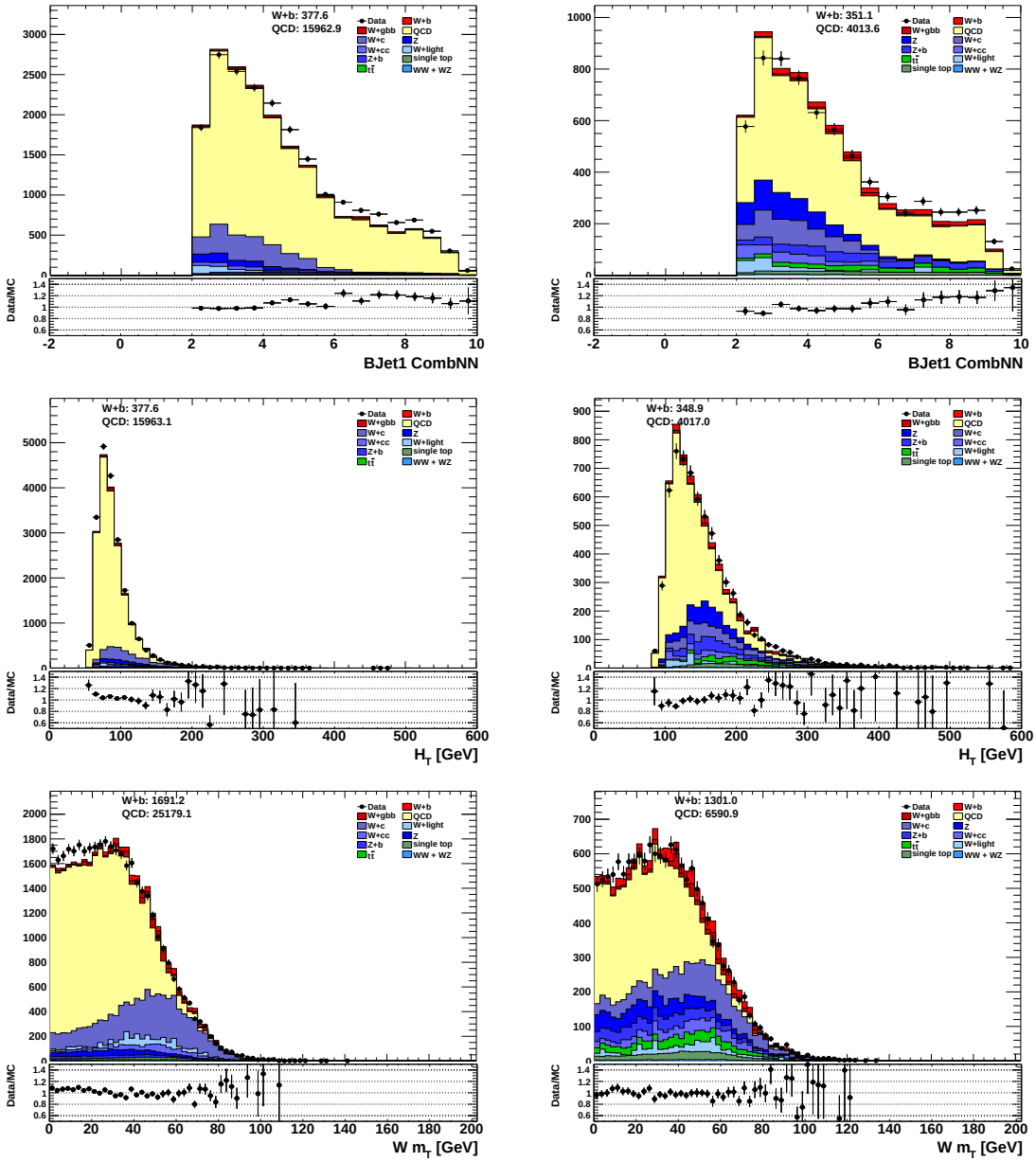

Figure A.4: Multijet kinematics in the electron channel in the control region defined by $E_{\mathrm{T}}^{\mathrm{miss}} < 25$ GeV and $m_T(W) < 40$ GeV (the $m_T(W) < 40$ GeV cut not applied in $m_T(W)$plot). The multijet template (yellow) is obtained using the modified leptonic selection described in the previous section. The 1-jet region is shown in the left column, the 2-jet region in the right one.

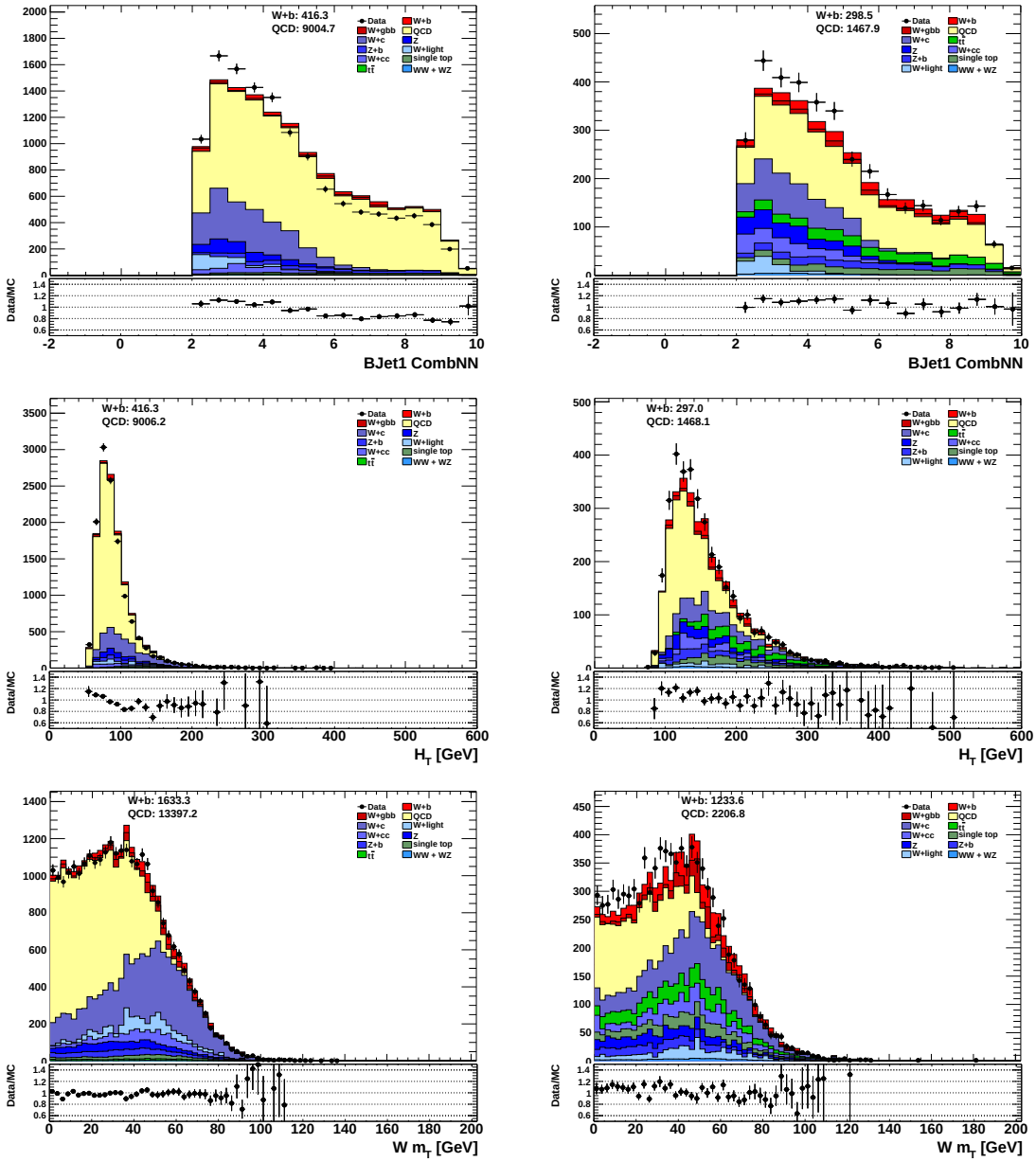

Figure A.5: Multijet kinematics in the muon channel in the control region defined by $E_{\mathrm{T}}^{\mathrm{miss}} < 25$ GeV and $m_T(W) < 40$ GeV (the $m_T(W) < 40$ GeV cut not applied in $m_T(W)$plot). The multijet template (yellow) is obtained using the modified leptonic selection described in the previous section. The 1-jet region is shown in the left column, the 2-jet region in the right one.

A.1.3 Multijet Background Normalization

The normalization of the multijet template is assessed, in each analysis region, by performing a fit to the $E_{\mathrm{T}}^{\mathrm{miss}}$ distribution in data after relaxing the $m_T(W)$ requirement from 60 GeV to 40 GeV, and removing the $E_{\mathrm{T}}^{\mathrm{miss}} > 25$ GeV requirement. The templates used in this fit for the W/Z+jets, $t\bar{t}$, single-top and diboson processes are based on Monte Carlo simulation. The multijet and the W+jets template normalizations are free parameters of the fit, while those of the other components are fixed to their expected cross-sections. The $E_{\mathrm{T}}^{\mathrm{miss}}$ distributions, normalized to the results of the fit, are presented in Figure A.6 for the 1-jet and 2-jet regions in the muon and electron channels. The multijet background, in yellow, is visibly larger in the electron channel, and concentrated at low $E_{\mathrm{T}}^{\mathrm{miss}}$ values.

To estimate the uncertainty of the multijet background normalization, the $E_{\mathrm{T}}^{\mathrm{miss}}$ fit results are compared in each analysis region with the results obtained by fitting the $m_T(W)$ and lepton p_{T} distributions. As a result of the comparison, an uncertainty of 50%, applied as a Gaussian constraint in subsequent ML fits, is assigned to the multijet background normalization in the 1-jet and 2-jet regions. In the 4-jet region used to estimate the $t\bar{t}$ background, this uncertainty is estimated from the different fit results to be 100%. The multijet background normalization resulting from fits to the three distributions are shown in Table A.2. In the differential measurement, the multijet background normalization is extrapolated from the inclusive estimates, and the same 50% uncertainty is applied as an independent Gaussian constraint in each $p_{\mathrm{T}}^{b-\mathrm{jet}}$ bin.

Since the W+jets component is left free in the signal region fits, and it is given a

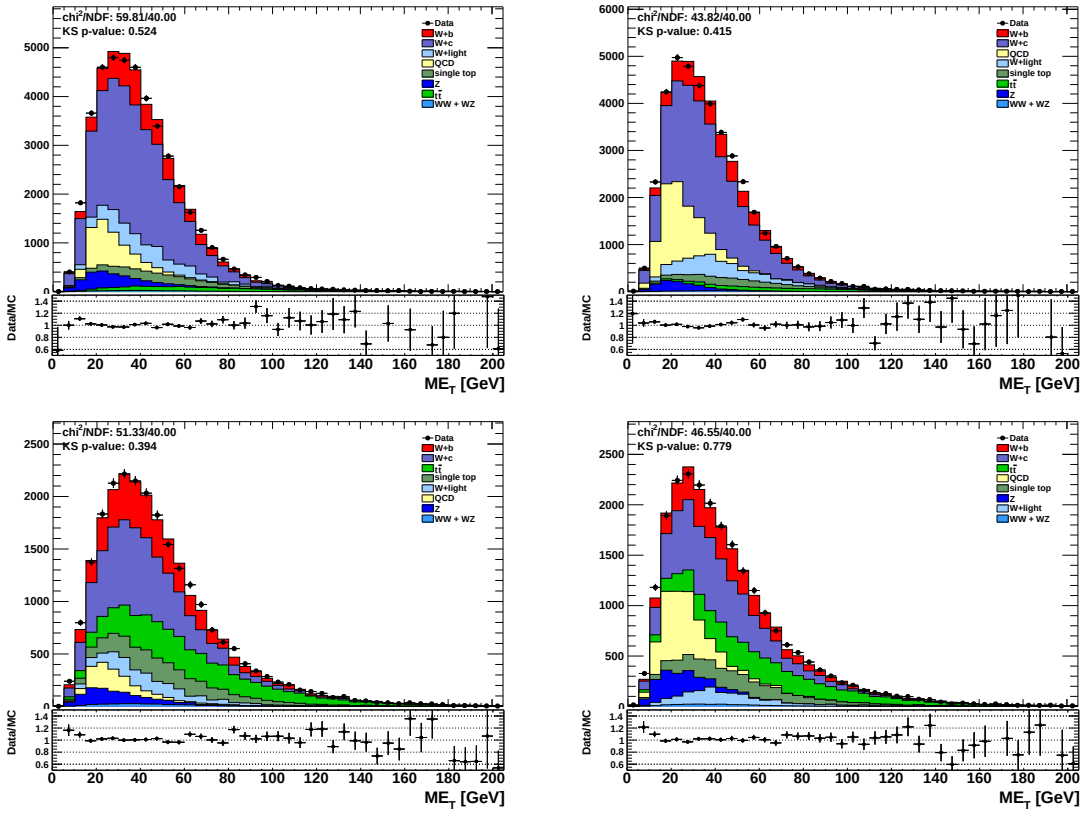

Figure A.6: $E_{\mathrm{T}}^{\mathrm{miss}}$ distribution in data and MC simulation in the 1-jet (top) and 2-jet (bottom) analysis regions, in the muon (left) and electron (right) channels. MC samples are normalized to the results of the multijet background fit. To enhance the multijet contribution in the fitted region, the $m_T(W)$ selection is loosened from 60 GeV to 40 GeV.

100% Gaussian constraint in the $t\bar{t}$ control region fits, the normalization scale factors obtained in the multijet fits are not taken into account except for the figures shown in this chapter and in Section 7.4.8. They are presented in Table A.3 as a reference.

The template derived from data using the modified leptonic selection also contains a considerable fraction of ElectroWeak (EW) events. This is due to the non-negligible number of signal leptons which are removed by the tight identification and isolation cuts, and re-included once these cuts are inverted. This fraction is estimated from

Monte Carlo and subtracted from the template, and in the muon (electron) sample it is found to be 36% (39%) for the 1-jet bin and 56% (52%) for the 2-jet bin. The $E_{\mathrm{T}}^{\mathrm{miss}}$ fit is iterated twice to verify that the uncertainties on the EW subtraction from the multijet template are negligible and already accounted for by the overall uncertainties on the multijet contribution. In the second iteration, the EW contribution to be subtracted from the multijet template is updated according to the fit result of the first iteration. No difference is observed by taking an additional iteration. The resulting templates produce variations no bigger than 2.8% on the fitted number of W+b-jets events with respect to the nominal results.

Table A.2: Normalization scale factors for the data-driven multijet background templates obtained in the template fits to the $E_{\mathrm{T}}^{\mathrm{miss}}$, $m_T(W)$, and lepton p_{T} distributions in different analyses regions.

Multijet fitted scale factor	$E_{\mathrm{T}}^{\mathrm{miss}}$ Fit	$m_T(W)$ Fit	Lepton p_{T} Fit
Electron 1Jet 1 b-tag	1.449 ± 0.067	1.531 ± 0.117	1.942 ± 0.154
Electron NJets>=1 1 b-tag	1.594 ± 0.065	1.599 ± 0.122	2.075 ± 0.159
Electron 2Jets 1 b-tag	2.047 ± 0.151	1.761 ± 0.266	1.885 ± 0.370
Electron 3Jets 1 b-tag	1.612 ± 0.399	1.257 ± 0.930	2.688 ± 0.897
Electron NJets>=4 1b-tag	1.075 ± 0.806	0.000 ± 0.667	0.000 ± 6.124
Muon 1Jet 1 b-tag	0.281 ± 0.024	0.212 ± 0.028	0.265 ± 0.027
Muon NJets>=1 1 b-tag	0.286 ± 0.023	0.213 ± 0.028	0.250 ± 0.028
Muon 2Jets 1 b-tag	0.298 ± 0.064	0.294 ± 0.080	0.214 ± 0.023
Muon 3Jets 1 b-tag	0.021 ± 1.423	0.096 ± 0.299	0.305 ± 0.228
Muon NJets>=4 1 b-tag	0.066 ± 1.690	0.601 ± 0.763	0.000 ± 1.226

Table A.3: Normalization scale factors for the W+jets templates obtained in the template fits to the $E_{\mathrm{T}}^{\mathrm{miss}}$, $m_T(W)$, and lepton p_{T} distributions in different analyses regions.

W+jets fitted scale factor	$E_{\mathrm{T}}^{\mathrm{miss}}$ Fit	$m_T(W)$ Fit	Lepton p_{T} Fit
Electron 1Jet 1 b-tag	1.275 ± 0.018	1.239 ± 0.019	1.213 ± 0.022
Electron NJets>=1 1 b-tag	1.266 ± 0.017	1.254 ± 0.018	1.227 ± 0.022
Electron 2Jets 1 b-tag	1.207 ± 0.033	1.201 ± 0.035	1.239 ± 0.046
Electron 3Jets 1 b-tag	1.470 ± 0.089	1.633 ± 0.137	1.483 ± 0.113
Electron NJets>=4 1 b-tag	2.244 ± 0.219	2.437 ± 0.278	2.342 ± 0.228
Muon 1Jet 1 b-tag	1.241 ± 0.017	1.242 ± 0.016	1.243 ± 0.015
Muon NJets>=1 1 b-tag	1.194 ± 0.014	1.182 ± 0.013	1.226 ± 0.014
Muon 2Jets 1 b-tag	1.143 ± 0.030	1.102 ± 0.028	1.192 ± 0.029
Muon 3Jets 1 b-tag	1.197 ± 0.062	1.194 ± 0.075	1.189 ± 0.082
Muon NJets>=4 1 b-tag	1.478 ± 0.260	1.228 ± 0.237	1.311 ± 0.173

A.2 $t\bar{t}$ background estimate: cross-checks

To verify the validity of the $t\bar{t}$ estimate, three cross-check estimates are investigated. The $t\bar{t}$ normalization scale factors resulting from the reference $t\bar{t}$ estimate and from these cross-check are summarized for the muon and electron channel in Table A.4.

The first cross-check uses the same $t\bar{t}$ control region ("at least 4 jets 1-b-tag"), but it is based on fitting an observable independent of the CombNN weight: the number of jets distribution. The fit projections corresponding to this fit are shown in Figure A.7 below.

The second cross-check uses a fit to the same observable as the $t\bar{t}$ estimate (CombNN weight), but in a different control region containing events with exactly three jets and exactly one b-tag ("3-jet 1-b-tag"). This control region is less powerful than the "at least 4 jets 1-b-tag" one due to the significant contamination from W+jets events, however it represents a useful cross-check since it is statistically independent from the reference. The same assumptions and constraints are applied to the fit, whose results are shown in Figure A.8.

Finally, the third cross-check uses the distribution of the number of jets in events with at least 1 jet and exactly 1 b-tag ("at least 1 jet 1-b-tag"). This method is not statistically independent from the others, since it shares most of the same events. However, it includes the information of additional jet bins, and it can be used to check the validity of the extrapolation of the reference estimate to the analysis region. The results of this fits are sown in Figure A.9.

The $t\bar{t}$ normalization scale factors estimated in these three cross-checks are pre-

sented in Table A.4, together with to the ones obtained using the standard fit (CombNN variable in "at least 4 jets 1-b-tag" region). The agreement between the different estimates is very good, giving confidence in the $t\bar{t}$ normalization scale factors used in the analysis.

Table A.4: $t\bar{t}$ normalization scale factors estimated using different strategies. The first column shows the reference estimate, based on a fit to the CombNN distribution in the "at least 4 jets 1-b-tag" control region. The second column is based on a fit to the same variable in the "3-jet 1-b-tag" region. The last two columns estimates are based on fits to the number of jets distribution in the "at least 4 jets 1-b-tag" and "at least 1 jet 1-b-tag" regions.

$t\bar{t}$ SF	CombNN (N $\geq$ 4)	CombNN (N = 3)	NJets (N $\geq$ 4)	NJets (N $\geq$ 1)
Muon	1.09 $\pm$ 0.06	0.91 $\pm$ 0.16	0.95 $\pm$ 0.04	1.08 $\pm$ 0.02
Electron	1.08 $\pm$ 0.07	1.09 $\pm$ 0.20	1.07 $\pm$ 0.05	1.12 $\pm$ 0.02

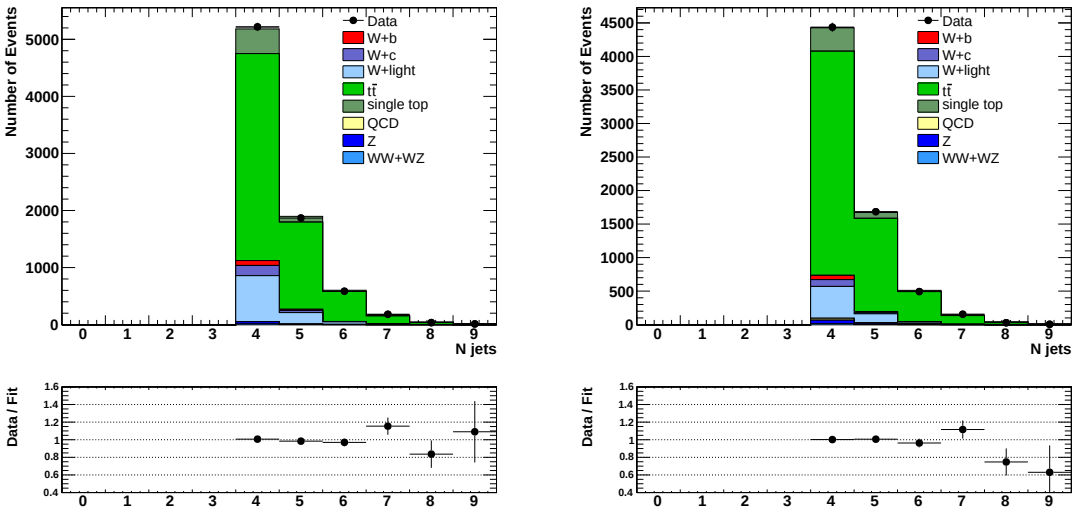

Figure A.7: Fitted number of jets distribution in the at least 4 jets 1-b-tag control region for the muon (left) and electron (right) samples. MC samples are normalized to the results of the fit. The results of this fit are used to cross-check the $t\bar{t}$ normalization scale factors. **Check flavor label in 4-jet plots.**

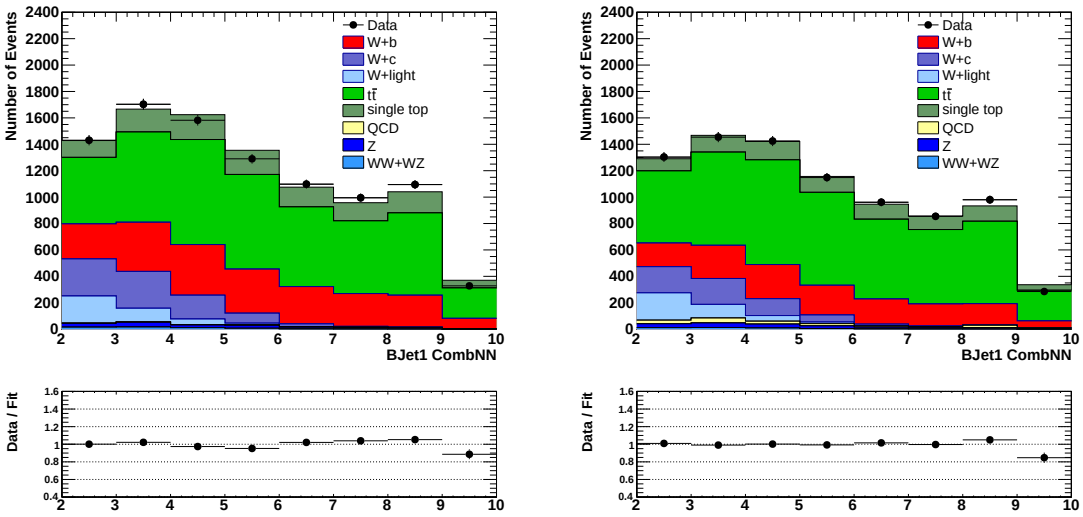

Figure A.8: Fitted CombNN distribution in the "3-jet 1-b-tag" control region for the muon (left) and electron (right) samples. MC samples are normalized to the results of the fit. The results of this fit are used to cross-check the $t\bar{t}$ normalization scale factors.

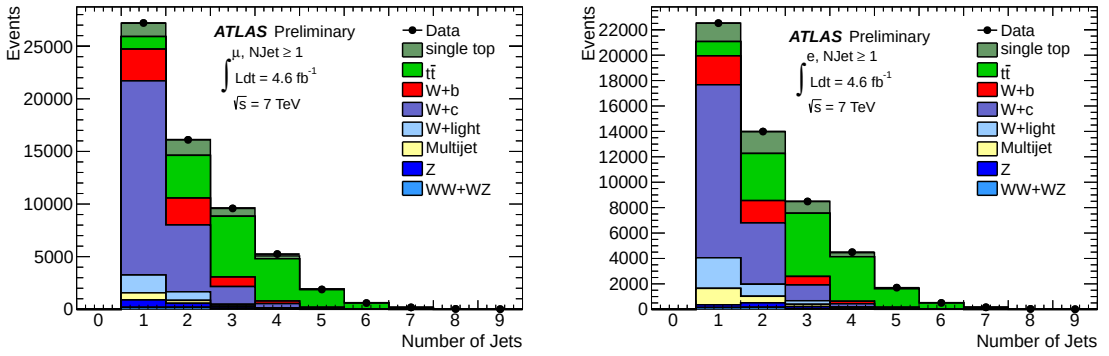

Figure A.9: Fitted number of jets distribution in the "at least 1 jet 1-b-tag" control region for the muon (left) and electron (right) samples. MC samples are normalized to the results of the fit. The results of this fit are used to cross-check the $t\bar{t}$ normalization scale factors.

A.3 Single-top background estimate: cross-checks

The discrepancy observed in Table 7.7 between the fits to the H_{T} and $m(Wb)$ distributions in the 1-jet region is not fully understood, but it is likely to arise from mismodelling of at least one of the two observables, H_T and $m(Wb)$. The table is added below (A.5) for convenience.

Table A.5: Single-top normalization scale factors estimated by fitting the H_{T} and the $m(Wb)$ distributions in the 1-jet and 2-jet analysis regions. The 2-jet scale factors based on the $m(Wb)$ distribution are applied in the 2-jet region. The 1-jet scale factors are not used, as described below. The AcerMC single-top Monte Carlo simulation is used for these estimates.

Observable	μ 1-jet	e 1-jet	μ 2-jet	e 2-jet
H_{T}	0.66 ± 0.17	0.77 ± 0.14	1.12 ± 0.11	1.17 ± 0.17
$m(Wb)$	1.02 ± 0.20	1.76 ± 0.25	1.09 ± 0.13	1.13 ± 0.15

To study the issue further, another set of single-top Monte Carlo samples, generated with MC@NLO interfaced to Herwig, is compared to the reference AcerMC interfaced to Pythia. Since both samples are scaled to the same NLO total cross-section, any difference observed in the predicted number of events can only be due to differences in acceptance (from inclusive to 1-jet cross-section) or shape.

In the 1-jet region, significant differences between these samples are found both in the number of predicted events and in the shape of each distribution, as shown in Figure A.10. In this region, MC@NLO estimates $\sim 27\%$ more events than AcerMC. This behavior is observed both in the muon and electron channel and also when considering the t-channel, s-channel and Wt single-top production separately. When using the MC@NLO templates scaled to the number of events predicted by AcerMC, the fit results for the H_T and $m(Wb)$ distributions are in rough agreement with those

observed in the AcerMC fits, and the discrepancy between the two distributions persists, as summarized in Table A.6.

Table A.6: Single-top normalization scale factors obtained using the AcerMC expected number of events, but the MC@NLO template shape.

Observable	μ 1-jet	e 1-jet	μ 2-jet	e 2-jet
H_T (MC@NLO Shape)	0.76 ± 0.15	0.77 ± 0.14	1.10 ± 0.11	1.14 ± 0.16
Wb Mass (MC@NLO Shape)	1.09 ± 0.18	1.50 ± 0.22	1.04 ± 0.12	1.14 ± 0.15

In the 2-jet region, the H_{T} and the $m(Wb)$ fits lead to consistent results. In this region, the AcerMC and MC@NLO predicted number of events are found to be in agreement at the 2% level, and only minor differences in shape can be observed, as shown in Figure A.10. Moreover, using MC@NLO to model the single-top shape and scaling it to the number of events predicted by AcerMC, the fit to the H_T and $m(Wb)$ distributions return normalization scale factors that are in good agreement with each other and with the corresponding fits that use AcerMC templates.

As shown in Figure A.11, the CombNN weight distributions of AcerMC and MC@NLO do not show any particular discrepancy in addition to those discussed in section 7.5.4 and attributed to the decay tables in Herwig and Pythia.

As a result of these cross-checks, the single-top estimate is used only in the 2-jet region. In the 1-jet region, the AcerMC expectation is used, with a normalization uncertainty (50%) consistent with the differences observed between AcerMC and MC@NLO, and between the H_{T} and $m(Wb)$ fits. Fortunately, the single-top background is much smaller in the 1-jet than in the 2-jet region, so the 1-jet region measurement is competitive with the one in the 2-jet region.

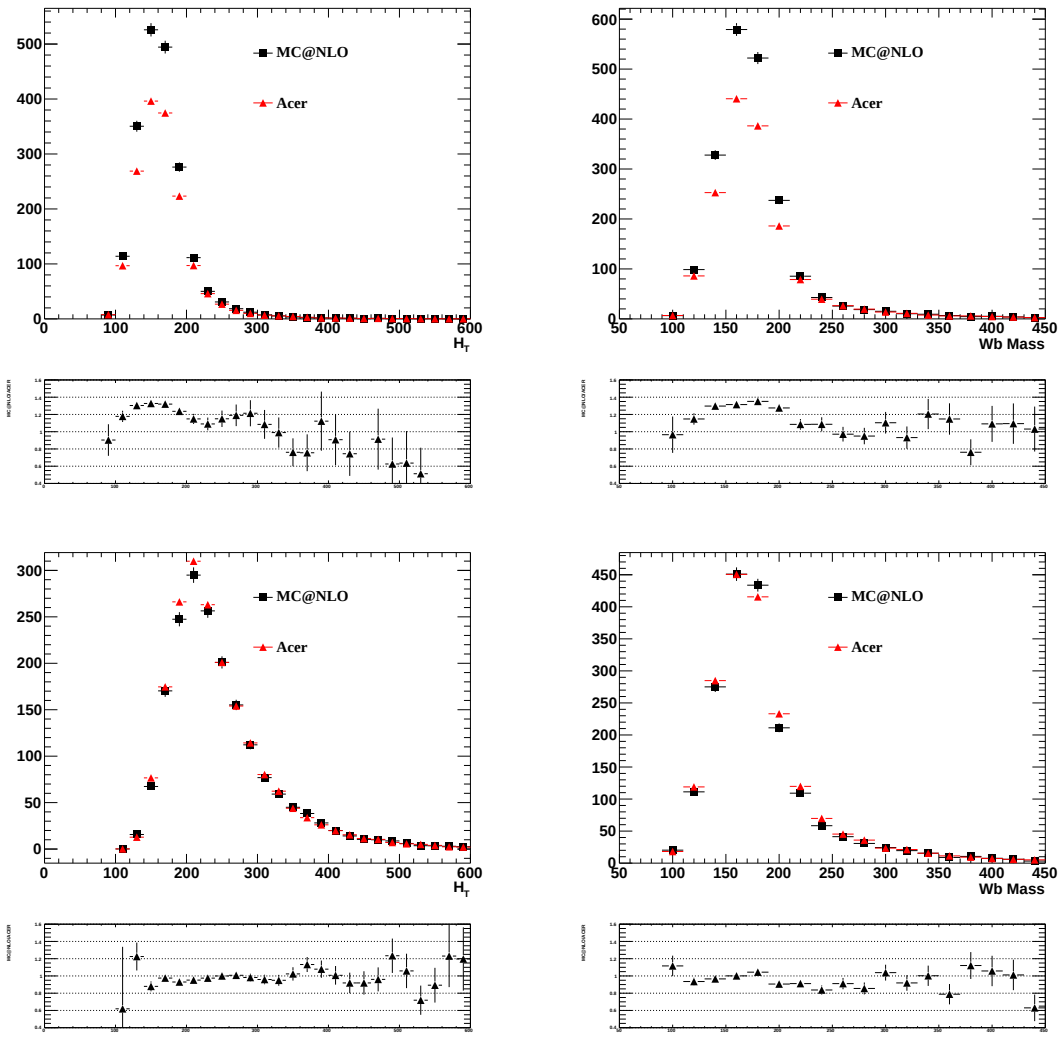

Figure A.10: Comparisons between AcerMC and MC@NLO single-top H_T (left) and $m(Wb)$ distributions (right) in the 1-jet (top) and 2-jet (bottom) analysis regions. Plots are normalized to the corresponding expectation. The difference observed in the 1-jet region are striking, and they result in a large normalization uncertainty.

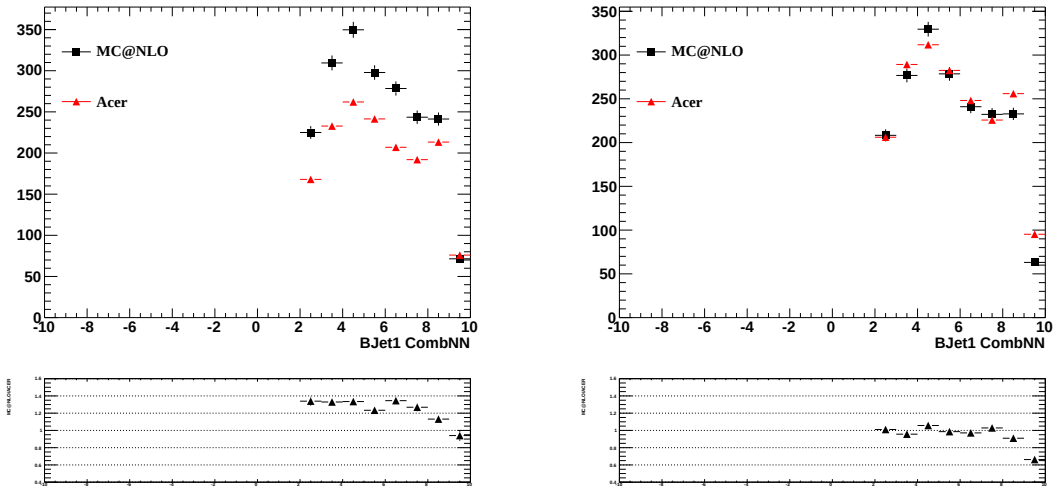

Figure A.11: Comparisons between AcerMC (showered with Pythia) and MC@NLO (showered with Herwig) single-top CombNN distribution in the 1-jet (left) and 2-jet (right) analysis regions. Plots are normalized to the corresponding Monte Carlo expectation. The shape differences observed in the high-CombNN region are consistent with the differences in the Pythia and Herwig decay tables.

A.4 W+jets template choice

The following sections discuss the motivation for choosing PYTHIA-based templates used for the CombNN shapes of the W+b-jets, W+c-jets, W+light-jets samples, as well as their preparation and validation.

In particular, Sections A.4.1 and A.4.2 discuss the comparisons of properties of b-tagged jets among different $t\bar{t}$ simulations and between simulation and data. These studies are performed in $t\bar{t}$ control regions highly enriched in b-jet content. Section A.4.3 presents generator-level studies of b-tagging-related quantities in different W+b-jets simulations. Finally, Section A.4.4 explains the method used to produce high statistics PYTHIA CombNN templates from Monte Carlo samples originally showered with HERWIG, and Section A.4.5 describes the validation of the PYTHIA-based templates.

A.4.1 Properties of b-tagged jets in $t\bar{t}$ MC

The $t\bar{t}$ signal dominates the "at least 4 jets 1-b-tag" control region, and the sample of b-tagged jets in $t\bar{t}$ events in this region consists almost entirely of true b-jets, as shown in Figure A.12. Therefore the $t\bar{t}$ control region can be used to study in detail the properties of b-jets in the available Monte Carlo samples and in data.

The shape of the CombNN weight for b-tagged jets in the $t\bar{t}$ control region is shown in Figure A.13 (left) for the three available simulations: MC@NLO interfaced to HERWIG for parton showering, POWHEG+PYTHIA and POWHEG+HERWIG. Discrepancies between the parton shower programs (PYTHIA and HERWIG) are clearly visible in the tail of the distribution, for values larger than 8, while only smaller

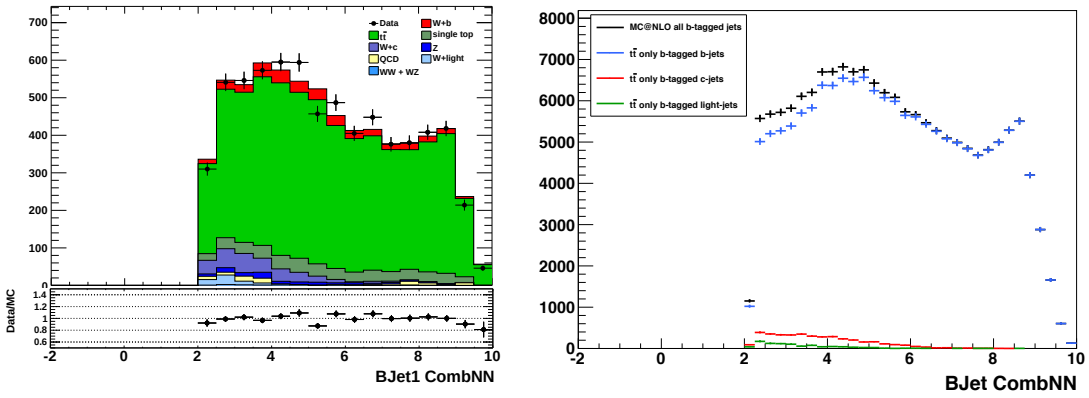

Figure A.12: *Left:* Distribution of CombNN weight for b-tagged jets in the $t\bar{t}$ control region in data and Monte Carlo. The $t\bar{t}$ component represents more than 80% of the sample. *Right:* The same distribution, only showing the $t\bar{t}$ Monte Carlo flavor composition: b-tagged jets in this region are for the most part (96.9%) true b-jets.

features are noticeable when comparing different matrix element simulations with the same parton shower (MC@NLO +Herwig and Powheg+Herwig). Since the kinematic distributions in MC@NLO and Powheg are very similar, as shown in the Figure A.13 (right), the discrepancies in the b-tagging weight must derive from the treatment of b-jets in the different parton shower programs. To validate this conclusion, the properties of the b-taggers were studied, and the discrepancies in the tagger weight between Herwig and Pythia were traced to differences in number of tracks per secondary vertex reconstructed by the b-tagging algorithm, as shown in Figure A.14.

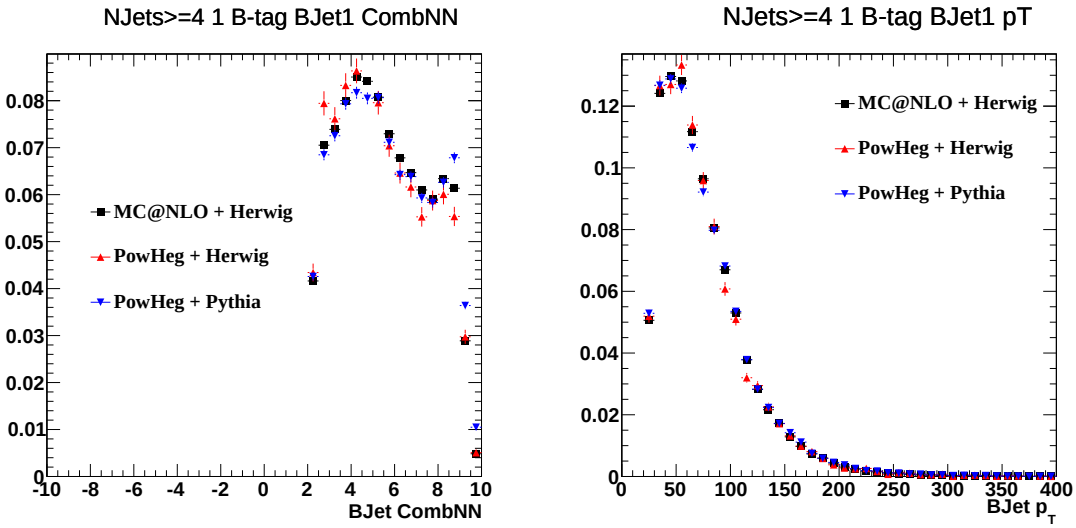

Figure A.13: Distribution of CombNN weight (left) and p_{T} (right) for the b-tagged b-jets in the $t\bar{t}$ control region, for the different available $t\bar{t}$ Monte Carlo simulations: MC@NLO +Herwig, PowHeg+Pythia and PowHeg+Herwig.

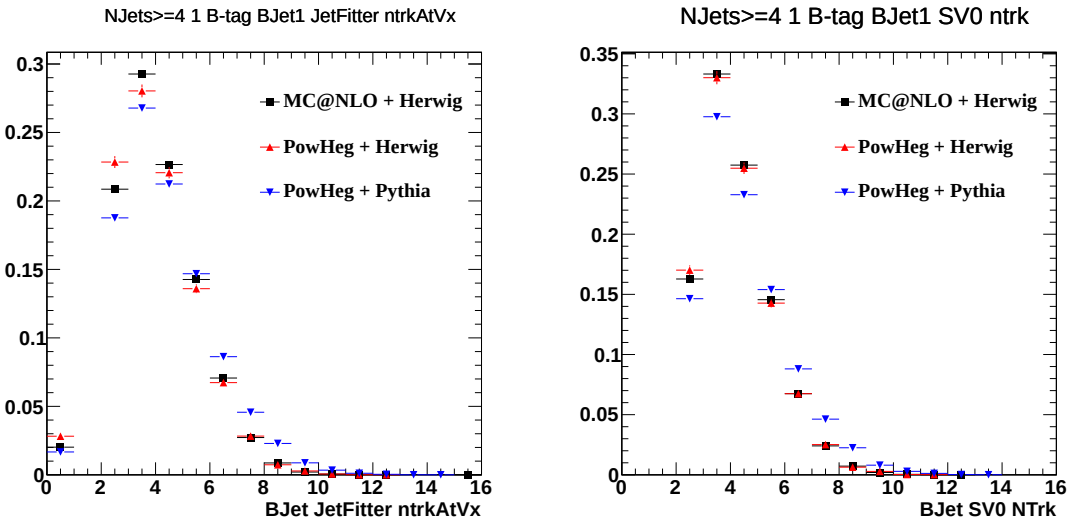

Figure A.14: Distribution of number of tracks per secondary vertex reconstructed by the JetFitter (left) and the SV0 (right) taggers in the $t\bar{t}$ control region, for the different available $t\bar{t}$ Monte Carlo simulations: MC@NLO +Herwig, PowHeg+Pythia and PowHeg+Herwig. Here the differences between Pythia and Herwig are the clearest.

A.4.2 Properties of b-tagged jets in $t\bar{t}$ data

Having observed differences in the CombNN b-tagging weight in different Monte Carlo simulations, data was used to determine which simulation to use for the W+b-jets templates of the signal region fit. The $t\bar{t}$ control region was tightened with an additional b-tag requirement to further reduce the contamination from W+c-jets and W+light-jets ("at least 4 jets 2-b-tags"), and it was used to compare directly the b-jets in data and Monte Carlo simulation[2].

Figure A.15 shows the distributions of the CombNN weight and of the number of tracks per secondary vertex reconstructed by the JetFitter algorithm, for MC@NLO +Herwig and Powheg+Pythia. Pythia templates show acceptable agreement with data, while Herwig templates show large biases, especially in the number of tracks per secondary vertex.

[2] This region has slightly lower statistics, and it suffers from a disagreement in normalization originating from the requirement of the second b-tagged jet. This disagreement, which has been observed in other analysis groups including the $t\bar{t}$ and $Z+b$ groups, is not of current interest and we therefore we normalize the total expected Monte Carlo to the number of events observed in data.

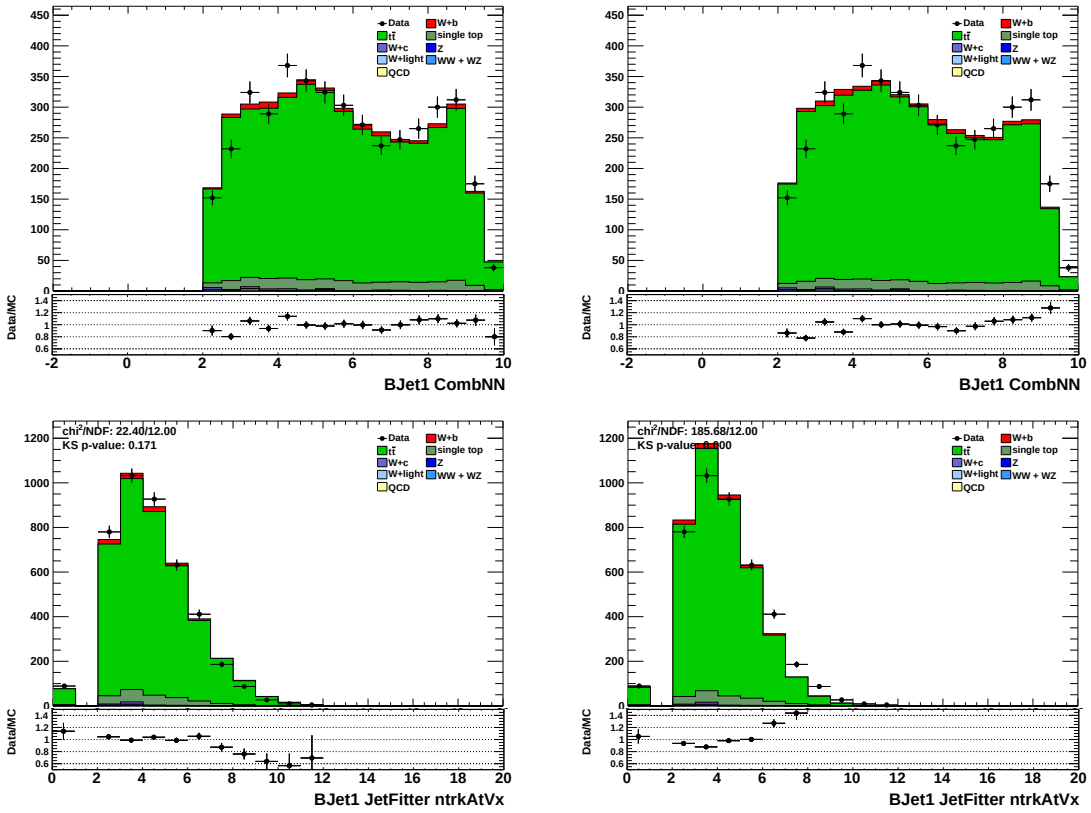

Figure A.15: Distribution of CombNN weight (top), and of the number of tracks per secondary vertex reconstructed by the JetFitter tagger (bottom), in the region with at least 4 jets and exactly 2 b-tags, for data and different $t\bar{t}$ Monte Carlo simulations: POWHEG+PYTHIA (left) and MC@NLO +HERWIG (right). The PYTHIA distributions (right) show better agreement with data.

A.4.3 Generator-level studies in W+b-jets MC

Since HERWIG and PYTHIA differ in both the fragmentation of b-quarks and in the decay tables of B-hadrons, reconstruction-level and generator-level distributions were studied to understand which of these two differences was causing the difference in number of tracks per secondary vertex.

A small sample of $W + b\bar{b}$ Monte Carlo events was generated using ALPGEN +PYTHIA and compared to the available ALPGEN +HERWIG sample. Subsequently, samples were generated using the EVTGEN [**?**] program to include up-to-date decay tables uniformly to both PYTHIA and HERWIG. The samples used in this section are:

- ALPGEN +HERWIG (default).
- ALPGEN +PYTHIA. Dataset IDs : 126530-126733.
- ALPGEN +HERWIG +EVTGEN. Dataset IDs : 126731-126734.
- ALPGEN +PYTHIA +EVTGEN. Dataset IDs : 126735-126738.

Comparisons between these four samples are shown in Figure A.16. While the b-jet kinematics are found to be very similar among the four samples, the properties of tracks inside b-tagged jets show ALPGEN +HERWIG as the clear outlier with respect to both the ALPGEN +PYTHIA and EVTGEN samples. In particular, the agreement between the two EVTGEN samples indicates that the main discrepancies between HERWIG and PYTHIA are caused by differences in the decay tables and not in the fragmentation schemes.

The discrepancies observed between ALPGEN +HERWIG and ALPGEN +PYTHIA at the reconstructed-level can also be seen at the generator-level. Figure A.17 shows

the number of particles with $p_{\mathrm{T}} > 300$ MeV and within $\Delta R = 0.4$ of a b-jet, as well as their relative momentum with respect to the b-jet. A large discrepancy is observed in the number of tracks, while the relative momenta of those tracks are found to be in agreement. This reinforces the conclusion that the differences between HERWIG and PYTHIA are due to decay tables and not fragmentation properties

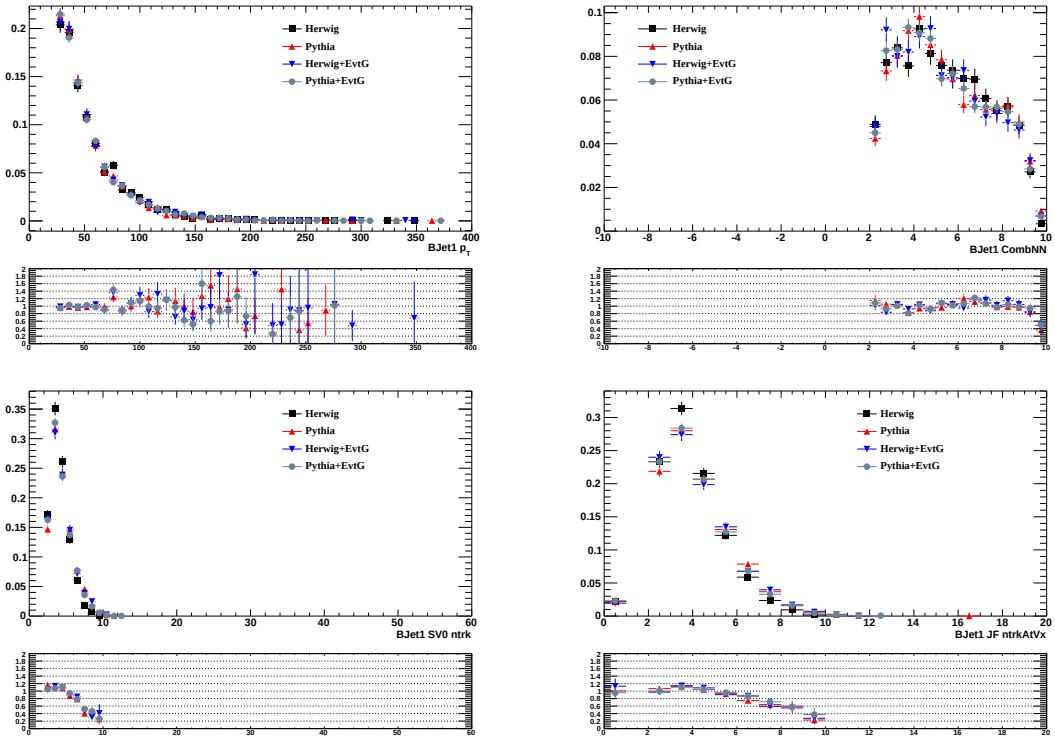

Figure A.16: Reconstruction-level kinematics (top left: b-jet p_{T}) and b-jet properties (top right: CombNN weight; bottom left and right: number of tracks per secondary vertex reconstructed by the SV0 and Jet Fitter algorithms) in ALPGEN showered with HERWIG and PYTHIA, with and without EVTGEN. The plots are normalized and the ratios are taken with respect to the default ALPGEN + HERWIG sample. The ALPGEN + HERWIG sample is found to underestimate the number of tracks and high CombNN values with respect to the other samples.

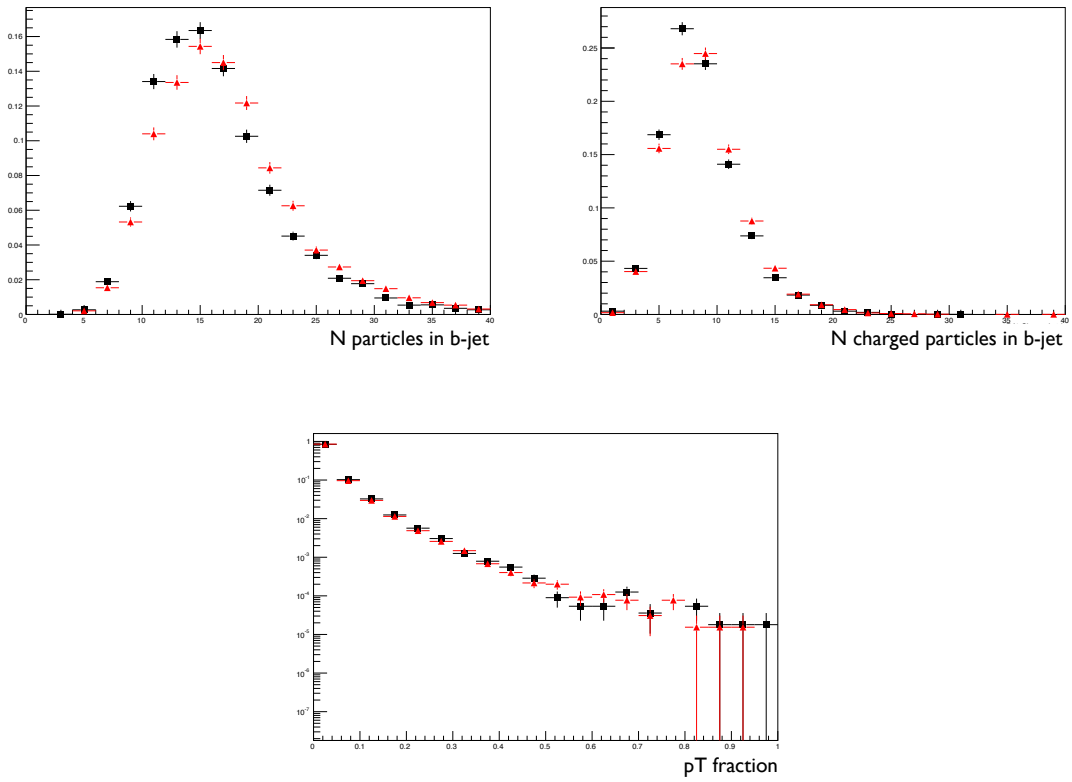

Figure A.17: Generator-level properties of tracks in b-jets in ALPGEN +HERWIG and ALPGEN +PYTHIA. Number of particles (left) and number of charged particles (right) found within the cone of b-jets ($p_{\mathrm{T}}^{b-\mathrm{jet}} > 25$ GeV). Bottom: fraction of b-jet p_{T} carried by each particle. Only particles with $p_{\mathrm{T}} > 300$ MeV are shown. Large discrepancies are observed between HERWIG and PYTHIA in terms of number of particles (related to decay tables), while the p_{T} of each particle (related to fragmentation) is found to be consistent in the two generators.

A.4.4 Production of Pythia-based templates for W+jets

In the previous sections, the HERWIG samples are found model B-hadron decays incorrectly. However, fully simulated, high statistics W+jets PYTHIA or EVTGEN samples[3] were not available at the time of the analysis. To overcome this issue, the available ALPGEN +HERWIG samples are integrated with PYTHIA-hadronized simulation. In other words the W+jets kinematics properties are simulated using ALPGEN +HERWIG, but their CombNN distributions are simulated using two PYTHIA samples, a PYTHIA Dijet sample and a POWHEG+PYTHIA $W+b\bar{b}$ sample, containing 8M and 10M events respectively.

The PYTHIA samples need to be reweighted to account for the correlation between the CombNN weight and the jet p_{T}. As shown in Figure A.18 for the $t\bar{t}$ control region, the CombNN distribution for low p_{T} jets is different from the CombNN distribution for high p_{T} jets. To remove the resulting bias, a correction is applied to the PYTHIA samples based on the jet p_{T} distribution found in the standard ALPGEN +HERWIG samples. To avoid migration between neighboring bins due to resolution effects, the generator-level p_{T} of jets is used (instead of the reconstructed-level p_{T}) when relating the PYTHIA and HERWIG simulations.

Since the reweighting is based on the generator-level jet p_{T}, a matching procedure is defined to associate reconstructed-level jets with generator-level jets. A simple angular matching is used: $\Delta\mathrm{R}(\mathrm{jet}^{\mathrm{gen}}, \mathrm{jet}^{\mathrm{reco}}) < 0.3$. A finely binned two-dimensional histogram is constructed from the generator-level jet p_{T} and the CombNN tagger

[3]The previously mentioned ALPGEN +PYTHIA, ALPGEN +HERWIG +EVTGEN, ALPGEN +PYTHIA +EVTGEN samples are only available as low statistics test samples. The large POWHEG+PYTHIA $W+b\bar{b}$ sample cannot be used since there are no corresponding NLO W+light-jets and $W+c$-jets samples.

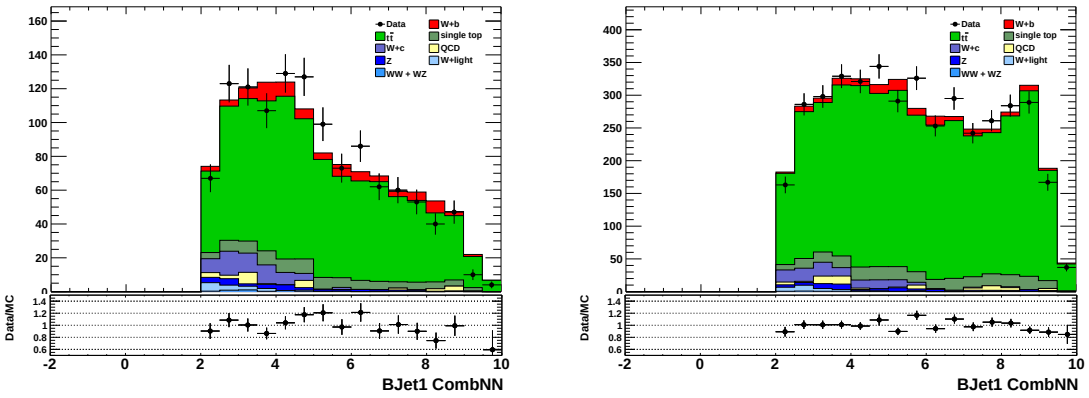

Figure A.18: CombNN tagger weight in the $t\bar{t}$ control region for b-tagged jets with p_{T} between 25 and 35 GeV (left) and between 100 and 125 GeV (right).

weight of reconstructed b-jets in the PYTHIA sample. This histogram is treated as a matrix and normalized in the p_{T} dimension to remove the p_{T} dependence present in the PYTHIA sample. In parallel, the ALPGEN +HERWIG W+b-jets sample is used to build another histogram, mapping generator-level to reconstructed-level jet p_{T} for all b-jets. No column or row normalization is applied to this histogram in order to maintain the information in the p_{T} spectrum of the ALPGEN sample. Treating these two histograms as matrices and multiplying them, a new two-dimensional histogram of reconstructed b-jet p_{T} vs CombNN tagger weight is obtained:

$$[\mathrm{CombNN}, p_{\mathrm{T}}^{\mathrm{gen}}]^{\mathrm{Pythia}} \times [p_{\mathrm{T}}^{\mathrm{gen}}, p_{\mathrm{T}}^{\mathrm{reco}}]^{\mathrm{Herwig}} = [\mathrm{CombNN}^{\mathrm{Pythia}}, p_{\mathrm{T}}^{\mathrm{reco,Herwig}}] \qquad \text{(A.1)}$$

Projecting this distribution onto the axis corresponding to the tagger weight gives the expected PYTHIA tagger weight distributions for the p_{T} spectrum of the ALPGEN +HERWIG W+jets sample. This projection can also be performed for a limited p_{T} range to obtain tagger weight templates for the differential measurement in $p_{\mathrm{T}}^{b-\mathrm{jet}}$. The same procedure is applied to c-jets and light-jets to obtain high statistics PYTHIA

templates to be used in place of the HERWIG ones.

A.4.5 Validation of Pythia-based templates for W+jets

The strategy described above to obtain PYTHIA templates for the W+b-jets, W+c-jets and W+light-jets processes is first validated on b-jets in $t\bar{t}$ simulation. $t\bar{t}$ events are used in place of W+jets events to fill the generator-level vs reconstructed-level p_{T} histogram, which is then multiplied by the p_{T} vs CombNN histogram obtained from the PYTHIA sample. In Figure A.19, the CombNN weight for b-jets is plotted for the MC@NLO +HERWIG template, the POWHEG+PYTHIA template, and the newly produced template based on the PYTHIA Dijet sample. The PYTHIA-based template is found to agree very well with the POWHEG+PYTHIA $t\bar{t}$ one, while the high-CombNN discrepancies characteristics of HERWIG are visible with respect to the HERWIG template. This is a remarkable result, since PYTHIA Dijet and POWHEG+PYTHIA $t\bar{t}$ processes have different kinematics, giving confidence that this procedure can be applied also in the W+jets case.

As further validation, the b-jet, c-jet and light-jet PYTHIA templates prepared with this procedure are compared to those extracted from the small W+jets ALPGEN +PYTHIA test samples. Within uncertainties, the high statistics PYTHIA templates are in good agreement with the corresponding ALPGEN +PYTHIA ones, as shown in Figure A.20.

In conclusion, a procedure was developed to obtain high-statistics PYTHIA-based templates of the CombNN variable for the W+b-jets, W+c-jets and W+light-jets samples. This procedure was validated in $t\bar{t}$ events, and–with lower statistics–in

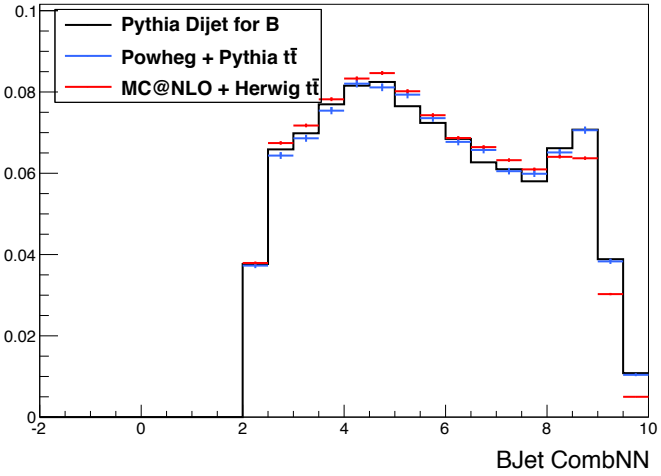

Figure A.19: Distribution of the CombNN tagger weight for the b-tagged jets in the $t\bar{t}$ control region in the MC@NLO +Herwig and Powheg+Pythia $t\bar{t}$ samples, and in the Pythia template obtained by combining the Pythia Dijet sample with the MC@NLO +Herwig $t\bar{t}$ one. The combined template sample successfully reproduces the Powheg+Pythia $t\bar{t}$ one in the CombNN variable.

W+jets events. The templates obtained were used in all the maximum likelihood fits to the CombNN distributions, both in the inclusive and differential measurements. The results of these fits are presented in the following section.

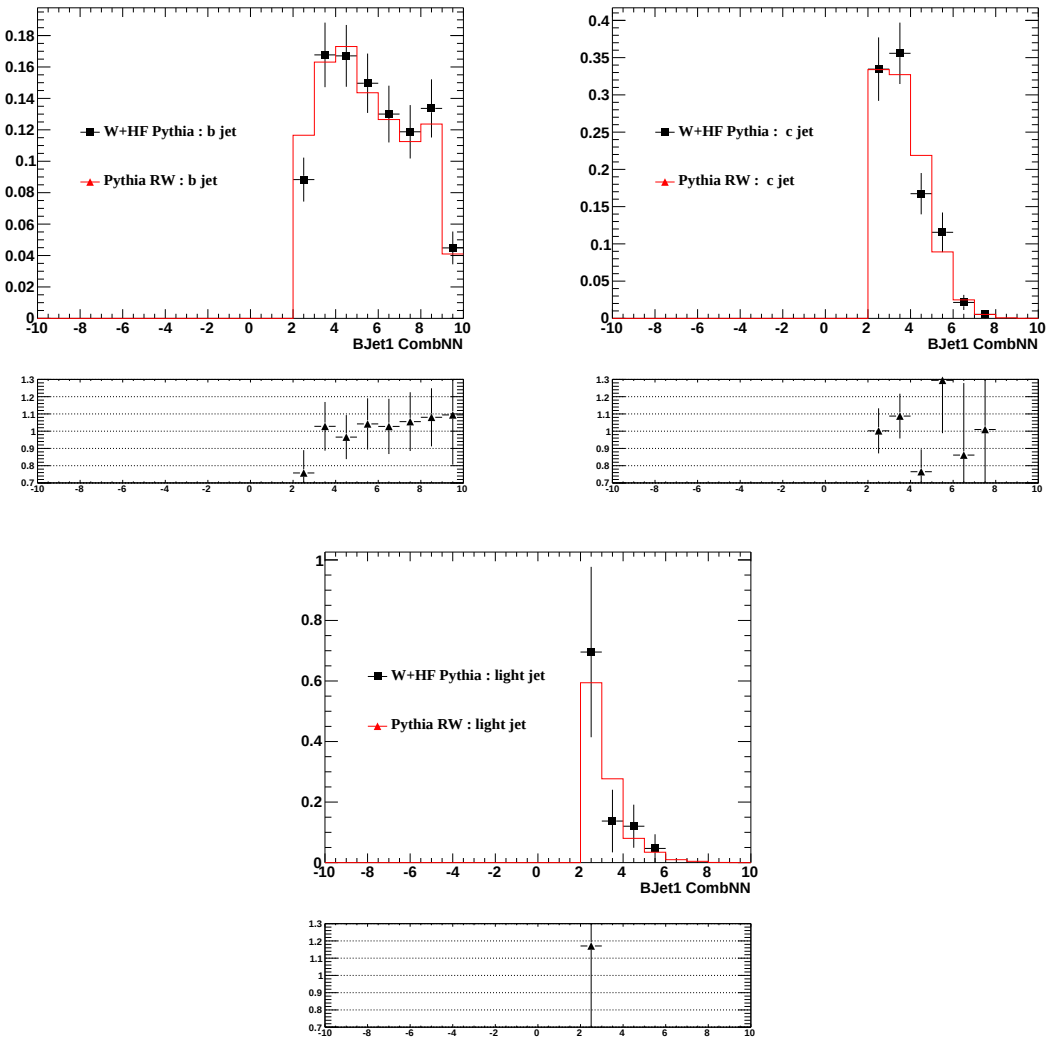

Figure A.20: Distribution of the CombNN tagger weight for the b-tagged jets in the 1-jet analysis region. The templates obtained from the ALPGEN +PYTHIA test samples (black) are compared to the templates obtained by reweighting (RW) the PYTHIA Dijet sample with the ALPGEN +HERWIG one. The combined templates are consistent with the small ALPGEN +PYTHIA ones for W+b-jets (left), W+c-jets (right) and W+light-jets (bottom).

Appendix B

Detailed fit results

B.1 Inclusive Fit Results for $W+b$-jets

Table B.1: Fit results in the Muon 1-jet.

Process	Expected	Fit	β
Wb	3173	5336 ± 444	1.68 ± 0.14
Wc	12741	15568 ± 568	1.22 ± 0.04
Wl	2301	1622 ± 512	0.70 ± 0.22
$t\bar{t}$	1233	1232 ± 121	1.00 ± 0.10
stop	1594	1708 ± 547	1.07 ± 0.34
Dib	181	181 ± 18	1.00 ± 0.10
Zjet	768.63	766.17 ± 76.11	1.00 ± 0.10
QCD	702	784 ± 326	1.12 ± 0.47

Table B.2: Fit results in the Electron 1-jet.

Process	Expected	Fit	β
Wb	2422	4802 ± 388	1.98 ± 0.16
Wc	10290	13335 ± 525	1.30 ± 0.05
Wl	1877	522 ± 469	0.28 ± 0.25
$t\bar{t}$	1105	1104 ± 108	1.00 ± 0.10
stop	1334	1357 ± 474	1.02 ± 0.36
Dib	139	139 ± 14	1.00 ± 0.10
Zjet	258.41	257.79 ± 25.80	1.00 ± 0.10
QCD	1252	999 ± 500	0.80 ± 0.40

Table B.3: Fit results in the Muon 2-jet.

Process	Expected	Fit	β
Wb	2632	3002 ± 263	1.14 ± 0.10
Wc	4447	4616 ± 394	1.04 ± 0.09
Wl	1017	1168 ± 333	1.15 ± 0.33
$t\bar{t}$	4183	4255 ± 406	1.02 ± 0.10
stop	2086	2261 ± 400	1.08 ± 0.19
Dib	185	185 ± 18	1.00 ± 0.10
Zjet	397.06	396.72 ± 39.72	1.00 ± 0.10
QCD	313	208 ± 153	0.67 ± 0.49

Table B.4: Fit results in the Electron 2-jet.

Process	Expected	Fit	β
Wb	1908	2220 ± 248	1.16 ± 0.13
Wc	3642	4019 ± 367	1.10 ± 0.10
Wl	737	493 ± 321	0.67 ± 0.44
$t\bar{t}$	3638	3691 ± 353	1.01 ± 0.10
stop	1795	1813 ± 347	1.01 ± 0.19
Dib	154	155 ± 15	1.00 ± 0.10
Zjet	365.88	365.08 ± 36.56	1.00 ± 0.10
QCD	683	1222 ± 288	1.79 ± 0.42

Table B.5: W+b-jets estimator uncertainties in the electron and muon channel.

Systematics	μ 1-jet	e 1-jet	μ 2-jets	e 2-jets
JesUP	-6.89	-14.20	-10.40	-20.13
JesDW	3.77	5.50	3.60	1.73
BsUP	2.06	2.00	3.92	2.74
BsDW	-1.68	-0.90	-2.70	-1.91
CsUP	0.31	1.37	-1.16	0.52
CsDW	0.14	-1.35	1.75	-0.16
LsUP	0.77	0.87	4.39	1.37
LsDW	-0.24	0.12	-3.22	-1.24
SmearUP	0.61	-0.28	0.21	-1.17
SmearDW	0.55	0.85	0.31	-0.79
TrigUP	0.54	0.15	0.95	0.71
TrigDW	0.27	0.02	0.70	0.71
HFORME	4.86	1.07	2.38	-2.51
HFORPS	0.63	7.00	-14.60	-10.37
MetPileUP	3.40	-2.70	0.57	-3.94
MetPileDW	-1.33	-2.03	-2.15	-2.09
MetClusterUP	4.14	-0.12	-3.14	-8.13
MetClusterDW	-2.38	-4.46	0.24	-1.86
BCombNN	3.08	2.18	5.67	4.81
CCombNN	3.46	5.11	0.85	3.26
LCombNN	1.07	-0.54	-2.63	4.46
IFSRUP	-2.07	-5.26	3.40	-9.59
IFSRDW	3.44	-1.70	12.27	1.72
RECOUP	0.37	0.57	0.66	0.20
RECODW	0.33	0.48	0.80	0.37
QCD	-1.16	5.71	-0.81	5.53
JER	-17.22	-12.02	0.50	6.49
Total +	20.14	17.23	16.19	11.97
Total -	19.56	21.78	19.89	28.88
Stat	14.00	16.00	10.00	13.00
Stat + Syst +	24.53	23.51	19.03	17.67
Stat + Syst -	24.06	27.03	22.26	31.67

B.2 Differential Fit Results for $W+b$-jets

Table B.6: Fit results in the Muon 1-jet; p_T [25-30] GeV.

Process	Expected	Fit	β
Wb	893	1344 ± 81	1.51 ± 0.09
Wc	2475	3521 ± 285	1.42 ± 0.12
Wl	827	354 ± 326	0.43 ± 0.39
$t\bar{t}$	68	68 ± 7	1.00 ± 0.10
stop	92	94 ± 45	1.02 ± 0.49
Dib	18	18 ± 2	1.00 ± 0.10
Zjet	148.57	148.12 ± 14.81	1.00 ± 0.10
QCD	143	142 ± 67	0.99 ± 0.47

Table B.7: Fit results in the Muon 1-jet; p_T [30-40] GeV.

Process	Expected	Fit	β
Wb	1048	1641 ± 84	1.57 ± 0.08
Wc	3873	5190 ± 295	1.34 ± 0.08
Wl	704	242 ± 308	0.34 ± 0.44
$t\bar{t}$	158	157 ± 16	1.00 ± 0.10
stop	244	229 ± 120	0.94 ± 0.49
Dib	43	43 ± 4	1.00 ± 0.10
Zjet	233.86	234.10 ± 23.33	1.00 ± 0.10
QCD	230	210 ± 112	0.92 ± 0.49

Table B.8: Fit results in the Muon 1-jet; p_T [40-60] GeV.

Process	Expected	Fit	β
Wb	762	1525 ± 99	2.00 ± 0.13
Wc	3810	4642 ± 270	1.22 ± 0.07
Wl	498	164 ± 249	0.33 ± 0.50
$t\bar{t}$	340	338 ± 34	0.99 ± 0.10
stop	574	519 ± 276	0.90 ± 0.48
Dib	66	66 ± 7	1.00 ± 0.10
Zjet	226.23	227.60 ± 22.69	1.01 ± 0.10
QCD	248	289 ± 119	1.17 ± 0.48

Table B.9: Fit results in the Muon 1-jet; p_T [60-140] GeV.

Process	Expected	Fit	β
Wb	448	981 ± 99	2.19 ± 0.22
Wc	2495	2576 ± 166	1.03 ± 0.07
Wl	254	292 ± 121	1.15 ± 0.48
$t\bar{t}$	627	629 ± 61	1.00 ± 0.10
stop	661	724 ± 317	1.10 ± 0.48
Dib	52	52 ± 5	1.00 ± 0.10
Zjet	153.54	152.95 ± 15.97	1.00 ± 0.10
QCD	84	101 ± 40	1.21 ± 0.48

Table B.10: Fit results in the Electron 1-jet; p_T [25-30] GeV.

Process	Expected	Fit	β
Wb	727	1055 ± 95	1.45 ± 0.13
Wc	1936	3102 ± 253	1.60 ± 0.13
Wl	690	-86 ± 292	-0.12 ± 0.42
$t\bar{t}$	52	52 ± 5	1.00 ± 0.10
stop	76	78 ± 38	1.02 ± 0.50
Dib	14	14 ± 1	1.00 ± 0.10
Zjet	36.59	36.56 ± 3.66	1.00 ± 0.10
QCD	275	192 ± 114	0.70 ± 0.42

Table B.11: Fit results in the Electron 1-jet; p_T [30-40] GeV.

Process	Expected	Fit	β
Wb	722	1389 ± 72	1.93 ± 0.10
Wc	3119	4282 ± 283	1.37 ± 0.09
Wl	562	-42 ± 282	-0.07 ± 0.50
$t\bar{t}$	148	148 ± 15	1.00 ± 0.10
stop	202	209 ± 99	1.03 ± 0.49
Dib	34	34 ± 3	1.00 ± 0.10
Zjet	74.57	74.55 ± 7.46	1.00 ± 0.10
QCD	464	349 ± 172	0.75 ± 0.37

Table B.12: Fit results in the Electron 1-jet; p_T [40-60] GeV.

Process	Expected	Fit	β
Wb	591	1660 ± 100	2.81 ± 0.17
Wc	3046	3995 ± 233	1.31 ± 0.08
Wl	373	96 ± 205	0.26 ± 0.55
$t\bar{t}$	302	305 ± 30	1.01 ± 0.10
stop	472	397 ± 228	0.84 ± 0.48
Dib	50	49 ± 5	1.00 ± 0.10
Zjet	79.68	80.12 ± 7.96	1.01 ± 0.10
QCD	391	8 ± 148	0.02 ± 0.38

Table B.13: Fit results in the Electron 1-jet; p_T [60-140] GeV.

Process	Expected	Fit	β
Wb	361	1131 ± 94	3.13 ± 0.26
Wc	2093	2424 ± 171	1.16 ± 0.08
Wl	237	118 ± 130	0.50 ± 0.55
$t\bar{t}$	557	546 ± 56	0.98 ± 0.10
stop	563	427 ± 262	0.76 ± 0.46
Dib	40	40 ± 4	1.00 ± 0.10
Zjet	62.77	62.64 ± 6.28	1.00 ± 0.10
QCD	151	35 ± 62	0.23 ± 0.41

Table B.14: Fit results in the Muon 2-jet; p_T [25-30] GeV.

Process	Expected	Fit	β
Wb	459	479 ± 50	1.04 ± 0.11
Wc	518	657 ± 169	1.27 ± 0.33
Wl	288	312 ± 189	1.09 ± 0.66
$t\bar{t}$	211	209 ± 21	0.99 ± 0.10
stop	128	129 ± 26	1.01 ± 0.20
Dib	23	23 ± 2	1.00 ± 0.10
Zjet	56.51	56.26 ± 5.67	1.00 ± 0.10
QCD	46	40 ± 23	0.87 ± 0.49

Table B.15: Fit results in the Muon 2-jet; p_T [30-40] GeV.

Process	Expected	Fit	β
Wb	666	810 ± 73	1.22 ± 0.11
Wc	1101	1235 ± 188	1.12 ± 0.17
Wl	240	255 ± 190	1.06 ± 0.79
$t\bar{t}$	522	522 ± 47	1.00 ± 0.09
stop	304	302 ± 68	0.99 ± 0.22
Dib	51	51 ± 5	1.00 ± 0.10
Zjet	100.49	100.24 ± 10.05	1.00 ± 0.10
QCD	68	62 ± 34	0.92 ± 0.50

Table B.16: Fit results in the Muon 2-jet; p_T [40-60] GeV.

Process	Expected	Fit	β
Wb	749	970 ± 135	1.30 ± 0.18
Wc	1367	1576 ± 199	1.15 ± 0.15
Wl	246	-40 ± 168	-0.16 ± 0.68
$t\bar{t}$	1139	1140 ± 114	1.00 ± 0.10
stop	620	614 ± 124	0.99 ± 0.20
Dib	64	64 ± 6	1.00 ± 0.10
Zjet	116.80	117.59 ± 11.67	1.01 ± 0.10
QCD	95	91 ± 46	0.96 ± 0.49

Table B.17: Fit results in the Muon 2-jet; p_T [60-140] GeV.

Process	Expected	Fit	β
Wb	687	910 ± 206	1.32 ± 0.30
Wc	1340	1196 ± 172	0.89 ± 0.13
Wl	212	372 ± 126	1.75 ± 0.59
$t\bar{t}$	2112	2083 ± 208	0.99 ± 0.10
stop	963	1013 ± 191	1.05 ± 0.20
Dib	44	45 ± 5	1.00 ± 0.10
Zjet	110.12	110.06 ± 11.02	1.00 ± 0.10
QCD	105	77 ± 51	0.73 ± 0.48

Table B.18: Fit results in the Electron 2-jet; p_T [25-30] GeV.

Process	Expected	Fit	β
Wb	330	371 ± 50	1.12 ± 0.15
Wc	443	761 ± 147	1.72 ± 0.33
Wl	165	4 ± 162	0.03 ± 0.98
$t\bar{t}$	185	182 ± 18	0.99 ± 0.10
stop	111	109 ± 22	0.99 ± 0.20
Dib	19	19 ± 2	1.00 ± 0.10
Zjet	57.97	57.83 ± 5.80	1.00 ± 0.10
QCD	150	130 ± 52	0.87 ± 0.34

Table B.19: Fit results in the Electron 2-jet; p_T [30-40] GeV.

Process	Expected	Fit	β
Wb	505	619 ± 71	1.22 ± 0.14
Wc	784	995 ± 189	1.27 ± 0.24
Wl	187	189 ± 187	1.01 ± 1.00
$t\bar{t}$	441	433 ± 43	0.98 ± 0.10
stop	254	259 ± 49	1.02 ± 0.19
Dib	40	40 ± 4	1.00 ± 0.10
Zjet	89.74	89.62 ± 8.97	1.00 ± 0.10
QCD	158	89 ± 63	0.56 ± 0.40

Table B.20: Fit results in the Electron 2-jet; p_T [40-60] GeV.

Process	Expected	Fit	β
Wb	515	948 ± 103	1.84 ± 0.20
Wc	1116	1353 ± 193	1.21 ± 0.17
Wl	170	-32 ± 162	-0.19 ± 0.96
$t\bar{t}$	971	981 ± 97	1.01 ± 0.10
stop	542	518 ± 108	0.96 ± 0.20
Dib	55	55 ± 6	1.00 ± 0.10
Zjet	106.24	105.83 ± 10.66	1.00 ± 0.10
QCD	275	156 ± 95	0.57 ± 0.35

Table B.21: Fit results in the Electron 2-jet; p_T [60-140] GeV.

Process	Expected	Fit	β
Wb	486	932 ± 160	1.92 ± 0.33
Wc	1191	829 ± 174	0.70 ± 0.15
Wl	182	319 ± 129	1.75 ± 0.71
$t\bar{t}$	1851	1864 ± 181	1.01 ± 0.10
stop	826	821 ± 161	0.99 ± 0.19
Dib	39	39 ± 4	1.00 ± 0.10
Zjet	101.22	101.13 ± 10.35	1.00 ± 0.10
QCD	166	156 ± 69	0.94 ± 0.41

Table B.22: W+b-jets estimator uncertainties in the electron and muon channel; p_T [25-30] GeV.

Systematics	μ 1-jet	e 1-jet	μ 2-jets	e 2-jets
JesUP	-22.49	-20.71	-5.63	-25.16
JesDW	2.75	8.00	7.97	13.05
BsUP	1.07	0.59	1.67	1.54
BsDW	-1.22	-0.79	-0.70	-1.64
CsUP	-0.24	-0.60	-0.48	-1.48
CsDW	0.30	0.08	1.49	1.77
LsUP	0.54	-1.14	2.21	-0.26
LsDW	-0.25	1.32	-1.48	-0.80
SmearUP	0.20	0.44	0.88	-1.23
SmearDW	0.22	0.21	0.90	-2.40
TrigUP	0.12	0.07	0.51	0.43
TrigDW	-0.25	0.03	-0.07	0.18
HFORME	0.90	0.99	-2.25	0.12
HFORPS	-1.45	16.77	-0.16	-15.02
MetPileUP	2.03	-4.29	0.79	-3.02
MetPileDW	-1.19	0.33	2.43	-0.69
MetClusterUP	0.82	0.07	-3.72	-4.82
MetClusterDW	-2.06	-0.69	6.00	-1.49
BCombNN	4.50	4.25	5.12	5.01
CCombNN	0.85	1.49	0.42	1.28
LCombNN	0.65	12.10	-4.39	2.28
IFSRUP	-0.49	-1.37	-0.74	-0.80
IFSRDW	1.39	-0.21	0.71	-0.98
RECOUP	0.05	-0.13	0.54	0.12
RECODW	-0.05	0.09	0.40	-0.34
QCD	-0.88	3.64	-1.08	3.61
JER	-24.66	-3.31	-21.06	-9.11
Total +	25.43	23.23	24.68	17.44
Total -	33.85	25.35	23.33	32.19
Stat	9.00	13.00	11.00	15.00
Stat + Syst +	26.98	26.62	27.02	23.00
Stat + Syst -	35.03	28.49	25.79	35.51

Table B.23: W+b-jets estimator uncertainties in the electron and muon channel; p_T [30-40] GeV.

Systematics	μ 1-jet	e 1-jet	μ 2-jets	e 2-jets
JesUP	-5.40	-14.11	-17.69	-26.58
JesDW	14.73	10.51	11.25	6.14
BsUP	1.89	1.62	0.76	0.54
BsDW	-1.58	-1.99	-0.46	-0.08
CsUP	-0.32	-0.05	-1.14	-0.18
CsDW	0.81	0.39	1.93	0.88
LsUP	0.39	0.08	2.20	1.07
LsDW	-0.04	-0.57	-1.72	-0.78
SmearUP	0.03	0.87	0.21	-1.03
SmearDW	0.04	0.14	0.33	-0.78
TrigUP	0.48	0.26	0.41	0.16
TrigDW	-0.24	-0.18	0.07	-0.08
HFORME	3.94	-1.68	0.54	1.08
HFORPS	-3.10	-17.54	-19.94	-24.65
MetPileUP	3.10	3.69	0.47	-1.38
MetPileDW	-0.95	-1.58	-3.05	-1.76
MetClusterUP	5.52	1.41	-1.97	-4.73
MetClusterDW	-2.31	0.35	-1.92	-0.24
BCombNN	4.61	4.72	6.06	4.63
CCombNN	2.14	0.83	0.50	0.80
LCombNN	1.32	-1.25	-0.66	4.58
IFSRUP	0.12	-0.36	4.04	0.11
IFSRDW	2.13	0.46	-0.60	-2.92
RECOUP	0.11	0.46	-0.07	0.20
RECODW	0.00	-0.39	0.21	-0.17
JER	3.71	-16.81	-1.43	-0.22
Total +	18.01	21.34	13.87	12.56
Total -	9.51	29.02	27.78	38.33
Stat	8.00	10.00	11.00	14.00
Stat + Syst +	19.71	23.57	17.70	18.81
Stat + Syst -	12.42	30.69	29.88	40.80

Table B.24: W+b-jets estimator uncertainties in the electron and muon channel; p_T [40-60] GeV.

Systematics	μ 1-jet	e 1-jet	μ 2-jets	e 2-jets
JesUP	-23.86	-26.26	-14.98	-14.60
JesDW	6.04	7.24	-2.62	22.03
BsUP	3.65	3.53	1.12	1.59
BsDW	-2.52	-2.14	-0.68	-0.31
CsUP	0.11	0.96	-1.82	-1.59
CsDW	1.23	1.71	2.63	0.91
LsUP	0.42	-0.27	4.15	2.35
LsDW	0.59	1.88	-3.95	-3.02
SmearUP	0.20	-0.03	0.71	-2.57
SmearDW	0.30	-0.26	0.74	-0.97
TrigUP	1.73	1.28	0.14	0.02
TrigDW	0.63	0.65	0.22	-0.40
HFORME	-8.46	-4.13	4.02	-9.13
HFORPS	10.50	24.76	1.83	9.90
MetPileUP	4.38	5.18	-1.26	-9.12
MetPileDW	-3.24	-2.72	-3.56	-4.51
MetClusterUP	2.78	2.69	-3.04	-15.42
MetClusterDW	-2.37	0.52	-1.43	-1.10
BCombNN	6.39	4.14	7.61	5.52
CCombNN	1.10	4.77	-0.27	1.44
LCombNN	8.39	-0.18	-0.81	0.75
IFSRUP	8.76	-12.87	-2.77	-2.29
IFSRDW	20.71	-4.13	7.56	-2.03
RECOUP	1.51	1.81	0.36	-0.37
RECODW	1.06	0.26	0.46	0.49
QCD	-4.77	0.33	-2.07	9.52
JER	-16.79	-15.72	-4.71	18.17
Total +	33.44	31.81	13.73	32.35
Total -	32.87	34.48	19.21	33.49
Stat	13.00	17.00	18.00	20.00
Stat + Syst +	35.88	36.07	22.64	38.03
Stat + Syst -	35.35	38.44	26.33	39.01

Table B.25: W+b-jets estimator uncertainties in the electron and muon channel; p_T [60-140] GeV.

Systematics	μ 1-jet	e 1-jet	μ 2-jets	e 2-jets
JesUP	-19.74	-42.88	-10.19	-22.55
JesDW	25.00	-3.98	1.50	7.71
BsUP	11.60	6.10	7.18	8.34
BsDW	-9.40	-10.11	-6.00	-7.79
CsUP	0.29	-0.62	-3.18	-1.21
CsDW	-0.54	0.23	3.10	-0.30
LsUP	0.09	-1.93	6.91	2.18
LsDW	-0.83	-2.20	-6.31	-4.72
SmearUP	-0.63	-3.79	0.92	-5.12
SmearDW	-1.15	-1.79	0.90	-1.38
TrigUP	1.83	-1.06	-0.23	-0.63
TrigDW	-0.24	-2.36	0.52	-0.72
HFORME	1.43	-22.26	-0.70	0.74
HFORPS	66.37	-37.62	-25.48	-10.26
MetPileUP	0.84	2.06	0.35	-9.93
MetPileDW	-7.25	-4.49	-2.96	-3.32
MetClusterUP	15.39	7.66	-3.45	-14.31
MetClusterDW	4.50	-15.70	0.66	-3.23
BCombNN	2.67	5.04	7.92	8.14
CCombNN	6.39	0.57	-1.41	2.27
LCombNN	-3.90	-15.03	-2.45	-2.35
IFSRUP	-27.27	-5.06	18.06	-9.32
IFSRDW	1.62	-14.60	36.20	1.49
RECOUP	-1.55	-3.01	-0.49	-0.46
RECODW	-0.52	-2.35	0.21	-0.51
QCD	5.96	2.32	-2.92	2.28
JER	-10.63	-36.11	-3.51	6.90
Total +	75.11	40.76	42.91	16.32
Total -	38.62	77.35	30.86	35.63
Stat	22.00	26.00	30.00	33.00
Stat + Syst +	78.27	48.35	52.36	36.82
Stat + Syst -	44.44	81.60	43.04	48.56

B.3 Inclusive Fit Results for W+b-jets plus single-top

Table B.26: W+b-jets plus single-top fit in the muon 1-jet region.

Process	Expected	Fit	β
Wb+Stop	4460	6982 ± 134	1.57 ± 0.03
Wc	12741	15672 ± 530	1.23 ± 0.04
Wl	2301	1581 ± 500	0.69 ± 0.22
$t\bar{t}$	1233	1228 ± 120	1.00 ± 0.10
Dib	181	181 ± 18	1.00 ± 0.10
Zjet	768.63	766.31 ± 75.62	1.00 ± 0.10
QCD	702	787 ± 317	1.12 ± 0.45

Table B.27: W+b-jets plus single-top fit in the electron 1-jet region.

Process	Expected	Fit	β
Wb+Stop	3470	6027 ± 174	1.74 ± 0.05
Wc	10290	13485 ± 505	1.31 ± 0.05
Wl	1877	449 ± 456	0.24 ± 0.24
$t\bar{t}$	1105	1097 ± 108	0.99 ± 0.10
Dib	139	139 ± 14	1.00 ± 0.10
Zjet	258.41	257.83 ± 25.79	1.00 ± 0.10
QCD	1252	1061 ± 468	0.85 ± 0.37

Table B.28: W+b-jets plus single-top fit in the muon 2-jet region.

Process	Expected	Fit	β
Wb+Stop	4305	5366 ± 172	1.25 ± 0.04
Wc	4447	4563 ± 380	1.03 ± 0.09
Wl	1017	1193 ± 340	1.17 ± 0.33
$t\bar{t}$	4183	4193 ± 412	1.00 ± 0.10
Dib	185	185 ± 19	1.00 ± 0.10
Zjet	397.06	396.26 ± 39.67	1.00 ± 0.10
QCD	313	199 ± 151	0.64 ± 0.48

Table B.29: W+b-jets plus single-top fit in the electron 2-jet region.

Process	Expected	Fit	β
Wb+Stop	3232	4055 ± 162	1.25 ± 0.05
Wc	3642	3990 ± 350	1.10 ± 0.10
Wl	737	506 ± 310	0.69 ± 0.42
$t\bar{t}$	3638	3688 ± 361	1.01 ± 0.10
Dib	154	155 ± 15	1.00 ± 0.10
Zjet	365.88	364.98 ± 36.54	1.00 ± 0.10
QCD	683	1219 ± 287	1.78 ± 0.42

Appendix C

Detailed unfolding results

Table C.1: $W+b$-jets fiducial cross-section measured in 1-jet muon channel.

Muon, 1 Jet	
	σ_{fiducial} [pb]
Expected (Alpgen)	2.69
Measured	4.68
Stat. Unc.	(14%)
Sys. Unc.	(24%)
Stat. Unc. (MC)	(2%)
JES	(13%)
JER	(16%)
C-Tag	(0%)
B-Tag	(5%)
L-Tag	(1%)
ISR/FSR	(3%)
HFOR	(7%)
LeptonResolution	(1%)
TriggerSF	(2%)
LeptonRecoSF	(1%)
METCluster	(4%)
METPileup	(3%)
ShapeB	(3%)
ShapeC	(3%)
ShapeL	(1%)
ShapeQCD	(1%)

Table C.2: $W+b$-jets fiducial cross-section measured in 1-jet electron channel.

Electron, 1 Jet	
	σ_{fiducial} [pb]
Expected (Alpgen)	2.71
Measured	5.47
Stat. Unc.	(16%)
Sys. Unc.	(27%)
Stat. Unc. (MC)	(2%)
JES	(18%)
JER	(12%)
C-Tag	(1%)
B-Tag	(6%)
L-Tag	(1%)
ISR/FSR	(5%)
HFOR	(10%)
LeptonResolution	(1%)
TriggerSF	(1%)
LeptonRecoSF	(2%)
METCluster	(2%)
METPileup	(2%)
ShapeB	(2%)
ShapeC	(5%)
ShapeL	(1%)
ShapeQCD	(6%)

Table C.3: $W+b$-jets fiducial cross-section measured in 2-jet muon channel.

Muon, 2 Jet	
	σ_{fiducial}n [pb]
Expected (Alpgen)	1.96
Measured	2.20
Stat. Unc.	(10%)
Sys. Unc.	(20%)
Stat. Unc. (MC)	(1%)
JES	(11%)
JER	(0%)
C-Tag	(2%)
B-Tag	(4%)
L-Tag	(4%)
ISR/FSR	(12%)
HFOR	(5%)
LeptonResolution	(0%)
TriggerSF	(2%)
LeptonRecoSF	(1%)
METCluster	(3%)
METPileup	(2%)
ShapeB	(6%)
ShapeC	(1%)
ShapeL	(3%)
ShapeQCD	(1%)

Table C.4: $W+b$-jets fiducial cross-section measured in 2-jet electron channel.

Electron, 2 Jet	
	σ_{fiducial} [pb]
Expected (Alpgen)	1.95
Measured	2.23
Stat. Unc.	(13%)
Sys. Unc.	(29%)
Stat. Unc. (MC)	(2%)
JES	(21%)
JER	(9%)
C-Tag	(1%)
B-Tag	(5%)
L-Tag	(1%)
ISR/FSR	(10%)
HFOR	(2%)
LeptonResolution	(2%)
TriggerSF	(1%)
LeptonRecoSF	(2%)
METCluster	(9%)
METPileup	(3%)
ShapeB	(5%)
ShapeC	(3%)
ShapeL	(4%)
ShapeQCD	(6%)

Table C.5: W+b-jets fiducial cross-section measured in the electron 1-jet and 2-jet channels.

Electron, 1 Jet + 2 Jet	
	σ_{fiducial} [pb]
Expected (Alpgen)	4.66
Measured	7.58
Stat. Unc.	(12%)
Sys. Unc.	(25%)
Stat. Unc. (MC)	(1%)
JES	(19%)
JER	(5%)
C-Tag	(1%)
B-Tag	(6%)
L-Tag	(1%)
ISR/FSR	(7%)
HFOR	(8%)
LeptonResolution	(1%)
TriggerSF	(1%)
LeptonRecoSF	(2%)
METCluster	(3%)
METPileup	(3%)
ShapeB	(3%)
ShapeC	(5%)
ShapeL	(1%)
ShapeQCD	(6%)

Table C.6: W+b-jets fiducial cross-section measured in the combined muon 1-jet and 2-jet channels.

Muon, 1 Jet + 2 Jet	
	σ_{fiducial} [pb]
Expected (Alpgen)	4.66
Measured	6.75
Stat. Unc.	(10%)
Sys. Unc.	(19%)
Stat. Unc. (MC)	(1%)
JES	(12%)
JER	(10%)
C-Tag	(1%)
B-Tag	(5%)
L-Tag	(2%)
ISR/FSR	(7%)
HFOR	(4%)
LeptonResolution	(0%)
TriggerSF	(2%)
LeptonRecoSF	(1%)
METCluster	(2%)
METPileup	(2%)
ShapeB	(4%)
ShapeC	(3%)
ShapeL	(0%)
ShapeQCD	(1%)

Table C.7: Unfolded results including uncertainties for the $p_{\mathrm{T}}^{b-\mathrm{jet}}$ distribution in the Muon 1-jet channel, showing the central unfolded values and statistical and systematic uncertainties in summary as well as a detailed list of signal and background systematics. Also shown, and included in the systematic uncertainty, is the effect of applying the Bayesian unfolding algorithm with one fewer iteration.

Muon, 1 Jet				
	Cross Section [nb/GeV]			
Bin [GeV]	25 - 30	30 - 40	40 - 60	60 - 140
Expected (Alpgen)	192.	88.6	26.7	3.57
Measured	266.	141.	54.4	8.76
Stat. Unc.	(10%)	(7%)	(14%)	(23%)
Stat. Unc. (MC)	(3%)	(3%)	(3%)	(3%)
Sys. Unc.	(29%)	(18%)	(38%)	(45%)
AlternativeUnfolding	(3%)	(1%)	(1%)	(2%)
JES	(24%)	(14%)	(21%)	(27%)
JER	(9%)	(1%)	(17%)	(13%)
C-Tag	(0%)	(1%)	(1%)	(1%)
B-Tag	(7%)	(5%)	(4%)	(4%)
L-Tag	(1%)	(0%)	(1%)	(1%)
ISR/FSR	(4%)	(2%)	(22%)	(27%)
HFORME	(5%)	(5%)	(4%)	(7%)
LeptonResolution	(0%)	(0%)	(0%)	(1%)
TriggerSF	(2%)	(1%)	(2%)	(2%)
LeptonRecoSF	(1%)	(0%)	(1%)	(2%)
METCluster	(4%)	(5%)	(4%)	(14%)
METPileup	(3%)	(4%)	(3%)	(8%)
ShapeB	(4%)	(5%)	(7%)	(3%)
ShapeC	(1%)	(2%)	(1%)	(6%)
ShapeL	(1%)	(1%)	(9%)	(3%)
ShapeQCD	(0%)	(1%)	(6%)	(6%)

Table C.8: Correlation matrices of statistical (left) and systematics (right) uncertainties for the $p_{\mathrm{T}}^{b-\mathrm{jet}}$ distribution in the Muon 1-jet channel.

1	0.372	-0.40	-0.02	1	0.923	0.736	0.749
	1	0.088	-0.18		1	0.653	0.661
		1	-0.13			1	0.859
			1				1

Table C.9: Unfolded results including uncertainties for the $p_{\mathrm{T}}^{b-\mathrm{jet}}$ distribution in the Muon 2-jet channel, showing the central unfolded values and statistical and systematic uncertainties in summary as well as a detailed list of signal and background systematics. Also shown, and included in the systematic uncertainty, is the effect of applying the Bayesian unfolding algorithm with one fewer iteration.

Muon, 2 Jet				
	Cross Section [nb/GeV]			
Bin [GeV]	25 - 30	30 - 40	40 - 60	60 - 140
Expected (Alpgen)	73.1	51.1	27.5	5.99
Measured	76.2	58.5	34.6	7.61
Stat. Unc.	(13%)	(10%)	(19%)	(31%)
Stat. Unc. (MC)	(4%)	(3%)	(3%)	(2%)
Sys. Unc.	(25%)	(22%)	(21%)	(41%)
AlternativeUnfolding	(3%)	(0%)	(1%)	(0%)
JES	(14%)	(16%)	(16%)	(11%)
JER	(15%)	(11%)	(5%)	(3%)
C-Tag	(1%)	(2%)	(2%)	(3%)
B-Tag	(6%)	(6%)	(5%)	(1%)
L-Tag	(1%)	(2%)	(4%)	(7%)
ISR/FSR	(3%)	(4%)	(4%)	(38%)
HFORME	(4%)	(1%)	(4%)	(0%)
LeptonResolution	(1%)	(1%)	(1%)	(1%)
TriggerSF	(2%)	(2%)	(2%)	(2%)
LeptonRecoSF	(1%)	(1%)	(1%)	(1%)
METCluster	(5%)	(2%)	(3%)	(3%)
METPileup	(3%)	(2%)	(4%)	(3%)
ShapeB	(5%)	(6%)	(7%)	(8%)
ShapeC	(1%)	(1%)	(0%)	(1%)
ShapeL	(4%)	(2%)	(0%)	(3%)
ShapeQCD	(0%)	(0%)	(2%)	(3%)

Table C.10: Correlation matrices of statistical (left) and systematics (right) uncertainties for the $p_{\mathrm{T}}^{b-\mathrm{jet}}$ distribution in the Muon 2-jet channel.

1	0.606	-0.48	-0.10	1	0.954	0.798	0.424
	1	0.103	-0.31		1	0.920	0.481
		1	-0.17			1	0.536
			1				1

Table C.11: Unfolded results including uncertainties for the $p_{\mathrm{T}}^{b-\mathrm{jet}}$ distribution in the Electron 1-jet channel, showing the central unfolded values and statistical and systematic uncertainties in summary as well as a detailed list of signal and background systematics. Also shown, and included in the systematic uncertainty, is the effect of applying the Bayesian unfolding algorithm with one fewer iteration.

Electron, 1 Jet				
	Cross Section [nb/GeV]			
Bin [GeV]	25 - 30	30 - 40	40 - 60	60 - 140
Expected (Alpgen)	201.	85.9	27.0	3.50
Measured	252.	143.	78.5	12.1
Stat. Unc.	(17%)	(10%)	(18%)	(26%)
Stat. Unc. (MC)	(4%)	(4%)	(3%)	(4%)
Sys. Unc.	(31%)	(22%)	(39%)	(72%)
AlternativeUnfolding	(8%)	(3%)	(3%)	(1%)
JES	(20%)	(16%)	(28%)	(47%)
JER	(8%)	(9%)	(19%)	(39%)
C-Tag	(1%)	(0%)	(2%)	(1%)
B-Tag	(8%)	(5%)	(5%)	(3%)
L-Tag	(1%)	(0%)	(2%)	(2%)
ISR/FSR	(2%)	(1%)	(13%)	(15%)
HFORME	(1%)	(0%)	(1%)	(24%)
LeptonResolution	(1%)	(1%)	(2%)	(4%)
TriggerSF	(1%)	(0%)	(2%)	(2%)
LeptonRecoSF	(2%)	(2%)	(2%)	(5%)
METCluster	(3%)	(3%)	(6%)	(15%)
METPileup	(7%)	(1%)	(7%)	(4%)
ShapeB	(4%)	(5%)	(4%)	(5%)
ShapeC	(1%)	(1%)	(5%)	(1%)
ShapeL	(15%)	(3%)	(0%)	(15%)
ShapeQCD	(4%)	(5%)	(1%)	(2%)

Table C.12: Correlation matrices of statistical (left) and systematics (right) uncertainties for the $p_{\mathrm{T}}^{b-\mathrm{jet}}$ distribution in the Electron 1-jet channel.

1	0.533	-0.33	-0.01	1	0.677	0.478	0.289
	1	-0.14	-0.14		1	0.875	0.775
		1	-0.18			1	0.892
			1				1

Table C.13: Unfolded results including uncertainties for the $p_{\mathrm{T}}^{b-\mathrm{jet}}$ distribution in the Electron 2-jet channel, showing the central unfolded values and statistical and systematic uncertainties in summary as well as a detailed list of signal and background systematics. Also shown, and included in the systematic uncertainty, is the effect of applying the Bayesian unfolding algorithm with one fewer iteration.

Electron, 2 Jet				
	Cross Section [nb/GeV]			
Bin [GeV]	25 - 30	30 - 40	40 - 60	60 - 140
Expected (Alpgen)	74.1	51.0	26.4	5.97
Measured	70.6	56.4	42.8	11.8
Stat. Unc.	(21%)	(13%)	(22%)	(33%)
Stat. Unc. (MC)	(5%)	(4%)	(4%)	(3%)
Sys. Unc.	(37%)	(29%)	(37%)	(37%)
AlternativeUnfolding	(8%)	(6%)	(3%)	(1%)
JES	(33%)	(25%)	(22%)	(25%)
JER	(11%)	(6%)	(17%)	(8%)
C-Tag	(2%)	(1%)	(1%)	(1%)
B-Tag	(6%)	(6%)	(6%)	(1%)
L-Tag	(1%)	(0%)	(2%)	(5%)
ISR/FSR	(1%)	(3%)	(3%)	(9%)
HFORME	(2%)	(4%)	(11%)	(2%)
LeptonResolution	(3%)	(1%)	(2%)	(6%)
TriggerSF	(1%)	(1%)	(0%)	(1%)
LeptonRecoSF	(1%)	(2%)	(2%)	(2%)
METCluster	(2%)	(4%)	(14%)	(17%)
METPileup	(2%)	(1%)	(8%)	(10%)
ShapeB	(5%)	(4%)	(5%)	(8%)
ShapeC	(1%)	(1%)	(1%)	(2%)
ShapeL	(3%)	(5%)	(2%)	(3%)
ShapeQCD	(2%)	(7%)	(11%)	(2%)

Table C.14: Correlation matrices of statistical (left) and systematics (right) uncertainties for the $p_{\mathrm{T}}^{b-\mathrm{jet}}$ distribution in the Electron 2-jet channel.

1	0.555	-0.41	-0.07	1	0.843	0.462	0.645
	1	0.031	-0.26		1	0.757	0.793
		1	-0.22			1	0.831
			1				1

Table C.15: Unfolded results including uncertainties for the $p_{\mathrm{T}}^{b-\mathrm{jet}}$ distribution in the combined electron and muon 1-jet channel, showing the central unfolded values and statistical and systematic uncertainties in summary as well as a detailed list of signal and background systematics. Also shown, and included in the systematic uncertainty, is the effect of applying the Bayesian unfolding algorithm with one fewer iteration.

Combined, 1 Jet				
	Cross Section [nb/GeV]			
Bin [GeV]	25 - 30	30 - 40	40 - 60	60 - 140
Expected (Alpgen)	197.	87.2	26.9	3.53
Measured	259.	143.	64.9	10.3
Stat. Unc.	(9%)	(6%)	(12%)	(18%)
Stat. Unc. (MC)	(3%)	(2%)	(2%)	(3%)
Sys. Unc.	(24%)	(19%)	(33%)	(54%)
AlternativeUnfolding	(5%)	(2%)	(3%)	(1%)
JES	(21%)	(15%)	(25%)	(37%)
JER	(0%)	(7%)	(17%)	(27%)
C-Tag	(1%)	(0%)	(2%)	(0%)
B-Tag	(7%)	(5%)	(4%)	(2%)
L-Tag	(0%)	(0%)	(1%)	(1%)
ISR/FSR	(1%)	(1%)	(9%)	(16%)
HFORME	(2%)	(3%)	(2%)	(16%)
LeptonResolution	(0%)	(1%)	(1%)	(3%)
TriggerSF	(1%)	(1%)	(2%)	(1%)
LeptonRecoSF	(1%)	(1%)	(2%)	(3%)
METCluster	(1%)	(3%)	(1%)	(12%)
METPileup	(2%)	(3%)	(5%)	(6%)
ShapeB	(4%)	(5%)	(5%)	(4%)
ShapeC	(1%)	(1%)	(3%)	(3%)
ShapeL	(5%)	(2%)	(5%)	(10%)
ShapeQCD	(2%)	(1%)	(3%)	(4%)

Table C.16: Correlation matrices of statistical (left) and systematics (right) uncertainties for the $p_{\mathrm{T}}^{b-\mathrm{jet}}$ distribution in the combined electron and muon 1-jet channel.

1	0.415	-0.38	-0.02	1	0.893	0.740	0.582
	1	-0.01	-0.17		1	0.887	0.750
		1	-0.14			1	0.875
			1				1

Table C.17: Unfolded results including uncertainties for the $p_{\mathrm{T}}^{b-\mathrm{jet}}$ distribution in the combined electron and muon 2-jet channel, showing the central unfolded values and statistical and systematic uncertainties in summary as well as a detailed list of signal and background systematics. Also shown, and included in the systematic uncertainty, is the effect of applying the Bayesian unfolding algorithm with one fewer iteration.

Combined, 2 Jet				
	Cross Section [nb/GeV]			
Bin [GeV]	25 - 30	30 - 40	40 - 60	60 - 140
Expected (Alpgen)	73.6	51.1	26.9	5.98
Measured	73.4	57.6	38.2	9.31
Stat. Unc.	(12%)	(8%)	(14%)	(23%)
Stat. Unc. (MC)	(3%)	(2%)	(2%)	(2%)
Sys. Unc.	(26%)	(22%)	(21%)	(31%)
AlternativeUnfolding	(5%)	(3%)	(2%)	(0%)
JES	(19%)	(19%)	(14%)	(18%)
JER	(14%)	(4%)	(5%)	(2%)
C-Tag	(1%)	(1%)	(2%)	(2%)
B-Tag	(6%)	(6%)	(6%)	(1%)
L-Tag	(0%)	(1%)	(3%)	(6%)
ISR/FSR	(2%)	(3%)	(2%)	(19%)
HFORME	(1%)	(1%)	(3%)	(1%)
LeptonResolution	(1%)	(0%)	(1%)	(3%)
TriggerSF	(1%)	(1%)	(1%)	(2%)
LeptonRecoSF	(1%)	(1%)	(1%)	(1%)
METCluster	(2%)	(3%)	(8%)	(10%)
METPileup	(2%)	(1%)	(5%)	(5%)
ShapeB	(5%)	(5%)	(6%)	(8%)
ShapeC	(1%)	(1%)	(1%)	(0%)
ShapeL	(1%)	(1%)	(1%)	(3%)
ShapeQCD	(1%)	(3%)	(4%)	(0%)

Table C.18: Correlation matrices of statistical (left) and systematics (right) uncertainties for the $p_{\mathrm{T}}^{b-\mathrm{jet}}$ distribution in the combined electron and muon 2-jet channel.

1	0.585	-0.45	-0.08	1	0.900	0.550	0.544
	1	0.069	-0.29		1	0.795	0.719
		1	-0.20			1	0.775
			1				1